THE UNIVERSITY *of* EDINBURGH

Bioinspired Materials and Membranes for Energy-efficient Liquid Separation

Ting CHEN

A thesis submitted for the Degree of Doctor of Philosophy

The University of Edinburgh

2021

Declaration

The author declares that the work undertaken in this thesis has been carried out and composed by her unless stated or acknowledged otherwise. This work has not been submitted or accepted in the fulfillment of any other degree or qualification, at any other university.

Ting CHEN

Acknowledgements

I would first like to express my deepest sense of thanks and gratitude to my principal supervisor Dr. Yi Huang for all of his guidance and wisdom throughout my PhD study. It would not have been possible to finish this PhD project, have my publications, and write this thesis without the support of Dr. Yi Huang. I deeply appreciate the continuous support, unwavering patience, and motivation from Dr. Yi Huang. His timely advice and kind supervision have helped me to a very great extent to accomplish this work. His vision, dynamism, and immense knowledge for research deeply inspire me. His cheerful enthusiasm has encouraged me all the time to overcome difficulties during my PhD study. All the things I learned from Dr. Huang are invaluable to me for the rest of my life. It is a great honour to work under his supervision. I will always be grateful for having the opportunity to study in the Huang Research Group.

I would like to thank my second supervisor Dr. Andrea Joana Correia Semiao for her precious advice on my work, including my annual review reports, presentations, and my manuscripts for publication. Besides my supervisors, I would like to thank Professor Huanting Wang at Monash University for his valuable suggestions on my work in Chapter 4 and Chapter 5 of this thesis. I would also like to thank Professor Xianfeng Fan for his useful suggestions on my work in Chapter 4 of this thesis. My sincere thanks also go to Professor Maria-Chiara Ferrari, Professor Lev Sarkisov, Dr. Sam Lau, Dr. Norbert Radacsi, Dr. Leonardo Rios Solis, for their advice and support for my PhD work. I am also grateful for the laboratory assistance from Dr. Nicholas Odling, Mr.

Fergus Dingwall, and Mr. Stuart Martin.

I would also like to acknowledge with gratitude, the financial support from the University of Edinburgh. Without the Edinburgh Global Research Scholarship, and the Principal's Career Development PhD Scholarship from the University of Edinburgh, it would be difficult for me to finish my PhD work.

I also owe my deepest gratitude to my dear family for their love, caring and tremendous support throughout my life. Also, I express my thanks to my friends and colleagues at the University of Edinburgh. Their caring and help have contributed a lot to making my PhD life in Edinburgh a pleasant and interesting experience.

Abstract

Liquid separations play a significant role in a wide range of industrial applications, including water purification, food and pharmaceutical industries. Membrane separation has been proved to be promising for liquid separations due to its high efficiency, low operation cost and energy-saving performance. Despite progress in recent decades, the development of advanced materials and membranes for energy-efficient liquid separations is highly desired. Fortunately, nature provides a rich source of inspiration for fresh ideas in smart materials design. This work focuses on the design of films, nanomaterials, and membranes with bioinspired superwetting surface properties or nacre-like lamellar structures for energy-efficient liquid separations, including oil/water separation and molecular separation.

Bioinspired materials with superwetting surfaces have attracted widespread interest, particularly for liquid separations. Although considerable progress has been made in the past decade, it is still challenging to scale up the application of bioinspired materials in liquid separations. This is because the majority of existing bioinspired materials are either expensive to fabricate or involve energy-intensive, and/or time-consuming production processes. In this work, energy-effective and time-saving methods were explored to develop bioinspired materials. Zeolitic imidazolate frameworks (ZIFs), were employed as major building blocks for the bioinspired materials and membranes design. Applications of the prepared bioinspired materials in oil/water separation and molecular separation in organic solvents were systematically investigated.

Inspired by superwetting surfaces in nature, mesh films with switchable superwettability were fabricated using two dimensional ZIF-L nanoplates. The preparation process was completed within 2 hours through a rapid seeding and secondary growth process under ambient conditions. The ZIF-L mesh films exhibited in-air superamphiphilic, underwater superoleophobic and underoil superhydrophobic properties, and showed outstanding performance in solely-gravity-driven oil/water mixture separation. A prewetting-induced switchable permeation function was found for the hierarchical ZIF-L surface, achieving both “oil-blocking” and “water-blocking” separation.

Chemical stability is one of the most important factors affecting the long-term applications of ZIFs based materials in liquid separations. To enhance the chemical stability of ZIFs, a novel oil/water interfacial assembly strategy was developed to prepare oleic acid (OA) decorated ZIFs, which was denoted as ZIF−OAs. The prepared ZIF−OAs exhibited bioinspired superhydrophobic surface properties and showed exceptional water stability and chemical stability. Furthermore, a simple sequential drop-casting method was developed to coat as-synthesized ZIF−OAs onto porous membrane surfaces. The molecular separation performances of the prepared ZIF−OAs coated membranes were explored.

Another important aspect considered in this work for realizing energy-efficient liquid separation is enhancing the permeation rate of the membrane materials. Membranes with ultrafast solvent transport rates can largely reduce the energy consumption in the separation processes. To enhance the membrane permeability, graphene oxide (GO)/ZIF-8 composite membranes with ultrafast diffusion nanochannels were developed. ZIF-8 nanocrystals were intercalated in the GO interlayers via *in situ* self-assembly using a facile vacuum-assisted filtration method. The obtained GO/ZIF-8 membranes showed a nacre-like lamellar structure and exhibited well-defined nanochannels with ultrafast solvent transport. Moreover, these membranes provided selective molecular separation performance for various binary dye mixtures with high separation efficiencies.

The results presented in this thesis make a valuable contribution to promoting the facile preparation of bioinspired materials and membranes. The fabrication strategies developed in this work are time-saving and energy-effective, thus are beneficial for the mass production of bioinspired materials at a large scale. In addition, this work could also contribute to promoting the practical applications of bioinspired materials and membranes in liquid separations. The smart superwetting surface properties, exceptional chemical stability, and superior permeability enable the materials and membranes to realize energy-efficient oil/water separation and molecular separation with long-term stability.

Contents

List of Publications

1. **T. Chen**, F. S. Butt, M.Zhang, X. Wei, A. Lewis, N. Radacsi, A. J. C. Semiao, J. Han, Y. Huang*, **2021**. Ultra-permeable zeolitic imidazolate frameworks-intercalated graphene oxide membranes for unprecedented ultrafast molecular separation. **Chem. Eng. J.**, 419, 129507.

2. **T. Chen**, A. Lewis, Z. Chen, X. Fan, N. Radacsi, A. J. C. Semiao, H. Wang, Y. Huang*, **2020**. Smart ZIF-L mesh films with switchable superwettability synthesized via a rapid energy-saving process. **Sep. Purif. Technol.**, 240, 116647.

3. Y. Huang, Y. Jiao, **T. Chen**, Y. Gong, S. Wang, Y. Liu, D. S. Sholl, K. S. Walton*, **2020**. Tuning the Wettability of Metal−Organic Frameworks via Defect Engineering for Efficient Oil/Water Separation. **ACS Appl. Mater. Interfaces.**, 12, 34413-34422. (co-first author)

4. A. Lewis, **T. Chen**, F. Butt, X. Wei, N. Radacsi, X. Fan, Y. Huang*, **2021**. Facile synthesis of hierarchical ZIF-L hollow fiber membranes via continuous fluid circulation. **Nanoscale**, DOI: 10.1039/D1NR03112K.

5. **T. Chen**, X. Wei, D. Morin, V. A. Sarai, Y. Huang*, **2021**. Designing energy-efficient separation membranes: knowledge from nature for a sustainable future". (submitted)

6. X. Wei, **T. Chen**, F. S. Butt, Y. Huang*, **2021**. A facile method for the preparation

of ZIF-8 coated materials for energy-efficient oil/water separations. (co-first author, ready for submission)

7. **T. Chen**, X. Wei, N. Radacsi, Y. Huang*, **2021**. Direct synthesis of exceptionally water-stable 1D MOF nanotubes via rolling up 2D MOF nanosheets. (ready for submission)

(*denotes the corresponding author)

List of Figures

List of Tables

List of Symbols

γ_{lv} ..... Surface tension

π ..... Pi

m ..... Mass of graphene oxide

ρ ..... Density

V ..... Volume

h ..... Membrane thickness

S ..... Membrane area

F ..... Permeance of the membrane

A ..... Effective filtration area

Δt ..... Filtration time

ΔP ..... Applied pressure

ΔP_e ..... Experimental intrusion pressure

R ..... Rejection rate

C_p ..... Concentration of oil or dyes in the permeate solution

C_f ..... Concentration of dyes in the feed solution

C_0 ..... Concentration of oils in the feed solution

θ ..... Contact angle of an ideal smooth surface

θ' ..... Contact angle of an ideal smooth surface and a rough surface

r_f ..... Non-dimensional surface factor

f ..... Area fraction of the solid surface

g.....Acceleration of gravity

h_{max}.....Maximum height of the oil or water

Q.....Amount of adsorbed dyes

Abbreviations and Acronyms

MOF .....Metal organic frameworks

ZIF.....Zeolitic imidazolate frameworks

SS..... Stainless steel

OA.....Oleic acid

GO .....Graphene oxide

rGO..... Reduced graphene oxide

SLGO .....Single-layer graphene oxide

2D.....Two-dimensional

1D..... One-dimensional

CA.....Contact angle

OCA.....Oil contact angle

WCA.....Water contact angle

AAO..... Anodic Aluminum Oxide

DI .....Deionised

UF .....Ultrafiltration

NF ..... Nanofiltration

OSN .....Organic solvent filtration

DOPA 3,4-dihydroxy-L-phenylalanine

PDA .....Polydopamine

PS-b-P2VP .....Polystyrene-block-poly(2-vinylpyridine)

PS-b-P4VP ..... Polystyrene-block-poly(2-vinylpyridine)

PS-b-PAA ..... Polystyrene-block-poly (acrylic acid)

PVA ..... Poly (vinyl alcohol)

PEC ..... Polyelectrolyte complex

PDMS ..... Polydimethylsiloxane

SNIPS ..... Self-assembly and nonsolvent-induced phase separation

PEI ..... Polyetherimide

PSS ..... Poly (sodium 4-styrene-sulfonate)

PAN ..... Polyacrylonitrile

PS ..... Polystyrene

MOS_2 ..... Molybdenum disulfide

WSe_2 ..... Tungsten diselenide

PTFE ..... Polytetrafluoroethylene

PVDF ..... Polyvinylidene fluoride

CVD ..... Chemical vapor deposition

UV ..... Ultraviolet

POSS ..... Polyhedral oligomeric silsesquioxane

NIPS ..... Nonsolvent-induced phase separation

HFP ..... Hexafluoropropylene

FD-POSS ..... Fluorinated decyl polyhedral oligomeric silsesquioxanes

FAS ..... Fluorinated alkyl silane

PNIPAM ..... Poly (N-isopropylacrylamide)

P(3-MTH) Poly-3-methylthiophene

SI-ATRP..... Surface initiated atom transfer radical polymerization

SET-LRP.....Single electron transfer-living radical polymerization

RAFT.....Reversible addition-fragmentation chain-transfer

APTES.....Aminopropyltriethoxysilane

TA..... Tannic acid

TFC.....Thin-film composite

TFN..... Thin-film nanocomposite

BSA.....Bovine serum albumin

PEO .....Poly(ethylene oxide)

RB..... Rose bengal

RB5..... Reactive black 5

RhB.....Rhodamine B

MW.....Molecular weight

COF .....Covalent organic framework

g-C_3N_4.....Graphitic carbon nitride

MB .....Methylene blue

NR.....Neutral red

UA..... Uniblue A

MO.....Methyl orange

AFM ..... Atomic force microscopy

SEM.....Scanning electron microscope

XRD.....X-Ray Diffraction

FT-IR.....Fourier-transform infrared spectroscopy

TGA.....Thermogravimetric analysis

Chapter 1: Introduction

1.1 Project background and motivation

Liquid separations, such as oil/water separation [1], desalination [2] and organic solvent nanofiltration (OSN) [3], play a major role in a wide range of industrial applications, including water purification, food and pharmaceutical industries. These separation processes have three primary purposes: concentration, fractionation, and purification [4]. Energy-efficient liquid separation techniques are highly desired in various industrial processes to address energy and environmental challenges. Conventional techniques that have been commonly used for liquid separations in industry mainly include: distillation, evaporation, condensation, and flotation [4, 5]. Although an effective separation can be achieved, these traditional techniques usually have limitations of complex operation, high energy consumption, and low separation efficiency [4]. In recent decades, membrane separation technique has been proven to be promising for energy-efficient liquid separations due to their convenient operation, easy regeneration, and reduced secondary pollution compared to conventional techniques [4, 5]. The development of advanced materials or techniques for high-performance membranes is of vital importance for improving energy-efficient liquid separations.

Membrane separation is an emerging separation technique and has been experiencing a blossoming since the early 1990s. With the rapid advancement in recent decades, membrane separation-based techniques are now well established and have found

diverse applications, including gas separation [6], air pollution control [7], water purification [8], desalination [9], and wastewater reclamation [10], etc. The rising demand for the application of membrane separation-based techniques naturally leads to the desire to develop novel membranes with superior performance as well as long-term sustainability. Key design criteria for an effective membrane including the following factors: decently sized pores, a narrow pore size distribution, a thin active layer, a high level of chemical and physical stability, robust mechanical strength, and meanwhile uncomplicated fabrication technique [11]. Extensive efforts have been invested in designing new membrane materials/structures in recent decades. However, there are still limitations such as high production costs, high energy consumption and low sustainability [12]. Developing approaches to optimizing membrane production, functionalities, and sustainable improvement is still highly desired in the field of membrane design. Fortunately, a blueprint for efficiently and sustainably designing novel membrane materials with improved structures have been discovered, that is: nature [13].

Nature is indeed a school for scientists and engineers. In fact, nature has far superior capabilities to humans, presenting lasting solutions to the arising challenges. For example, synthetic membranes always exhibit a trade-off between permeability and selectivity, while biological membranes in nature are usually both highly permeable and highly selective [10]. During the 4.5 billion years of evolution, nature has developed a multitude of highly effective principles, functional dynamics, and energy-efficient

processes [14]. In all living organisms, nature has introduced a diversity of mechanisms, architectures, and systems. As a result, natural materials exhibit unique and fascinating characteristics. More importantly, nature built such highly sophisticated materials with merely a few elements under ambient and atmospheric conditions. This provides materials scientists with exceptional inspirations for designing materials with maximized functionality while minimized energy [15]. Hence, remarkable knowledge can be learnt from nature in terms of developing effective materials, structures, processes and systems with reduced costs in energy and materials [15]. Applying knowledge from nature can effectively motivate nonconventional and innovative approaches to synthesizing new materials and modifying their properties for various applications [15]. Especially, consulting models and principles from nature have become a shortcut to designing novel efficient membranes for energy and environmental applications.

Over the course of the “natural selection” process, living organisms in nature have already completed the “benefit-cost study” by experimenting with diverse combinations of compositions, structures, and properties, achieving optimized designs for particular performances [16]. For instance, some living organisms in nature demonstrate fascinating surface superwetting properties due to a combination of unique surface compositions and micro/nanoscale surface roughness. In this regard, nature as an enormous laboratory has provided an exhaustive “solution manual” [16] with sophisticated design prototypes for membrane preparation [17]. The successful transfer

of innovation from nature to engineered design requires appropriate scientific approaches [17]. In the field of membrane design, this transfer can be achieved through two categories of approaches: (1) studying biological membrane systems as models for membrane preparation, leading to biomimetic membranes. (2) implementing inspiring principles originating from nature for membrane functionalization, producing bioinspired membranes. It should be noted that in some literature the term - biomimetics and bioinspiration are presented as if they were synonyms [18, 19]. This might be appropriate when one indicates the final outcome of these approaches, as both biomimetics and bioinspiration can represent inventions that are achieved by using knowledge originating from nature [18]. However, there is an essential difference between them if one focuses on the process of these approaches. From a process point of view, biomimetics refers to the study of selected biological systems as models for engineering design or the imitation of natural solutions for practical problems [18, 20]. Bioinspiration, on the other hand, indicates the implementation of ideas originating from nature in a creative way, attempting to construct novel design solutions to engineering challenges [18, 20].

Although great progress has been made in the development of bioinspired materials in the last decades, it is still challenging to realize the facile fabrication of bioinspired membranes for energy-efficient separations. In this PhD project, a series of materials and membranes with bioinspired surface properties have been developed for energy-efficient liquid separations. Zeolitic imidazolate frameworks (ZIFs), including ZIF-L

and ZIF-8 were selected as candidate materials for preparing different bioinspired materials due to their mild preparation conditions and comparatively good stability under liquid conditions. First, inspired by the low oil adhesion of shark skin underwater, zeolitic imidazolate frameworks (ZIFs) coated mesh films with switchable superwetting properties have been developed for gravity-driven oil/water mixture separations. ZIF-Ls were selected as the coating material because their unique two-dimensional morphology and intergrowth behavior are beneficial for producing nanoscale surface roughness which is crucial for constructing superwetting surfaces. Then inspired by the water repellent properties of lotus leaf surface, ZIFs nanotubes with superhydrophobic surface properties have been prepared for enhanced stability under a water environment. Furthermore, ZIFs-coated porous polymeric membranes have been fabricated for small molecules separations. In addition, inspired by the lamellar strucuter of nacres, a graphene oxide-based lamellar membrane has been developed for dye molecules separations with enhanced solvent transport rate. ZIF-8 was selected as the intercalation material in GO interlayers because of its adsorption capability towards different organic dye molecules. In this way, not only could the permeability of the prepared lamellar membrane be enhanced due to expanded nanochannels, the overall rejection of the membrane could also be maintained.

The techniques developed in this thesis are expected to promote the industrial application of bioinspired materials and membranes for challenging liquid separations in the future. For example, the rapid seeding and secondary growth technique developed

in this work can be used to prepare bioinspired superwetting materials for efficient oily wastewater treatment. The oil/water interfacial assembly technique and the sequential drop-casting method designed in this work can be used to directly synthesize superhydrophobic MOF nanomaterials-based porous materials for efficient water purification. The *in situ* assembly technique presented in this work can be used to prepare various MOF-containing lamellar membranes for ultrafast selective molecular separations.

1.2 Thesis structure

This thesis is structured into 8 chapters.

In chapter 1, an introduction of the project background and motivation to this thesis was presented. The main objective and the contribution of this PhD project were briefly stated. Chapter 2 provides the literature review relevant to this project. Background information about bioinspired materials, including their design principles, synthesis methods, and applications in separation processes, were provided. In chapter 3, information about materials that have been used, and main methodologies that have been developed for different experiments in this work were provided.

Contents in chapter 4 to chapter 7 were the main body of this thesis. In these four chapters, experimental results and discussions on the preparation of a series of bioinspired materials and their applications in liquid separations are presented.

In chapter 4, the preparation of novel ZIF-L coated mesh films with shark skin-like superwetting properties and their application in switchable oil/water separations are studied. A simple seeding and secondary growth method were developed for the preparation of ZIF-L coated mesh films. The morphologies of surface properties of the prepared ZIF-L coated mesh films are characterized. The switchable oil/water separation performance, i.e., the "oil-blocking" separation and the "water-blocking" separation, of the ZIF-L coated mesh films were explored. The chemical stability and cyclic separation performance of the ZIF-L coated mesh films are also discussed.

Chapter 5 investigates the preparation of oleic acid (OA) modified ZIF (ZIF−OA) nanostructures with lotus leaf-like superhydrophobic properties and enhanced water stability compared to ZIF-L synthesized in chapter 4. An oil/water interfacial assembly approach was developed for the synthesis of ZIF−OA nanostructures with two-dimensional morphology or one-dimensional nanotube morphology. The influence of the synthesis conditions on the morphology and size of the synthesized ZIF−OA nanostructures are investigated. Characterizations on the surface property of the ZIF−OA nanostructures are discussed. A comparison of the chemical stability of the synthesized ZIF−OA nanostructures with regular ZIF-L and ZIF-8 is presented.

In chapter 6, superhydrophobic ZIF−OAs synthesized in chapter 5 were coated onto porous membrane surfaces and applied for molecular separations. The optimization of the preparation methods, including a contra-diffusion method and a sequential drop-casting method, is discussed. The influence of preparation conditions on the

morphology and surface property of ZIF−OAs coated membrane is investigated. The organic dye molecules separation performance of ZIF−OAs coated membranes is explored.

Chapter 7 presents the preparation of graphene oxide (GO)/ZIF-8 composite membranes with nacre-like lammelar structures for molecular separations with enhanced permeability compared to the membranes prepared in chapter 6. A vacuum filtration assisted *in situ* assembly strategy was developed for the intercalation of ZIF-8 nanocrystals into GO interlayers. Characterizations on the morphology and surface property of the prepared GO/ZIF-8 lamellar membranes are presented. The influence of the synthesis conditions on the properties of GO/ZIF-8 membranes is discussed. The permeation performance for different organic solvents, and the separation performance for different organic dye molecules of the GO/ZIF-8 lamellar membranes are explored.

Chapter 8 presents the major conclusions and highlights the significance of this work. The limitations of this study are addressed, and suggestions for future work are also proposed.

1.3 Reference

[1] Gupta, RK., Dunderdale, GJ., England, MW., Hozumi, A. Oil/water separation techniques: a review of recent progresses and future directions. J. Mater. Chem. A. 2017; 5: 16025-16058.

[2] Elimelech, M., Phillip, W. A. The future of seawater desalination: energy, technology, and the environment. Science. 2011; 333: 712-717.

[3] Koh, DY., McCool, BA., Deckman, HW., Lively, RP. Reverse osmosis molecular differentiation of organic liquids using carbon molecular sieve membranes. Science. 2016; 353, 804-807.

[4] Li X, Liu Y, Wang J, Gascon J, Li J, Bart VB. Metal–organic frameworks based membranes for liquid separation. Chem. Soc. Rev. 2017; 46, 7124-7144.

[5] Koros WJ., Zhang C. Materials for next-generation molecularly selective synthetic membranes. Nat. Mater. 2017;16, 289-297.

[6] Qiao Z, Zhao S, Sheng M, Wang J, Wang S, Wang Z, Zhong C, Guiver MD. Metal-induced ordered microporous polymers for fabricating large-area gas separation membranes. Nat. Mater. 2019; 18: 163-168.

[7] Zhu Q, Tang X, Feng S, Zhong Z, Yao J, Yao Z. ZIF-8@SiO_2 composite nanofiber membrane with bioinspired spider web-like structure for efficient air pollution control. J. Membr. Sci. 2019; 581:252-261.

[8] Liu T, Liu X, Graham N, Yu W, Sun K. Two-dimensional MXene incorporated graphene oxide composite membrane with enhanced water purification performance. J.

Membr. Sci. 2020; 593:117431.

[9] Yao Y, Zhang P, Jiang C, DuChanois RM, Zhang X, Elimelech M. High performance polyester reverse osmosis desalination membrane with chlorine resistance. Nat. Sustain. 2021; 4: 138-146.

[10] Dong X, Ge Q. Metal Ion-bridged forward osmosis membranes for efficient pharmaceutical wastewater reclamation. ACS Appl. Mater. Interfaces 2019; 11: 37163-37171.

[11] Park HB, Kamcev J, Robeson LM, Elimelech M, Freeman BD. Maximizing the right stuff: The trade-off between membrane permeability and selectivity. Science. 2017; 356: 6343.

[12] Wagh P, Escobar IC. Biomimetic and bioinspired membranes for water purification: A critical review and future directions. Environ Prog Sustain Energy. 2019;38: e13215.

[13] Perera AS, Coppens MO. Re-designing materials for biomedical applications: from biomimicry to nature-inspired chemical engineering. Philos Trans A Math Phys Eng Sci. 2019; 377: 20180268.

[14] Speck O, Speck T. An overview of bioinspired and biomimetic self-repairing materials. Biomimetics. 2019; 4: 26.

[15] Mano JF. Biomimetic approaches for biomaterials development. John Wiley & Sons. 2013.

[16] Naik RR, Singamaneni S. Introduction: bioinspired and biomimetic materials. Chem. Rev. 2017; 117: 12581-12583.

[17] Fish FE, Beneski JT. Evolution and bio-inspired design: natural limitations.

Biologically Inspired Design. 2014; 287-312.

[18] Fayemi PE, Wanieck K, Zollfrank C, Maranzana N, Aoussat A. Biomimetics: process, tools and practice. Bioinspir Biomim. 2017; 12: 011002.

[19] Vincent JF, Bogatyreva OA, Bogatyrev NR, Bowyer A, Pahl AK. Biomimetics: its practice and theory. J. R. Soc. Interface. 2006; 3: 471-482.

[20] Ralston E, Swain G. Bioinspiration--the solution for biofouling control? Bioinspir Biomim. 2009; 4: 015007.

Chapter 2: Theoretical background and literature review

2.1 Inspiration from nature for bioinspired materials design

Considerable effort has been devoted to designing advanced materials with improved structures. In recent years, researchers have become increasingly interested in borrowing concepts or learning strategies from nature for designing new materials for energy-efficient separations. This is motivated by the fact that after 4.5 billion years of evolution, nature has become a school for scientists and engineers, offering astonishing models for inspiration. In the area of materials science, inspirations from nature for materials design mainly include self-assembly behaviour in nature, biomineralization, organisms with superwetting surfaces, and bioadhesion.

2.1.1 Self-assembly in nature

Self-assembly refers to the spontaneous organization of a disordered collection of individual units into sophisticated arrangements without external control [1]. The self-assembly process is ubiquitous in nature. In natural systems, self-assembly allows chemically simple molecular building blocks to be converted into complicated supramolecular structures with optimized properties, morphology and functionality [2]. For example, natural proteins which are the element basis of life, tend to self-assemble to form highly ordered architectures in biological systems [3]. Through protein self-

assembly, a remarkably complex set of structures that encompasses varying length scales and structural properties are produced in living organisms ranging from bacteria to humans [1]. Self-assembly has been a source of inspiration for the design of synthetic materials with well-defined structures and desired functions. In particular, a range of highly ordered nanoporous membranes has been rationally designed inspired by the concept of self-assembly.

Nature uses self-assembly to elegantly organize biological systems. Over the past two decades, molecular self-assembly has gained increasing interest in materials design as it offers a great platform for constructing materials with a high level of precision under mild conditions [4]. Understanding self-assembly principles is essential for the successful development of synthetic materials with hierarchal structures and desired properties. The molecular self-assembly process is predominantly driven by a series of non-covalent interactions, including electrostatic interactions, hydrophobic effect, hydrogen bonding, aromatic stacking (π-π stacking), van der Waals interaction, and metal coordination [4]. These interactions are individually weak, but collectively powerful enough to produce highly stable assemblies. By exquisitely regulating these weak yet powerful interactions, self-assembling molecules aggregate from a less ordered state to a final highly ordered state [1].

A wide range of self-assembling biomolecules, such as proteins, phospholipids and carbohydrates, have been utilized by nature to construct biological functional materials. Among these building blocks, proteins demonstrate one of the most fascinating

examples of self-assembly [5]. In fact, protein self-assembly is one of the best strategies to produce ordered supramolecular structures. In biological systems, proteins are assembled to form materials with a structural hierarchy ranging from the nano- to the macroscale. One of the well-known examples is silk fibroin, which is a self-assembling protein produced by silkworms. Silk fibroin is essentially a block copolymer composed of a heavy chain polypeptide (~390 kDa) and a light chain polypeptide (~25 kDa) linked by a single disulfide bond [6]. During the silk fibroin self-assembly process, hydrogen bonding and hydrophobic interactions are formed between fibroin molecules, generating a structural transition in fibroin from random coil to stacked β-sheet structure. Inspired by the principles in the protein self-assembly processes, artificial building blocks have been designed to assemble into specific architectures with desired properties. In particular, a class of block copolymers have been designed to assemble into nanostructured membranes with a narrow pore size distribution. Moreover, liquid crystal polymers have been developed to assemble into nanoporous membranes with sub-nanometer pores.

2.1.2 Biomineralization in nature

Biominerals are a class of natural composite materials manufactured by living organisms via the process known as biomineralization which has been used by nature for over 500 million years in the development of life [7]. Biomineralization processes occur in a variety of species and tissues, such as marine shells, bone minerals, and tooth enamel [8]. With a high degree of control over composition, morphology and structure

during biomineralization, biominerals usually exhibit fascinating properties that surpass their synthetic counterparts. For example, the toughness of the nacre is 3000 times higher than its mineral constituent [9]. Moreover, the production of biominerals in living organisms is performed under mild conditions of ambient temperature, neutral pH, and an aqueous environment. This is highly energy efficient as opposed to synthetic technologies that mostly require complicated conditions or high energy consumption. Hence, biominerals have fascinated researchers for decades and provided rich inspirations for the design of biomimetic materials with enhanced functionality. Nacre, also known as the mother of pearl, is one of the most extensively studied biominerals, especially in the field of membrane design [10].

In the biomineralization process, inorganics with tunable size and well-designed morphology are generated in an organic matrix (proteins, lipids, chitin, etc.) under mild conditions. Meanwhile, the organic phase and the inorganic phase are typically arranged in a staggered manner, forming hierarchical hybrid nanostructures [10]. In this process, Organic matrixes not only serve as structural templates, but also play key roles in controlling the nucleation and growth of inorganic materials [11]. Learning from the mechanisms of biomineralization, biomimetic inorganic-organic composite membranes with hierarchical structures have been well explored. In particular, nacre has emerged as one of the most extensively studied models due to its special “brick-and-mortar” nanostructure.

Nacre is produced by some molluscs as the inner shell layer and is well-known for its

surprisingly high strength and high toughness. Nacre is composed of 95 wt% inorganic aragonite (a crystallographic form of calcium carbonate) nanoplatelets conjugated with 5 wt% organic biopolymer layers (protein and chitin) [12, 13]. These platelets (~200-500 nm thick) and bonding layers (~10-50 nm thick) are arranged in an alternating layered arrangement [14, 15], as shown in Figure 2.1.

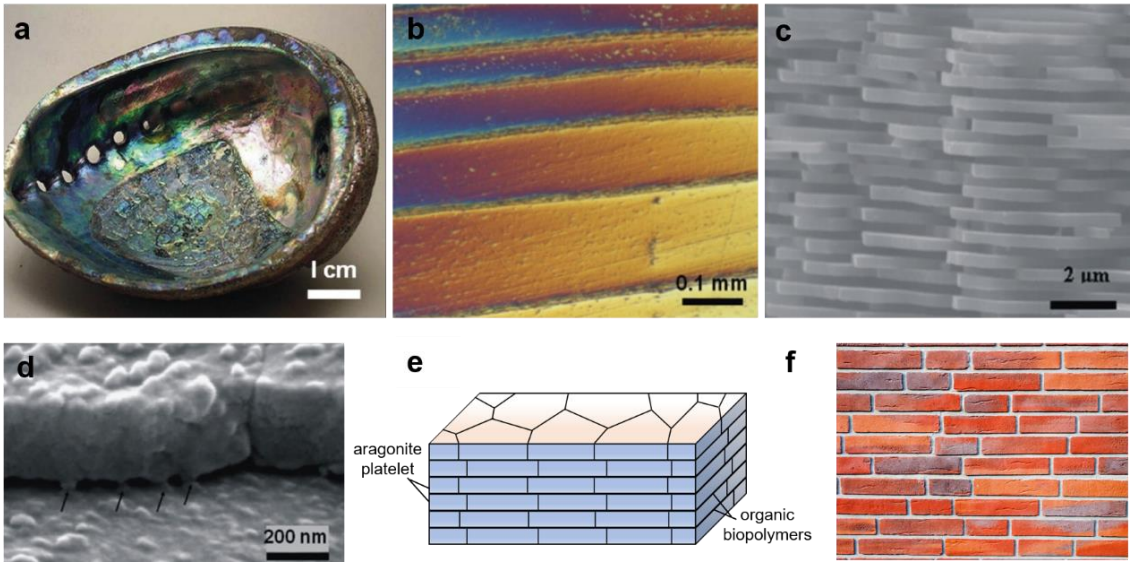

Figure 2.1. "Brick-and-mortar" hierarchical structure of an abalone nacre. (a)-(d) [15].

As shown in Figure 2.1, the peculiar arrangement leads to the formation of a hierarchical "brick-and-mortar" nanostructure with inorganic aragonite as bricks and organic biopolymers as the mortar connecting two adjacent inorganic layers [16]. The highly ordered "brick-and-mortar" arrangement combines the elasticity of organic layers and the strength of inorganic layers, enabling efficient loading transfer between the two phases [17]. As a result, nacre exhibits exceptionally excellent mechanical property that is superior to most synthetic ceramics and composites. In addition, nacre

displays continuous growth based on the mechanism known as the “Christmas tree” grow pattern and is able to self-heal once damaged. These extraordinary features make nacre a sophisticated model for designing laminated composite membranes with ultrahigh mechanical stability through biomimetic strategies [10].

2.1.3 Superwetting surfaces in nature

After billions of years of evolution, some living organisms in nature demonstrate fascinating surface superwettability, as shown in Figure 2.2. These superwetting biological surfaces provide perfect models for the development of functional surfaces with extreme wettability to solve engineering problems.

In general, superwetting biological surfaces that have been found in nature can be classified into four types: (i) superhydrophobic surfaces showing water-repellent performance in air, such as lotus leaf [18], rose petal [19], salvinia biloba [20], water strider leg [21], gecko feet [22] and butterfly wings [23] (Figure 2.2a-f); (ii) superhydrophilic surfaces showing exceptional water affinity in air such as nepenthes alata [24], calathea zebrina [25], ruellia devosiana [26], spider silk [27], tree frog [28], and lizard skin [29] (Figure 2.2g-l), (iii) underwater superoleophobic surfaces showing ultralow adhesive performance in water environment, such as shark skin [30], fish scale [31], clam shell [32], and snail shell [33] (Figure 2.2m-p), and (iv) superoleophobic surfaces showing ultralow oil adhesive performance in air, mainly including leafhoppers [34] and some springtails [35] (Figure 2.2q - t).

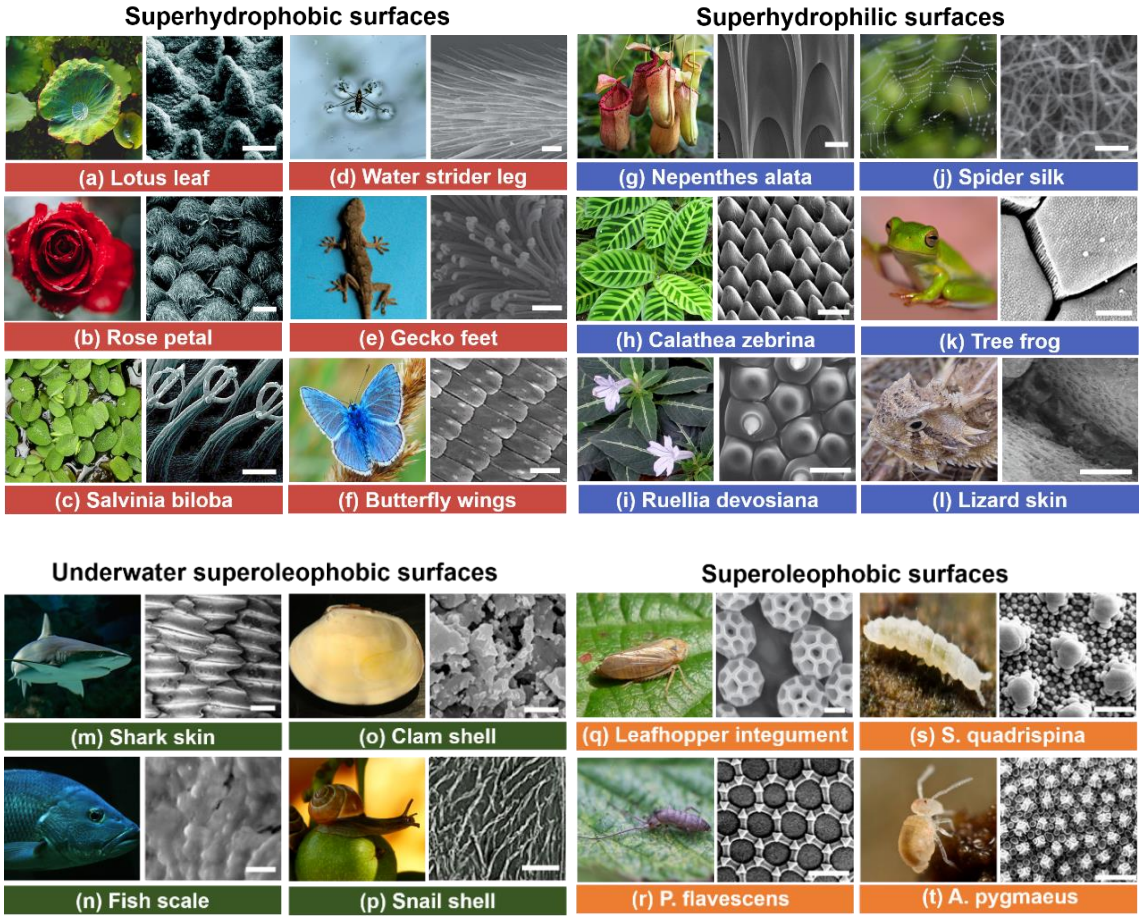

Figure 2.2. Superwetting biological surfaces in nature and their micro/nanoscale structures. (a) Lotus leaf, scale bar 10 µm [25], (b) rose petal, scale bar 10 µm [19], (c) salvinia biloba, scale bar 300 µm [25], (d) water strider leg, scale bar 20 µm [21], (e) gecko feet, scale bar 20 µm [22], (f) butterfly wings, scale bar 50 µm [23], (g) nepenthes alata, scale bar 20 µm [24], (h) calathea zebrina, scale bar 30 µm [25], (i) ruellia devosiana, scale bar 40 µm [26], (j) spider silk, scale bar 200 nm [27], (k) tree frog, scale bar 2.5 µm [28], (l) lizard skin, scale bar 100 µm [29], (m) shark skin, scale bar 100 µm [30], (n) fish scale, scale bar 2 µm [31], (o) calm shell, scale bar 1 µm [32], (p) snail shell, scale bar 20 µm [33], (q) leafhopper, scale bar 2 µm [34], (r), (s), (t) springtails, scale bar 2 µm [40].

Superhydrophobic surfaces refer to surfaces exhibiting apparent water (surface tension γlv = 72.1 mN/m) contact angles greater than 150° [36]. These surfaces usually demonstrate fascinating water-repellent performance due to their ultralow contact angle hysteresis. The most well-known natural prototype of a superhydrophobic surface is found on the lotus leaf. As reported by Barthlott and Ehler in 1977 for the first time [18], lotus leaves allow waterdrops to bead up into spheres and easily roll off whilst collecting adherent dirt along the way, presenting self-cleaning property which is also known as the "lotus effect". The "lotus effect" is attributed to a clever design of the lotus leaf that combines a hierarchically rough nanostructure (Figure 2.2a) and a waxy nonpolar coating, which both discourage surface interactions with water. Another well-known prototype of the superhydrophobic surface is the rose petal. Feng et al. [19] first reported that the red rose petal surface comprises a close array of microscale papillae with many nanoscale wrinkled folds on the top of each micro papillae (Figure 2.2b). These hierarchically organized micro- and nanostructures disfavour the spreading of waterdrops on the rose petal, thus forming the superhydrophobic surface. Salvinia leaf (Salvinia Biloba) which is a floating fern also displays superhydrophobic surface property [20]. A Salvinia leaf surface is composed of densely packed microscale complex hairs (Figure 2.2c) that are covered by a layer of hydrophobic nanoscale wax crystals [25]. The synergetic effect of the hairy microstructure and wax layer enable the Salvinia leaf to retain an air film for up to months when positioned underwater. Superhydrophobic hairy surface microstructures are also found in animals, such as water striders and geckos [25]. Water striders distinguish themselves by having the

unusual ability to skip across the water surface. In 2004, Gao et al. [21] revealed that water strider (Gerris remigis) legs are covered by thousands of microscopic hairs (Figure 2.2d) with fine nanogrooves. This multiscale hierarchical structure endows the water strider legs with superhydrophobicity and thus strong water resistance as well as supporting force. Thereby, water striders are able to stay afloat even in a rainstorm or in waves. Geckos are well-known for their ability to scale vertical walls. The high adhesion force of the gecko foot arises from hundreds of microscale hairs called setae (Figure 2.2e), which spits off into hundreds of nanoscale bristles called spatulae [22]. In 2002, Autumn et al. [37] first reported that gecko setae are superhydrophobic with a water contact angle of ~160º. When waterdrops contact the gecko foot, they tend to clump together and ultimately self-propelled off the surface due to the superhydrophobic hairy microstructures. The self-cleaning property can also be found in butterfly wings. In 2007, Zheng et al. [23] first demonstrated that the butterfly (Morpho aega) wings are superhydrophobic with directional adhesion to waterdrops. It was revealed that the butterfly wing surfaces are composed of densely packed quadrate scales that overlap each other (Figure 2.2f). Each scale surface consists of ridging nanoscale stripes that are stacked by tilted cuticle lamellae along the radial outward direction. Hence, a waterdrop easily rolls off the wing surfaces along the radial outward direction once the butterfly waves its wings.

Superhydrophilic biological surfaces also widely exist in nature. For example, Nepenthes alata which is a tropical pitcher plant has a superhydrophilic peristome

surface. Continuously directional water transport was observed on the peristome because of a two-order hierarchy of parallel microgrooves on the surface (Figure 2.2g) [24]. Calathea zebrina which is s a perennial foliage plant allows a water droplet to completely spread with a CA of 0º on its leaf surface within a few seconds [25]. Uniform microscale conical cells on the leaf surface are found to be responsible for such high hydrophilicity (Figure 2.2h). Ruellia devosiana which is a green ornamental plant displays a fascinating rapid spreading of water on its leaf surface. A water droplet can completely spread with a CA of 0º within less than 0.3 s, and there are no other plant species known to have comparable water spreading ability [26]. Such excellent superhydrophilicity is attributed to a combination of various microstructures (e.g., conical cells, hydrophilic glands, multicellular hairs and hair-papilla) on the leaf surface (Figure 2.2i) [26]. Spider silk is able to capture and hold water on a dewy morning, forming stunning pearl-like water drops on the silk web. In 2010, Zheng et al. [27] revealed that the water-collecting ability of a cribellate spider is due to a unique spindle-knots fiber structure in the silk. The wettability of the silk is enhanced by highly hydrophilic nanofibrils (Figure 2.2j), which favours the condensation of water drops. Tree frogs which spend a major portion of their lifespans in trees are remarkable for their ability to cling to a variety of surfaces using adhesive toe pads. The adhesive wetting state of tree frog toe pads benefits from the epidermis with microscale peg-studded hexagonal cells (Figure 2.2k) and superhydrophilicity [28]. Lizards that usually live in semiarid/arid regions on the planet also have the moisture-harvesting capability. Their special skin enables them to capture water sources even in a scorching

environment. In 2015, Comanns et al. [29] demonstrated that a water droplet is able to spread on the integument of a Texas horned lizard within 5 s, by means of a network of interconnected capillary channels between the scales (Figure 2.2l).

Nature has also created biological surfaces that are able to repel low surface tension liquids such as oils, namely superoleophobic surfaces. In 2009, Liu et al. [31] reported the unique underwater superoleophobic behaviour of fish scales. Indeed, fishes are found to keep their body clean even if in oil-contaminated water. It was revealed that the fish scale is composed of oriented micro papillae with rough surfaces (Figure 2.2m). The hierarchical structures enable the fish scale to trap water and form a water barrier that effectively repels oils, thus resulting in underwater superoleophobicity. This unique low-adhesive superoleophobic property has also been found in sharks. The shark skin is covered by dermal denticles which are ribbed with longitudinal microgrooves (Figure 2.2n), allowing an underwater drag reduction ability as well as underwater superoleophobicity [30, 38]. Similarly, the clam shell was also found to possess the low-adhesive superoleophobic property underwater. A synergetic effect of high energy composition of $CaCO_3$ and microscale hierarchical surface structure (Figure 2.2o) is responsible for the underwater superoleophobicity [32]. Snails which usually come out on rainy days exhibit similar superoleophobic properties on their shell. A snail shell is composed of aragonite and a protein top layer. The surface of a snail shell shows a rough structure consisting of line grooves, (Figure 2.2p) which allows the shell to trap water molecules to repel oils [33].

Although the above-mentioned biological surfaces have excellent superoleophobicity underwater, they are usually oleophilic in air. According to theoretical models (i.e., Young equation, Wenzel and Cassie–Baxter equations), superoleophobic surfaces that are able to resist the wetting of low surface tension liquids (γ_{lv} =18~33 mN/m) require extremely low surface energy [35]. Among synthetic materials, only a few chemicals like perfluorinated compounds meet this requirement [38]. In 2013, Rakitov and co-workers [34] reported that leafhoppers can resist the wetting of water as well as low surface tension liquids like diiodomethane and ethylene glycol with the average CAs of 165º–172º, indicating extraordinary superhydrophobicity and superoleophobicity. The integuments of these leafhoppers are coated by brochosomes which are hollow proteinaceous nanospheres with honeycombed walls (Figure 2.2q). The brochsome-coated integuments are detected to possess an apparent surface free energy as low as 0.74 mN/m. Another important example of a superoleophobic surface is found in springtails, also known as collembola [35]. Springtails often live in wet soil, or damp organic materials like decaying straw and rotting leaves, where water is severely contaminated by hazardous microorganisms [35, 39]. As skin-breathing arthropods, springtails have developed excellent superoleophobic properties on their cuticles to survive in this environment. Nickerl and co-workers [40] investigated the microstructures of 40 different species of springtails. They found that these springtails skins are covered by highly ordered microstructures, such as hexagonal or rhombic comb-like patterns (Figure 2.2r) and hexagonal patterns with secondary granules (Figure 2.2s, t). More importantly, the profiles of the ridges and granules are negatively

overhung, forming a re-entrant surface topography which provides the basis for the superoleophobic property [39-41]. In 2014, Nickerl and co-workers [42] further revealed the chemical composition of the cuticle of a springtail (Tetrodontophora bielanensis). They found that the cuticle is composed of three characteristic layers, which include a lamellar chitin skeleton, a protein-rich epicuticular structure, and a lipid-rich topmost envelope. These findings provide perfect new models to design robust superoleophobic surfaces without using fluorinated chemicals.

2.1.4 Bioadhesion in nature

Many marine organisms, such as the common mussel Mytilus Edulis, are observed to display incredible bio-adhesive qualities. Mussels are able to attach to virtually any surface, natural or man-made (including those designed to be adhesion resistant) and stay attached despite the saline environment and constant forces of the tides [43]. The source of this adhesion has long been identified as coming from certain proteins secreted from the tips of the 'byssal threads', which extend outwards from the mussel foot [44]. Various Mytilus Edulis foot proteins [43] (or simply mussel adhesive proteins [45]) have been found to contain varying quantities of 3,4-dihydroxy-L-phenylalanine (DOPA), which with lysine amino acids also present are believed to be the source of the adhesion.

While the mechanisms behind the adhesion are not fully known, and it is believed that the exact mechanism may in fact vary depending on the surface involved [45-47], it is

highly suspected that the interactions of the catechol groups present in DOPA are primarily responsible [48]. These groups interact with inorganic surfaces through various non-covalent processes, such as hydrogen bonding, π- π interactions and bidentate metal oxide coordination [45]. Secondary covalent reactions also between the amino acid groups present at the byssus-surface interface (such as lysine) and ortho-quinone, a highly reactive oxidised derivative of catechol groups [48, 49]. These secondary reactions create significant cross-linking between proteins, which contributes to the strong adhesion. As a result of this mix of bonding types and the cross-linking, the adhesive is able to quickly self-polymerise and solidify under wet conditions on a variety of surface types.

The potential of mussel byssus adhesion for application was first spotted by Lee et al. [43] in 2007, recognizing the requirement for "simple and versatile strategies for surface modification of multiple classes of materials" and how the versatility of mussel bio-adhesion could be employed. It was shown that bio-inspired mimics of the mussel foot proteins containing catechol and lysine groups could be used to assist in the surface enhancement of various materials, by self-polymerising on the substrate material and acting as an intermediate layer for future modifications. This was demonstrated with dopamine, a useful analogue as it is a simple compound which contains both a catechol and lysine functional group, which when exposed to substrate material under alkaline conditions (pH 8.5) readily forms a polydopamine (PDA) layer of variable thickness on the surface [43]. Since this initial paper, PDA coatings have proven to be the focus of

much of the discussion and research into ‘mussel inspired chemistry’ [46-50], to the point where the terms are almost synonymous.

The key advantages of this kind of bio-mimetic for surface engineering include its versatility to different substrates [43]; controllable application through concentration [45], pH [47] and deposition time [51]; stability at a wide range of pH conditions (with the exception being strongly alkaline) [52]; lack of external stimuli required for self-polymerisation [50]; and the use not only as a direct surface enhancement but the ability to functionalize a substrate, with the potential for future modification [43].

The polymer layer can, on its own through direct deposition, enhance some of the desired surface properties of the material. For example, numerous studies have shown a direct surface coating of PDA can improve hydrophilicity and fouling resistance [51, 53], which are important properties for the design of membranes for water treatment. However, further use of mussel-inspired chemistry in surface engineering can be made through the application of more advanced techniques and strategies, including the implementation of bio-inspired materials as intermediates to produce more complex membranes.

2.2 Methods of bioinspired membranes design

A systematic understanding of underlying design principles in a selected natural prototype is essential for the conscious implementation of an idea from nature for bioinspired membrane design. The procedure of designing membranes by consulting

nature can be concluded to a five-step process as shown in Figure 2.3.

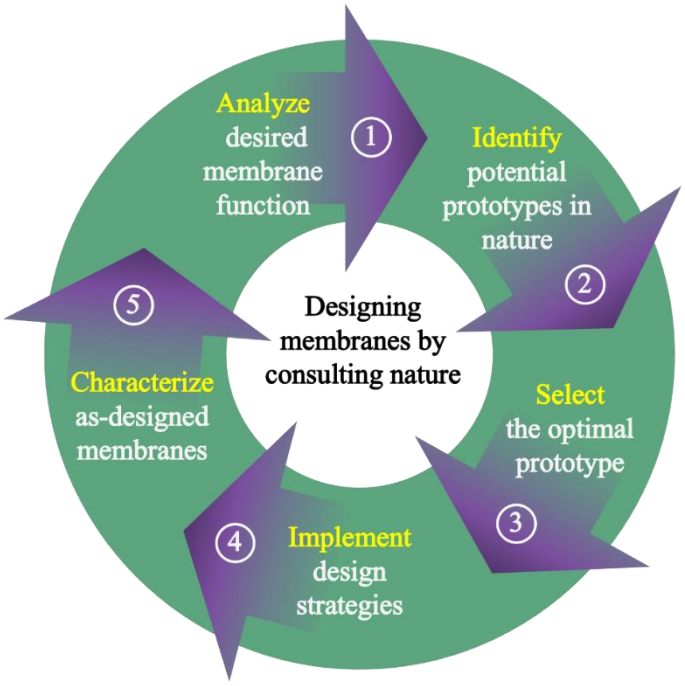

Figure 2.3. Steps in designing membranes by consulting nature.

The process starts with analysing and defining the desired membrane function (step 1), thus establishing a goal for the design process. Next, identify potential prototypes in nature that might provide solutions to achieve the desired membrane performance (step 2). Then select the optimal prototype that may provide the most efficient and feasible solution (step 3). In step 4, adopt an appropriate design strategy (either imitation-based or inspiration-based) to implement the membrane design. After that, characterize the as-designed membrane (step 5) to evaluate whether the desired property or performance has been achieved. This unified process model in Figure 2.3 is expected to act as a clear guide to make the implementation of the membrane design process easier for practitioners.

2.2.1 Self-assembled materials-based membranes

Inspired by the self-assembly concept in nature, nanostructured membranes based on self-assembled materials have been gaining increasing interest during the last two decades. This is motivated by the fact that self-assembly ensures a molecular level of control over the building blocks, which is highly promising for the construction of membranes with controllable and highly ordered pores for precise separation [54]. Two major classes of self-assembled materials have been developed to design nanostructured membranes: 1) block copolymers that can assemble into a rich variety of highly ordered nanostructures through micro-phase separation; 2) liquid crystal polymers that can assemble into lyotropic or thermotropic liquid crystalline mesophases [54, 55].

Block copolymers usually consist of two or more covalently bonded thermo-dynamically incompatible blocks. The incompatibility between the blocks forces block copolymers to phase-separate yet the space for their phase separation is limited due to the presence of covalent bonds [56]. As a result, this so-called micro-phase separation leads to the formation of diverse periodic nanoscale domains, such as spheres, cylinders, gyroids, and lamellae [56]. Such self-assembly behaviour of block copolymers has been utilized for designing nanostructured membranes with uniform pores. According to different pore-forming strategies, approaches for the design of self-assembled block copolymers-based membranes can be categorized into three types. The first type of design approach is selectively removing blocks of copolymers during film casting [56,

57]. In this approach, block copolymer solutions are cast to form thin films, followed by selectively etching the minor components of the copolymer to generate monodisperse nanoscale pores. For example, Philip and co-workers [58] fabricated a poly (styrene-b-lactide) block copolymer-based nanoporous membrane with monodisperse pores by selectively etching the polylactide block under alkaline treatment. The second type of approach involves the addition of small molecules or homopolymers into the block copolymers. Then the additives are selectively removed after the self-assembly of block copolymers, leading to the formation of highly ordered pores. For example, Wei et al. [59] fabricated homoporous membranes with tailored pores by blending block copolymer of polystyrene-block-poly(2-vinylpyridine) (PS-b-P2VP) P2VP homopolymers and selective removing the P2VP homopolymer under ethanol soaking treatment. The pore size could be controlled in the range of 15 nm to 50 nm by simply regulating the soaking conditions. The two types of approaches mentioned above are simple and straightforward ways to prepare block copolymer-based membranes with well-defined pores. However, these approaches involve the transfer of a thin block copolymer film from a dense substrate to a porous support, which can be time consuming and unfriendly for large-scale production. Recently, another type of strategy combining self-assembly and nonsolvent-induced phase separation (SNIPS) has emerged as a more industry-friendly method. In this strategy, an integral asymmetric membrane with a thin selective top layer and a mechanically stable bottom layer can be produced in a single step [56, 60].

The SNIPS approach is a simple, fast, and readily scalable process to prepare porous block copolymer-based membranes. The process usually starts with casting the polymer solution homogeneously onto a porous substrate. Then the casted film is subjected to the "phase separation" by transferring it into a non-solvent environment, leading to the formation of a thin porous top layer on the substrate [60]. The porosity of the top layer can be controlled by adjusting the casting solution properties, such as concentration, viscosity, temperature, molecular weight of the polymer, and the presence of additives. The solvent evaporation rate and time, and the humidity of the surrounding environment are also found to have influences on the pore formation on the selective layer. Membranes prepared using this strategy show ordered pores with a narrow pore size distribution. Qiu et al. [61] fabricated an integral asymmetric membrane based on amphiphilic block copolymer (PS-b-P4VP) using the SNIPS approach. The membrane showed a thin selective layer containing densely packed highly ordered cylindrical channels with a uniform pore size of ~34 nm. Radjabian and co-workers [62] prepared isoporous asymmetric polystyrene-block-poly(4-vinylpyridine) (PS-b-P4VP) hollow fiber membranes by combining the SNIPS approach with a dry-jet wet-spinning process. The prepared hollow fiber membranes showed a highly oriented and tightly packed structure in the inner selectively layer, and regular pores with a size of ~29 nm on the outer surface. Recently, Cheng and co-workers [63] reported the fabrication of a polystyrene-block-poly (acrylic acid) (PS-b-PAA) isoporous membrane through a metal ions doped SNIPS approach (Figure 2.4).

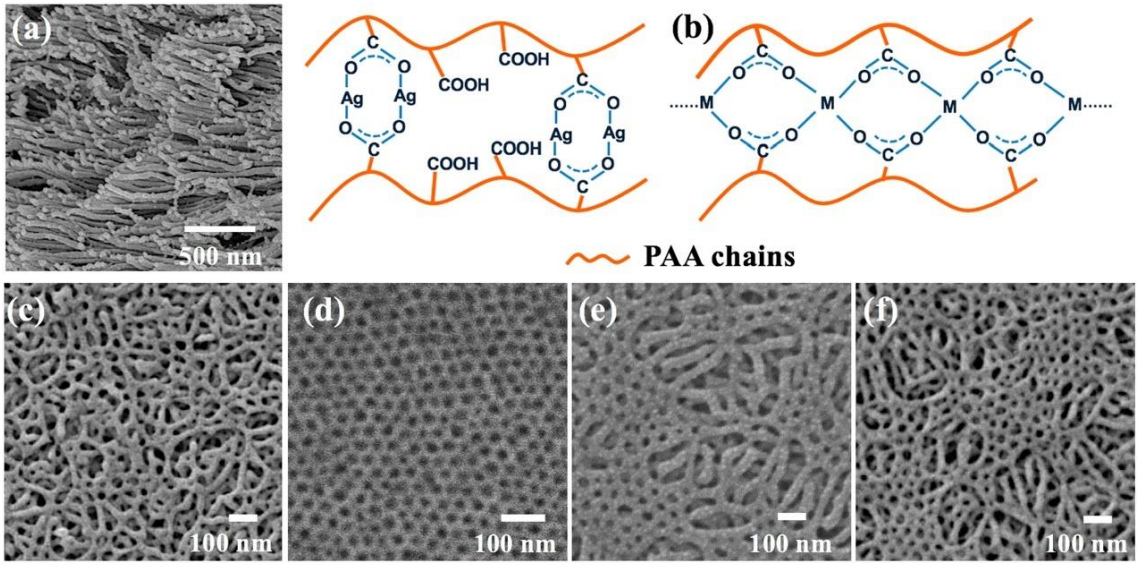

Figure 2.4. (a) SEM image of block copolymer cylindrical micelles. (b) Schematic illustration of the coordination between metal ions (M) and the PAA chains. (c)-(f) SEM images of silver salt doped isoporous membrane surfaces with different evaporation times: (c) 5s, (d) 10 s, (e) 15 s, (f) 20 s [63].

During the preparation, different antibacterial metal ions were doped in the copolymer casting solution to effectively control the pore size of the membrane. Monodisperse pores with diameters in the range of 3 nm to 30 nm were obtained in membranes doped with different metal ions. Overall, SNIPS is a fast and industry-friendly approach to designing block-copolymer self-assembled membranes. However, further research efforts are still needed to address issues such as membrane pore size adjustment, antifouling performance control, and mechanical stability enhancement.

Liquid crystal polymer (LC) is another class of self-assembled materials that have been developed for the design of nanostructured membranes. In liquid crystal polymers, an additional phase between the isotropic liquid phase and the anisotropic crystalline phase

exists and is known as mesophase. Liquid crystal polymers can self-assemble into various forms of mesophases, such as hexagonal phases, lamellar phases and bicontinuous cubic phases [54]. These self-assembled mesophases can be utilized to design well-defined nanoporous structures in membranes. Lyotropic and thermotropic liquid crystal polymers are most extensively studied for porous membrane preparation. A commonly used strategy for membrane fabrication is polymerization of a liquid crystalline monomer, followed by selective removal of a part of the liquid crystalline molecule. Henmi et al. [64] prepared a thermotropic liquid crystalline mesophase-based nanostructured membrane using a sacrificial layer of poly (vinyl alcohol) (PVA). The membrane showed a thin polymerized LC layer with a thickness of 50-100 nm on the substrate and contained self-organized pores of average size 0.60 nm. Sakamoto and co-workers [65] developed self-organized nanostructured membranes based on thermotropic liquid crystals by spin-coating and photopolymerization of ionic columnar or bicontinuous cubic liquid crystals (Figure 2.5). These membranes displayed a 100 nm thick polymerized LC layer which contained monodisperse sub-nanopores.

Recently, Gupta and co-workers [66] reported the design of nanoporous liquid crystalline membranes by incorporating a photocleavable group in columnar liquid crystal monomers. These membranes showed a thin polymerized LC layer with a thickness of ~400 nm and contained nanopores with an average size of ~0.6 nm to 2.4 nm.

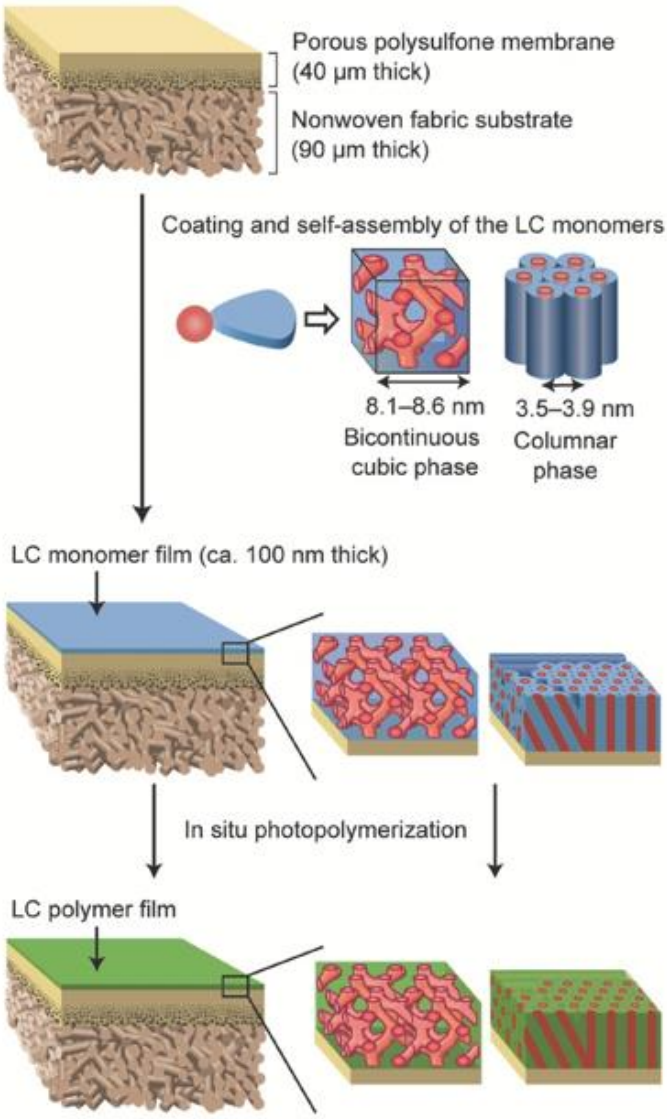

Figure 2.5. Schematic illustration for the preparation of the composite membranes from liquid crystal (LC) monomers [65].

Despite above mentioned recent advances, challenges remain in the design of self-assembled liquid crystal polymer-based membranes. Further research efforts on the development of thin, defect-free, and mechanically stable LC membranes are still needed.

2.2.2 Nacre-like composite membranes

The unique hierarchical structure in nacre is formed by an alternating layered arrangement of inorganic aragonite nanoplatelets and organic biopolymer layers. By learning from the layered nanostructure and biomineralization mechanism in nacre, a diversity of composite membranes/films with outstanding mechanical stabilities have been fabricated through different strategies. The fabrication strategies and some examples for membranes with nacre-like structures are summarized in Table 2.1. Solution casting, layer-by-layer (LbL) assembly, and vacuum filtration strategy are the most commonly used strategies for the design of nacre-mimetic membranes. Two-dimensional inorganic materials such as graphene oxide (GO) and Zeolitic imidazolate framework (ZIF-L) are preferentially used as the building blocks. The arrangement of inorganic and organic layers, interfacial interactions and interfacial compatibility between the two phases are vital factors determining the fabricated membrane properties.

Solution casting method is a commonly used technique to prepare self-supporting membranes. In this method, polymeric solutions with certain viscosity are spread across a flat plate with a casting blade. Then the solution is left to stand, allowing the solvent to evaporate to form a uniform membrane. Zhao et al. [67] prepared polyelectrolyte complex/graphene oxide (PEC@GO) nanocomposites with nacre-like brick-and-mortar structures using the solution casting method.

Table 2.1. Design strategies and examples for membranes/films with nacre-like structure

Strategy	Membrane composition	Membrane/film type	Application	Reference
Solution casting	PEC/GO	Freestanding hybrid membrane	/	[67]
	PVA/GO	GOF membrane	Acetic acid/water separation	[68]
	PDMS/ZIF-L	MMMs	Alcohol/water separation	[69]
Layer-by-layer assembly	Gelatin/GO	Supported ultrathin membrane	Ethanol/water separation	[73]
	PEI/PSS-$CaCO_3$	Supported multilayer membrane	Metal ions separation	[74]
	MXene	Freestanding hybrid membrane	/	[75]
	PS/GO	Freestanding hybrid membrane	/	[76]
Vacuum filtration	Bacteria cellulose/GO	Freestanding hybrid membrane	Ion separation	[77]
	MoS_2/WSe_2	Supported bilayer membrane	/	[78]

As-synthesized PEC@GO nanocomposites were dispersed in an alkali aqueous solution to fabricate large-area composite membranes by solution casting. The membrane showed a high mechanical strength with the tensile strength and modulus up to 115 MPa and 3.5 GPa. Lecaros et al. [68] fabricated a large area composite graphene oxide-framework membrane with a nacre-like structure. During the fabrication process, poly (vinyl alcohol) (PVA) was sued as a crosslinker in GO suspensions to bind GO nanosheets. Mao and co-workers [69] fabricated a series of mixed matrix membranes

(MMMs) with brick-and-mortar nanostructure via solution casting. Two-dimensional zeolitic imidazolate framework-L (ZIF-L) nanosheets were used as the building blocks, and Polydimethylsiloxane (PDMS) was chosen as the organic matrix. The fabricated MMMs displayed excellent mechanical properties and were effective in alcohol recovery from an aqueous solution. Very recently, Yang and co-workers [70] demonstrated the preparation of large-area GO-based membranes via the doctor-blade casting of gel-like slurries formed by incorporating different crosslinking agents in the GO suspension. (Figure 2.6a.) As-prepared membranes showed a nacre-like structure and outstanding stability under sonication. The solution casting is a simple process and can be performed at low temperatures, which favours the energy-efficient synthesis of membranes. In addition, this method allows simplified incorporation of various additives or fillers into the membrane, which is valuable for membrane modification or functionalization. These features make the solution casting technique versatile and industrially acceptable and scalable. However, this technique usually needs long cycle times, and air bubbles or moisture can be difficult to control during the preparation process, which may cause defects or pinholes in the resulting membrane.

Layer-by-layer (LbL) assembly is a bottom-up technique to develop multilayer membranes or films by sequentially depositing alternating layers of oppositely charged species on a substrate with wash steps in between.

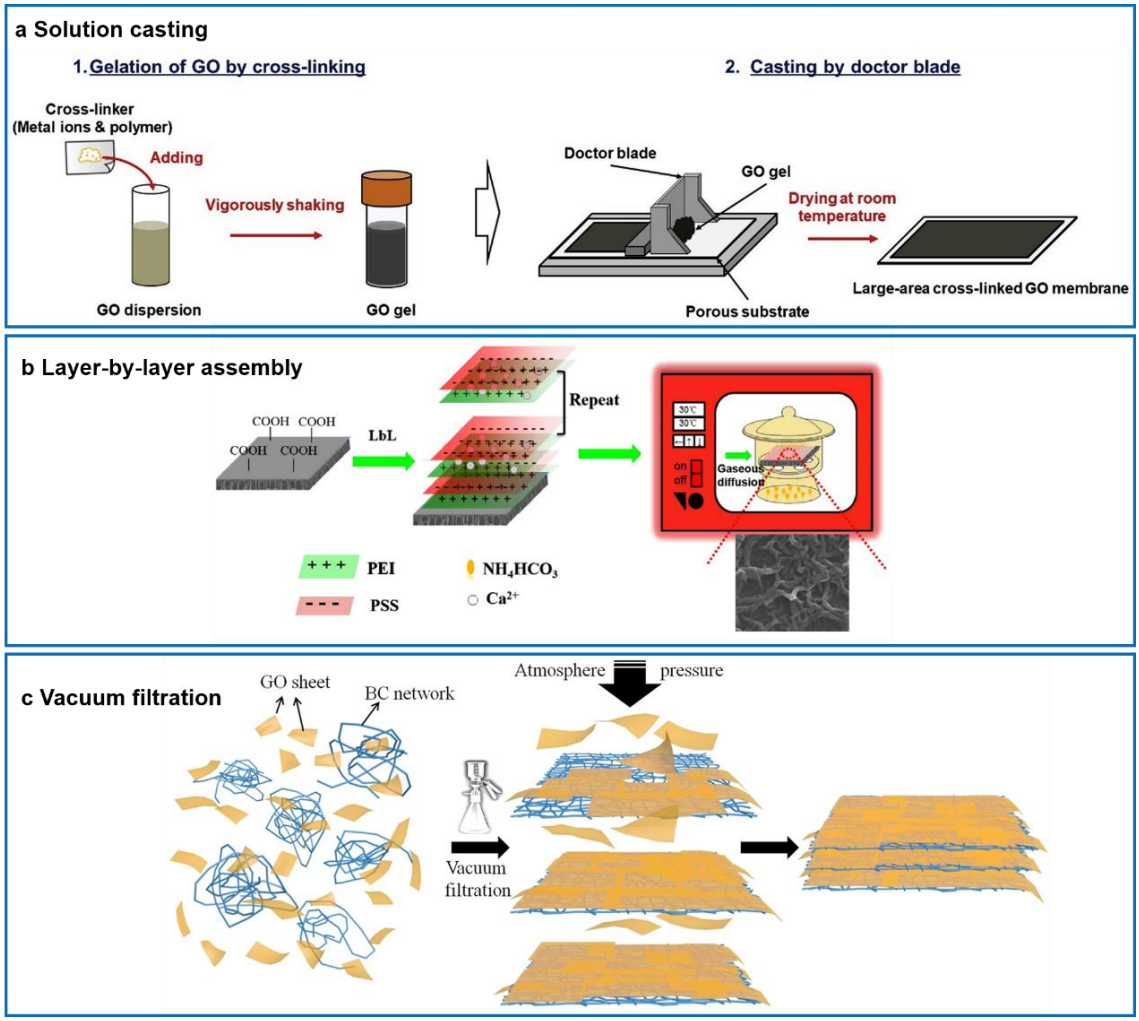

Figure 2.6. Examples of different fabrication strategies for nacre-mimetic membranes. (a) Schematic procedure for the fabrication of large-area GO membranes with a nacre-like structure using the solution casting method [70]. (b) Schematic illustration for in-situ fabrication of the nacre like-structured PEI/PSS-$CaCO_3$ nanocomposite membrane using the LbL-assembly method [72]. (c) Schematic illustration for the fabrication of free-standing composite membrane with a nacre-like structure using the vacuum filtration method [75].

Zhao et al. [71] fabricated composite membranes through LbL self-assembly of Gelatine and GO on hydrolysed polyacrylonitrile ultrafiltration membranes. The LbL

self-assembly process is driven by multiple interactions, including electrostatic interactions, hydrogen bonds and hydrophobic interactions. The membranes had a nacre-like multilayer structure with an ultrathin active layer (less than 115 nm). Qin et al. [72] prepared multi-layered Poly(ethyleneimine) (PEI) /poly(sodium4-styrenesulfonate) (PSS)-$CaCO_3$ nanocomposite membranes on Polyacrylonitrile (PAN) substrate (Figure 2.6b). The prepared nanocomposite membranes showed nacre-like structures and were effective for separating various divalent metallic ions in an aqueous solution. Recently, Lipton and co-workers [73] fabricated freestanding thin films via the layer-by-layer assembly of two-dimensional (2D) titanium carbide nanosheets (MXene) and clay nanoplatelets (montmorillonite). During the fabrication process, poly (vinyl alcohol) (PVA) was added as a flexible polymer binder. The prepared thin film exhibited high mechanic strength with a tensile strength of 138 MPa–225 MPa. Such high strength was believed to originate from the nacre-like brick-and-mortar structure. LbL assembly strategy represents an efficient and economic process for the fabrication of multi-layered membranes with controllable compositions and hierarchical nano structures. It shows the merits of tunable interfacial interactions and effective organization of the composite membrane. Hence, the thickness of the multi-layered membrane can be adjusted at the nanoscale by using this strategy. In addition, the membrane functionality can be tuned by rationally choosing the depositing materials or incorporating functional nanoparticles. These merits promote the LbL assembly to emerge as a versatile approach for the fabrication of multilayer membranes with nacre-like hierarchical nanostructures. However, the LbL strategy has the limitation of time

and labour consumption as it usually requires the repetitive deposition of different layers for multiple cycles.

Vacuum filtration is a commonly used strategy to fabricate supported asymmetric membranes. In this strategy, dispersions or mixtures containing desired building blocks are filtered through a porous membrane substrate under vacuum pressure. Wu et al. [74] demonstrated the design of a multi-layered membrane through vacuum filtration of polystyrene (PS) grafted graphene oxide (GO) with nacre as the structural model. In this process, GO served as the inorganic building block and PS acted as the organic binding agent. The prepared composite membrane exhibited a nacre like brick-and-mortar arrangement of PS and GO layers and showed outstanding mechanical properties. Fang et al. [75] fabricated a free-standing hybrid membrane using bacterial cellulose (BC) and GO via vacuum filtration (Figure 2.6c). During the filtration process, the BC was uniformly intercalated into the laminated GO layers, leading to the formation of a nacre-like nanostructure. The resulting composite membrane showed excellent tensile strength and improved stability in an aqueous environment. Feng et al. [76] reported the fabrication of nacre-mimetic molybdenum disulfide/tungsten diselenide (MoS_2/WSe_2) bi-layered membrane through a two-step vacuum filtration process. During the preparation process, dispersions containing MoS_2 and WSe_2 nanosheets were alternately filtrated across a nanoporous polycarbonate membrane support. The vacuum filtration strategy has been widely used for the fabrication of thin membranes due to its simplicity, low cost, and high production

efficiency. This method can afford a high degree of dispersion of the building blocks, producing membranes with high uniformity. In addition, in this strategy the membrane thickness can be readily modulated by simply adjusting the filtrated dispersion property. Therefore, the vacuum filtration method gains popularity in the deposition of ultrathin membranes with high and reproducible membrane quality. It is also the most commonly used method to prepare stacked lamellar membranes. However, toxic solvents are usually involved in order to obtain free-standing ultrathin membranes. The transfer of the ultrathin membrane onto arbitrary desired substrates still remains challenging.

2.2.3 Bioinspired superwetting membranes

In recent years, increasing attention has been paid to the design of surfaces with superwetting properties by mimicking the nanostructures of biological surfaces, and the exploration of their applications in various fields. In this PhD work, particular attention is paid to the design of bioinspired superwetting porous membranes (or films) that serve as selective barriers for efficient separation purposes. Bioinspired superwetting membranes are usually designed to exhibit opposite affinities toward water and oil, realizing the separation by allowing only one of the liquids to pass through while repelling the other one.

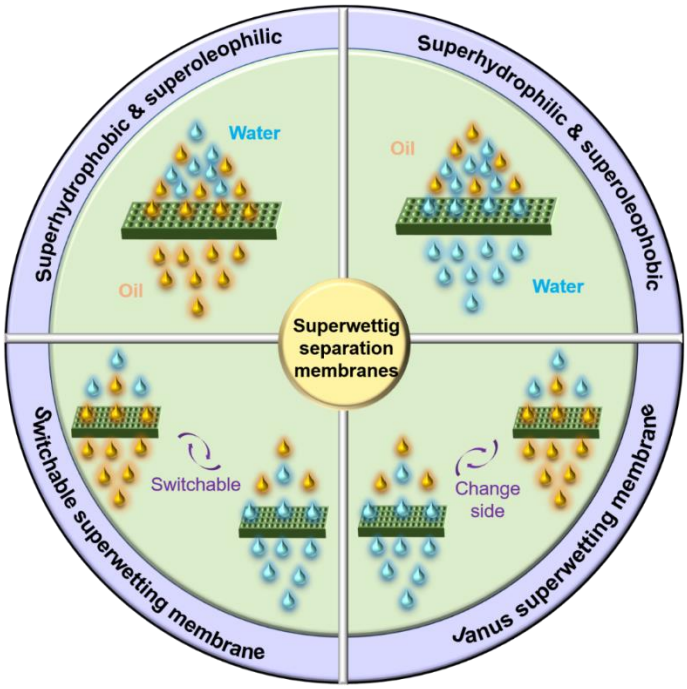

Figure 2.7. A diagram summarizing different types of superwetting separation membranes

In general, bioinspired superwetting membranes can be classified into four types as shown in Figure 2.7, including (1) superhydrophobic and superoleophilic membranes that only allow the permeation of oil while blocking water, (2) superhydrophilic and superoleophobic membranes that only allow the permeation of water while blocking oil, (3) superwetting Janus membranes that consist of two interconnected regions with asymmetric wettability, and (4) switchable superwetting membranes that are able to switch between "water-blocking" and "oil-blocking" mode when proper stimuli are applied.

The wetting property of a surface is governed by both surface energy and surface roughness [77]. It has been found that micro-/nanoscale rough structures have the

function of amplifying the original surface wettability, that is, making lyophilic surfaces more lyophilic and lyophobic surfaces more lyophobic. Therefore, the design of bioinspired superwetting membranes usually starts from the modification of the membrane surface composition as well as the construction of micro-/nanoscale structures on the membrane surface. Some most commonly applied methods for the fabrication of bioinspired superwetting membranes are summarized in Figure 2.8.

2.2.3.1 Designing superhydrophobic membranes

Superhydrophobic/superoleophilic membranes are generally designed by following two principles: (1) to roughen an intrinsic hydrophobic membrane surface by creating hierarchical micro-/nanostructures, and (2) to modify a rough membrane surface using low-surface-energy materials. Various methods have been developed to fabricate superhydrophobic/superoleophilic membranes by combined manipulation of the chemical composition and rough structure of the membrane surface (Figurea2.8a). Laser treatment is an effective way to roughen a surface by creating regularly patterned micro-/nanostructures. For example, Yong et al. [78] roughened a polytetrafluoroethylene (PTFE) film by a femtosecond laser ablation process. The roughened PTFE surface showed durable superhydrophobicity that was able to withstand harsh conditions like strong acid, strong alkali, and high temperature.

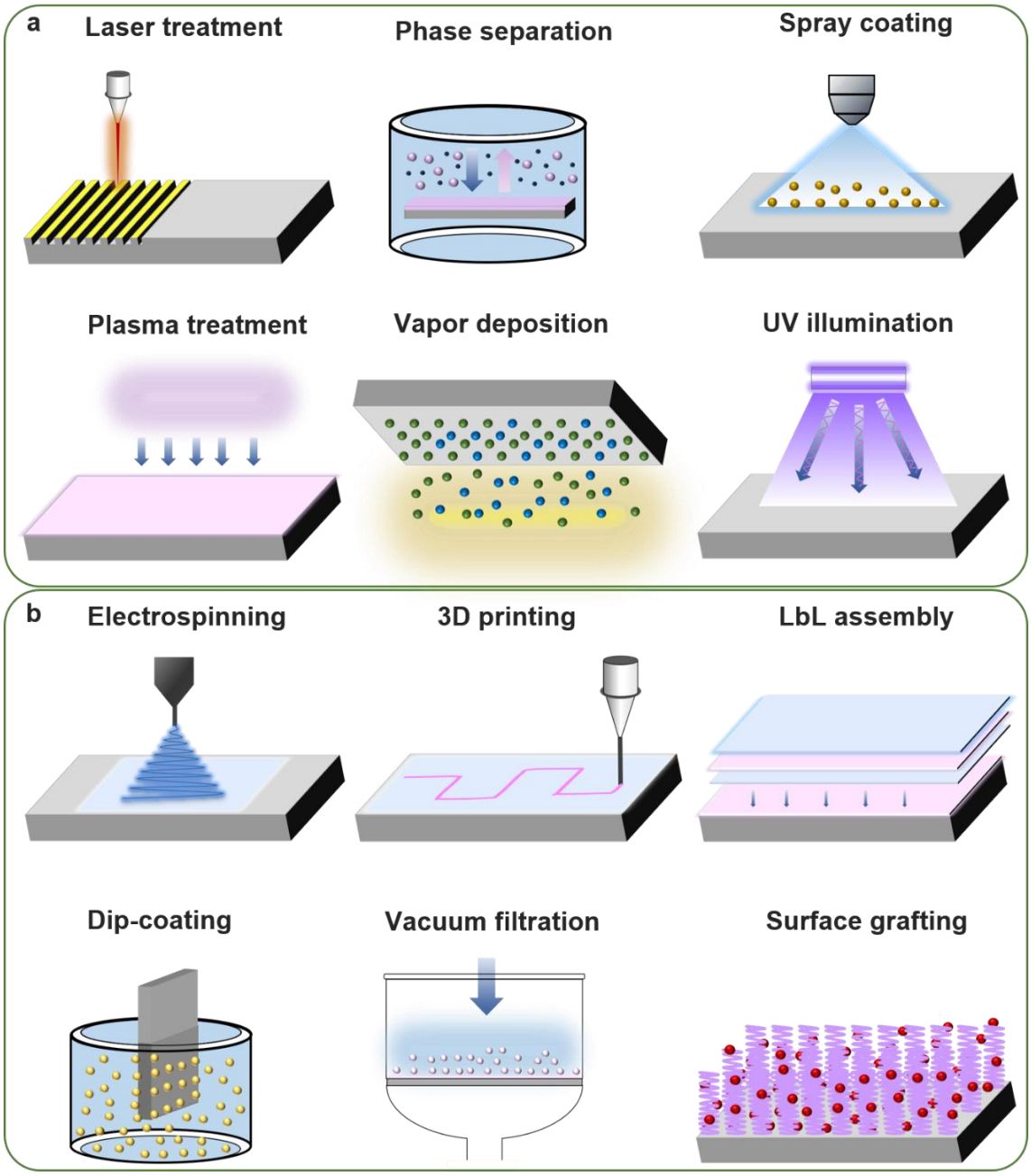

Figure 2.8. Commonly used methods for the fabrication of (a) superhydrophobic and superoleophilic membranes, and (b) superhydrophilic and underwater superoleophobic membranes.

The surface roughness can also be increased by creating micro-/nanoscale hierarchical structures on membranes during membrane formation via phase separation. Zhang and

co-workers [79] reported a superhydrophobic and superoleophilic polyvinylidene fluoride (PVDF) membrane fabricated by a modified phase separation process where ammonia water was added into the polymer solution. The superwetting characteristics of the membrane was attributed to micro-/nanoscale structures formed by spherical microparticles that are densely distributed on the membrane surface. Vapour deposition methods can create well-aligned nanoscale structures with a controlled thickness on membranes. Crick et al. [80] coated copper meshes with hydrophobic silicone elastomer by an aerosol assisted chemical vapour deposition (CVD) process. The coated mesh surfaces are composed of agglomerations of polymer microparticles and are superhydrophobic with water contact angles of 152–167°. The surface roughness of membranes can be further enhanced with the aid of external field stimulation, such as UV illumination. Chen and co-workers [81] prepared rough polydiacetylenes clusters on polyurethane PU fibrous membranes by short-time UV illumination treatment and heating treatment. The prepared membrane exhibited robust superhydrophobic/superoleophilic properties and maintained stability under strong acid or alkaline conditions. Spray coating is also effective in creating rough surface structures and has been widely used in the fabrication of superhydrophobic membranes. In this method, the rough structures are created by forming a new homogeneous layer of nanomaterials on top of the membrane surface. Very recently, Jia and co-workers [82] fabricated superhydrophobic membranes using hierarchically structured poly (dimethyl siloxane)-polyhedral oligomeric silsesquioxane (PDMS-POSS) via an electrospray coating process. In addition, spray coating is a simple way to lower the surface energy

of membrane surfaces. Lin and co-workers [83] fabricated superhydrophobic membranes by one-step spray-coating of fluorinated SiO_2 nanoparticles on the polyvinylidene fluoride (PVDF) membrane surface. After modification, the water contact angle of the membrane surface increased from ~ 110° to up to ~ 172° due to the decrease of the surface energy. Plasma treatment is another effective way to obtain low-surface-energy membrane surfaces. Yang et al. [84] prepared superhydrophobic PVDF membrane with a water contact angle of ~ 162° via a CF_4 plasma modification process.

2.2.3.2 Designing superoleophobic membranes

The design of superhydrophilic/superoleophobic membranes is comparatively more complicated. In general, to achieve an in-air superlyophobic surface, the surface tension of the solid material must be much lower than the surface tension of the wetting liquid. Therefore, an in-air superoleophobic surface must possess much lower surface tension than that of oils. However, surface tensions of common oils (~18–33 mN/m) are lower than the surface tension of water (~72.1 mN/m), which means that a superoleophobic surface is meanwhile superhydrophobic, making superhydrophilicity and superoleophobicity contradictory [77]. Fortunately, inspired by the ultralow oil-adhesion property of fish scales and shark skins underwater, superhydrophilicity and superoleophobicity have been effectively combined in underwater cases. Superhydrophilic/underwater superoleophobic membranes are usually designed by: (1) increasing micro-/nanoscale surface roughness of an intrinsic hydrophilic membrane, and (2) modifying a rough membrane surface using hydrophilic polymers or

nanomaterials. Some popular methods for the fabrication of superhydrophilic/underwater superoleophobic membranes are shown in Figure 2.8b. Electrospinning provides a straightforward approach for the fabrication of hydrophilic membranes with hierarchical micro-/nanostructures. Ghaffar and co-workers [85] recently fabricated a polyvinyl alcohol-graphene oxide (PVA-GO) nanofibrous membrane using the electrospinning technique. The membrane showed excellent superhydrophilicity and underwater superoleophobicity due to the hierarchical knotty nanostructure of the twisted nanofibers as well as the hydrophilicity of GO nanosheets. Three-dimensional (3D) printing is a powerful technique to create a geometrically complex feature in a range of materials, providing great potential to design membranes with micro-/nanoscale rough surfaces. Very recently, Li and co-workers [86] prepared a porous composite membrane using a direct inkjet writing 3D printing technique with cellulose acetate, poly (vinyl alcohol) (PVA), and silica nanoparticles (SiO_2) as the ink. The composite membrane showed robust superhydrophilicity and underwater superoleophobicity due to the decoration of hydrophilic SiO_2 nanoparticles on the rough, porous membrane surface. Layer-by-layer (LbL) assembly provides a versatile platform for fabricating various surfaces with well-tailored chemical compositions and structures, and thus has been widely used for the design of membranes with special surface wettability. Zhang et al. [87] fabricated a self-cleaning mesh film by the LbL assembly of sodium silicate and titanic titanium dioxide (TiO_2) nanoparticles on the stainless-steel mesh. The mesh demonstrated underwater superoleophobic property and can be easily regenerated under UV illumination. Vacuum filtration is another simple

and straightforward strategy to fabricate membranes with controllable chemical compositions and surface properties. Chen et al. [88] recently prepared a paper fiber membrane by anchoring polydopamine (PDA) and TiO_2 nanowires on the membrane surface via the vacuum filtration strategy. The membrane showed excellent superhydrophilic/underwater superoleophobic property with an underwater oil contact angle of ~156°. Alternatively, superhydrophilic/underwater superoleophobic membranes can be obtained by modifying a membrane substrate with hydrophilic micro-/nanoscale materials through various strategies. Liu and co-workers [89] recently prepared a polydopamine (PDA) and starch coated polyimide mesh via a simple dip-coating process. Due to the hybrid micro/nanoparticles coating, the mesh surface displayed increased surface roughness and showed superhydrophilicity and underwater superoleophobicity with an underwater oil contact angle of ~154°. Surface grafting is widely used to add hydrophilic polymer chains onto the membrane surface. Cheng and co-workers [90] recently fabricated a zwitterionic poly (sulfobetaine methacrylate)) grafted silk fabric membrane through a surface-initiated atom transfer radical polymerization reaction. The polymer brush-grafted membrane showed excellent superhydrophilic/underwater superoleophobic properties due to the hydrophilicity of the PSBMA brush layer as well as an increased surface roughness.

2.2.3.3 Designing Janus superwetting membranes

In ancient Roman myth, Janus is known as a god having two faces, since he looks to the future and to the past. In modern materials science, the term “Janus materials” are

defined as materials possessing opposite chemico-physical properties on two sides [91-94]. In particular, Janus superwetting membranes that have asymmetric superwettability on two sides have attracted great interest in diverse research fields due to their distinctive unidirectional mass transport behaviours [91, 92]. In the design of Janus superwetting membranes, the creation and regulation of the asymmetric wettability is the core task. The design strategies for Janus superwetting membranes can be classified into two categories, as summarized in Table 2.2. The first category of strategy is asymmetric fabrication, in which each side of the Janus membrane is fabricated respectively and then combined together. For example, Li et al. [94] prepared a Janus superwetting mesh by directly integrating a superoleophilic and an underwater superoleophobic single-layer copper mesh together. The composite mesh demonstrated underwater unidirectional oil penetration behaviour due to the wettability asymmetry. Wang et al. [95] fabricated a Janus nanofibrous membrane comprising a superhydrophobic layer and a superamphiphobic layer by a sequential electrospinning technique. The membrane exhibited directional oil-transport performance due to the opposite wettability on two sides. Yang et al. [96] prepared a composite Kevlar membrane with opposite superwettability by a sequential vacuum filtration method using FeOOH and ZnO nanoparticles. Song and co-workers [97] recently fabricated a polyester non-woven fabric-based Janus membrane via a non-solvent induced phase separation (NIPS) method.

Table 2.2. Design strategies for Janus superwetting membranes

Design strategy	Design principle	Fabrication route	Materials	References
Asymmetric fabrication	Double-layer compositing	Direct integration	Copper meshes	[96]
		Sequential electrospinning	PVDF-HFP/FD-POSS/FAS	[97]
		Sequential vacuum filtration	FeOOH-Kevlar/ ZnO-Kevlar	[98]
	Phase separation	Non-solvent induced phase separation	PVDF/PDA/PEI	[99]
		Unidirectional segregation during phase separation	PVP-VTES/PVDF	[96]
Asymmetric modification	Single-side coating	Spray coating	Glass fiber nonwovens	[101]
		Electro-deposition	Copper mesh /Ni-NiO /$Ni(OH)_2$	[102]
		Vapor deposition	PP/Al_2O_3	[103]
	Single-side irradiation	UV degradation	Copper mesh/TiO_2	[104]
		Photo grafting	Cotton fabric	[105]
		Plasma activation	Quartz fiber	[106]

Note: PVDF-HFP refers to poly (vinylidene fluoride-hexafluoropropylene); FD-POSS refers to fluorinated decyl polyhedral oligomeric silsesquioxanes, and FAS refers to (fluorinated alkyl silane)

The membrane showed asymmetric wettability with an underwater oil contact angle of ~152° on one side and an underoil water contact angle of ~153° on the other side. Li and co-workers [98] recently reported a single-step unidirectional segregation strategy

to fabricate a polymeric Janus membrane during phase separation. The prepared Janus membrane exhibited extremely opposite wetting property with the contact angle difference between top and bottom surface up to 150°. Another category of strategy for Janus superwetting membrane design is the asymmetric modification, in which one side or both sides of a membrane are modified separately. For example, Wei and co-workers [99] recently demonstrated the fabrication of a Janus fibrous membrane with asymmetric wettability via the single-side electro-spraying method. Luo et al. [100] synthesized a Janus copper mesh decorated with superhydrophilic Ni-NiO/Ni $(OH)_2$ core-shell nanoparticles via a selective electrodeposition method. Waldman et al. [101] reported the fabrication of Janus membrane with asymmetric wettability via a single side vapour deposition strategy. Chen et al. [102] fabricated a superhydrophobic/hydrophilic binary cooperative Janus copper mesh through a single-side UV degradation approach. Wang et al. [103] prepared a Janus cotton fabric membrane by photo grafting of copolymer brush on only onside of the fabric. Recently, Li et al. [104] reported a Janus Quartz fiber membrane showing excellent fouling resistance with the assistance of single-side plasma activation (Figure 2.9). In their method, the Quartz fiber membrane was first modified to be omniphobic on both faces by attaching silica nanoparticles followed by surface fluorination. Then the Janus membrane was prepared by plasma activation followed by zwitterionic polymer grafting on only one side of the membrane

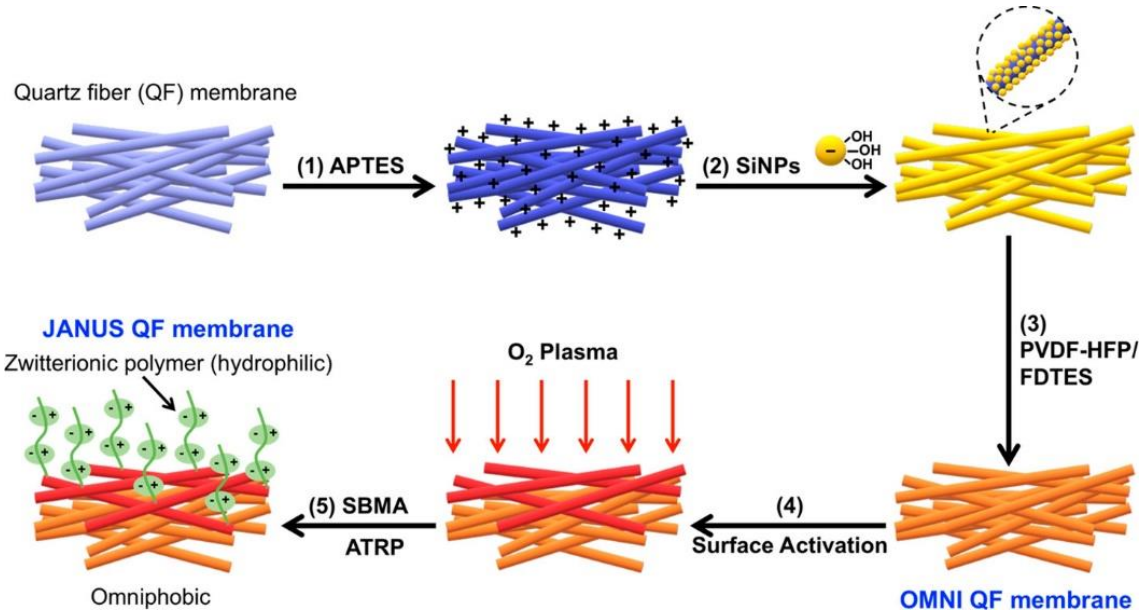

Figure 2.9. Schematic illustration of the Janus Quartz fiber membrane by a single-side plasma activation & zwitterionic polymer brush grafting approach [104].

2.2.3.4 Designing switchable superwetting membranes

Inspired by stimuli-responsive creatures in nature, smart membranes with switchable superwetting properties have been proposed and designed for efficient switchable separations. As mentioned above, surface wettability mainly depends on surface chemistry and surface roughness. Therefore, the switchable wettability can be triggered when the surface chemistry and surface roughness change under certain external stimuli, such as pH [105], light [106], magnetic field [107], thermal [108], electricity field [109], ions [110], gas [111], and hygro/solvent [112], as shown in Figure 2.10.

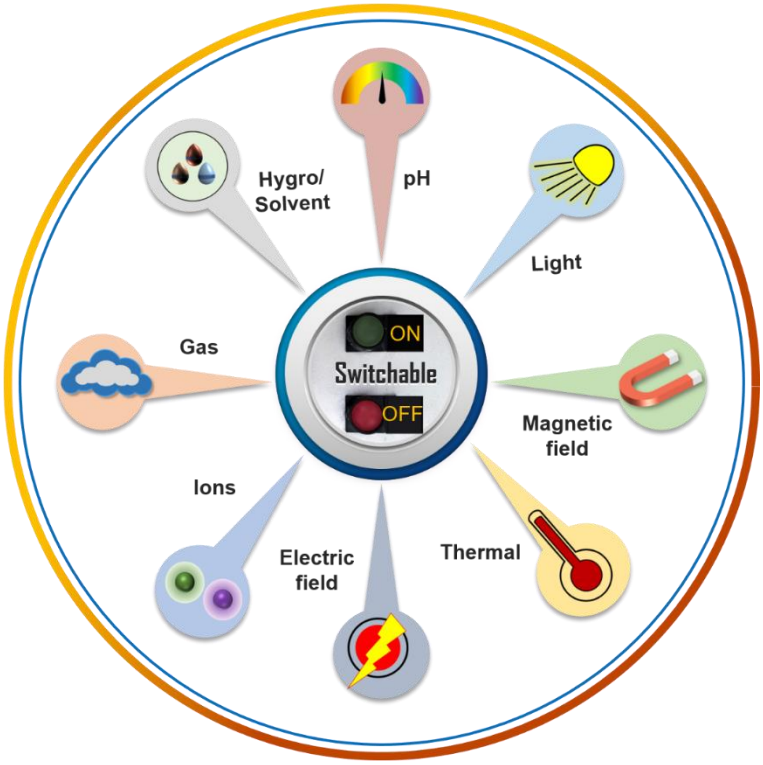

Figure 2.10. Different types of stimuli for smart membranes with switchable superwettability.

Compared to monotonous superwetting membranes, switchable superwetting membranes demonstrate better adaptability and controllability to achieve on-demand separation applications [113]. Ma et al. [105] prepared a nanofibrous polyimide-based membrane with pH-switchable wettability through electrospinning and dip-coating. The surface wettability of the membrane switched from hydrophobicity to superhydrophilicity when the pH condition changed from non-basic (pH = 7) to strong basic (pH = 12). The transition of the wettability was attributed to the variation of the protonation and deprotonation of the carboxyl groups on the membrane surface with the change of pH environment. Shami et al. [108] reported a smart poly (vinylidene

fluoride) (PVDF) and P25TiO_2 nanotextile with photo (UV/solar light)-induced switchable superwetting property by the electrospinning technique. The nanotextile showed excellent self-cleaning and antifouling performance due to the photocatalytic effect TiO_2. Yan et al. [109] prepared a magnetic textile fabric membrane with switchable wettability by immersing the fabric in lauric acid-TiO_2 composites and Fe_3O_4 nanoparticles. Although the magnetic field could not control the membrane wettability, it provides the driving force to manipulate the permeant transport across the membrane for efficient separations. Ou and co-workers [110] prepared a thermo-responsive polymer membrane using polyurethane microfiber and poly (N-isopropylacrylamide) (PNIPAM) hydrogel. The membrane demonstrated a reversible wettability transition from superhydrophilicity to superhydrophobicity in response to changes of temperature from 25 °C to 45 °C. The thermo-responsive property of the membrane was attributed to the reversible variation of hydrogen bonding from amide groups of PNIPAM chains below and above the lower critical solution temperature of PNIPAM. Du and co-workers [111] recently fabricated electro-responsive poly-3-methylthiophene (P(3-MTH))/carbon membranes with switchable superhydrophobicity/ superhydrophilicity via the electrospinning technique. The surface wettability conversion was achieved in less than 30 s by doping or dedoping the P(3-MTH) with ClO^{4-} under electro-stimuli. Xu et al. [112] prepared a mercury ion (Hg^{2+}) responsive poly (acrylic acid) (PAA) hydrogel coated stainless steel mesh with switchable wettability. The mesh surface was superhydrophilic without Hg^{2+} and switched to highly hydrophobic after immersion in Hg^{2+} solution due to the

complexation between PAA and Hg^{2+}. Wong et al. [111] demonstrated the gas-phase tuning of membrane surface wettability from superhydrophilicity to superhydrophobicity under room temperature. The wettability transition was realized by reversible amphiphilic functionalization of the membrane surface under gas phases. Liao et al. [112] fabricated a hierarchically porous PVDF-silica nanofibrous membrane with solvent-responsive switchable superwettability via electrospinning technique. The membrane is in-air superamphiphilic, and thus demonstrating underwater superoleophobic and underoil superhydrophobic properties as the prewetting solvent changes from water to oils.

2.2.4 Mussel-inspired membranes

There are numerous strategies employed in mussel-inspired membrane design to create multi-functional or otherwise highly complex materials. In a fairly straightforward method, PDA can be used to introduce reactive functional groups to an otherwise inert substrate, allowing for secondary reactions. Desirable compounds can be added by reacting their amino or thiol groups with the PDA layer through, for example, Michael addition or Schiff-base [114-116]. This is either done in a ‘one step’ process, whereby the desired compounds are mixed with the dopamine solution first before being introduced to the substrate (where PDA will self-polymerise with the added material); or in a ‘two-step’ process where the PDA layer is allowed to form on the substrate before the enhancing species is added [117-119]. Recently, Kwon and co-workers [118] fabricated mussel-inspired PDA modified thin-film composite forward osmosis

membrane by an aromatic solvent-based interfacial polymerization method (Figure 2.11). The PDA layer contributed to enhancing the hydrophilicity of the polyethylene support and the long-term operation stability of the prepared composite membrane.

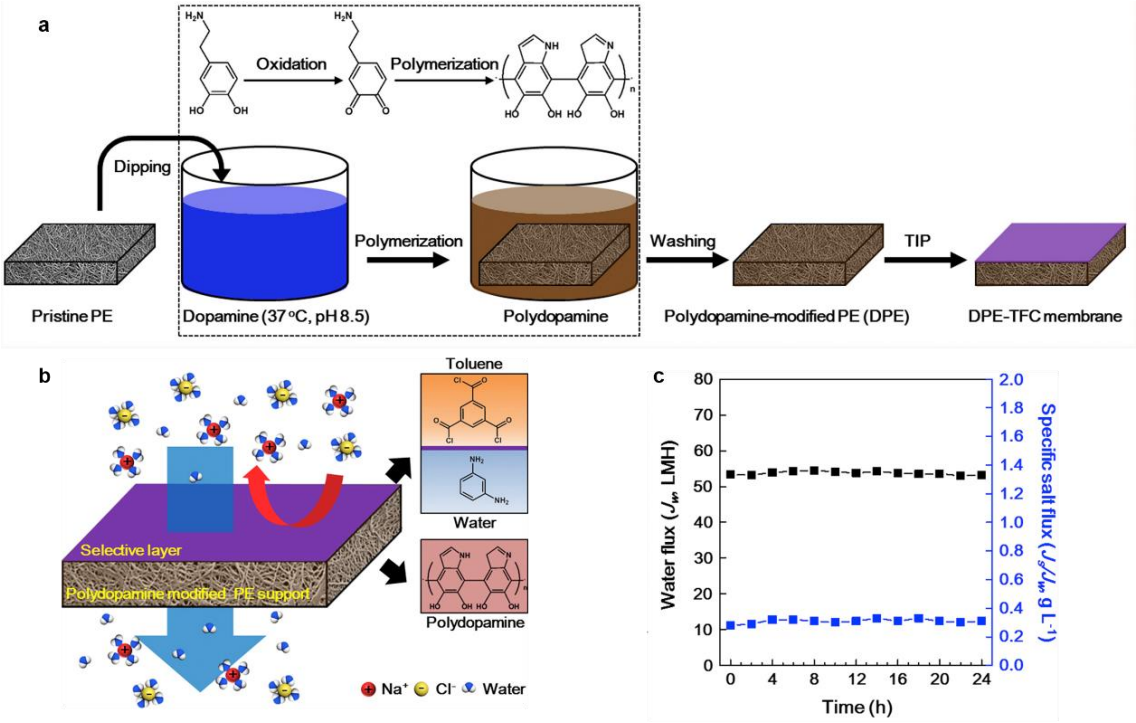

Figure 2.11. (a) Fabrication procedure of the PDA modified thin film composite membrane. (b) Salt rejection process of the prepared composite membrane. (c) Long-term operation stability of the composite membrane: both water flux and the specific salt flux of the composite membrane remained unchanged after 24 h operation [118].

Surface initiated atom transfer radical polymerization (SI-ATRP) [120] and single-electron transfer-living radical polymerization (SET-LRP) [121] are powerful techniques for creating a variety of polymers. Techniques which, to be used in surface engineering, require an immobilized initiator on the substrate surface before the desired

polymers can be produced. Through mussel-inspired chemistry, a substrate can easily be pre-treated with PDA, which due to its reactivity will readily accept and immobilize the initiator species to facilitate these processes [122, 123]. Reversible addition-fragmentation chain-transfer (RAFT) polymerization [124] is a similarly powerful tool for surface engineering which can benefit from mussel-inspired techniques, but unlike the aforementioned methods does not rely on immobilizing the initiators to the substrate with PDA. Rather, dopamine is utilized in the formation of the actual desired polymers before being introduced to the substrate, forming end groups which bind to the surface and form a PDA layer as normal while also binding the desired RAFT-created polymers [125].

Due to their aforementioned versatility in binding to organic and inorganic surfaces, derived from the ability to form strong metal-coordination bonds as well as covalent bonds, mussel-inspired bio-adhesives have also been used as intermediates to 'bridge' organic and inorganic layers for hybrid membranes [126]. Coating an inorganic base material such as porous Al_2O_3 [127] or stainless-steel mesh [128] with PDA, and then using that as a base upon which to grow a metal-organic-framework such as ZIF-8, has proven to be an effective strategy for stable and highly selective separation membranes. A promising area of research for mussel-inspired membrane design strategies is of light-irradiated initiated polymerisation, where exposure to visible or UV light triggers the polymerisation reaction of dopamine even at neutral conditions (as opposed to standard, basic conditions) [129]. The appeal of using light as the initiator is the ability to

accurately control the extent of the reactions, and through 'on/off' control allow the formation of complex patterns on substrate surfaces [130, 131]. A recent advancement in this has been in combining the UV-initiated technique with another rising surface engineering technology: inkjet printing [132]. The premise is that inkjet printing is a cost-effective and efficient method of performing surface engineering; depositing materials directly onto the substrate with precision; which could be used to deposit dopamine and any additional materials in complex patterns before irradiating the membrane with UV light to control the polymerisation. This technique was shown to be economical, efficient and environmentally friendly (with minimal waste and energy usage); and produced an effective membrane for oil-water separation, and so is a very promising area of future development.

As mentioned, the overwhelming focus of research and discussion into mussel-inspired chemistry for surface engineering focuses on dopamine and PDA. While PDA is an effective tool for membrane design it is not without drawbacks; with long deposition times, high cost of feedstock, lower than desired efficiency and even the colour (which can cause issues in some applications [133]) being cited as disadvantages yet to be overcome [134-136]. Furthermore, it should be pointed out that as many of the advanced techniques mentioned above require multiple steps to complete, increasing both the complexity of the procedure and the time required to produce the finished membranes over a simpler 'one step' method [137]. As such, numerous other mussels inspired materials have been explored in recent years, seeking to take the core concept

of bio-adhesion and mussel-inspired chemistry and expand it beyond dopamine.

At the core of this approach has been a shift from catechol-based to pyrogallol-based materials, with several studies, not just restricted to bioadhesion, actively comparing the performance of both classes of material [138-140]. Inspired by the tunicate, another marine organism, pyrogallol groups appear to exhibit better adhesive qualities than their catechol counterparts, showing up to 7 times stronger adhesion. This has been attributed to the additional -OH group present in pyrogallol, allowing both stronger tridentate interactions between molecules (as opposed to bidentate) and a greater degree of cross-linking [140]. It has therefore been theorised, due to the similarities between their structures and polymerisation, that not only are polygallols also applicable for use surface modification applications; but that they will be able to out-perform catechols.

This was tested with gallic acid (GA), a simple pyrogallol compound chosen for its economic and environmental credentials (being easily and cheaply plant-derived); using γ-aminopropyltriethoxysilane (APTES) as the source on amino groups (as unlike dopamine, pyrogallol compounds do not tend to contain -NH groups required for self-polymerisation) [141]. The general success of this, and the apparent confirmation that pyrogallols were an improvement on catechols, in turn, led to experimentation with polyphenol tannic acid (TA); which has been highlighted in a number of papers recently as a very promising alternative to dopamine-based methods [142, 143]. TA is interesting in that it contains five pairs of pyrogallol/catechol groups per molecule.

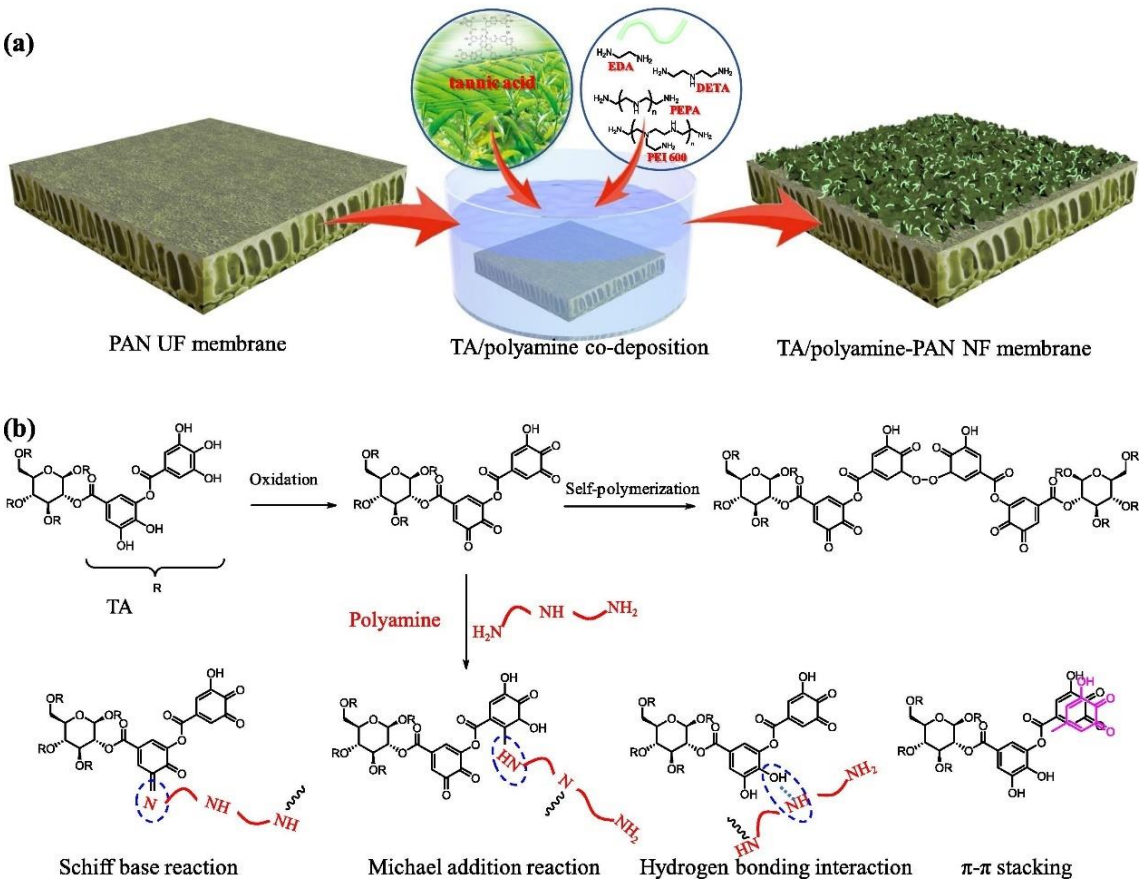

Figure 2.12. (a) Preparation process of the NF membrane via a simple co-deposition between tannic acid (TA) and amine; and (b) possible reaction mechanism between TA and amine [142].

Xu and co-workers [142] recently fabricated nanofiltration membranes with enhanced inorganic salt rejection performance by manipulating the mussel-inspired co-deposition of tannic acid and amine (Figure 2.12). They proposed that Michael addition reaction, Schiff base reaction, hydrogen bonding interaction, and π-π stacking are possible reaction mechanisms between TA and amine molecules. Based on the above findings, that pyrogallols are more effective at surface modification than catechols (and lacking many of the disadvantages of dopamine), this implies that TA will be a much more

powerful tool for surface engineering than dopamine. In addition to this, Yang et al. [136] suggested that an overlooked contributor to the strong bio-adhesion present in mussels is cysteine [144, 145]. As cysteine contains both amino and mercapto functional groups, this suggests that -SH groups contribute to the bio-adhesion property as well as -NH groups, and so both would be able to form covalent bonds with TA's functional groups. Therefore, they propose that a TA/cysteamine mixture would combine these observations into a much more potent mimic of the mussel foot proteins than dopamine (which only contains a single -NH group), with more functional groups and a greater propensity for cross-linking and cohesion. In the experiment, the hydrophilic membrane was produced in a one-step dip-coating of a substrate under alkaline conditions (pH 8.5) with no external energy input. The potential of this approach is clear, with the resulting membrane demonstrating efficient oil/water separation with fouling resistant properties. It should also be noted that, like TA can be produced cheaply from natural feedstocks such as Chinese Gall [136]. The promising results seen so far from TA suggest that there will be more research on it and other pyrogallol compounds in this field to come, investigating the optimal conditions for polymerisation and exploring new design methodologies for surface engineered membranes.

2.3 Applications of bioinspired membranes in separation processes

2.3.1 Self-assembled materials-based membranes

Self-assembled materials-based membranes usually exhibit a thin selective layer with high porosity and homogeneous pore size, indicating the remarkable potential for highly selective precise separations. For block copolymers-based membranes, their pore diameters generally lie in the range of 5 to 50 nm, which can be applied for wastewater treatment through ultrafiltration (UF) processes. For example, Qiu and co-workers [61] applied an amphiphilic block copolymer-based membrane with regular nanopores for selective separation of similarly sized proteins. The membrane demonstrated a water flux above 3200 L m^{-2} h^{-1} bar^{-1}, which was an order of magnitude higher than fluxes of commercially available ultrafiltration membranes with similar pore sizes. The membrane was effective for the separation of bovine serum albumin (BSA) with a diameter of 6.8 nm and globulin-γ with a diameter of 14 nm by a separation factor of 87. Moreover, the membrane was applied to effectively separate proteins with nearly identical molecular weights by regulating the external pH. Zhu et al. [146] designed block copolymer-based isoporous membranes with sub-10 nm pores and applied them for protein separation. The membranes possessed regularly arranged pores with diameters of ~8.6 nm and pore density of $1.3\times10^{15}/m^2$ and displayed successful separation of BSA (7×3.8×3.8 nm) from haemoglobin (6.4×5.5×5 nm). For liquid crystal polymer-based membranes, their pore size usually lies in the range of 0.5 to 2 nm, which is promising for precise small molecules or ions separations. Henmi and

co-workers [64] developed liquid-crystalline nanostructured membranes for selective ions permeation. The membrane possessed self-organized pores of average size 0.60 nm and showed a rejection of ~78% for $MgCl_2$ with a flux of ~21 L m^{-2} h^{-1}. Sakamoto et al. [65] developed thermotropic liquid crystals-based sub-nanoporous membranes for selective ions separation. This membrane exhibited a NaCl rejection of ~70% with a flux of ~39 L m^{-2} h^{-1}. Recently, Gupta and co-workers [66] reported liquid crystalline membranes free from pinhole defects for high-performance virus removal from water. These membranes demonstrated a virus (Qβ Bacteriophage) rejection of 99.99% with a tunable water flux up to 61 L m^{-2} h^{-1}.

2.3.2 Nacre-like composite membranes

Nacre-inspired hybrid membranes usually exhibit lamellar microstructures with well-regulated interlayer nanochannels. They have shown great potential for gas separation and sophisticated liquid separations, such as permselective pervaporation and selective ion separation. Lecaros et al. [68] applied a nacre-like structure for the dehydration of acetic acid from water by pervaporation. The membrane showed a permeation flux of 463.9 g m^{-2} h^{-1} and a water concentration of 97.7% in permeate at 80 °C. Mao et al. [69] applied a PDMS/ZIF-L based mixed matrix membrane with nacre-like brick-and-mortar architecture for alcohol permselective pervaporation. The membrane displayed a permeation flux of 402 g m^{-2} h^{-1} with a high separation factor of 57.6 when separating 1.0 wt% n-butanol aqueous solution at 40 °C. Zhao et al. [71] applied a graphene oxide/gelatine ultrathin hybrid membrane for pervaporation dehydration of ethanol

aqueous solution. The membrane achieved a high permeation flux of 2275 g m^{-2} h^{-1}, and water concentration in permeate of 98.7% at 350 K. Qin et al. [72] evaluated the metallic ions rejection performance of a multi-layered PEI/PSS-$CaCO_3$ nanocomposite membrane with a nacre-like structure. The membrane demonstrated ≥99.3% rejection for divalent metal ions such as Mg^{2+}, Cu^{2+}, Ca^{2+}, Ni^{2+}, Zn^{2+}, and Cd^{2+} in an aqueous solution with the permeation flux ≥49.1 L m^{-2} MPa^{-1} h^{-1}. Fang et al. [75] evaluated the inorganic/organic ions selective permeation performance of a freestanding bacterial cellulose/graphene oxide composite membrane. The membrane effectively rejected organic ions such as rhodamine B and methyl orange, while allowed the permeation of inorganic ions such as K^+, Ni^{2+}, Mn^{2+}, Cl^- and $[Fe(CN)6]^{3-}$. Feng et al. [76] Recently, Yang et al. [70] applied various crosslinker-stabilized GO lamellar membranes for molecular nanofiltration and gas separation. In their work, the Fe^{3+}-crosslinked GO membrane demonstrated complete rejection of different organic dyes, such as rose Bengal, rhodamine B and methylene blue. The PEO-crosslinked GO membrane achieved excellent separation of carbon dioxide (CO_2) and nitrogen (N_2) gases with a CO_2/N_2 selectivity of 52.

2.3.3 Bioinspired superwetting membranes

Superwetting membranes have been playing a tremendous part in high-performance oil/water separations. Recently, Lin et al. [83] reported a superhydrophobic PVDF based membrane for gravitational water-in-oil emulsion separation. The membrane displayed consistent separation efficiencies up to ~99.9% for water-in-oil emulsions,

and excellent recyclability over 40 cycles. Li and co-workers [86] recently reported a 3D printed underwater superoleophobic composite membrane for gravity-driven oil/water mixture separation. The printed membrane achieved a high separation efficiency of ~99% for various oil/water mixtures. Moreover, the membrane exhibited good anti-fouling performance and maintained high separation efficiency after 50 cycles of separation tests. Ghaffar et al. [85] applied an underwater superoleophobic PVA-GO nanofibrous membrane for emulsified oily water treatment under gravitational force. The membrane showed a separation efficiency of above 99% for both surfactant-free and surfactant-stabilized oil-in-water emulsions, with the water flux up to 45 L m^{-2} h^{-1}. Li et al. [98] reported a Janus PVDF based membrane with extremely opposite superwetting surfaces for oil/water emulsion separation. Due to its anisotropic wettability, the membrane showed excellent switchable separation performance for both oil-in-water emulsions and water-in-oil emulsions. Recently, Ma et al. [105] applied a magnetic nanofibrous membrane with pH-switchable wettability for oil/water mixture separations. The membrane demonstrated high-efficient separation for both heavy and light oil/water mixtures at different pH values, with permeation fluxes above 2824 ± 100 L m^{-2} h^{-1}, and separation efficiencies higher than 99%. Liao et al. [112] applied a PVDF based nanofibrous membrane with prewetting triggered switchable superwettability for various oil/water mixtures and emulsions separation. The membrane was capable of separating both oil-in-water and water-in-oil mixtures/emulsions with or without surfactants, with a flux up to 2000 L m^{-2} h^{-1} and separation efficiency above 99.99%. In addition, the membrane exhibited good

antifouling performance and recyclability in a 50-h continuous operation.

Superwetting membranes have also been applied in the membrane distillation process. For example, Yang et al. [84] reported a superhydrophobic PVDF-based membrane for direct contact membrane distillation. The membrane displayed a rejection rate of 99.98% towards 4 wt% NaCl solution, with a flux of above 20 kg m^{-2} h^{-1}. Li and co-workers [104] recently reported an antifouling Janus membrane for desalination by membrane distillation. A crude-oil-in-saline (NaCl) water emulsion was synthesized to simulate highly saline oily wastewater. The membrane displayed a consistent water flux and nearly complete salt rejection during the membrane distillation process. Very recently, Jia and co-workers [82] applied a superhydrophobic membrane with cauliflower-shaped beads in the direct contact membrane distillation process. The membrane exhibited excellent desalination performance towards synthetic seawater containing 0.1 mM sodium dodecyl sulphate (SDS) with salt rejection above 99.9%. In addition, the membrane maintained a high rejection rate in a 200-h continuous operation.

2.3.4 Mussel-inspired membranes

There are a number of applications for membranes inspired by marine organisms, particularly in the field of water treatments. Oil/water separation is an area that has attracted increasing attention recently due to the pressing need for effective, economical and reusable membranes for treating industrial oily wastewater and environmental spills. The design goal here is often to enhance the hydrophilicity and resistance to

fouling of the membrane, so that water will be able to pass through the membrane while oil is stopped, as well as to test the reusability of the membrane after multiple cycles. There are multiple examples of excellent oil rejection efficiencies, permeate fluxes and anti-fouling properties being achieved recently through more eco-friendly fabrication techniques (with environmental implications being clearly stated in the design goals); such as the aforementioned novel inkjet printing with UV light method [132] and novel tannic acid and cysteamine [136], and a novel PDA with graphene-oxide hollow fibre membrane [147]. All three of which also exhibited promising reusability. However, it remains to be seen if these materials will prove economical for industrial scale-up, especially considering the reusability tests only covered a few (3-5) cycles. A promising oil/water separation from a different approach is the one-step superhydrophobic membrane design, which aims to achieve extreme water rejection while allowing oil to pass through unhindered. The single-step method uses TA and APTES, is designed to reduce wasted material and can be applied to a variety of configurations. The reusability was particularly impressive, with little to no loss of separation efficiency over 30 cycles.

Desalination is another area of emerging interest for membrane design, with the need for low energy methods to meet the world's freshwater needs [148]. Continuing the aforementioned trend of pyrogallols being investigated for their superior surface modification properties, Zhang et al. [149] recently investigated the use of epigallocatechin gallate derived from green tea with polyethyleneimine (PEI) for the synthesis of a nanofiltration membrane for water desalination (removal of dyes from

the water was also tested, as a means of verifying the membrane performance). This combines the generally greener and more cost-effective pyrogallol approach to mussel-inspired membrane design with nanofiltration, which is designed to have low energy consumption. The results were promising, showing acceptable salt rejection, good dye separation efficiency and stability. It was a successful look into utilizing pyrogallols for desalination and shows a promising avenue for future development in this area.

2.4 References

[1] Zhao L, Zou Q, Yan X. Self-assembling peptide-based nanoarchitectonics. Bull. Chem. Soc. Jpn. 2019; 92: 70-79.

[2] Levin A, Hakala TA, Schnaider L, Bernardes GJL, Gazit E, Knowles TPJ. Biomimetic peptide self-assembly for functional materials. Nat. Rev. Chem. 2020; 4: 615-634.

[3] Bai Y, Luo Q, Liu J. Protein self-assembly via supramolecular strategies. Chem. Soc. Rev. 2016; 45: 2756-2767.

[4] Mendes AC, Baran ET, Reis RL, Azevedo HS. Self-assembly in nature: using the principles of nature to create complex nanobiomaterials. Wiley Interdiscip Rev Nanomed Nanobiotechnol. 2013; 5: 582-612.

[5] Li J, Wang J, Zhao Y, Zhou P, Carter J, Li Z, et al. Surfactant-like peptides: From molecular design to controllable self-assembly with applications. Coord Chem Rev. 2020; 421: 213418.

[6] Dubey P, Murab S, Karmakar S, Chowdhury PK, Ghosh S. Modulation of self-assembly process of fibroin: an insight for regulating the conformation of silk biomaterials. Biomacromolecules. 2015; 16: 3936-3944.

[7] Yu S-H, Chen S. Biomineralization: self-assembly processes. Encyclopedia of Inorganic Chemistry. 2006.

[8] Collier JH, Messersmith PB. Phospholipid strategies in biomineralization and biomaterials research. Annu. Rev. Mater. Res. 2001; 31: 237-263.

[9] Bryant SJ, Anseth KS, Lee DA, Bader DL. Crosslinking density influences the morphology of chondrocytes photoencapsulated in PEG hydrogels during the application of compressive strain. J Orthop Res. 2004; 22: 1143-1149.

[10] Xu L-P, Peng J, Liu Y, Wen Y, Zhang X, Jiang L, et al. Nacre-inspired design of mechanical stable coating with underwater superoleophobicity. ACS nano. 2013; 7: 5077-5083.

[11] Zhao X, Su Y, Cao J, Li Y, Zhang R, Liu Y, et al. Fabrication of antifouling polymer–inorganic hybrid membranes through the synergy of biomimetic mineralization and nonsolvent induced phase separation. J. Mater. Chem. 2015; 3: 7287-7295.

[12] Sun J, Bhushan B. Hierarchical structure and mechanical properties of nacre: a review. RSC Adv. 2012; 2: 7617.

[13] Gao E, Xu Z. Bio-inspired graphene-derived membranes with strain-controlled interlayer spacing. Nanoscale. 2018; 10: 8585-8590.

[14] Yao HB, Tan ZH, Fang HY, Yu SH. Artificial nacre-like bionanocomposite films from the self-assembly of chitosan-montmorillonite hybrid building blocks. Angew. Chem. Int. Ed. 2010; 49: 10127-10131.

[15] Meyers MA, Chen PY, Lopez MI, Seki Y, Lin AY. Biological materials: a materials science approach. J Mech Behav Biomed Mater. 2011; 4: 626-657.

[16] Appelman TP, Mizrahi J, Elisseeff JH, Seliktar D. The influence of biological motifs and dynamic mechanical stimulation in hydrogel scaffold systems on the phenotype of chondrocytes. Biomaterials. 2011; 32: 1508-1516.

[17] Tang Z, Kotov NA, Magonov S, Ozturk B. Nanostructured artificial nacre. Nat. Mater. 2003; 2: 413-418.

[18] Neinhuis C, Barthlott W. Characterization and distribution of water-repellent, self-cleaning plant surfaces. Ann Bot. 1997; 79: 667-677.

[19] Feng L, Zhang Y, Xi J, Zhu Y, Wang N, Xia F, et al. Petal effect: a superhydrophobic state with high adhesive force. Langmuir. 2008; 24: 4114-4119.

[20] Liu M, Wang S, Jiang L. Nature-inspired superwettability systems. Nat. Rev. Mater. 2017; 2: 1-17.

[21] Gao X, Jiang L. Water-repellent legs of water striders. Nature. 2004; 432: 36-36.

[22] Liu K, Du J, Wu J, Jiang L. Superhydrophobic gecko feet with high adhesive forces towards water and their bio-inspired materials. Nanoscale. 2012; 4: 768-772.

[23] Zheng Y, Gao X, Jiang L. Directional adhesion of superhydrophobic butterfly wings. Soft Matter. 2007; 3: 178-182.

[24] Chen H, Zhang P, Zhang L, Liu H, Jiang Y, Zhang D, et al. Continuous directional water transport on the peristome surface of Nepenthes alata. Nature. 2016; 532: 85-89.

[25] Koch K, Barthlott W. Superhydrophobic and superhydrophilic plant surfaces: an inspiration for biomimetic materials. Philos Trans A Math Phys Eng Sci. 2009; 367: 1487-1509.

[26] Koch K, Blecher IC, König G, Kehraus S, Barthlott W. The superhydrophilic and superoleophilic leaf surface of Ruellia devosiana (Acanthaceae): a biological model for spreading of water and oil on surfaces. Funct Plant Biol. 2009; 36: 339-350.

[27] Zheng Y, Bai H, Huang Z, Tian X, Nie FQ, Zhao Y, et al. Directional water

collection on wetted spider silk. Nature. 2010; 463: 640-643.

[28] Scholz I, Barnes WJ, Smith JM, Baumgartner W. Ultrastructure and physical properties of an adhesive surface, the toe pad epithelium of the tree frog, Litoria caerulea White. J Exp Biol. 2009; 212: 155-162.

[29] Comanns P, Buchberger G, Buchsbaum A, Baumgartner R, Kogler A, Bauer S, Baumgartner W. Directional, passive liquid transport: the Texas horned lizard as a model for a biomimetic 'liquid diode'. J. R. Soc. Interface. 2015; 12: 20150415.

[30] Liu W, Ni H, Wang P, Zhou Y. Investigation on drag reduction performance of pipeline with bioinspired microgrooved surface. Beilstein Archives. 2019; 1: 17.

[31] Liu M, Wang S, Wei Z, Song Y, Jiang L. Bioinspired design of a superoleophobic and low adhesive water/solid interface. Adv Mater. 2009; 21: 665-669.

[32] Liu X, Zhou J, Xue Z, Gao J, Meng J, Wang S, et al. Clam's shell inspired high-energy inorganic coatings with underwater low adhesive superoleophobicity. Adv. Mater. 2012; 24: 3401-3405.

[33] Nishimoto S, Bhushan B. Bioinspired self-cleaning surfaces with superhydrophobicity, superoleophobicity, and superhydrophilicity. RSC Adv. 2013; 3: 671-690.

[34] Rakitov R, Gorb SN. Brochosomal coats turn leafhopper (Insecta, Hemiptera, Cicadellidae) integument to superhydrophobic state. Proc Biol Sci. 2013; 280: 20122391.

[35] Hensel R, Finn A, Helbig R, Braun HG, Neinhuis C, Fischer WJ, et al. Biologically inspired omniphobic surfaces by reverse imprint lithography. Adv. Mater. 2014; 26:

2029-2033.

[36] Tuteja A, Choi W, Ma M, Mabry JM, Mazzella SA, Rutledge GC, et al. Designing superoleophobic surfaces. Science. 2007; 318: 1618-1622.

[37] Autumn K, Sitti M, Liang YA, Peattie AM, Hansen WR, Sponberg S, et al. Evidence for van der Waals adhesion in gecko setae. Proc Natl Acad Sci U S A. 2002; 99: 12252-12256.

[38] Darmanin T, Guittard F. Superhydrophobic and superoleophobic properties in nature. Mater Today. 2015; 18: 273-285.

[39] Yong J, Chen F, Yang Q, Huo J, Hou X. Superoleophobic surfaces. Chem. Soc. Rev. 2017; 46: 4168-4217.

[40] Nickerl J, Helbig R, Schulz H-J, Werner C, Neinhuis C. Diversity and potential correlations to the function of Collembola cuticle structures. Zoomorphology. 2012; 132: 183-195.

[41] Nosonovsky M, Bhushan B. Why re-entrant surface topography is needed for robust oleophobicity. Philos Trans A Math Phys Eng Sci. 2016; 374: 20160185.

[42] Nickerl J, Tsurkan M, Hensel R, Neinhuis C, Werner C. The multi-layered protective cuticle of Collembola: a chemical analysis. J. R. Soc. Interface. 2014; 11: 20140619.

[43] Lee H, Dellatore SM, Miller WM, Messersmith PB. Mussel-inspired surface chemistry for multifunctional coatings. Science. 2007; 318: 426-430.

[44] Waite J, Tanzer M. The bioadhesive of Mytilus byssus: a protein containing L-dopa. Biochem Biophys Res Commun. 1980; 96: 1554-1561.

[45] Ye Q, Zhou F, Liu W. Bioinspired catecholic chemistry for surface modification. Chem. Soc. Rev. 2011; 40: 4244-4258.

[46] Dreyer DR, Miller DJ, Freeman BD, Paul DR, Bielawski CW. Perspectives on poly(dopamine). Chem. Sci. 2013; 4: 3796.

[47] Liu Y, Ai K, Lu L. Polydopamine and its derivative materials: synthesis and promising applications in energy, environmental, and biomedical fields. Chem. Rev. 2014; 114: 5057-5115.

[48] Yu M, Hwang J, Deming TJ. Role of L-3, 4-dihydroxyphenylalanine in mussel adhesive proteins. J Am Chem Soc. 1999; 121: 5825-5826.

[49] Waite JH, Tanzer ML. Polyphenolic substance of Mytilus edulis: novel adhesive containing L-dopa and hydroxyproline. Science. 1981; 212: 1038-1040.

[50] Patil N, Jérôme C, Detrembleur C. Recent advances in the synthesis of catechol-derived (bio)polymers for applications in energy storage and environment. Prog Polym Sci. 2018; 82: 34-91.

[51] Kasemset S, Lee A, Miller DJ, Freeman BD, Sharma MM. Effect of polydopamine deposition conditions on fouling resistance, physical properties, and permeation properties of reverse osmosis membranes in oil/water separation. J. Membr. Sci. 2013; 425-426: 208-216.

[52] Wei H, Ren J, Han B, Xu L, Han L, Jia L. Stability of polydopamine and poly (DOPA) melanin-like films on the surface of polymer membranes under strongly acidic and alkaline conditions. Colloids Surf B Biointerfaces. 2013; 110: 22-28.

[53] Cheng C, Li S, Zhao W, Wei Q, Nie S, Sun S, et al. The hydrodynamic permeability

and surface property of polyethersulfone ultrafiltration membranes with mussel-inspired polydopamine coatings. J. Membr. Sci. 2012; 417-418: 228-236.

[54] Kloos J, Joosten N, Schenning A, Nijmeijer K. Self-assembling liquid crystals as building blocks to design nanoporous membranes suitable for molecular separations. J. Membr. Sci. 2020: 118849.

[55] Radjabian M, Abetz V. Advanced porous polymer membranes from self-assembling block copolymers. Prog Polym Sci. 2020; 102: 101219.

[56] Lee JW, Kim JH, An DJ, Lee JK, Kim N, Kim SH. Mesoporous composite membrane based on block copolymer self-Assembly. Macromol. Res. 2019; 27: 974-981.

[57] Cummins C, Lundy R, Walsh JJ, Ponsinet V, Fleury G, Morris MA. Enabling future nanomanufacturing through block copolymer self-assembly: A review. Nano Today. 2020; 35: 100936.

[58] Phillip WA, O'Neill B, Rodwogin M, Hillmyer MA, Cussler EL. Self-assembled block copolymer thin films as water filtration membranes. ACS Appl. Mater. Interfaces 2010; 2: 847-853.

[59] Wei M, Sun W, Shi X, Wang Z, Wang Y. Homoporous Membranes with tailored pores by soaking block copolymer/homopolymer blends in selective solvents: dissolution versus swelling. Macromolecules. 2015; 49: 215-223.

[60] Abetz V. Isoporous block copolymer membranes. Macromol Rapid Commun. 2015; 36: 10-22.

[61] Qiu X, Yu H, Karunakaran M, Pradeep N, Nunes SP, Peinemann K-V. Selective

separation of similarly sized proteins with tunable nanoporous block copolymer membranes. ACS nano. 2013; 7: 768-776.

[62] Radjabian M, Koll J, Buhr K, Vainio U, Abetz C, Handge UA, et al. Tailoring the morphology of self-assembled block copolymer hollow fiber membranes. Polymer. 2014; 55: 2986-2997.

[63] Cheng J, Xu M, Cheng P, Zhang W, Li N, Wang Y, et al. Metal ions 'sewing' isoporous membranes with polystyrene-block-poly (acrylic acid) block copolymer. J. Membr. Sci. 2019; 587: 117086.

[64] Henmi M, Nakatsuji K, Ichikawa T, Tomioka H, Sakamoto T, Yoshio M, et al. Self-organized liquid-crystalline nanostructured membranes for water treatment: selective permeation of ions. Adv. Mater. 2012; 24: 2238-2241.

[65] Sakamoto T, Ogawa T, Nada H, Nakatsuji K, Mitani M, Soberats B, et al. Development of nanostructured water treatment membranes based on thermotropic liquid crystals: molecular design of sub-nanoporous materials. Adv. Sci. 2018; 5: 1700405.

[66] Gupta M, Suzuki Y, Sakamoto T, Yoshio M, Torii S, Katayama H, et al. Polymerizable photocleavable columnar liquid crystals for nanoporous water treatment membranes. ACS Macro Letters. 2019; 8: 1303-1308.

[67] Zhao Q, An Q-F, Liu T, Chen J-T, Chen F, Lee K-R, et al. Bio-inspired polyelectrolyte complex/graphene oxide nanocomposite membranes with enhanced tensile strength and ultra-low gas permeability. Polym. Chem. 2013; 4: 4298.

[68] Lecaros RLG, Mendoza GEJ, Hung W-S, An Q-F, Caparanga AR, Tsai H-A, et al.

Tunable interlayer spacing of composite graphene oxide-framework membrane for acetic acid dehydration. Carbon. 2017; 123: 660-667.

[69] Mao H, Zhen H-G, Ahmad A, Li S-H, Liang Y, Ding J-F, et al. Highly selective and robust PDMS mixed matrix membranes by embedding two-dimensional ZIF-L for alcohol permselective pervaporation. J. Membr. Sci. 2019; 582: 307-321.

[70] Yang E, Karahan HE, Goh K, Chuah CY, Wang R, Bae T-H. Scalable fabrication of graphene-based laminate membranes for liquid and gas separations by crosslinking-induced gelation and doctor-blade casting. Carbon. 2019; 155: 129-137.

[71] Zhao J, Zhu Y, Pan F, He G, Fang C, Cao K, et al. Fabricating graphene oxide-based ultrathin hybrid membrane for pervaporation dehydration via layer-by-layer self-assembly driven by multiple interactions. J. Membr. Sci. 2015; 487: 162-172.

[72] Qin Z, Ren X, Shan L, Guo H, Geng C, Zhang G, et al. Nacrelike-structured multilayered polyelectrolyte/calcium carbonate nanocomposite membrane via Ca-incorporated layer-by-layer-assembly and CO_2 -induced biomineralization. J. Membr. Sci. 2016; 498: 180-191.

[73] Lipton J, Weng GM, Alhabeb M, Maleski K, Antonio F, Kong J, et al. Mechanically strong and electrically conductive multilayer MXene nanocomposites. Nanoscale. 2019; 11: 20295-20300.

[74] Wu Y, Cao R, Ji L, Huang W, Yang X, Tu Y. Synergistic toughening of bioinspired artificial nacre by polystyrene grafted graphene oxide. RSC Adv. 2015; 5: 28085-28091.

[75] Fang Q, Zhou X, Deng W, Zheng Z, Liu Z. Freestanding bacterial cellulose-graphene oxide composite membranes with high mechanical strength for selective ion

permeation. Sci. Rep. 2016; 6: 33185.

[76] Feng Y, Ding L, Ji D, Wang L, Guo W. Highly rectified ion transport through 2D WSe_2/MoS_2 bi-layered membranes. Chin Chem Lett. 2018; 29: 892-894.

[77] Wang S, Liu K, Yao X, Jiang L. Bioinspired surfaces with superwettability: new insight on theory, design, and applications. Chem. Rev. 2015; 115: 8230-8293.

[78] Yong J, Fang Y, Chen F, Huo J, Yang Q, Bian H, et al. Femtosecond laser ablated durable superhydrophobic PTFE films with micro-through-holes for oil/water separation: Separating oil from water and corrosive solutions. Appl. Surf. Sci. 2016; 389: 1148-1155.

[79] Zhang W, Shi Z, Zhang F, Liu X, Jin J, Jiang L. Superhydrophobic and superoleophilic PVDF membranes for effective separation of water-in-oil emulsions with high flux. Adv. Mater. 2013; 25: 2071-2076.

[80] Crick CR, Gibbins JA, Parkin IP. Superhydrophobic polymer-coated copper-mesh; membranes for highly efficient oil–water separation. J. Mater. Chem. 2013; 1: 5943-5948.

[81] Chen L, Wu F, Li Y, Wang Y, Si L, Lee KI, et al. Robust and elastic superhydrophobic breathable fibrous membrane with in situ grown hierarchical structures. J. Membr. Sci. 2018; 547: 93-98.

[82] Jia W, Kharraz JA, Choi PJ, Guo J, Deka BJ, An AK. Superhydrophobic membrane by hierarchically structured PDMS-POSS electrospray coating with cauliflower-shaped beads for enhanced MD performance. J. Membr. Sci. 2020; 597: 117638.

[83] Lin J, Lin F, Liu R, Li P, Fang S, Ye W, et al. Scalable fabrication of robust

superhydrophobic membranes by one-step spray-coating for gravitational water-in-oil emulsion separation. Sep Purif Technol. 2020; 231: 115898.

[84] Yang C, Li X-M, Gilron J, Kong D-f, Yin Y, Oren Y, et al. CF4 plasma-modified superhydrophobic PVDF membranes for direct contact membrane distillation. J. Membr. Sci. 2014; 456: 155-161.

[85] Ghaffar A, Chen C, Zhu X, Chen B. Underwater superoleophobic PVA–GO nanofibrous membranes for emulsified oily water purification. Environ. Sci. Nano. 2019; 6: 3723-3733.

[86] Li X, Shan H, Zhang W, Li B. 3D printed robust superhydrophilic and underwater superoleophobic composite membrane for high efficient oil/water separation. Sep Purif Technol. 2020; 237: 116324.

[87] Zhang L, Zhong Y, Cha D, Wang P. A self-cleaning underwater superoleophobic mesh for oil-water separation. Sci. Rep. 2013; 3: 1-5.

[88] Chen Y, Xie A, Cui J, Lang J, Yan Y, Li C, et al. UV-driven antifouling paper fiber membranes for efficient oil–water separation. Ind Eng Chem Res. 2019; 58: 5186-5194.

[89] Liu S, Wang J. Eco-friendly and facile fabrication of polyimide mesh with underwater superoleophobicity for oil/water separation via polydopamine/starch hybrid decoration. Sep Purif Technol. 2020; 250: 117228.

[90] Cheng Y, Wang J, Li M, Fu F, Zhao Y, Yu J. Zwitterionic polymer-grafted superhydrophilic and superoleophobic silk fabrics for anti-oil applications. Macromol Rapid Commun. 2020; 41: 2000162.

[91] Zhou H, Guo Z. Superwetting Janus membranes: focusing on unidirectional

transport behaviors and multiple applications. J. Mater. Chem. 2019; 7: 12921-12950.

[92] Li HN, Yang J, Xu ZK. Asymmetric surface engineering for Janus membranes. Adv. Mater. Interfaces. 2020; 7: 1902064.

[93] Wang G-J, Wu B-H, Xu Z-K, Wan L-S. Janus polymer membranes prepared by single-side polydopamine deposition for dye adsorption and fine bubble aeration. Mater. Chem. Front. 2019; 3: 2102-2109.

[94] Li H, Cao M, Ma X, Zhang Y, Jin X, Liu K, et al. “Plug-and-Go”-type liquid diode: integrated mesh with Janus superwetting properties. Adv. Mater. Interfaces. 2016; 3: 1600276.

[95] Wang H, Zhou H, Niu H, Zhang J, Du Y, Lin T. Dual-layer superamphiphobic/superhydrophobic-oleophilic nanofibrous membranes with unidirectional oil-transport ability and strengthened oil-water separation performance. Adv. Mater. Interfaces. 2015; 2: 1400506.

[96] Yang J, Wen G, Gou X, Song H, Guo Z. A study on the manufacture of Kevlar membrane modified by inorganic nanoparticles with universal applicability in separating diffident types of emulsions. J. Membr. Sci. 2018; 563: 326-335.

[97] Song H-M, Chen C, Shui X-X, Yang H, Zhu L-J, Zeng Z-X, et al. Asymmetric Janus membranes based on in situ mussel-inspired chemistry for efficient oil/water separation. J. Membr. Sci. 2019; 573: 126-134.

[98] Li T, Liu F, Zhang S, Lin H, Wang J, Tang CY. Janus Polyvinylidene fluoride membrane with extremely opposite wetting surfaces via one single-step unidirectional segregation strategy. ACS Appl. Mater. Interfaces 2018; 10: 24947-24954.

[99] Wei X, Zhou H, Chen F, Wang H, Ji Z, Lin T. High-efficiency low-resistance oil-mist coalescence filtration using fibrous filters with thickness-direction asymmetric wettability. Adv. Funct. Mater. 2019; 29: 1806302.

[100] Luo Z-Y, Lyu S-S, Fu Y-X, Heng Y, Mo D-C. The Janus effect on superhydrophilic Cu mesh decorated with Ni-NiO/Ni $(OH)_2$ core-shell nanoparticles for oil/water separation. Appl. Surf. Sci. 2017; 409: 431-437.

[101] Waldman RZ, Yang H-C, Mandia DJ, Nealey PF, Elam JW, Darling SB. Janus membranes via diffusion-controlled atomic layer deposition. Adv. Mater. Interfaces. 2018; 5: 1800658.

[102] Chen J, Liu Y, Guo D, Cao M, Jiang L. Under-water unidirectional air penetration via a Janus mesh. Chem Comm. 2015; 51: 11872-11875.

[103] Wang Z, Wang Y, Liu G. Rapid and efficient separation of oil from oil-in-water emulsions using a Janus cotton fabric. Angew Chem. 2016; 128: 1313-1316.

[104] Li C, Li X, Du X, Tong T, Cath TY, Lee J. Antiwetting and antifouling Janus membrane for desalination of saline oily wastewater by membrane distillation. ACS Appl. Mater. Interfaces 2019; 11: 18456-18465.

[105] Ma W, Zhang M, Li Y, Kang M, Huang C, Fu G. Flexible, durable and magnetic nanofibrous membrane with pH-switchable wettability for efficient on-demand oil/water separation. Environ. Sci. Nano. 2019; 6: 3699-3711.

[106] Shami Z, Holakooei P. Durable light-driven three-dimensional smart switchable superwetting nanotextile as a green scaled-up oil-water separation technology. ACS omega. 2020; 5: 4962-4972.

[107] Yan T, Chen X, Zhang T, Yu J, Jiang X, Hu W, et al. A magnetic pH-induced textile fabric with switchable wettability for intelligent oil/water separation. Chem. Eng. J. 2018; 347: 52-63.

[108] Ou R, Wei J, Jiang L, Simon GP, Wang H. Robust thermoresponsive polymer composite membrane with switchable superhydrophilicity and superhydrophobicity for efficient oil-water separation. Environ Sci Technol. 2016; 50: 906-914.

[109] Du L, Quan X, Fan X, Chen S, Yu H. Electro-responsive carbon membranes with reversible superhydrophobicity/superhydrophilicity switch for efficient oil/water separation. Sep Purif Technol. 2019; 210: 891-899.

[110] Xu L, Liu N, Cao Y, Lu F, Chen Y, Zhang X, et al. Mercury ion responsive wettability and oil/water separation. ACS Appl. Mater. Interfaces 2014; 6:13324-13329.

[111] Wong WSY, Gengenbach T, Nguyen HT, Gao X, Craig VSJ, Tricoli A. Dynamically gas-phase switchable super(de)wetting states by reversible amphiphilic functionalization: a powerful approach for smart fluid gating membranes. Adv. Funct. Mater. 2018; 28: 1704423.

[112] Liao Y, Tian M, Wang R. A high-performance and robust membrane with switchable super-wettability for oil/water separation under ultralow pressure. J. Membr. Sci. 2017; 543: 123-132.

[113] Wei Y, Qi H, Gong X, Zhao S. Specially wettable membranes for oil–water separation. Adv. Mater. Interfaces. 2018; 5: 1800576.

[114] Huang N, Zhang S, Yang L, Liu M, Li H, Zhang Y, et al. Multifunctional electrochemical platforms based on the michael addition/schiff base reaction of

polydopamine modified reduced graphene oxide: construction and application. ACS Appl. Mater. Interfaces 2015; 7: 17935-17946.

[115] Cheng C, Nie S, Li S, Peng H, Yang H, Ma L, et al. Biopolymer functionalized reduced graphene oxide with enhanced biocompatibility via mussel inspired coatings/anchors. J. Mater. Chem. B. 2013; 1: 265-275.

[116] Zhang X, Zeng G, Tian J, Wan Q, Huang Q, Wang K, et al. PEGylation of carbon nanotubes via mussel inspired chemistry: Preparation, characterization and biocompatibility evaluation. Appl. Surf. Sci. 2015; 351: 425-432.

[117] Kang SM, Hwang NS, Yeom J, Park SY, Messersmith PB, Choi IS, et al. One-step multipurpose surface functionalization by adhesive catecholamine. Adv Funct Mater. 2012; 22: 2949-2955.

[118] Kwon SJ, Park S-H, Shin MG, Park MS, Park K, Hong S, et al. Fabrication of high performance and durable forward osmosis membranes using mussel-inspired polydopamine-modified polyethylene supports. J. Membr. Sci. 2019; 584: 89-99.

[119] Lee H, Rho J, Messersmith PB. Facile conjugation of biomolecules onto surfaces via mussel adhesive protein inspired coatings. Adv. Mater. 2009; 21: 431-434.

[120] Yu W, Kang E, Neoh K. Controlled grafting of well-defined epoxide polymers on hydrogen-terminated silicon substrates by surface-initiated ATRP at ambient temperature. Langmuir. 2004; 20: 8294-8300.

[121] Waldron C, Zhang Q, Li Z, Nikolaou V, Nurumbetov G, Godfrey J, et al. Absolut “copper catalyzation perfected”; robust living polymerization of NIPAM: Guinness is good for SET-LRP. Polym Chem. 2014; 5: 57-61.

[122] Wan Q, Liu M, Tian J, Deng F, Zeng G, Li Z, et al. Surface modification of carbon nanotubes by combination of mussel inspired chemistry and SET-LRP. Polym. Chem. 2015; 6: 1786-1792.

[123] Ma Z, Jia X, Hu J, Liu Z, Wang H, Zhou F. Mussel-inspired thermosensitive polydopamine-graft-poly(N-isopropylacrylamide) coating for controlled-release fertilizer. J Agric Food Chem. 2013; 61: 12232-12237.

[124] Zhang X, Ji J, Zhang X, Yang B, Liu M, Liu W, et al. Mussel inspired modification of carbon nanotubes using RAFT derived stimuli-responsive polymers. RSC Adv. 2013; 3: 21817.

[125] Isakova A, Topham PD, Sutherland AJ. Controlled RAFT Polymerization and Zinc Binding Performance of Catechol-Inspired Homopolymers. Macromolecules. 2014; 47: 2561-2568.

[126] Chen P-C, Wan L-S, Xu Z-K. Bio-inspired $CaCO_3$ coating for superhydrophilic hybrid membranes with high water permeability. J. Mater. Chem. 2012; 22: 22727.

[127] Liu Q, Wang N, Caro J, Huang A. Bio-inspired polydopamine: a versatile and powerful platform for covalent synthesis of molecular sieve membranes. J. Am. Chem. Soc. 2013; 135: 17679-17682.

[128] Huang A, Liu Q, Wang N, Caro J. Highly hydrogen permselective ZIF-8 membranes supported on polydopamine functionalized macroporous stainless-steel-nets. J Mater Chem A. 2014; 2: 8246-8251.

[129] Sheng W, Li B, Wang X, Dai B, Yu B, Jia X, et al. Brushing up from “anywhere” under sunlight: a universal surface-initiated polymerization from polydopamine-coated

surfaces. Chem. Sci. 2015; 6: 2068-2073.

[130] Du X, Li L, Li J, Yang C, Frenkel N, Welle A, et al. UV-triggered dopamine polymerization: control of polymerization, surface coating, and photopatterning. Adv. Mater. 2014; 26: 8029-8033.

[131] Wang J, Ma G, Huang W, He Y. Visible-light initiated polymerization of dopamine in a neutral environment for surface coating and visual protein detection. Polym. Chem. 2018; 9: 5242-5247.

[132] Li R, Li J, Rao L, Lin H, Shen L, Xu Y, et al. Inkjet printing of dopamine followed by UV light irradiation to modify mussel-inspired PVDF membrane for efficient oil-water separation. J. Membr. Sci. 2021; 619: 118790.

[133] Kohri M, Kohma H, Shinoda Y, Yamauchi M, Yagai S, Kojima T, et al. A colorless functional polydopamine thin layer as a basis for polymer capsules. Polym. Chem. 2013; 4: 2696.

[134] Yan Z, Zhang Y, Yang H, Fan G, Ding A, Liang H, et al. Mussel-inspired polydopamine modification of polymeric membranes for the application of water and wastewater treatment: A review. Chem Eng Res Des. 2020; 157: 195-214.

[135] Zhang X, Huang Q, Deng F, Huang H, Wan Q, Liu M, et al. Mussel-inspired fabrication of functional materials and their environmental applications: Progress and prospects. Appl. Mater. Today. 2017; 7: 222-238.

[136] Yang H, Zheng WH. Chiral-organotin-catalyzed kinetic resolution of vicinal amino alcohols. Angew. Chem. Int. Ed. 2019; 58: 16177-16180.

[137] Huang S. Mussel-inspired one-step copolymerization to engineer hierarchically

structured surface with superhydrophobic properties for removing oil from water. ACS Appl. Mater. Interfaces 2014; 6: 17144-17150.

[138] Sileika TS, Barrett DG, Zhang R, Lau KHA, Messersmith PB. Colorless multifunctional coatings inspired by polyphenols found in tea, chocolate, and wine. Angew Chem Int Ed. 2013; 52: 10766-10770.

[139] Zhan K, Ejima H, Yoshie N. Antioxidant and adsorption properties of bioinspired phenolic polymers: A comparative study of catechol and gallol. ACS Sustain. Chem. Eng. 2016; 4: 3857-3863.

[140] Zhan K, Kim C, Sung K, Ejima H, Yoshie N. Tunicate-inspired gallol polymers for underwater adhesive: a comparative study of catechol and gallol. Biomacromolecules. 2017; 18: 2959-2966.

[141] Yang X, Sun H, Pal A, Bai Y, Shao L. Biomimetic silicification on membrane surface for highly efficient treatments of both oil-in-water emulsion and protein wastewater. ACS Appl. Mater. Interfaces 2018; 10: 29982-29991.

[142] Xu Y, Guo D, Li T, Xiao Y, Shen L, Li R, et al. Manipulating the mussel-inspired co-deposition of tannic acid and amine for fabrication of nanofiltration membranes with an enhanced separation performance. J Colloid Interface Sci. 2020; 565: 23-34.

[143] Zhang J, Zhao J, Qu W, Li X, Wang Z. One-step, low-cost, mussel-inspired green method to prepare superhydrophobic nanostructured surfaces having durability, efficiency, and wide applicability. J Colloid Interface Sci. 2020; 580: 211-222.

[144] Xu Y, Guo D, Li T, Xiao Y, Shen L, Li R, et al. Manipulating the mussel-inspired co-deposition of tannic acid and amine for fabrication of nanofiltration membranes with

an enhanced separation performance. J Colloid Interface Sci. 2020; 565: 23-34.

[145] Zhao H, Waite JH. Linking adhesive and structural proteins in the attachment plaque of Mytilus californianus. J Biol Chem. 2006; 281: 26150-26158.

[146] Zhu G-d, Ying Y-r, Li X, Liu Y, Yang C-y, Yi Z, et al. Isoporous membranes with sub-10 nm pores prepared from supramolecular interaction facilitated block copolymer assembly and application for protein separation. J. Membr. Sci. 2018; 566: 25-34.

[147] Wang X, Peng X, Zhao Y, Yang C, Qi K, Li Y, et al. Bio-inspired modification of superhydrophilic iPP membrane based on polydopamine and graphene oxide for highly antifouling performance and reusability. Mater Lett. 2019; 255: 126573.

[148] Choudhury RR, Gohil JM, Mohanty S, Nayak SK. Antifouling, fouling release and antimicrobial materials for surface modification of reverse osmosis and nanofiltration membranes. J. Mater. Chem. 2018; 6: 313-333.

[149] Zhang N, Huang Z, Yang N, Zhang L, Jiang B, Sun Y, et al. Nanofiltration membrane via EGCG-PEI co-deposition followed by cross-linking on microporous PTFE substrates for desalination. Sep Purif Technol. 2020; 232: 115964.

Chapter 3: Materials and methods

3.1 Materials

3.1.1 Membrane synthesis

Information of materials used for the synthesis of different types of membranes has been summarized in Table 3.1.

Table 3.1. Materials for the synthesis of different types of membranes

Materials	Source
Stainless steel meshes	The Mesh Company (Warrington) Ltd.
Nylon membrane	Whatman, Inc.
2-methylimidazole (99%)	Sigma-Aldrich Company Ltd.
Zinc nitrate hexahydrate (98%)	Alfa Aesar
Single-layered graphene oxide	Cheap Tubes, Inc. (Brattleboro, VT, USA).
Oleic acid (natural, FCC)	Sigma-Aldrich Company Ltd.
Hydrochloric acid (~37%)	Fisher Scientific UK Ltd.
sodium hydroxide (97%)	Fisher Scientific UK Ltd.

In brief, stainless steel meshes (200 mesh/77 μm; 270 mesh/58 μm; 325 mesh/42 μm; 400 mesh/34 μm) were purchased from The Mesh Company (Warrington) Ltd. Nylon membranes (47 mm diameter, 0.2 μm pore size) was ordered from Whatman, Inc. 2-methylimidazole (2-mim; 99%) was purchased from Sigma-Aldrich Company Ltd.

Zinc nitrate hexahydrate ($Zn(NO_3)_2 \cdot 6H_2O$; 98%) was obtained from Alfa Aesar. Single-layered graphene oxide (SLGO) powder with lateral dimensions in the range of 300-800 nm was purchased from Cheap Tubes, Inc. (Brattleboro, VT, USA). Hydrochloric acid (HCl, ~37%) and sodium hydroxide (NaOH, ≥97%) were supplied by Fisher Scientific UK Ltd.

3.1.2 Oil/water separation

Information of materials used in oil/water separation experiments has been summarized in Table 3.2.

Table 3.2. Materials for oil/water separation experiments

Materials	**Density (g/cm^3)**	**Source**
n-heptane (99%)	0.684	Fisher Scientific UK Ltd
n-hexane (~95%)	0.659	Fisher Scientific UK Ltd
Cyclohexane (99%)	0.779	Fisher Scientific UK Ltd
Decane (99%)	0.733	Fisher Scientific UK Ltd
Dodecane (99%)	0.753	Fisher Scientific UK Ltd
Chloroform (99%)	1.492	Fisher Scientific UK Ltd
Dichloromethane (99%)	1.325	Fisher Scientific UK Ltd
Methylene blue (80%)	/	Alfa Aesar
Oil red O (90%)	/	Alfa Aesar

In brief, n-heptane (99%), n-hexane (~95%), cyclohexane (99%), decane (99%),

dodecane (99%), chloroform (99%), dichloromethane (99%), were supplied by Fisher Scientific UK Ltd and were used as received. These chemicals were used as oils in the oil/water mixture separation experiment. Oil red O and methylene blue, which were used to dye oils and water, respectively, were obtained from Alfa Aesar. All chemicals were used as received.

3.1.2 Molecular separation

Table 3.3. Materials for the synthesis of different types of membranes

Materials	Molecular weight (g mol^{-1})	Source
Acetone (99%)	58.1	Fisher Scientific UK Ltd Fisher
Methanol (99%)	32.0	Fisher Scientific UK Ltd
Ethanol (99%)	46.1	Fisher Scientific UK Ltd
N,N-Dimethylmethanamide (99.5%)	73.1	Fisher Scientific UK Ltd
n-Propanol (99%)	60.1	Fisher Scientific UK Ltd
Isopropanol (99%)	60.1	Fisher Scientific UK Ltd
Methylene blue (80%)	319.9	Alfa Aesar
Neutral red (90%)	288.8	Alfa Aesar
Rhodamine B (95%)	479.0	Alfa Aesar
Rose bengal (95%)	1017.6	Alfa Aesar
Reactive black 5 (50%)	991.8	Alfa Aesar
Uniblue A (70%)	506.5	Alfa Aesar
Methyl orange (85%)	327.3	Alfa Aesar

Information of materials used for molecular separation experiments has been summarized in Table 3.3. In brief, acetone (99%), methanol (99%), ethanol (99%), N,

N-dimethylmethanamide (99.5%), n-propanol (99%), and isopropanol (99%) were supplied by Fisher Scientific UK Ltd. These chemicals were used as solvents in the molecular separation experiments for membrane permeation flux tests. methylene blue ($C_{16}H_{18}ClN_3S$), neutral red ($C_{15}H_{17}ClN_4$), Rhodamine B ($C_{28}H_{31}ClN_2O_3$), rose bengal ($C_{20}H_2Cl_4I_4Na_2O_5$), reactive black 5 ($C_{26}H_{21}N_5Na_4O_{19}S_6$), uniblue A ($C_{22}H_{16}N_2O_7S_2$), and methyl orange ($C_{14}H_{14}N_3NaO_3S$) were obtained from Alfa Aesar. These chemicals were used as dye molecules for membrane selectivity tests. All chemicals were used as received.

3.2 Experimental methodologies

3.2.1 Smart mesh films for oil/water separation

3.2.1.1 Fabrication of ZIF-L coated meshes

Stainless steel meshes with a size of 4 cm ×4 cm were sequentially cleaned ultrasonically in acetone, ethanol, and deionized (DI) water to remove surface impurities, followed by soaking in 0.1 M hydrochloric acid solution and then rinsing by DI water to remove surface oxide. The ZIF-L coated mesh was fabricated simply following a pre-seeding and secondary growth process [1]. The synthesis solution was prepared according to a previous study [2] with small modifications. Typically, aqueous solutions of Zn $(NO_3)_2 \cdot 6H_2O$ and 2-methylimidazole were mixed (V: V = 1:1) and stirred for 30 minutes at room temperature (~25 ℃). A piece of cleaned stainless steel mesh was then vertically placed in the synthesis solution for 15 minutes. After that, the

seeded mesh was vertically immersed in the freshly prepared synthesis solution at room temperature for secondary growth. After 1 h, the mesh was removed and washed with deionized water repeatedly. After room temperature drying, the ZIF-L coated mesh was then ready for oil/water mixture separation tests.

3.2.1.2 Switchable oil/water separation experiment

The oil/water separation performance of the ZIF-L coated mesh was tested by conducting a series of gravity-driven oil/water mixture separation experiments [1, 3]. Oil/water mixtures were prepared by simply mixing water with the oil(s). For better observation, water was dyed with methylene blue and oils were dyed with oil red O. A home-made separation apparatus was designed for gravity-driven oil/water mixture separation experiments. The mesh was placed between two identical glass tubes with a diameter of 25 mm and then sealed firmly with clamps. In a separation test, the oil/water mixture was poured directly onto the mesh. The permeate was collected, and its real-time flux was monitored at the same time. In a switchable oil/water separation test, the mesh was firstly pre-wetted with water by simply pouring ~50 mL of deionized water onto the mesh surface. Then a mixture of water and cyclohexane was poured into the top funnel, and the permeated water was collected in a beaker, realizing the “oil-blocking” separation. After that, the mesh was gently shaken in methanol using tweezers and kept soaking for 30 min, followed by air drying for 5 min. The cleaned mesh was then fixed in the separation apparatus and pre-wetted with oil by pouring ~50 mL of dichloromethane onto the mesh surface. A mixture of dichloromethane and water

was then poured into the top funnel, and the permeated dichloromethane was collected, realizing the "water-blocking" separation.

3.2.2 Superhydrophobic ZIF−OAs

3.2.2.1 Interfacial assembly of ZIF−OAs

Hydrophobic two-dimensional ZIF−OAs were synthesized through a simple oil/water interfacial assembly method. Typically, 5 mL of an aqueous solution of Zn $(NO_3)_2 \cdot 6H_2O$ with a concentration of 1M was first added to a petri dish (with a diameter of ~60 mm). Then, 1 mL of 2-methylimidazole which was dissolved in oleic acid with a concentration of 0.4 M was added dropwise to the surface of the Zn $(NO_3)_2 \cdot 6H_2O$ solution in the petri dish. The two-phase mixture was aged for ~24 h under room temperature to obtain two-dimensional ZIF−OAs layers. For the preparation of 1D ZIF−OA nano-scrolls and nanotubes, the two-phase mixture was aged for ~12 h ~48 h under 50 ℃ in an oven. The product was collected by centrifugation at ~5000 rpm for 10 min, followed by methanol wash. After repeating the centrifugation process three times, the final product was dried in an oven at 50 ℃ for further characterizations.

3.2.2.2 Preparation of ZIF-L and ZIF-8

ZIF-L nanosheets were prepared according to a previous study [2] with small modifications. Typically, 40 mL of Zn $(NO_3)_2 \cdot 6H_2O$ aqueous solutions and 40 mL of 2-methylimidazole aqueous solution were mixed and stirred under 500 rpm for 1 h at room temperature (~25 ℃). Then the milky white mixture was centrifuged at 5000 rpm

for 10 min. The collected powder product was rinsed with deionized water. The centrifuge-rinse procedure was repeated three times. After that, the product was dried in an oven at 60 ℃ for further characterizations.

ZIF-8 nanocrystals were prepared by adding ethanol into the ZIF-L synthesis solution [5]. Briefly, 40 mL of Zn $(NO_3)_2 \cdot 6H_2O$ aqueous solutions, 40 mL of 2-methylimidazole aqueous solution, and 20 mL of ethanol were mixed and stirred under 500 rpm for 1 h at room temperature (~25 ℃). Then the milky white mixture was centrifuged at 5000 rpm for 10 min. The collected powder product was rinsed with deionized water. The centrifuge-rinse procedure was repeated three times. After that, the product was dried in an oven at 60 ℃ for further characterizations.

3.2.3 Superwetting ZIF−OA coated Janus membranes

3.2.3.1 ZIF−OA coated membranes by contra-diffusion

A piece of microporous nylon membrane substrate was fixed between two contra-diffusion cells. The water phase consisting of an aqueous solution of Zn $(NO_3)_2 \cdot 6H_2O$ with a concentration of 1M was first added into one side of the contra-diffusion cells. After ~10s, the oil phase consisting of 2-methylimidazole (0.4 M) dissolved in a mixture of oleic acid was added into the other side of the contra-diffusion cells. After 1 h of reaction at room temperature (~22 ℃), the membrane was taken out and rinsed with methanol, and then dried at room temperature.

3.2.3.2 ZIF−OA coated membranes by sequential drop-casting

A piece of nylon membrane was immersed in Zn $(NO_3)_2.6H_2O$ aqueous solution (1M) for 1 h. Then the aqueous solution of Zn $(NO_3)_2.6H_2O$ (1.5 mL) was preferentially cast onto the nylon membrane surface, followed by the casting of oleic acid solution (0.2 mL) containing 2-methylimidazole ligands. Then the membranes were cured for 12 h at room temperature and 50 ℃, respectively, producing different ZIF−OA nanostructures on the membrane surfaces.

3.2.4 Lamellar membranes for molecular separation

3.2.4.1 Preparation of SLGO membranes

SLGO powder was firstly dispersed in deionized water under vortex mixing (VELP Scientifica Advanced IR Vortex Mixer) at 2400 rpm for 3min, followed by a 2 h sonication (Fisherbrand FB11002). The dispersion was then centrifuged at 12000 rpm for 1 h at 20 ℃ (Biofuge primo R, Heraeus) to remove large aggregates in the suspension. The obtained dispersion was used as the stock SLGO solution. SLGO nanosheets were characterized by atomic force microscopy (AFM). The SLGO coated membrane was fabricated by depositing the SLGO dispersion onto nylon membrane support with 200 nm pores (Whatman) via vacuum filtration (Millipore filtration system). The thickness of the SLGO layer can be predicted by calculating the amount of SLGO in the suspension that was used for the filtration, which was determined by Ultraviolet-Visible (UV-Vis) Spectroscopy (Thermo Scientific Evolution 60) The

actual thickness of the SLGO layer was determined by performing a cross-sectional Scanning Electron Microscope (SEM) analysis.

The SLGO-membrane was fabricated by depositing the SLGO nanosheets onto the surface of nylon membrane support with 200 nm pores (Whatman) via vacuum filtration (Millipore filtration system). The GO layer thickness can be roughly controlled by calculating the amount of GO in the SLGO suspension according to the following equation: $m = \rho V = \rho Sh$. In this equation, m is the amount of GO in the SLGO suspension, ρ is the density of GO (ρ = 2.1 g/cm^3), S is the effective filtration area, and h is the ideal thickness of the GO layer.

3.2.4.2 Fabrication of SLGO/ZIF-8 membranes

SLGO stock solution containing 0.40 mg GO was diluted in 200 mL deionized water, followed by a 1 h sonication. Then Zn $(NO_3)_2$•$6H_2O$ (0.05 M, 0.25 M, 0.5M) was added to the solution and kept vigorous stirring for 1 h under room temperature to allow the adsorption of zinc ions on GO nanosheets. After that, the mixture was filtrated through the microporous nylon membrane support, and the resulting membrane was dried under room temperature (25 ℃) overnight. The membrane was subsequently immersed in Zn $(NO_3)_2$•$6H_2O$ solution with a concentration of 0.05 M, 0.25 M, or 0.5M for 2 h under room temperature. Next, 200 mL of 2-methylimidazole solution (0.40 M) was filtrated through the zinc ion saturated GO membrane [4]. The prepared membrane was then dried under room temperature overnight.

3.2.4.3 Molecular filtration performance evaluation

The molecular filtration performance of the membrane was evaluated using the same vacuum filtration apparatus under a vacuum pressure of 0.5 bar. The permeance (F) of the membrane was determined by calculating the volume of permeate in unit time, according to the equation:

$$F = V / (A \bullet \Delta t \bullet \Delta P) \quad (3.1)$$

where V (L) is the volume of permeate, A (m^2) is the effective filtration area, Δt (h) is the filtration time, and ΔP is the applied pressure. The permeance of the membrane for various organic dyes was tested by repeatedly filtering 20 mL of the feed solution across the membrane for at least three times. The dye concentration was measured by using a UV-Vis spectrophotometer (Thermo Scientific Evolution 60). The dye rejection (R) was calculated according to the equation:

$$R = (1 - C_p/C_f) \times 100\% \quad (3.2)$$

where C_p is the dye concentration in permeate, and C_f is the dye concentration in the feed solution.

3.2.5 Characterization methods

3.2.5.1 Scanning electron microscope (SEM)

Morphology of all the synthesized materials in this work was characterized by using a JEOS JSM-IT100 Scanning Electron Microscope (SEM). Each SEM sample was sputter-coated with ~15 nm gold layer prior to analysis. For cross-sectional morphology

of membrane samples, all samples were attained by freeze fracturing a piece of membrane in liquid nitrogen.

3.2.5.2 Contact angle measurements

Contact angle (CA) measurements were performed using the Ossila contact angle goniometer and software. For underwater and underoil contact angle measurements, a transparent rectangular container prefilling with water or oil was used. The samples were then soaked horizontally in the water. An oil or water droplet was gently placed onto the mesh film surface using a home-made curved needle. The final contact angle values were obtained by averaging the contact angles at three different positions on each sample surface.

3.2.5.3 UV-Vis measurements

UV−Vis spectra were obtained to analyze the dye concentrations using a Thermo Scientific Evolution 60 UV−Vis spectrophotometer. All sample measurements were performed in a wavelength range of 300 nm to 800 nm, with an interval of 1 nm.

3.2.5.4 Oil content analysis

In oil/water mixture separation experiments, the residual oil content in the permeate solutions was characterized by an OCMA-220 oil content analyzer. The instrument was warmed up for ~60 minutes prior to calibration and sample measurements.

3.2.5.5 Other characterizations

Atomic force microscopy (AFM) images were obtained on a Multimode Nanoscope V system (Veeco, Santa Barbara, CA), under tapping mode. The crystalline structure of the synthesized ZIF-L was determined by X-ray diffractometer (XRD, Bruker D8 Advance) with Cu Kα radiation in a 2θ range of 4.0° ~ 40.0°. Fourier transform infrared spectroscopy (FT-IR) characterizations were performed on a Nicolet iS10 FT-IR spectrometer. Nitrogen-sorption characterizations were performed on a Quantachrome Autosorb IQ instrument. Thermogravimetric (TGA) characterizations were performed on a Mettler Toledo TGA/DSC instrument.

3.3 References

[1] Chen, T., Lewis, A., Chen, Z., Fan, X., Radacsi, N., Semiao, A.J., Wang, H. Huang, Y. Smart ZIF-L mesh films with switchable superwettability synthesized via a rapid energy-saving process, Sep. Purif. Technol. 2020; 240: 116647.

[2] Zhong, Z., Yao, J., Chen, R., Low, Z., He, M., Liu, J.Z. and Wang, H. Oriented two-dimensional zeolitic imidazolate framework-L membranes and their gas permeation properties, J. Mater. Chem. A. 2015; 3: 15715-15722.

[3] Huang, Y., Jiao, Y., Chen, T., Gong, Y., Wang, S., Liu, Y., Sholl, D.S., Walton, K.S. Tuning the wettability of metal−organic frameworks via defect engineering for efficient oil/water separation, ACS Appl. Mater. Interfaces. 2020; 12: 34413-34422.

[4] Chen, T., Butt, F.S., Zhang, M., Wei, X., Lewis, A., Radacsi, N., Semiao, A.J., Han, J., Huang, Y. Ultra-permeable zeolitic imidazolate frameworks-intercalated graphene oxide membranes for unprecedented ultrafast molecular separation, Chem. Eng. J., 2021; 419: 129507.

[5] Lewis, A., Chen, T., Butt, F.S., Wei, X., Radacsi, N., Fan, X., Huang, Y. Facile synthesis of hierarchical ZIF-L hollow fiber membranes via continuous fluid circulation, Nanoscale, 2021; DOI: 10.1039/D1NR03112K.

Chapter 4: Bioinspired superwetting mesh films for oil/water separation[1]

4.1 Introduction

Oily wastewater generated from various industrial processes and frequent oil spill accidents has become a pressing environmental concern, posing severe threats to both the global ecosystem and human health [1-5]. The development of cost-effective, energy-efficient, and environmentally friendly approaches to address these environmental and economic challenges has been very demanding. Membrane separation technology has rapidly developed during the past decades due to its economic efficiency, infrastructure agility, and operational simplicity [6, 7]. Recently, bioinspired membranes with rationally designed smart surfaces have been recognized as attractive candidates for highly-efficient oil/water separation [8-13]. Metallic-based meshes with low cost and long-term durability have been regarded as an effective substrate [14]. However, most of existing techniques to impart superwetting properties onto mesh surfaces involve expensive/toxic chemicals, sophisticated devices, or high synthesis temperatures in the manufacturing process [15-20]. Thus, there is an immediate need for an energy-effective, scalable, and environmentally friendly approach to fabricate intelligent mesh-supported membranes/films with tunable

[1] This chapter has been published in Separation and Purification Technology 2020; 240:116647

superwetting properties.

Superhydrophilic surfaces with micro/nano-hierarchical architectures can trap abundant water in the rough surfaces, forming a water barrier between the oils and membrane surface and thus generating underwater superoleophobicity [21-29]. A wide range of materials, such as metal hydroxide [30], graphene oxide [31], TiO_2 nanoparticles [32], and polyaniline nanowire [33], have been employed to prepare underwater superoleophobic membranes with excellent oil/water separation efficiency. Very recently, intelligent materials with a switchable wetting surface have been reported with a promising performance in treating various types of oil/water mixtures [34-38]. The special wettability of the smart surfaces was usually switchable between superhydrophobicity-superoleophilicity and superhydrophilicity-superoleophobicity once the external driving force, such as heat [34], electricity [35], gas [36], pH variation [37], or light irradiation [38], was applied. However, the preparation of these intelligent materials usually is very complex and energy-consuming. As switchable oil/water separation requires additional heat or chemical treatment of the surface, the separation procedure can be further complicated, and excess energy consumption could be necessary. Therefore, it is very challenging to fabricate such intelligent surfaces for a more sustainable oil/water separation.

Metal-organic frameworks (MOFs), a class of multifunctional crystalline materials, are of great interest in their application as intelligent membrane materials due to their beneficial characteristics such as unique chemical versatility, flexible structural design,

and abundant functionalities [39-43]. Among them, zeolitic imidazolate frameworks (ZIFs) are a typical type of MOFs with topologies analogous to those known for zeolites [44]. In recent years, both the crystalline form and amorphous form of ZIFs have been extensively studied due to their tunable pore structure and functional properties [45, 46]. Because of the good stability under humid environments, ZIFs have also been attracting particular attention for liquid separation [47, 48].

In this chapter, we demonstrated a facile, energy-effective, and scalable approach to grow ZIF-L nanoplates on various stainless steel meshes at room temperature and ambient pressure. The as-synthesized ZIF-L meshes with extremely rough micro-/nano-hierarchical surface structures exhibited outstanding in-air superamphiphilic, underwater superoleophobic and underoil superhydrophobic properties. Such special superwetting property towards oil and water molecules achieved switchable oil/water mixtures separation without applying any external driving force or chemical treatment. The energy-efficient, timesaving, and environmentally friendly fabrication process developed in this work has great potential to scale up the manufacturing of ZIF-based films for widespread applications in mixture liquid separation.

4.2 Morphology and structure of ZIF-L mesh film

The hierarchical ZIF-L mesh films were fabricated using a fast seeding and secondary growth process, as displayed in the schematic diagram in Figure 4.1a. After dip-coating in the synthesis solution at room temperature (25 °C ± 1 °C) for 15 min, the stainless-

steel mesh (size 400) which initially had a smooth surface (Figure 4.1b, c) was covered by a thin layer of ZIF-L seeds (Figure 4.1d). Then, a new synthesis solution with the same composition was prepared and used to promote the fast secondary growth of ZIF-L film at room temperature. The seeded stainless-steel mesh was placed vertically in the reactor. After only 1 h of synthesis, the mesh surface was uniformly covered by ZIF-L nanoplates (Figure 4.1e), forming a very rough surface.

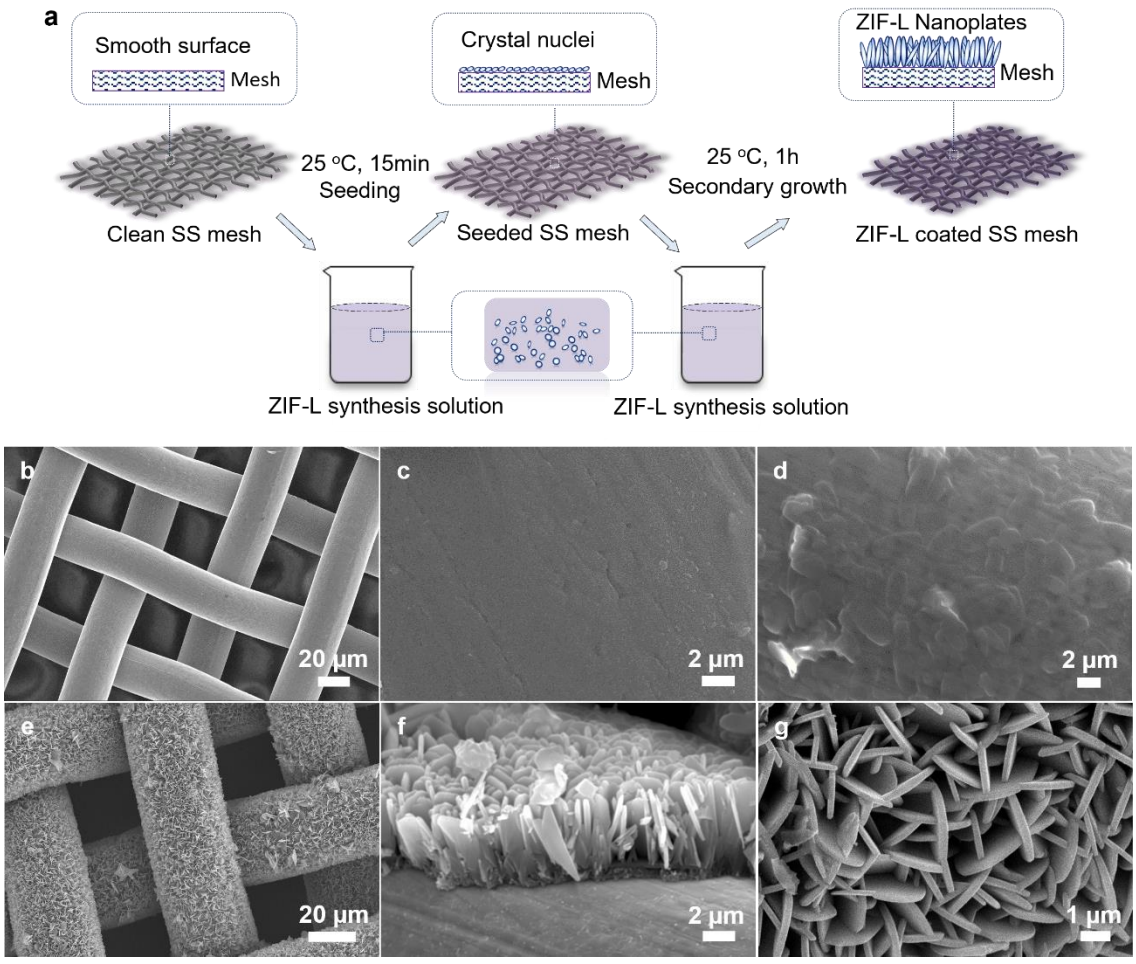

Figure 4.1. Fabrication and morphology of the ZIF-L coated mesh. a) Schematic illustration of the fabrication process of ZIF-L coated meshes. SEM image of b) the pristine stainless-steel mesh, c) an enlarged view of the pristine stainless steel mesh

surface, d) the ZIF-L seeded mesh wire, e) the ZIF-L coated mesh, f) a cross-sectional view of the ZIF-L film, and g) a close top-view of the intergrown ZIF-L nanoplates on the mesh wire

After secondary growth, the average mesh aperture size was decreased from 34 μm to ~25 μm (Figure 4.1e). The cross-sectional SEM image of the mesh wire revealed that the ZIF-L nanoplates with an average length of ~5 μm have vertically grown on the mesh surface (Figure 4.1f). A high-magnification SEM image again confirmed that the mesh surface was fully covered by well-intergrown ZIF-L nanoplates with an average thickness of ~200 nm (Figure 4.1g). The XRD pattern of the powder collected at the bottom of the reactor showed characteristic ZIF-L diffraction patterns [49], and the XRD pattern of the ZIF-L mesh film further confirms that the mesh surface is composed of a thin layer of ZIF-L crystals. (Figure 4.2)

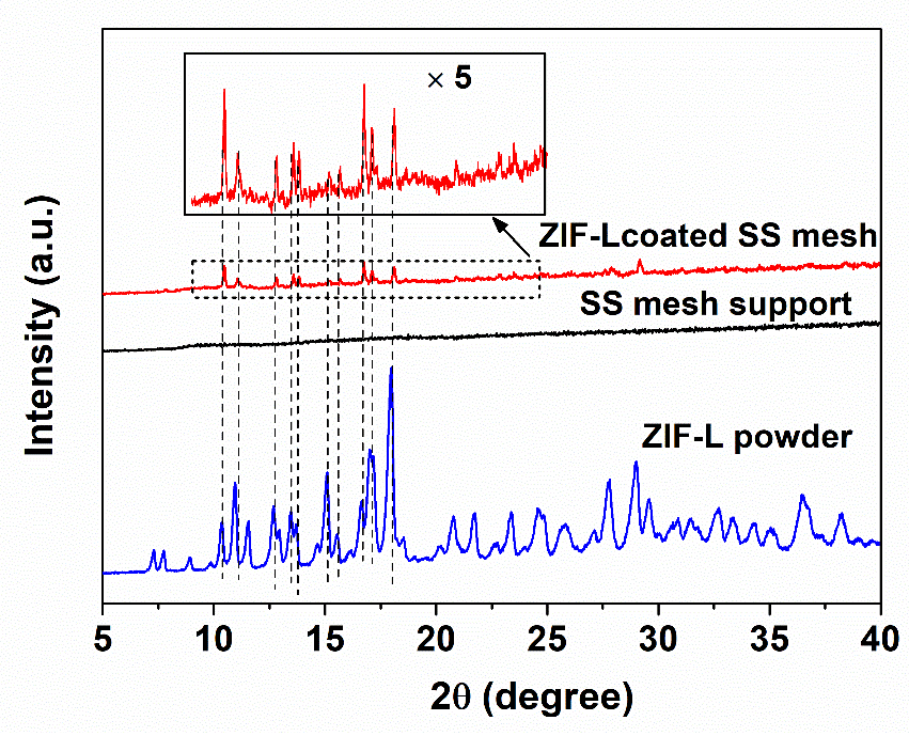

Figure 4.2. The XRD patterns of the stainless steel (SS) mesh support, ZIF-L SS mesh film, and the as-synthesized ZIF-L powder. The inset shows an enlarged view of the XRD patterns in the 2θ range of 9 ~ 25°.

As shown in Figure 4.2, it is clear that the ZIF-L coated SS mesh shows the characteristic peaks of ZIF-L, confirming that the mesh is coated by a layer of ZIF-L nanoplates. Note, the peaks are weak as compared to those of the as-synthesized ZIF-L powder. This is reasonable because the intensity of the XRD patterns of ZIF-L coating is proportional to its mass content in the sample.

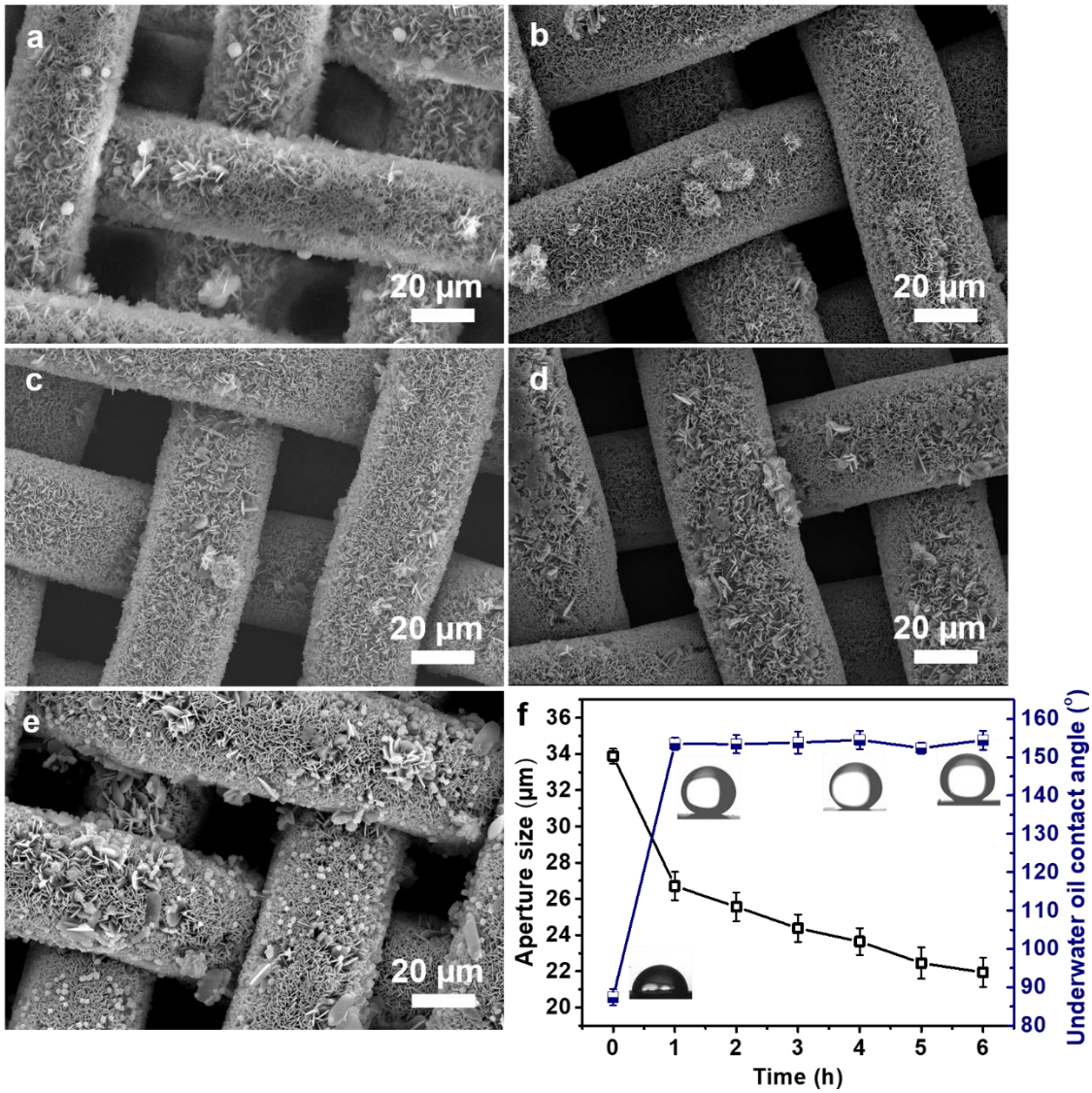

Figure 4.3. SEM images of ZIF-L coated meshes synthesized after different secondary growth time. a) 2 h, b) 3 h, c) 4 h, d) 5 h, e) 6 h, and f) the influence of secondary growth time on the effective aperture size as well as the underwater oil contact angle of the membrane.

In our mesh film sample, the stainless-steel mesh support provided the most weight and therefore, significantly affected the intensity of ZIF-L XRD patterns. Abundant micro- and nano-sized pores were observed on the continuous, hierarchical ZIF-L mesh film.

With further increase of the secondary growth time, the mesh surface morphology showed no significant change except the effective aperture size which decreased from 34 down to ~22 μm after 6 h of secondary growth due to bigger ZIF-L crystals forming on the mesh wires. Therefore, the effective aperture size of the ZIF-L mesh film can be readily adjusted by merely controlling the ZIF-L growth time (Figure 4.3).

However, the underwater oil contact angle (OCA) of the ZIF-L meshes did not improve with higher secondary growth time (i.e., > 1 h), indicating that a short reaction time was sufficient to fabricate a ZIF-L mesh with the excellent underwater superoleophobic property. By using different mesh films (e.g., mesh sizes 200, 270, and 325), very similar ZIF-L structures were fabricated on the mesh surfaces (Figure 4.4). It is worthwhile mentioning that ZIF-L membranes/coatings have been successfully formed on anodic aluminum oxide (AAO) [49] and polymer substrates [48] For example, Zhong et al. have successfully prepared oriented two-dimensional zeolitic imidazolate framework-L membranes on an AAO support [49] Very recently, Bruggen et al. reported a two-step deposition of ZIF-Ls on 3D printed polyamide membranes [50]. However, to the best of the authors' knowledge, it is the first time that the unique hierarchical ZIF-L structure with switchable transport function was easily fabricated on the metal surface (stainless steel in this work) under ambient conditions.

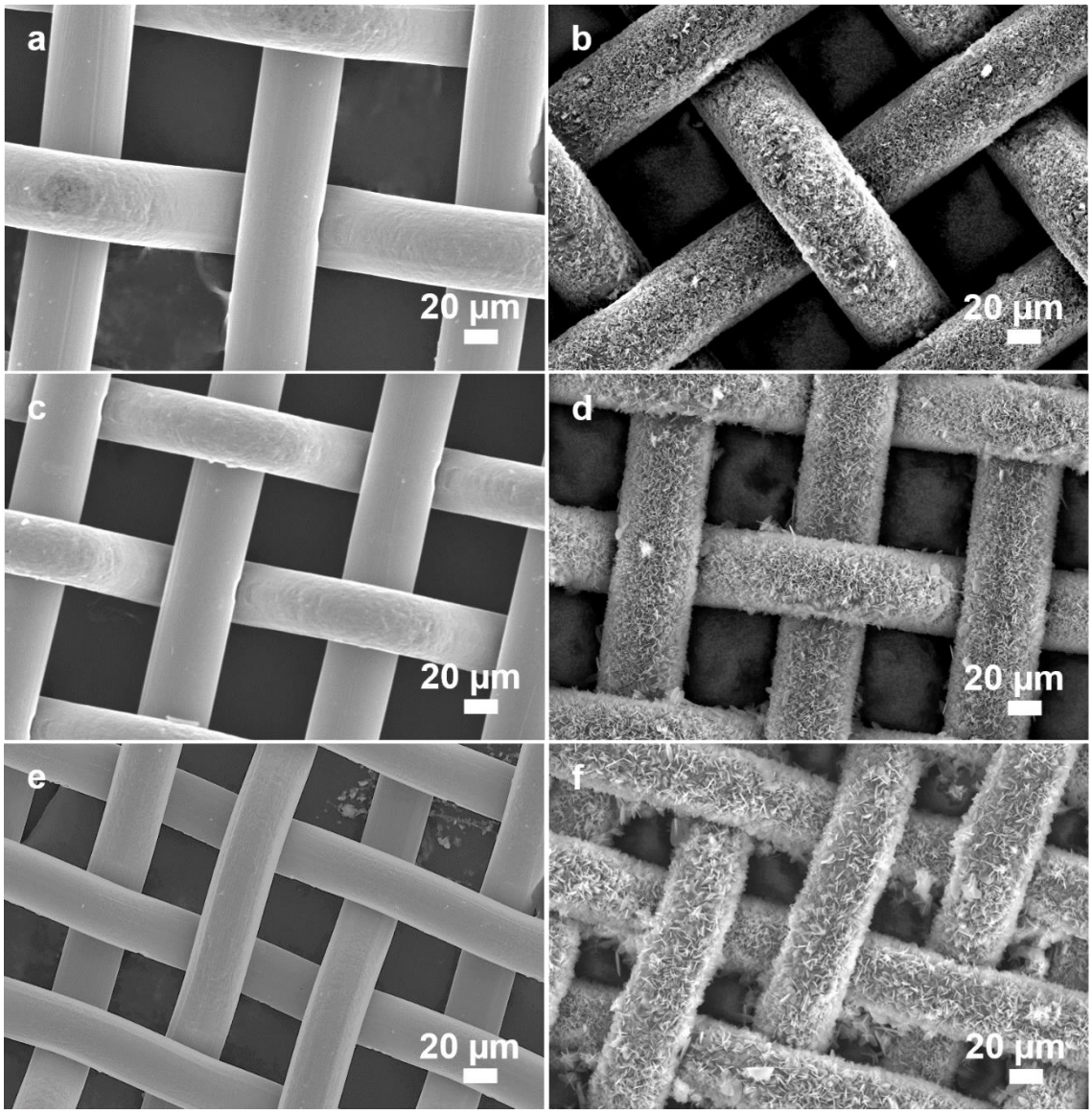

Figure 4.4. SEM images of bare stainless steel meshes with different mesh numbers. a) Mesh 200/77 µm; b) mesh 270/58 µm, c) mesh 325/42 µm, d) ZIF-L coated mesh 200/77 µm, e) ZIF-L coated mesh 270/58 µm, and f) ZIF-L coated mesh 325/42 µm.

In the fabrication process, mesh seeding was a crucial step for the growth of continuous and dense ZIF-L nanoplates on the mesh surface. Without pre-seeding, no ZIF-L nanoplates were formed on the surface after one-hour direct growth (Figure 4.5a, b). A minimum growth time of 7 h was found necessary to have adequate ZIF-L coverage on

mesh wires in the absence of seeds, which was significantly longer than that required in the presence of seeds (Figure 4.5c-f).

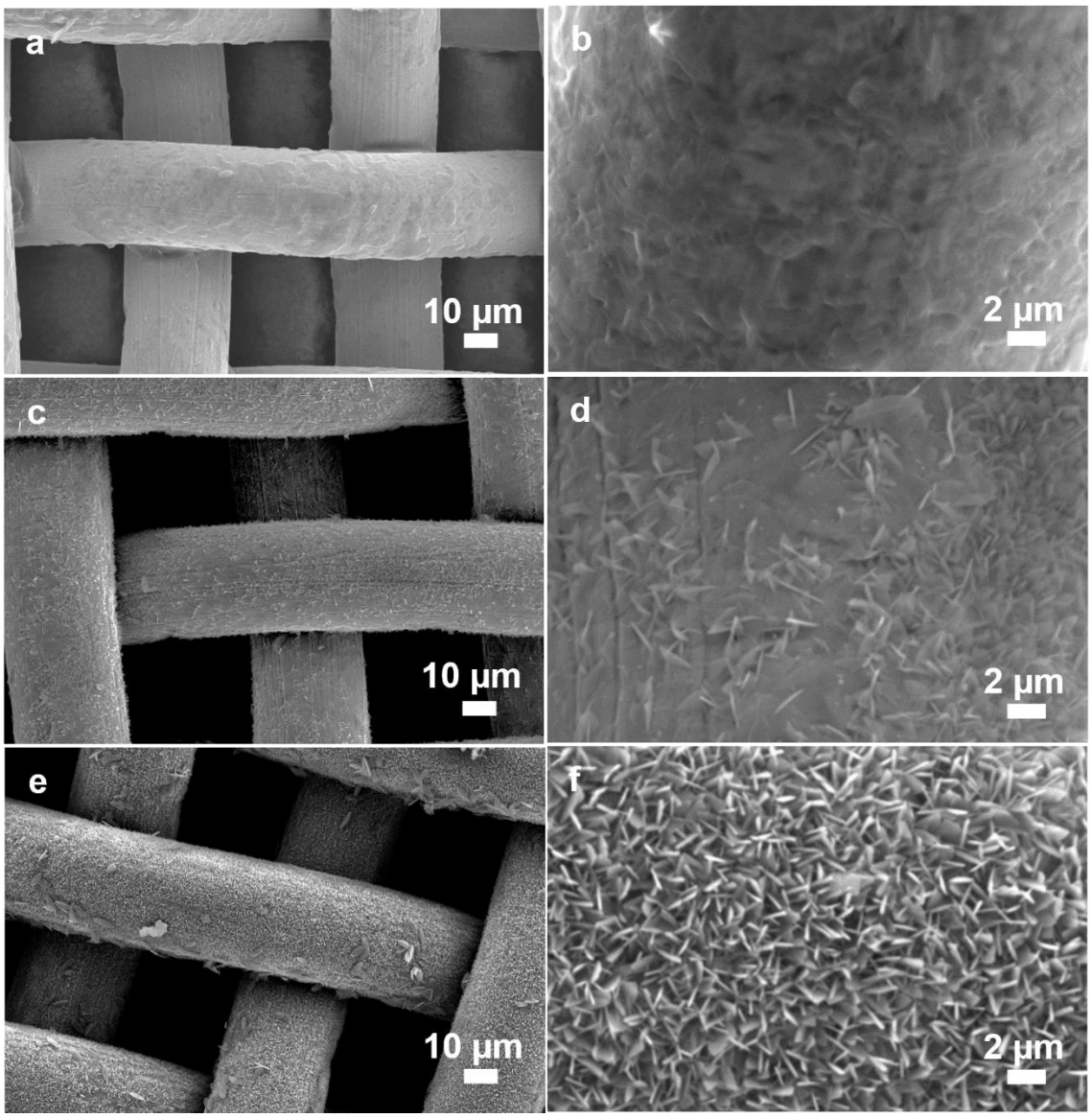

Figure 4.5. SEM images of the mesh surface after direct growth in ZIF-L synthesis solution. a) and b): 1 h direct growth, c) and d): 6 h direct growth, and e) and f): 7 h direct growth. a), c) and e) are low-magnification SEM images, while b), d), and f) are high-magnification SEM images.

The slow crystallization was attributed to the unfavorable nucleation and crystal growth on the unseeded mesh surface. Therefore, a longer growth time was required to form a continuous ZIF-L coating on the surface. In contrast, in the presence of seeds, ZIF-L nucleation and crystallization was more favorable and much faster on the mesh surface. It has been reported that the existing seeds can considerably lower the activation energies associated with nucleation and subsequent crystallization, making the synthesis system more favorable for fast crystal growth at ambient conditions [40, 49]. In this work, by applying seeding, a thick and continuous ZIF-L nanoplate film was successfully formed on the metal surface for one hour at room temperature.

The wettability of the bare stainless-steel mesh and the ZIF-L nanoplate meshes were characterized using contact angle measurements. The bare mesh exhibited in-air hydrophobicity and oleophilicity with a water contact angle (WCA) of ~117° ± 2° and an OCA of ~0° (Figure 4.6a, b). After ZIF-L growth, the mesh surface became hydrophilic with a low WCA of ~20° (Figure 4.7a). Underwater wettability was explored by immersing the mesh in water and performing oil contact angle measurements. The underwater OCA of the clean mesh was ~65° ± 2° (Figure 4.6c). After growing ZIF-L nanoplates on the surface, however, the mesh showed an underwater OCA of ~156° ± 2°, suggesting an outstanding underwater superoleophobic surface was formed (Figure 4.7b).

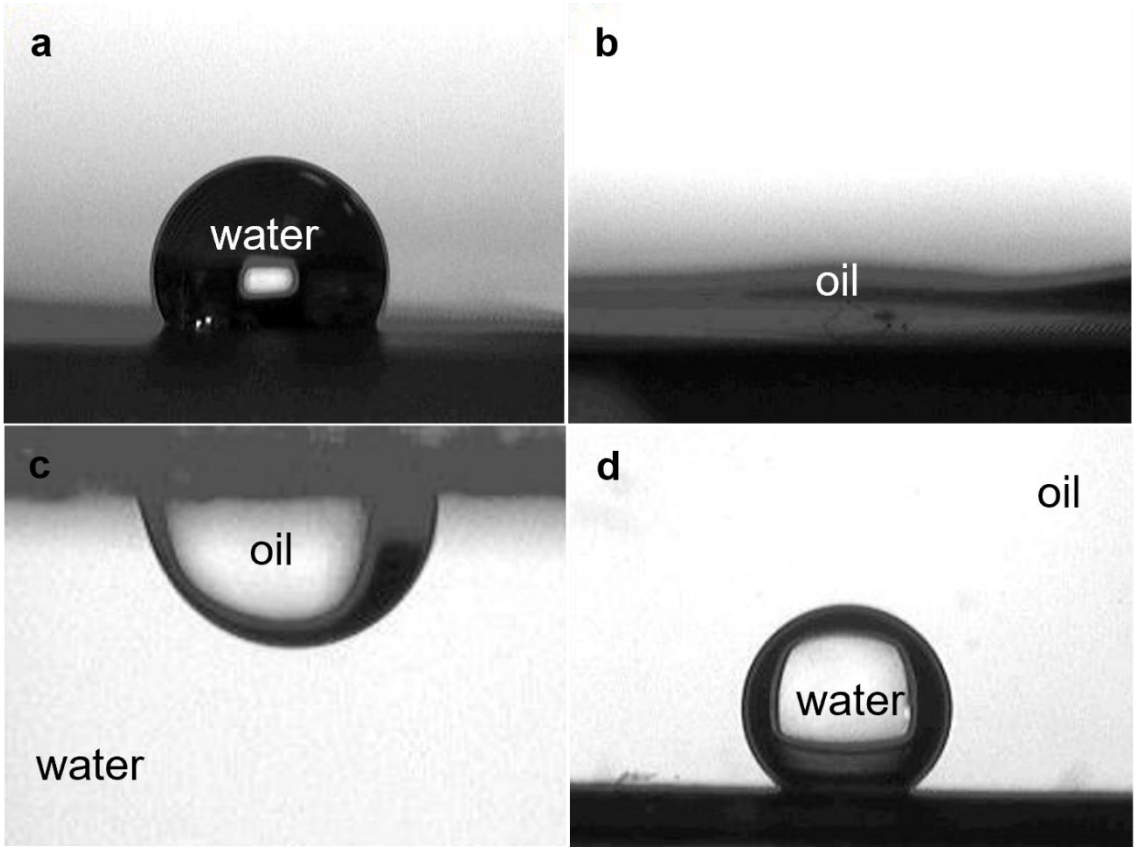

Figure 4.6. Surface wetting properties of the bare stainless-steel mesh 400. a) water contact in the air, b) oil contact in the air, c) underwater oil contact, and d) underoil water contact.

Similar to many other works [34-38], the obtained superwettable meshes preferentially allowed the permeation of water while blocking the oil phase, achieving the "oil-blocking" separation of "water-rich" oil/water mixtures. On the other hand, the mesh surface was superoleophilic in air, as oil droplets quickly spread out once contacting the surface (Figure 4.7c). It was expected that such in-air superoleophilic surfaces could efficiently adsorb oil molecules in their nano/microstructures and form a repulsive oil film to the water phase, exhibiting underoil superhydrophobic behavior.

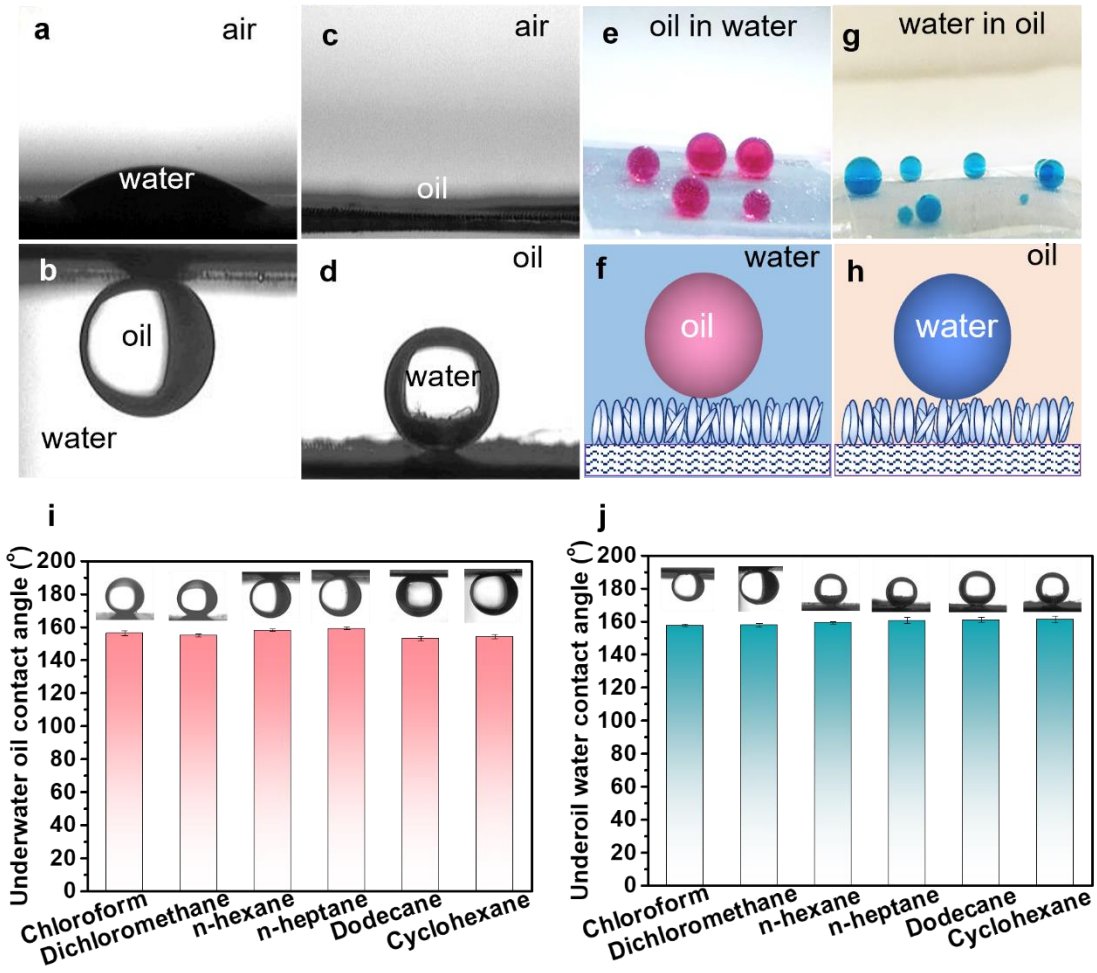

Figure 4.7. Surface wetting performance of the ZIF-L coated mesh. a) In-air water contact angle, b) underwater oil (cyclohexane) contact angle, c) in-air oil contact angle, d) underoil water contact angle, e) underwater oil droplets (chloroform) on the ZIF-L coated mesh, f) schematic illustration of oil wetting on the ZIF-L coated mesh with a micro-hierarchical structure in water, g) under-oil water droplets on the ZIF-L coated mesh, h) schematic illustration of water wetting on the ZIF-L coated mesh with a micro/nano-hierarchical structure in oil, i) underwater oil contact angles of various oils, and j) underoil water contact angle under different oils.

The underoil wettability of the ZIF-L coated mesh was examined by immersing it into

a representative oil, cyclohexane. The results confirmed that the ZIF-L mesh exhibited excellent underoil superhydrophobicity with an underoil WCA of ~160° ± 2° (Figure 4.7d), while the bare mesh only showed an underoil WCA of ~135° ± 2° (Figure 4.6d).

Once prewetted with an oil phase, these intelligent surfaces favored oil permeation but rejected water, achieving "water-blocking" separation of "oil-rich" aqueous mixtures. Figures 4.7e, g display images of underwater oil droplets (dyed with Oil red O) and underoil water droplets (dyed with methylene blue) on the ZIF-L mesh film, respectively. In both analyses, the oil or water droplets can easily roll over on the mesh surface while retaining the same size, suggesting ultralow surface oil-adhesion and water-adhesion properties, respectively. The sketches in Figure 4.7f, h diagrammatically explain the underwater and underoil wetting mechanisms of the hierarchical ZIF-L mesh surface, respectively. Contact angles in the oil/water/solid three-phase environment can be illustrated by the modified Cassie model, [8,9] as shown in the following equation:

$$\cos\theta' = r_f f \cos\theta + f - 1 \qquad (4.1)$$

where θ and θ′ represent the underwater oil contact angle (or underoil water contact angle) of an ideal smooth surface and a rough surface, respectively. r_f is the non-dimensional surface factor, which refers to the ratio of the surface area to the projected area; f is the area fraction of the underwater (or underoil) solid surface contact with oil (or water). In our case, the closely packed 2-dimensional ZIF-L nanoplates generated

extremely rough surface, resulting in a sharp decrease in the area fraction, f, thus significantly increasing underwater oil contact angles (or underoil water contact angles). To further explore the surface wettability of the ZIF-L coated mesh, underwater contact angles of a series of oils (Figure 4.7i) and underoil water contact angles in different oils (Figure 4.7j) were measured. According to these Figures, our mesh films have indeed exhibited excellent underwater superoleophobicity for various oils with all OCAs higher than ~155° ± 2°. Meanwhile, the mesh film also displayed extraordinary superhydrophobicity under different oil phases with WCAs close to ~160° ± 2°.

4.3 Oil/water separation performance of the ZIF-L mesh film

In this work, a series of gravity-driven oil/water separation tests were carried out because the superior superwetting properties of our ZIF-L coated mesh films allowed the separation driven solely by gravity. Their separation principle was schematically illustrated in Figure 4.8a. Briefly, when prewetted with water, the water molecules preferentially permeated through the mesh film while the oil molecules were rejected completely and remained on top of the surface, due to its underwater superoleophobicity as well as ultralow oil-adhesion property. In contrast, when prewetted with oil, our ZIF-L mesh film preferentially allowed the permeation of oil, while rejected water above the surface because of its superior underoil superhydrophobic property.

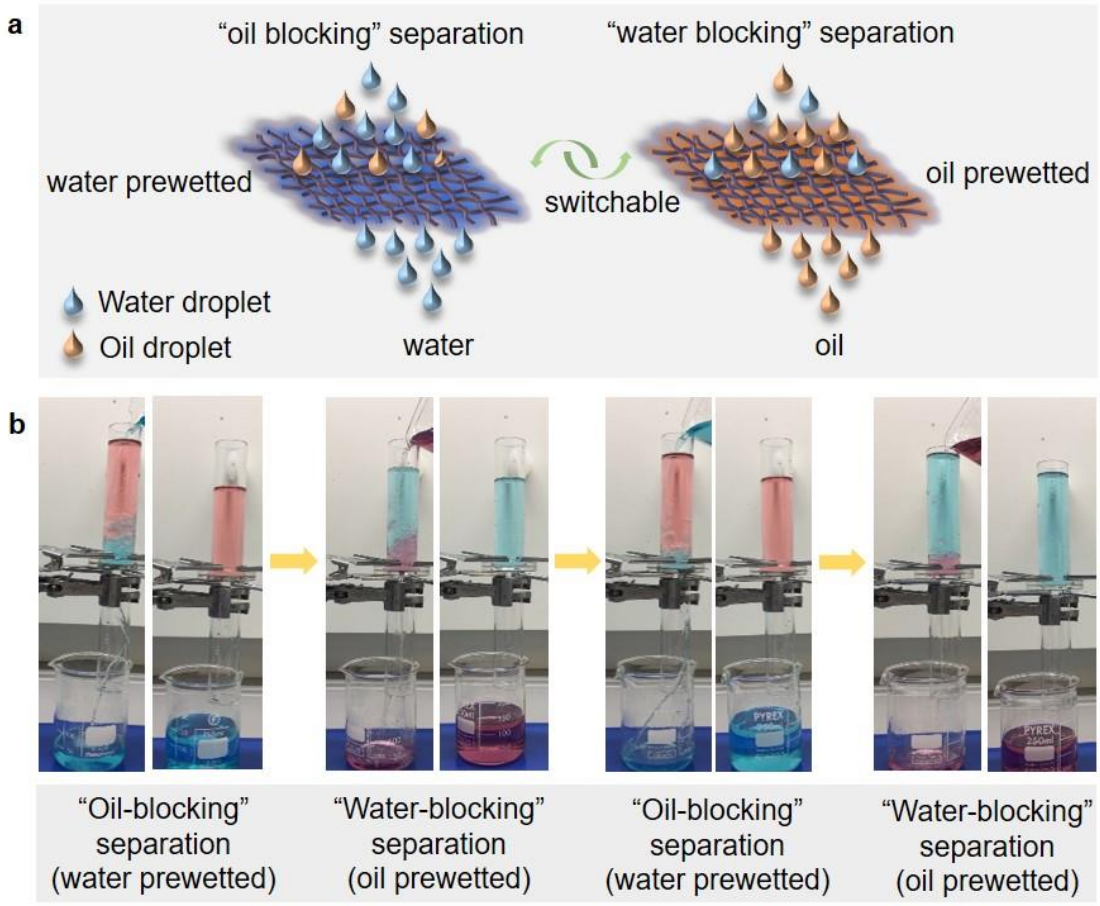

Figure 4.8. Switchable separation process of the ZIF-L coated mesh. a) Schematic illustration of the prewetting induced switchable separation property of the ZIF-L coated mesh and b) photographs of one cycle of the switchable gravity-driven oil/water separation process. When prewetted by water, the mesh works under the "oil-blocking" mode, and thus oil (cyclohexane, dyed with Oil red) was rejected. When prewetted by oil (cyclohexane), the mesh switches to the "water-blocking" mode: water (dyed with methyl blue) was rejected while oil can permeate through the mesh film. In water-blocking separation, a heavier oil, dichloromethane (dyed with Oil red), was used for better visualization.

Figure 4.8b showed the photographs of the ZIF-L coated mesh at a different stage in a switchable oil/water separation test. Firstly, a mixture of oil red-dyed cyclohexane and

methylene blue-dyed water ($\rho_{water} > \rho_{oil}$) was poured onto the water-prewetted mesh, triggering "oil-blocking" separation as cyclohexane was rejected above the mesh surface despite being in contact with the surface at the beginning. After a simple cleaning with methanol and fast air drying, the ZIF-L mesh was prewetted with cyclohexane. Then, a mixture of water and dichloromethane ($\rho_{oil} > \rho_{water}$) was poured into the top funnel. It was observed that only dichloromethane permeated through the mesh while the water was completely blocked, confirming that the separation was successfully switched to the "water-blocking" separation mode. All the separation processes were solely driven by gravity, and no external pressure was applied. Note, the switchable separation performance of our mesh film was realized by merely changing the prewetting media before the tests. No expensive chemical or heat treatment was required, confirming that the switchable separation using our ZIF-L mesh was highly energy- and time-effective.

The separation performance of the mesh towards a series of oil/water mixtures was also explored in this work. The permeate flux (F) of the mesh was calculated from the volume of the permeation in unit time, according to:

$$F = V / A \cdot t \tag{4.2}$$

Where V is the volume of the filtrate (L), A is the effective filtration area of the mesh (m^2), and t is the permeation time (h). The separation efficiency (R) was calculated using the following equation:

$$R(\%) = \left(1 - \frac{C_p}{C_0}\right) \times 100 \tag{4.3}$$

where C_p is the residual oil concentration in the collected filtrate, C_0 is the original oil concentration in the feed oil/water mixture.

As presented in Figure 4.9a, the separation efficiencies of ZIF-L mesh film (size 400) for all oils tested in this work were above 99% (or more precisely less than ~30 ppm of oil content in the filtrate) with an averaged permeate flux as high as ~1.35×10^5 L m^{-2} h^{-1}, suggesting the mesh was capable of realizing highly efficient separation of various types of oil/water mixtures. The influence of the secondary ZIF-L growth time on the mesh separation performance was also studied. As shown in Figure 4.9b, all ZIF-L coated meshes showed excellent separation performance with an oil rejection above 99%. However, it was found that with the increase of the secondary growth time, the permeation flux declined from ~1.35×10^5 down to 0.86×10^5 L m^{-2} h^{-1}. This decrease in flux was caused by a thicker and denser ZIF-L nanoplates film formed on the mesh wires, resulting in the decrease in the aperture size and consequently a reduced water permeation through the mesh. The separation performances of the mesh with different mesh numbers were also examined. As shown in Figure 4.9c, the permeate flux increased while the separation efficiency slightly decreased when a smaller mesh number was used. It is worthwhile mentioning that our results showed that excellent oil/water separation could be obtained on mesh 200, which had open apertures of 77 μm in size. To the best of our knowledge, this is the largest mesh aperture size used for meshed-based oil/water separation in the literature.

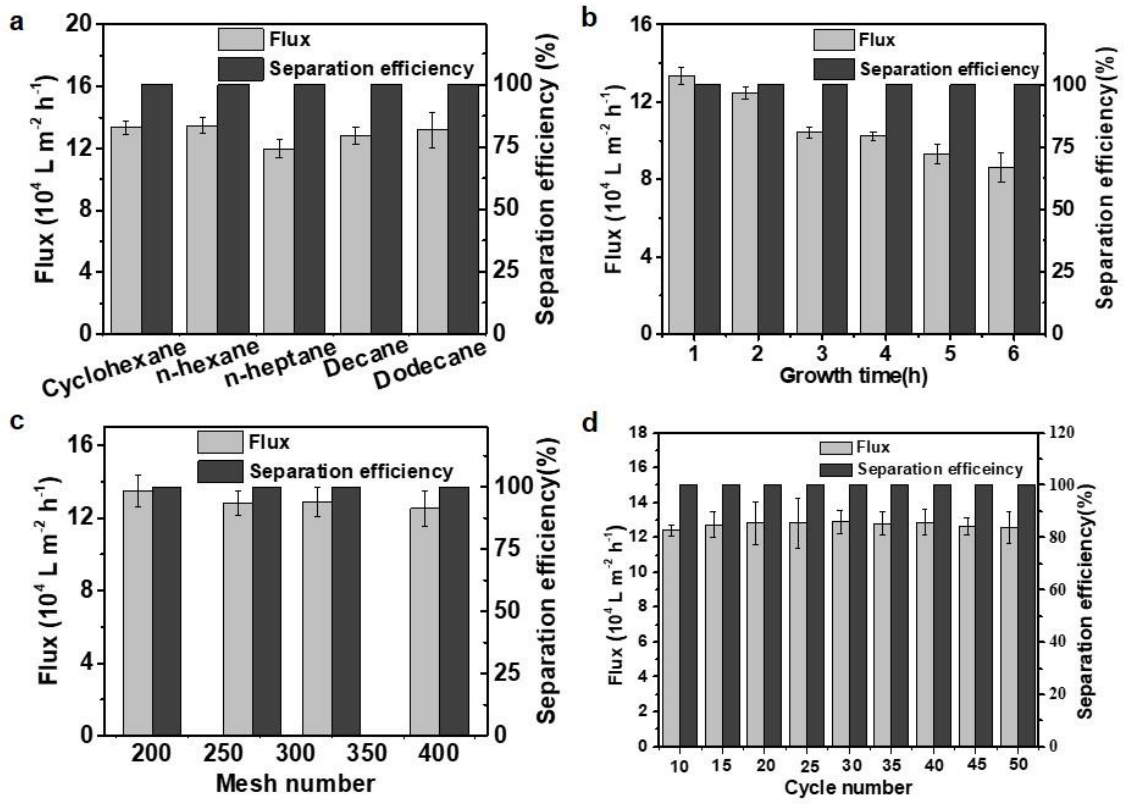

Figure 4.9. Oil/water separation performance of the ZIF-L coated mesh. a) Permeate flux and separation efficiency of the ZIF-L coated mesh for a series of oil/water mixtures, b) the influence of growth time of ZIF-L on the separation performance, c) permeate flux and separation efficiency of mesh with different mesh numbers, and d) permeate flux and separation efficiency variations of the ZIF-L coated mesh in a cyclic test.

We ascribed this superior performance to the extraordinary superwetting property endowed by the unique hierarchical ZIF-L structure. Additionally, the use of a large-aperture mesh with low cost and improved mechanical strength has great potential in reducing capital investment and is of great importance in designing large-scale

applications with this membrane.

"Water-blocking" separation performance of the ZIF-L coated mesh was also studied using different types of oil/water mixtures. The "water-blocking" separation is suitable for the separation of heavy oil/water mixtures, in which the density of oil is greater than that of water (such as dichloromethane, trichloromethane, bromobenzene, and carbon tetrachloride, and tetrachloroethane). Although there are limited cases of heavy oil/water mixtures reported, the separation of heavy oils is still significant and should not be ignored. It was revealed that the oil prewetted mesh exhibited superior separation performance towards all the tested oil-enriched mixtures (Figure 4.10).

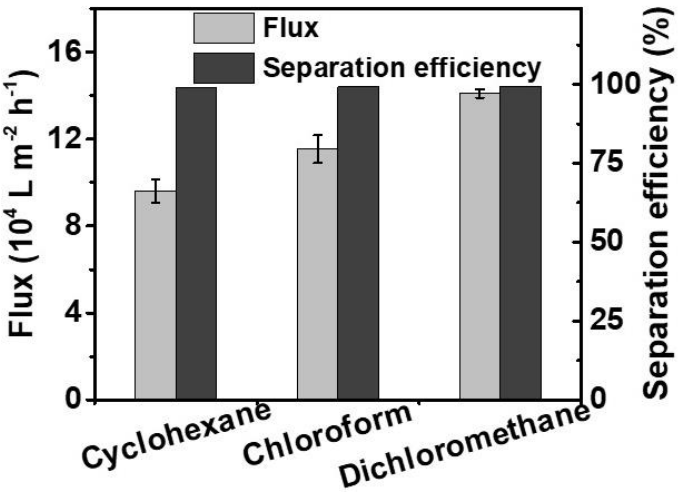

Figure 4.10. "Water-blocking" separation performance of the ZIF-L coated mesh towards different types of oil/water mixtures.

The results confirmed that the ZIF-L coated mesh was capable of realizing the highly efficient separation of various types of oil/water mixtures under both water-removal and oil-removal modes. As compared to those "single-separation" mesh materials, our

ZIF-L mesh films with switchable separation functions were more cost-effective and easy-to-use, and thereby they are more promising for economic on-demand oil/water separation.

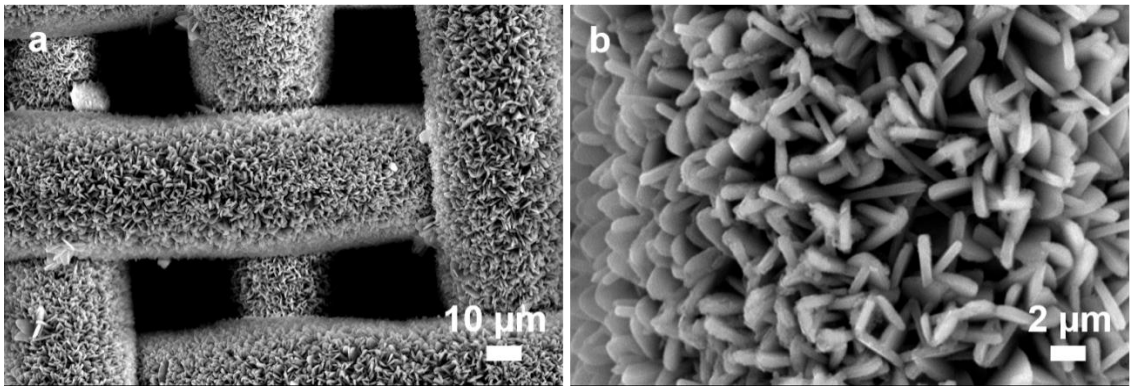

Figure 4.11. (a) low-magnification and (b) high-magnification SEM images of the mesh surface after 50 cycles of oil/water separation.

Finally, long-term cyclic separation tests were performed in order to test the stability of the separation performance. At least 50 cycles of oil/water separation were randomly tested for over 6 months. As shown in Figure 4.9d, an oil rejection rate greater than 99 % was obtained for all 50 cycles, and the water flux was maintained higher than ~1.24×10^5 L m^{-2} h^{-1}. SEM images of the mesh film after 50 cycles (Figure 4.11) showed that full coverage of ZIF-L was maintained on the mesh surface, suggesting that our ZIF-L mesh films were highly stable after a short period of intense tests.

To further understand the prewetting induced switchable separation mechanism, four schematic models were displayed in Figure 4.12a-d.

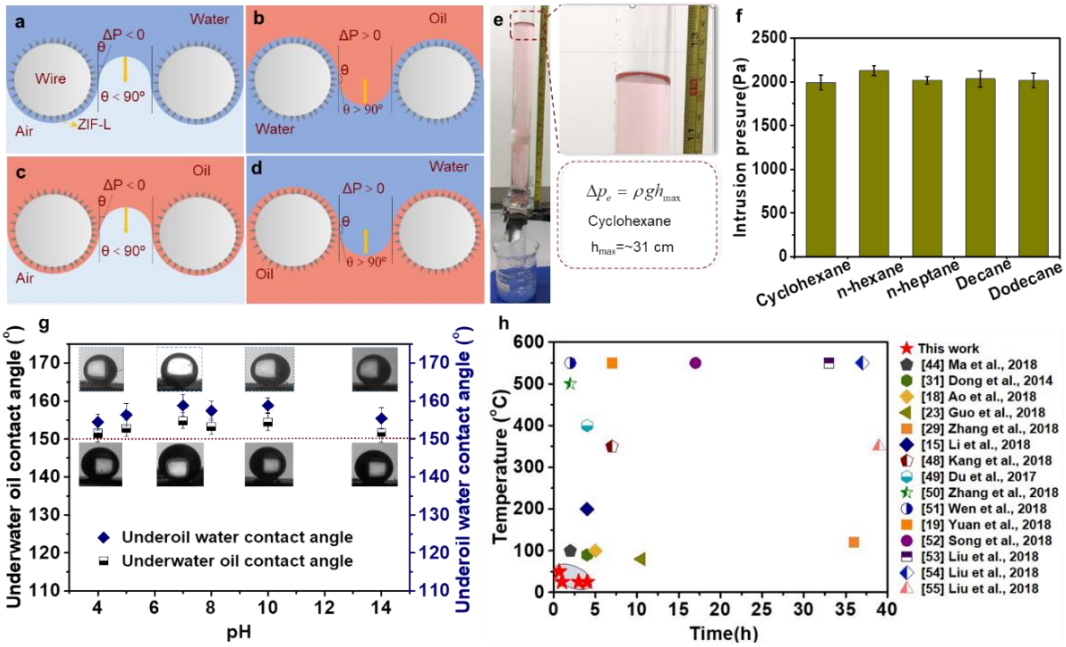

Figure 4.12. Schematic illustration of the liquid-wetting modes on the hierarchical ZIF-L coated mesh. a) The mesh showed superhydrophilicity in air, and water can permeate through the mesh because $\Delta p < 0$; b) the mesh displayed underwater superoleophobicity, and oil can be sustained because $\Delta p > 0$; c) the mesh was superoleophilic in air and was permeable to oil because $\Delta p < 0$; d) the mesh was superhydrophobic underoil, and water cannot pass through because $\Delta p > 0$; e) oil column (cyclohexane) above the ZIF-L coated mesh; f) the intrusion pressure (Δp_e) of the ZIF-L coated mesh for a series of oils; g) wettability of the mesh in an acidic and alkaline environment; and h) comparison of the reported fabrication conditions (temperature and time) of superwetting meshes.

Theoretically, the intrusion pressure (Δp), which refers to the pressure that the mesh can hold before the onset of oil permeation, can be determined as follows:

$$\Delta p = \frac{2\gamma}{R} = \frac{-l\gamma\cos\theta}{A} \tag{4.4}$$

Where γ is the interfacial tension, R is the radius of the meniscus, l is the perimeter of the mesh pore, A is the area of the pore and θ is the advancing contact angle on the mesh surface.

The underlying mechanism of the prewetting induced switchable separation performance can be explained as follows (Figure 4.12 a-d): When water (or oil) is in contact with the mesh surface, θ is nearly 0º due to the superamphiphilicity of the mesh surface in air. Thus, the intrusion pressure (Δp) is negative (Δp < 0) according to Equation 4.4, suggesting water (or oil) can freely permeate through the mesh film (Figure 4.12a, c). When the mesh is prewetted by water, abundant water molecules are trapped into the submicron- and nanoscale structures, forming a layer of water barrier against oil. At this time, θ is greater than 90° and Δp > 0, indicating the mesh can withstand a certain height of oil (or aqueous) phase on top (Figure 4.12b, d). Therefore, the mesh displayed underwater superoleophobicity, and oil can be sustained. Similarly, when the mesh is prewetted by oil, abundant oil molecules are trapped into the nanoscale rough structures, forming an oil barrier against water. In this case, the mesh is superhydrophobic underoil, and water cannot pass through. The above analyses clearly explain the excellent reversibility between superhydrophilicity/underwater superoleophobicity and superoleophobicity/underoil superhydrophobicity of our unique hierarchical ZIF-L mesh films.

The experimental intrusion pressure (Δp_e) was evaluated by measuring the maximum height of the oil column that the mesh can support (Figure 4.12e) and calculated according to the following equation:

$$\Delta p_e = \rho g h_{\max} \tag{4.5}$$

Where Δp_e is the experimental intrusion pressure, ρ is the density of the oil (or water), g is the acceleration of gravity, and h_{max} is the maximum height of the oil (or water) that the mesh can support before the onset of oil permeation (or water permeation)

Table 4.1. Comparison of previously reported superwetting meshes for efficient oil/water separation with this work

Substrate	**Material**	**Temperature, °C**	**Time, h**	**Separation efficiency**	**Flux, $\times 10^4$ L m^{-2} h^{-1}**	**Intrusion pressure, kPa**	**Ref.**
Stainless steel mesh	ZIF-8	100	2 ~ 37	>99.90%	18.0	~ 0.95	(40)
Wire mesh	Graphene oxide	90	2 ~3	>98.00%	N/A	N/A	(24)
Wire mesh	Cellulose hydrogel	100	>5	>98.90%	1.29	1.94	(16)
Stainless steel mesh	POSS hybrid	80	~10.5	>99.00%	N/A	4.11	(17)
Stainless steel mesh	UiO-66	120	~36	>99.99%	12.7	2.93	(22)
Copper mesh	CuO	200	~4	>99.97%	0.4	N/A	(12)
Ti mesh	TiO_2	350	>7	>99.20%	~ 1.7	0.85	(44)
Stainless steel mesh	TiO_2	400	~4	99.90%	1.36	1.70	(45)

Copper mesh	Silica	500	~2	>99.99%	N/A	N/A	(46)
Stainless steel mesh	PDMS	550	>2	>99.00%	8	3.46	(47)
Copper mesh	TiO_2/CuO	550	>7	>99.99%	8	N/A	(16)
Stainless steel mesh	$BiVO_4$	550	>17	>98.60%	N/A	N/A	(48)
Stainless steel mesh	MFI	550	~33	>99.00%	>1.4	0.96	(49)
Stainless steel mesh	MFI	550	~37	>99.00%	>8	N/A	(50)
Stainless steel mesh	CeO_2/Co_3O_4	350	~39	>99.99%	~ 0.14	N/A	(51)
Stainless steel mesh	**ZIF-L**	**25**	**1**	**>99.99%**	**~ 13.5**	**~ 2.0**	**This work**
Stainless steel mesh	**ZIF-L**	**50**	**<1**	**>99.99%**	**~ 13.5**	**~ 2.0**	**This work**

In this work, the Δp_e was estimated using different oils. As shown in Figure 4.12f, our ZIF-L meshes displayed an intrusion pressure of ~2.0 kPa, which was higher than most of the reported values (Table 4.1).

4.4 Chemical and hydrothermal stabilities of the ZIF-L mesh film

Industrial oily wastewater usually exists under different pH environments (either acidic or basic) and contains specific concentrations of salts (e.g., NaCl). Therefore, satisfactory structural stability of the mesh in these harsh environments is essential for long-term industrial applications. In this work, mesh stability was systematically evaluated by monitoring the wettability change of the mesh surface under different conditions. As shown in Figure 4.12g, our ZIF-L meshes showed excellent stability under different pH conditions with both underwater oil and underoil water contact

angles higher than 150°. The corresponding SEM images further confirmed that the hierarchical ZIF-L nanostructure was mostly retained after soaking in a strongly acidic HCl or basic NaOH aqueous environment for 6 h at room temperature (Figure 4.13).

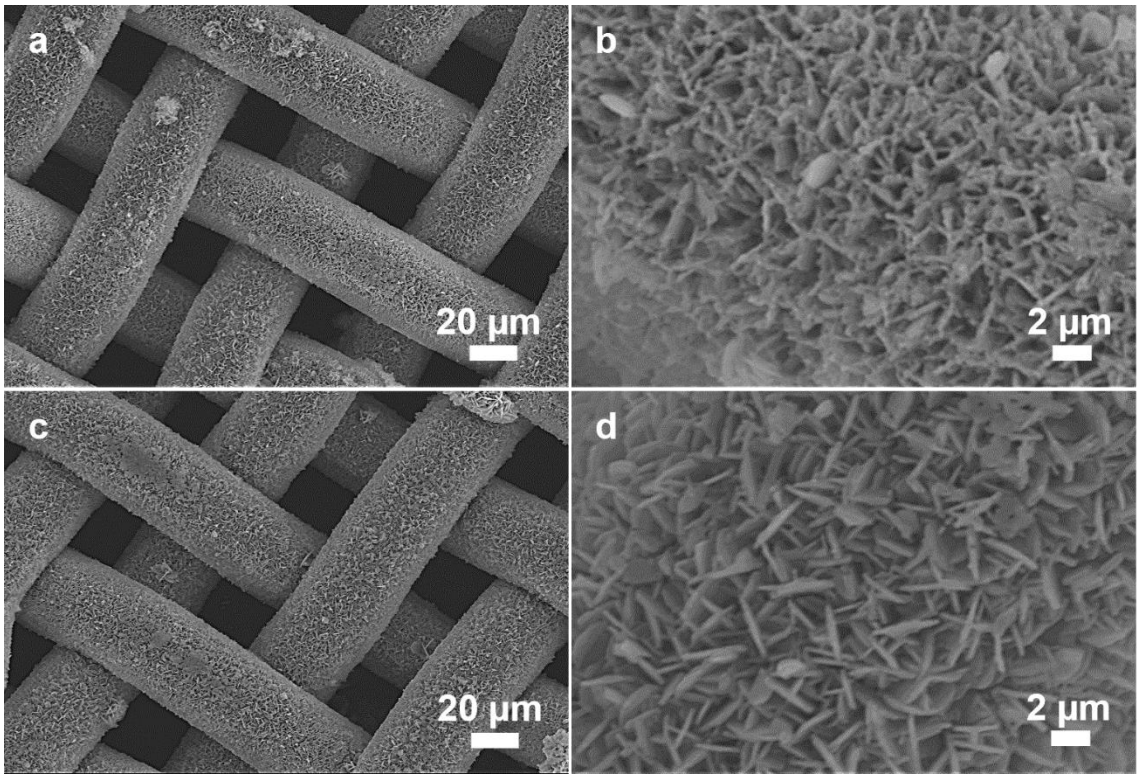

Figure 4.13. SEM images of ZIF-L coated mesh film after soaked in an acidic and alkaline environment. a) and b): ZIF-L coated mesh film after soaked in acidic HCl solution (pH = 4) for 6 h, c) and d): the ZIF-L coated mesh film after soaked in basic NaOH solution (pH = 14) for 6 h, and b) and d) are high-magnification views of the mesh surface.

Furthermore, the stability of the mesh against aqueous salt solutions was studied by immersing the mesh in different NaCl solutions (up to 10 wt% in water) for a period of 6 h at room temperature. According to the results, our ZIF-L mesh exhibited satisfactory

stability in all salt solutions. Both underwater oil and underoil water contact angles were retained above 150° (Figure 4.14a). SEM images confirmed that the ZIF-L meshes displayed excellent chemical stability at low salt concentrations (Figure 4.14b, c). However, they still showed satisfactory stability at extremely high salt concentrations (10 wt%), although a change of surface morphology was observed. (Figure 4.14d, e).

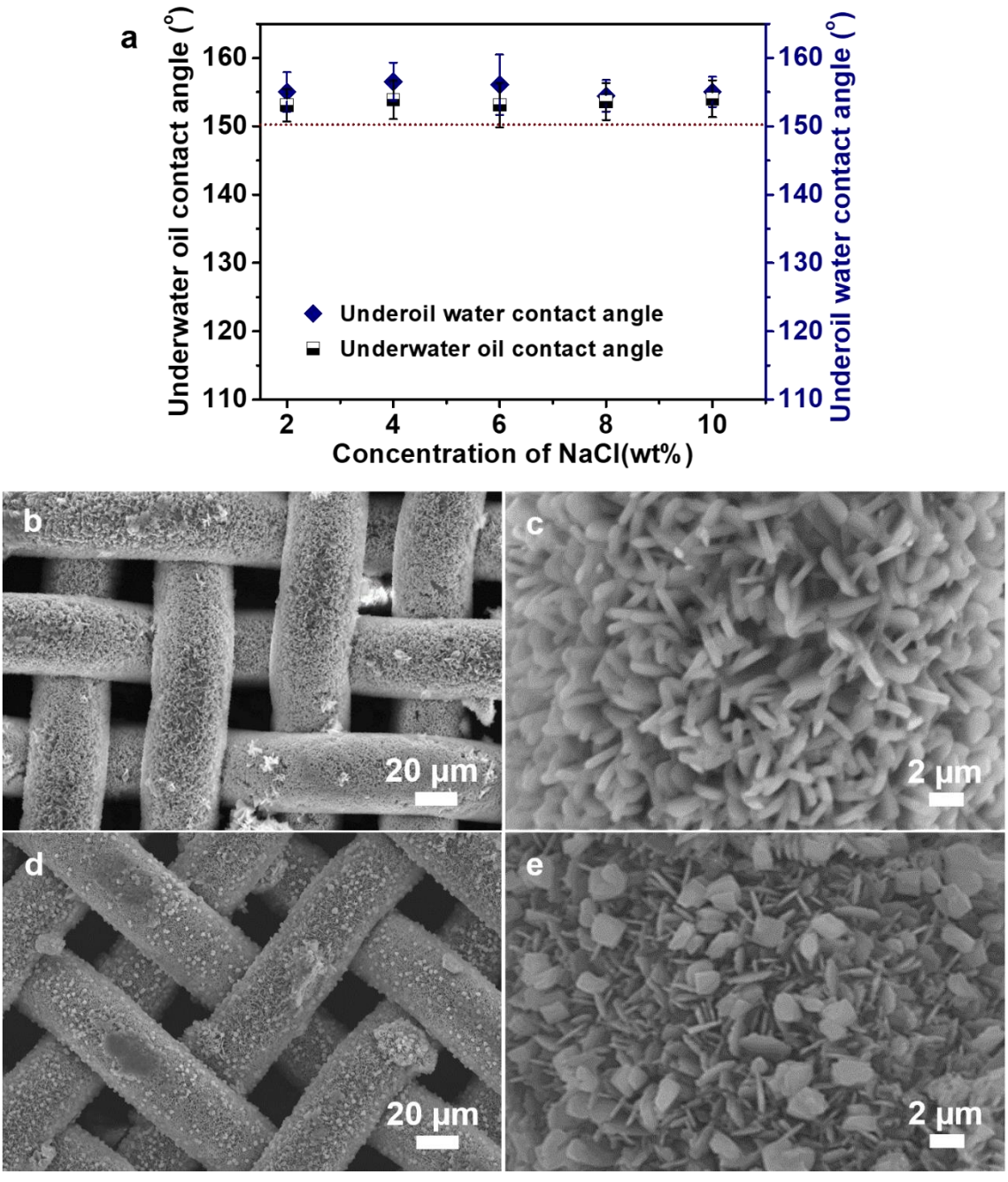

Figure 4.14. Stability of the ZIF-L coated mesh film in aqueous salt solutions. a) Underoil water contact angle and underwater oil contact angles of ZIF-L mesh after soaked in NaCl solutions with different concentrations, b) SEM image and c) a high-magnification view of the mesh surface after soaking in 8 wt% NaCl solution for 6 h, and d) SEM image and e) a high-magnification view of the mesh surface after soaking in a 10 wt% NaCl solution for 6 h.

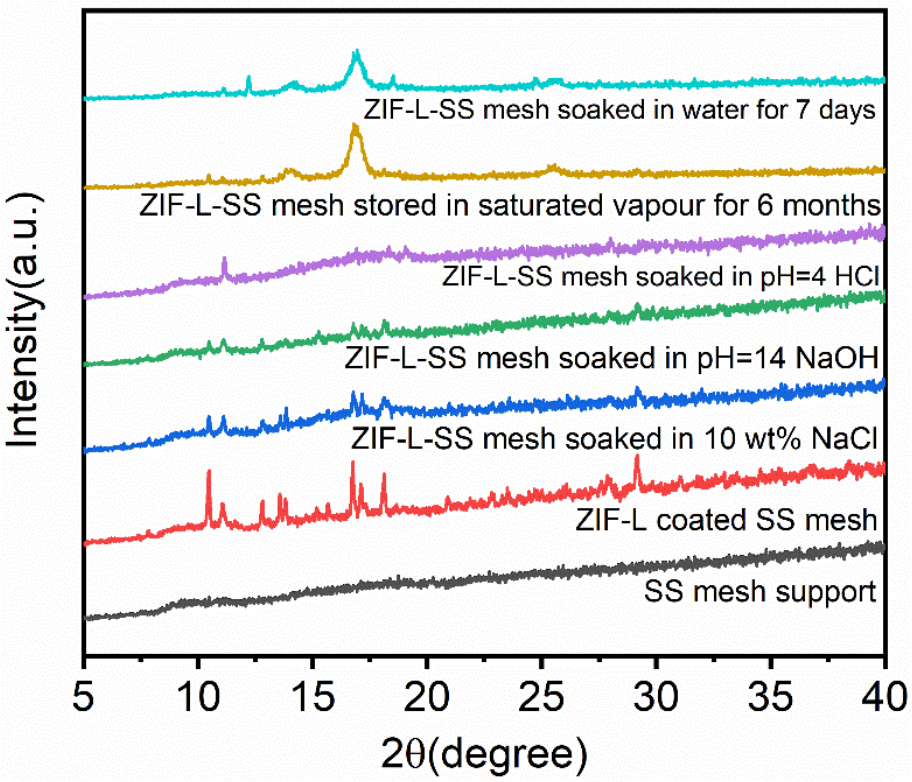

Figure 4.15. XRD patterns of the ZIF-L mesh films after soaked in acidic HCl solution (pH = 4), in basic NaOH solution (pH = 14), in 10 wt% NaCl solution for 6 h, in wet air (~60% RH) for 6 months, and DI water for 7 days

The stability of ZIF-L mesh films under both acidic and basic conditions was examined by soaking the as-synthesized samples in an acidic HCl solution (pH = 4) and a basic

NaOH solution (pH = 14) for 6 h, respectively. As shown in Figure 4.15, both mesh samples still retained characteristic ZIF-L X-ray diffraction patterns, although a lower intensity was observed in the sample after strong acid treatment. The results underscored that our ZIF-L mesh films exhibited better structural stability under basic conditions. However, it is worthwhile mentioning that the ZIF-L amorphization in both stability studies has not significantly influenced the overall hierarchical morphology of the intergrown ZIF-L layer and also their separation performance. The long-term stability of our ZIF-L meshes was further studied by exposing them in wet air with a relative humidity (RH) of around 60 % at room temperature for 6 months and then soaking under DI water for 7 days. As suggested by the XRD results in Figure 4.15 and SEM images in Figure 4.16a,b, ZIF-L nanoplate structure was well retained on the mesh surface after stored in wet air for a long period, while significant water dissolution was observed after soaking in water for 7 days which is consistent to the results reported previously [39]. However, the liquid water-soaked sample still exhibited almost a complete coverage of thinner, flexible nanosheet materials, forming similar hierarchical roughness on the mesh surface (Figure 4.16a, b). According to the above results, it's critically important to tackle the weak long-term hydrostability of ZIF materials in aqueous solutions, although they have shown excellent stability in wet air over a period of 6 months.

Last but not least, the facile fabrication process developed in this work was highly energy-efficient and time-effective compared with those reported in other works. Figure

4.12h and Table 4.1 summarized some recent synthesis conditions of mesh-based materials.

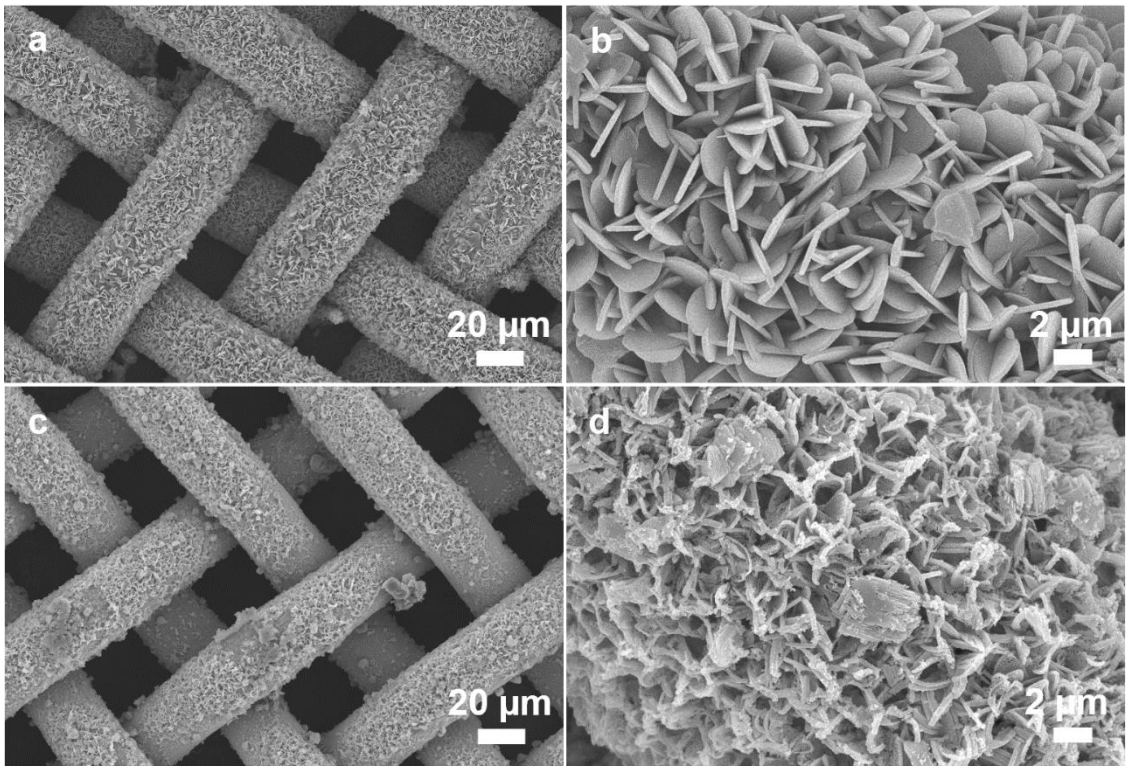

Figure 4.16. SEM images of ZIF-L coated mesh film after stored in saturated vapor and water environment. a) and b): ZIF-L coated mesh film after storing in wet air (~60% RH) for 6 months, c) and d): ZIF-L coated mesh film after soaking in water for 7 days, and b) and d) are high-magnification views of the mesh surface.

It is evident that either a long synthesis time (>2 h) or a high-temperature pre- (or post-) treatment (>100 °C) was inevitably involved. In fact, in many studies, the high-temperature calcination (up to ~550 °C) step was essential to activate or regenerate the as-synthesized materials before applying for oil/water separation. In this work, our synthesis was completed in one hour under ambient conditions (25 °C and atmospheric

pressure). Meanwhile, the separation efficiency and flux of our ZIF-L mesh films were superior as compared to previously reported mesh films (Figure 4.17).

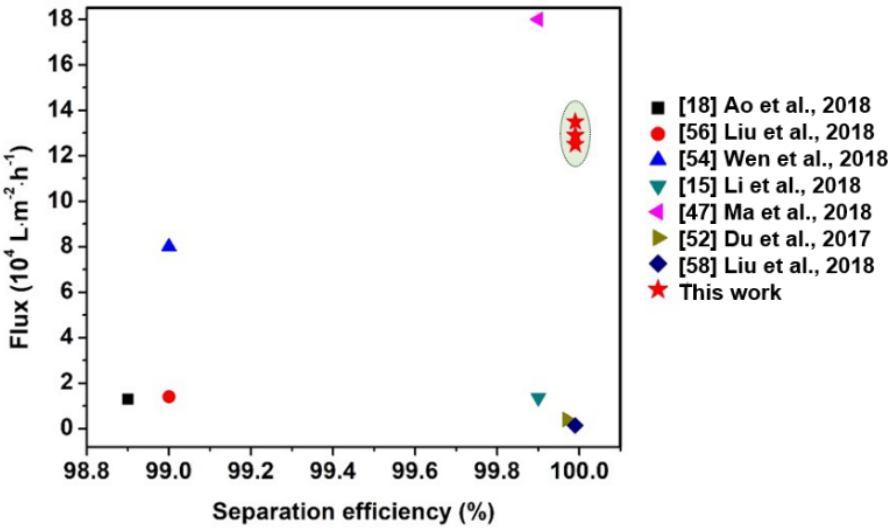

Figure 4.17. Separation performance comparison (separation efficiency and flux) of previously reported mesh films for oil/water separation.

The obtained ZIF-L meshes showed intelligent prewetting-induced switchable separation function and satisfactory chemical stability in harsh environments. From the energy consumption and economic point of views, our fabrication method is highly promising for the energy-effective production of ZIF-based membranes/films for many other important practical applications, e.g., natural gas purification or CO_2 capture from flue gases.

4.5 Summary

In this chapter, a simple seeding and secondary growth process was applied to prepare ZIF-L nanoplates coated stainless steel mesh films. The prepared mesh films showed

bioinspired superwetting surfaces, and they were applied for oil/water mixture separations. The main results can be summarized as:

(1) The ZIF-L coated mesh film can be fabricated rapidly under ambient conditions, i.e., 1 h at 25 °C and 101 kPa. This time-saving fabrication process with low energy consumption contributed to promoting the large-scale mass production of ZIF-based materials.

(2) The as-synthesized mesh films exhibited interesting bioinspired superwetting surfaces, i.e., in-air superamphiphilicity, underwater superoleophobicity, and underoil superhydrophobicity. Such superwetting surface property was attributed to the microscale hierarchical porous structures constructed by ZIF-L nanoplates on the mesh surface.

(3) The intelligent superwetting properties enabled the ZIF-L mesh films to realize switchable separation performance for different types of immiscible oil/water mixtures. The permeation flux was ~1.35×10^5 L m^{-2} h^{-1}, and the oil (or water) rejection rate was above 99%. In addition, the mesh films exhibited a high oil (or water) intrusion pressure as high as ~2.0 kPa, indicating their potential for large-scale separations.

4.6 References

[1] Shannon M. A., Bohn P. W., Elimelech M., Georgiadis J. G., Marinas B. J., Mayes A. M., Science and technology for water purification in the coming decades, Nature, 2008; 452: 301-310.

[2] Jamaly S., Giwa A., Hasan S. W., Recent improvements in oily wastewater treatment: Progress, challenges, and future opportunities, J. Environ. Sci., 2015; 37: 15-30.

[3] He D. X., Ding F. X., Hu H., Chiang S. H., A multiple-loop flotation column for wastewater treatment, Sep. Technol., 1995; 5: 133-138.

[4] Benker B., Wollmann A., Sievers M., Centrifugal flotation applied to the separation of oil and fat from wastewater, Eng. Life Sci., 2003; 3: 61-65.

[5] Suzuki Y., Maruyama T., Removal of emulsified oil from water by coagulation and foam separation, Sep. Sci. Technol., 2005; 40: 3407-3418.

[6] Zhu Y., Wang D., Jiang L., Jin J., Recent progress in developing advanced membranes for emulsified oil/water separation, NPG Asia Mater, 2014; 6: e101.

[7] Padaki M., Murali R. S.,. Abdullah M. S, Misdan N., Moslehyani A., Kassim M. A., Hilal N., Ismail A.F., Membrane technology enhancement in oil–water separation. A review, Desalination, 2015; 357: 197-207.

[8] Ge M., Cao C., Huang J., Zhang X., Tang Y., Zhou X., Zhang K., Chen Z., Lai Y., Rational design of materials interface at nanoscale towards intelligent oil–water separation, Nanoscale Horiz., 2018; 3: 235-260.

[9] Wen L., Tian Y., Jiang L., Bioinspired super‐wettability from fundamental research

to practical applications, Angew. Chem. Int. Ed., 2015; 54: 3387-3399.

[10] Zhang W., Zhu Y., Liu X., Wang D., Li J., Jiang L., Jin J., Salt-induced fabrication of superhydrophilic and underwater superoleophobic PAA-g-PVDF membranes for effective separation of oil-in-water emulsions, Angew. Chem. Int. Ed., 2014; 53: 856-860.

[11] Chen T., Duan M., Fang S., Fabrication of novel superhydrophilic and underwater superoleophobic hierarchically structured ceramic membrane and its separation performance of oily wastewater, Ceram. Int., 2016; 42: 8604-8612.

[12] Jiang J., Zhu L., Zhu L., Zhang H., Zhu B., Xu Y., Antifouling and antimicrobial polymer membranes based on bioinspired polydopamine and strong hydrogen-bonded poly (N-vinyl pyrrolidone), ACS Appl. Mater. Inter., 2013; 5: 12895-12904.

[13] Su C., Xu Y., Zhang W., Liu Y., Li J., Porous ceramic membrane with superhydrophobic and superoleophilic surface for reclaiming oil from oily water, Appl. Surf. Sci., 2012; 258: 2319-2323.

[14] Xue Z., Wang S., Lin L., Chen L., Liu M., Feng L., Jiang L., A novel superhydrophilic and underwater superoleophobic hydrogel-coated mesh for oil/water separation, Adv. Mater., 2011; 23: 4270-4273.

[15] Li X., Zhang W., Liu N., Qu R., Wei Y., Feng L., Superwetting copper meshes based on self-organized robust CuO nanorods: efficient water purification for in situ oil removal and visible light photodegradation, Nanoscale, 2018; 10: 4561-4569.

[16] Du Z., Ding P., Tai X., Pan Z., Yang H., Facile preparation of Ag-coated superhydrophobic/superoleophilic mesh for efficient oil/water separation with

excellent corrosion resistance, Langmuir, 2018; 34: 6922-6929.

[17] Zhou C., Cheng J., Hou K., Zhu Z., Zheng Y., Preparation of $CuWO_4$@ Cu_2O film on copper mesh by anodization for oil/water separation and aqueous pollutant degradation, Chem. Eng. J., 2017; 307: 803-811.

[18] Ao C., Hu R., Zhao J., Zhang X., Li Q., Xia T., Zhang W., Reusable, salt-tolerant and superhydrophilic cellulose hydrogel-coated mesh for efficient gravity-driven oil/water separation, Chem. Eng. J., 2018; 338: 271-277.

[19] Yuan S., Chen C., Raza A., Song R., Zhang T., Pehkonen S. O., Liang B., Nanostructured TiO_2/CuO dual-coated copper meshes with superhydrophilic, underwater superoleophobic and self-cleaning properties for highly efficient oil/water separation, Chem. Eng. J., 2017; 328: 497-510.[20] Zhang L., Gu J., Song L., Chen L., Huang Y., Zhang J., Chen T., Underwater superoleophobic carbon nanotubes/core–shell polystyrene@ Au nanoparticles composite membrane for flow-through catalytic decomposition and oil/water separation, J. Mater. Chem. A., 2016; 4: 10810-10815.

[21] Wang B., Liang W., Guo Z., Liu W., Biomimetic super-lyophobic and super-lyophilic materials applied for oil/water separation: a new strategy beyond nature, Chem. Soc. Rev., 2015; 44: 336-361.

[22] Zhang W., Shi Z., Zhang F., Liu X., Jin J., Jiang L., Superhydrophobic and superoleophilic PVDF membranes for effective separation of water‐in‐oil emulsions with high flux, Adv. Mater., 2013; 25: 2071-2076.

[23] Guo D., Hou K., Xu S., Liu Y., Li L., Wen X., Pi P., Superhydrophobic–superoleophilic stainless steel meshes by spray-coating of a POSS hybrid acrylic

polymer for oil–water separation, J. Mater. Sci., 2018; 53: 6403-6413.

[24] Yang J., Zhang Z., Xu X., Zhu X., Men X., Zhou X., Superhydrophilic–superoleophobic coatings, J. Mater. Chem. A., 2012; 22: 2834-2837.

[25] Tutej A., Choi W., Ma M., Mabry J. M., Mazzella S. A., Rutledge G. C., McKinley G. H., Cohen R. E., Designing superoleophobic surfaces, Science, 2007, 318: 1618-1622.

[26] Zhu Z., Zheng S., Peng S., Zhao Y., Tian Y., Superlyophilic interfaces and their applications, Adv. Mater., 2017; 29: 1703120.

[27] Meng X., Wang M., Heng L., Jiang L., Underwater mechanically robust oil-repellent materials: combining conflicting properties using a heterostructure, Adv. Mater., 2018; 30: 1706634.

[28] Han Z., Feng X., Guo Z., Niu S., Ren L., Flourishing bioinspired antifogging materials with superwettability: progresses and challenges, Adv. Mater., 2018; 30: 1704652.

[29] Zhang X., Zhao Y., Mu S., Jiang C., Song M., Fang Q., Xue M., Qiu S., Chen B., UiO-66 coated mesh with underwater superoleophobicity for high-efficiency oil-water separation, ACS Appl. Mater. Inter., 2018; 10: 17301-17308.

[30] Zhang F., Zhang W., Shi Z., Wang D., Jin J., Jiang L., Nanowire-haired inorganic membranes with superhydrophilicity and underwater ultralow adhesive superoleophobicity for high-efficiency oil/water separation, Adv. Mater., 2013; 25: 4192-4198.

[31] Dong Y., Li J., Shi L., Wang X., Guo Z., Liu W., Underwater superoleophobic

graphene oxide coated meshes for the separation of oil and water, Chem. Comm., 2014; 50: 5586-5589.

[32] Huang J., Lai Y., Wang L., Li S., Ge M., Zhang K., Fuchs H., Chi L., Controllable wettability and adhesion on bioinspired multifunctional TiO_2 nanostructure surfaces for liquid manipulation, J. Mater. Chem. A., 2014; 43: 18531-18538.

[33] Ding C., Zhu Y., Liu M., Feng L., Wan M., Jiang L., PANI nanowire film with underwater superoleophobicity and potential-modulated tunable adhesion for no loss oil droplet transport, Soft Matter, 2012; 35: 9064-9068.

[34] Xin B., Hao J., Reversibly switchable wettability, Chem. Soc. Rev., 2010; 39: 769-782.

[35] Lin X., Lu F., Chen Y., Liu N., Cao Y., Xu L., Zhang W., Feng L., Electricity-induced switchable wettability and controllable water permeation based on 3D copper foam, Chem. Comm., 2015; 51: 16237-16240.

[36] Che H., Huo M., Peng L., Fang T., Liu N., Feng L., Wei Y., Yuan J., CO_2-responsive nanofibrous membranes with switchable oil/water wettability, Angew. Chem. Int. Ed., 2015; 54: 8934-8938.

[37] Dang Z., Liu L., Li Y., Xiang Y., Guo G., In situ and ex situ pH-responsive coatings with switchable wettability for controllable oil/water separation, ACS Appl. Mater. Inter., 2016; 8: 31281-31288.

[38] Chang Y. H., Hau N. Y., Liu C., Huang Y. T., Li C. C., Shih K., Feng S. P., A short-range ordered–disordered transition of a $NiOOH/Ni(OH)_2$ pair induces switchable wettability, Nanoscale, 2014; 6: 15309-15315.

[39] Rodenas T., Luz I., Prieto G., Seoane B., Miro H., Corma A., Kapteijn F., Xamena F. X. L., Gascon J., Metal–organic framework nanosheets in polymer composite materials for gas separation, Nat. Mater., 2015; 14: 48-55.

[40] Li X., Liu Y., Wang J., Gascon J., Li J., Bruggen B. V., Metal–organic frameworks based membranes for liquid separation, Chem. Soc. Rev., 2017; 46: 7124-7144.

[41] Dhakshinamoorthy A., Garcia H., Catalysis by metal nanoparticles embedded on metal–organic frameworks, Chem. Soc. Rev., 2012; 41: 5262-5284.

[42] Ma S., Zhou H. C., Gas storage in porous metal–organic frameworks for clean energy applications, Chem. Comm. 2010; 46: 44-53.

[43] Cheng Y., Wang X., Jia C., Wang Y., Zhai L., Wang Q., Zhao D., Ultrathin mixed matrix membranes containing two-dimensional metal-organic framework nanosheets for efficient CO_2/CH_4 separation, J. Membrane. Sci., 2017; 539: 213-223.

[44] Phan A., Doonan C. J., Uribe-romo F. J., Knobler C. B., O'keeffe M., Yaghi O. M., Synthesis, structure, and carbon dioxide capture properties of zeolitic imidazolate frameworks, Acc. Chem., 2010; 43: 58-67.

[45] Zhong Z., Yao J., Low Z., Chen R., He M., Wang H., Carbon composite membrane derived from a two-dimensional zeolitic imidazolate framework and its gas separation properties, Carbon., 2014; 72: 242-249.

[46] Conrad S., Kumar P., Xue F., Ren L., Henning S., Xiao C., Mkhoyan K. A., Tsapatsis M., Controlling dissolution and transformation of zeolitic imidazolate frameworks by using electron-beam-induced amorphization, Angew. Chem. Int. Ed., 2018; 57: 13592-13597.

[47] Ma Q., Li G., Liu X., Wang Z., Song Z., Wang H., Zeolitic imidazolate framework-8 film coated stainless steel meshes for highly efficient oil/water separation, Chem. Comm., 2018; 54: 5530-5533.

[48] Gu Q., Albert T. C., Sun Q., Elshahawy A. M. K., Lyu Z., He Z., Zhang L., Yong H., Zeng K., Wang J., Heterogeneous ZIF-L membranes with improved hydrophilicity and anti-bacterial adhesion for potential application in water treatment, RSC Adv., 2019; 9: 1591-1601.

[49] Zhong Z., Yao J., Chen R., Low Z., He M., Liu J. Z., Wang H., Oriented two-dimensional zeolitic imidazolate framework-L membranes and their gas permeation properties, J. Mater. Chem. A. 2015; 3: 15715-15722.

[50] Yuan S., Zhu J., Li Y., Zhao Y., Li J., Puyveldea P. V., Bruggen B. V., Structure architecture of micro/nanoscale ZIF-L on a 3D printed membrane for a superhydrophobic and underwater superoleophobic surface, J. Mater. Chem. A., 2019; 7: 2723-2729.

[51] Kang H., Cheng Z., Lai H., Ma H., Liu Y., Mai X., Wang Y., Shao Q., Xiang L., Guo X., Guo Z., Superlyophobic anti-corrosive and self-cleaning titania robust mesh membrane with enhanced oil/water separation, Sep. Purif. Technol., 2018; 201: 193-204.

[52] Du X., You S., Wang X., Wang Q., Lu J., Switchable and simultaneous oil/water separation induced by prewetting with a superamphiphilic self-cleaning mesh, Chem. Eng. J., 2017; 313: 398-403.

[53] Zhang F., Shi Z., Xu C., Huo D., Zhang W., Peng C., Self-fibering growth in the

soot-templated CVD coating of silica on mesh for efficient oil/water separation, Mater. Des., 2018; 154: 370-377.

[54] Wen N., Miao X., Yang X., Long M., Deng W., Zhou Q., Deng W., An alternative fabrication of underoil superhydrophobic or underwater superoleophobic stainless steel meshes for oil-water separation: Originating from one-step vapor deposition of polydimethylsiloxane, Sep. Purif. Technol., 2018; 204: 116-126.

[55] Song S., Yang H., Zhou C., Cheng J., Jiang Z., Lu Z., Miao J., Underwater superoleophobic mesh based on $BiVO_4$ nanoparticles with sunlight-driven self-cleaning property for oil/water separation, Chem. Eng. J., 2017; 320: 342-351.

[56] Liu R., Young S., Dangwal S., Shaik I., Echeverria E., McIlroy D., Aichele C., Kim S. J., Boron substituted MFI-type zeolite-coated mesh for oil-water separation, Colloid Surf. A., 2018; 550: 108-114.

[57] Liu R., Dangwal S., Shaik I., Aichele C., Kim S., Hydrophilicity-controlled MFI-type zeolite-coated mesh for oil/water separation, Sep. Purif. Technol., 2018; 195: 163-169.

[58] Liu Y., Liu N., Chen Y., Zhang W., Qu R., Zhang Q., Shih T., Feng L., Wei Y., A versatile CeO_2/Co_3O_4 coated mesh for food wastewater treatment: simultaneous oil removal and UV catalysis of food additives, Water Res., 2018; 137: 144-152.

Chapter 5: Superhydrophobic ZIF−OAs with enhanced water stability

5.1 Introduction

Metal-organic frameworks (MOFs) are an evolving class of highly porous, crystalline materials composed of metal ions bridged by organic linkers [1, 2]. MOFs have received enormous attention over the last decades because of their unique chemical versatility and tremendous structural flexibility. MOF-based materials have thus been extensively investigated for applications in a wide range of fields, such as sensing [3], catalysis [4], energy storage [5], gas adsorption/separation [6], and water treatment [7]. In particular, two-dimensional (2D) MOF nanosheets [8], and one-dimensional (1D) MOF nanotubes [9], nanorods [10], and nanowires [10, 11], etc., are drawing extensive research interest in recent years. This is because they effectively combine the exceptional features of MOFs, such as tunable pore structure, with the distinctive properties of low-dimensional nanomaterials, such as high aspect ratio and plentiful active sites [8-11]. Although the advantageous properties of these MOFs nanomaterials have been well proven, significant research efforts are still highly required regarding their large-scale preparation and real-world applications.

Apart from an effective synthesis approach to the preparation, exceptional stability of the synthesized MOF material is equally important for promoting their real-world applications in various fields [12]. The majority of MOFs are known to be sensitive to

water content due to their weak metal-ligand coordination bonding, and only a few MOFs were reported to possess satisfactory water stability [12]. The instability issue has considerably limited any real-world application of MOFs, since water or moisture is ubiquitous in most industrial processes. To overcome this problem, researchers have made great efforts to enhance the water stability of MOFs. Existing methods to enhance the water stability of MOFs can be categorized into two types: (1) Synthesizing MOFs with strong coordination bonds by employing high oxidation state metals (such as Zr^{4+}) and carboxylic acid ligands [13], or using alkali metals and nitrogen-donor ligands [14]; (2) Functionalizing existing MOFs by the hydrophobic functionalization of organic linkers [15], or the hydrophobic post-modification of external MOF surfaces [16]. For example, Omary et al. [17] demonstrated that highly hydrophobic fluorous metal-organic frameworks exhibiting remarkable air and water stability. Despite recent progress, water-stable MOFs are still in great demand among the scientific community.

In this chapter, an interfacial assembly strategy was developed for the preparation of exceptionally water-stable 2D zeolitic imidazolate framework (ZIF) nanosheets and 1D ZIF nanotubes. Oleic acid which is an amphiphilic fatty acid naturally exists in various animal fats and vegetable oils, was employed as the solvent for the oil phase. Two dimensional (2D) ZIF structures were produced at the oil/water interface through the coordination of zinc ions from the water phase and imidazole ligands from the oil phase under room temperature. Interestingly, when increasing the temperature, 2D ZIFs were observed to self-scroll, producing 1D ZIF nanoscrolls and nanotubes. Oleic acid

molecules were found to link to ZIF structures during the synthesis. These interfacial synthesized ZIFs, which we propose to name as ZIF−OAs, showed highly hydrophobic character with water contact angles up to ~150° ± 2º. As a result, the synthesized ZIF−OAs demonstrated superior water stability and chemical stability, which are significant for their practical applications.

5.2 Morphology and structure of ZIF−OAs

Water stable ZIF−OA structures were prepared by a simple oil/water interfacial assembly process. Aqueous solution of Zn $(NO_3)_2.6H_2O$ (1M, 5mL) was first added to a petri dish, then oleic acid (OA) solution of 2-methylimidazole (0.4 M, 1mL) was added dropwise to the surface of the aqueous solution to form an oil/water interface. At the formed interface, zinc ions (Zn^{2+}) from the aqueous phase are expected to coordinate with imidazole linkers from the oil phase to produce zeolitic imidazolate framework (ZIF) structures. OA molecules with long aliphatic chains are expected to decorate on the ZIF structures to form a shell layer with superior hydrophobicity. The synthesized product can thus be denoted as ZIF−OA. The two-phase solution was aged for 24 h under room temperature and 50 ℃, respectively, to produce 2D ZIF−OA layers and 1D ZIF−OA nanotubes.

Morphologies of synthesized ZIF−OA structures are observed using SEM (Figure 5.1a-f). As shown in Figure 5.1a, ZIF−OAs synthesized at the oil/water interface under room temperature showed two-dimensional layered morphologies. The width of these 2D

ZIF−OA layers was estimated to vary from 2 μm to 10 μm.

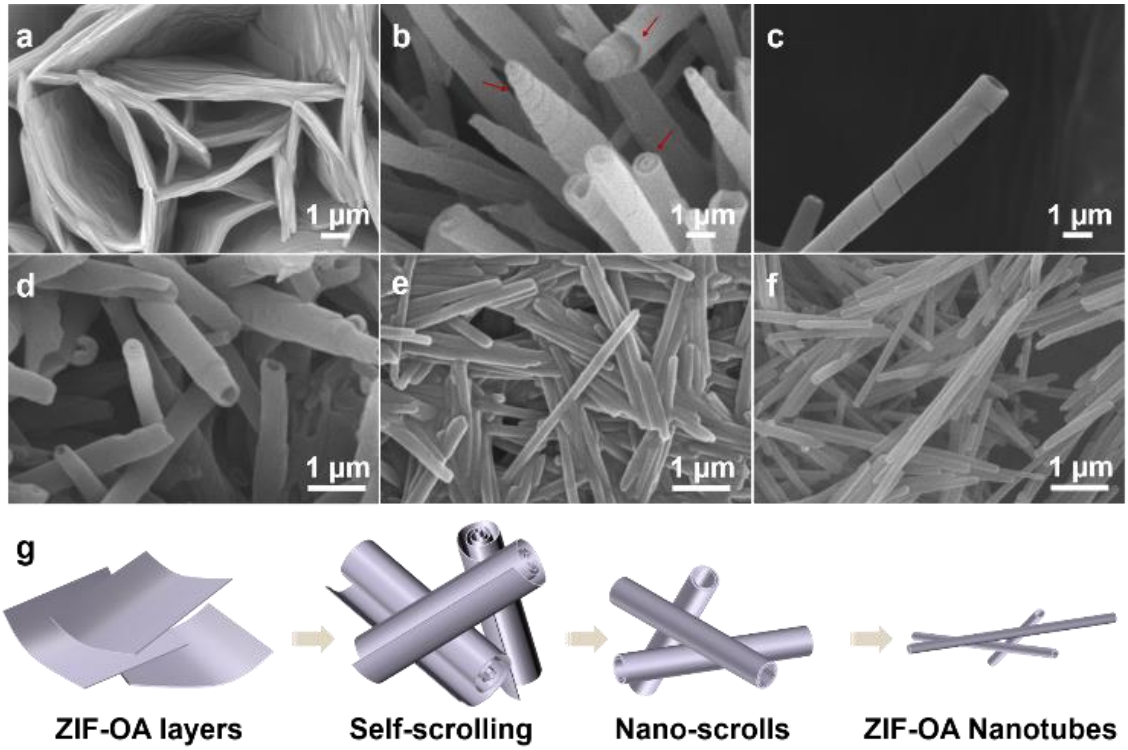

Figure 5.1. Morphologies of the synthesized ZIF−OA structures. (a) 2D ZIF−OA layers synthesized by the interfacial assembly process under room temperature; (b) self-scrolled 2D ZIF−OA with Archimedean spiral morphology formed under 50 ℃ for 12 h; (c) self-scrolled ZIF−OA with rolled-up straws-like morphology formed under 50 ℃ for 12 h; (d) 1D ZIF−OA nanotubes synthesized under 50 ℃ for 16 h; (e) 1D ZIF−OA nanotubes synthesized under 50 ℃ for 24 h; (f) 1D ZIF−OA nanotubes synthesized under 50 ℃ for 48 h; (g) schematic illustration showing a self-scrolling process of 2D ZIF−OA layers to form 1D ZIF−OA nanotubes.

Interestingly, unlike traditional 2D MOFs which usually have rigid structures (such as ZIF-L), these 2D ZIF−OA layers are observed to be soft and flexible. When increasing

the synthesis temperature to 50 ℃, large flexible 2D ZIF−OA layers tend to self-scroll, forming an Archimedean spiral morphology (Figure 5.1b) or a rolled-up straws-like morphology (Figure 5.1c).

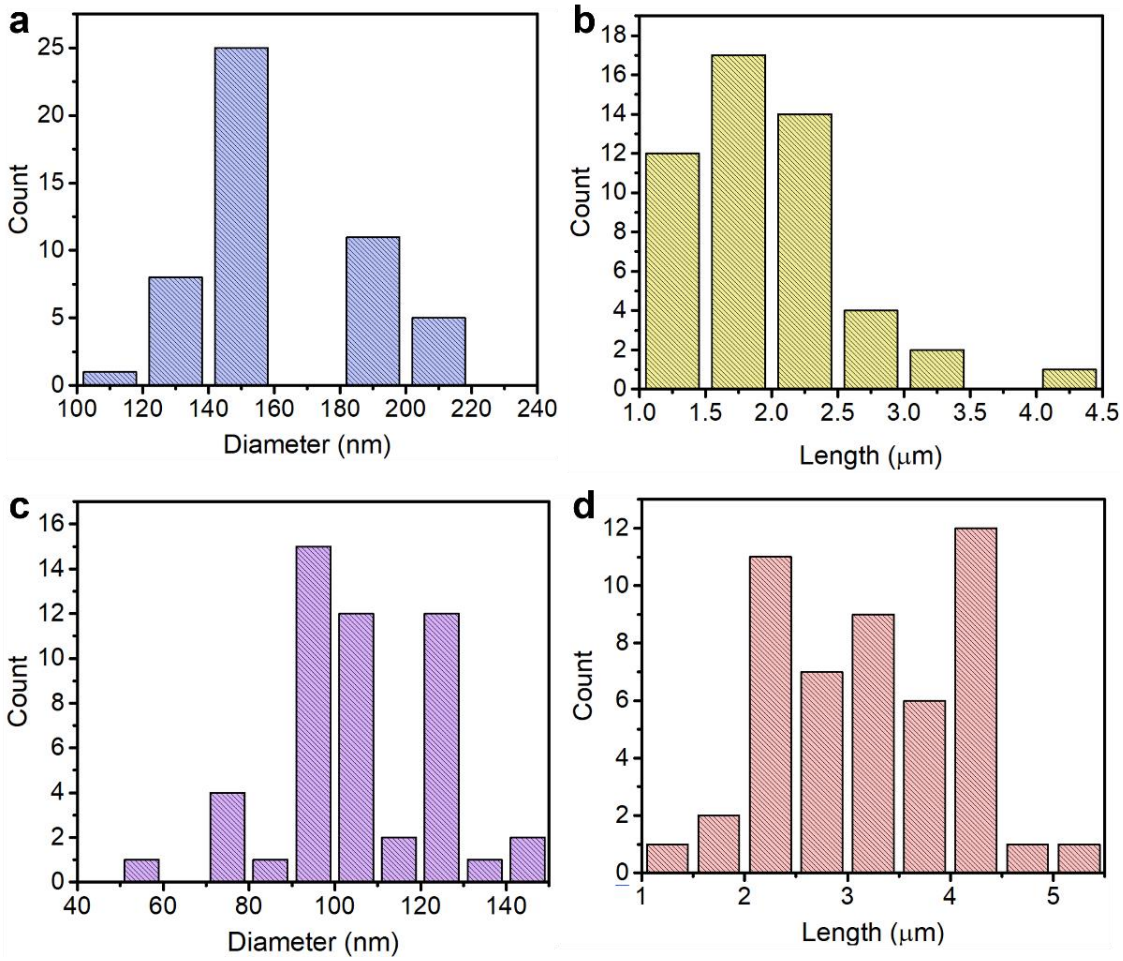

Figure 5.2. The estimated size distribution of (a) the diameter, and (b) the length of the ZIF−OA nanotubes synthesized under 50 ℃ for 24 h; (c) the diameter, and (d) the length of the ZIF−OA nanotubes synthesized under 50 ℃ for 48 h.

Moreover, an increase of the synthesis time promotes the scrolling of the majority of ZIF−OA layers including those with small lateral size, forming ZIF−OA scrolls with an average diameter of ~357 nm and length of ~2.0 μm (Figure 5.1d). A further increase

of the synthesis time favors the one-dimensional growth of ZIF−OA scrolls, producing 1D ZIF−OA nanotubes with a uniform morphology. As presented in Figures 1e and f, ZIF−OA nanotubes with an average diameter of ~160 nm and ~105 nm, and an average length of ~2.0 μm and ~3.2 μm were obtained when the synthesis time was increased to 24 h, and 48 h, respectively. Size distribution of the nanotube diameter and length can be found in Figure 5.2. Based on SEM characterizations, a schematic illustration showing the formation of 1D ZIF−OA nanotubes by the self-scrolling of 2D ZIF−OA layers is presented in Figure 5.1g.

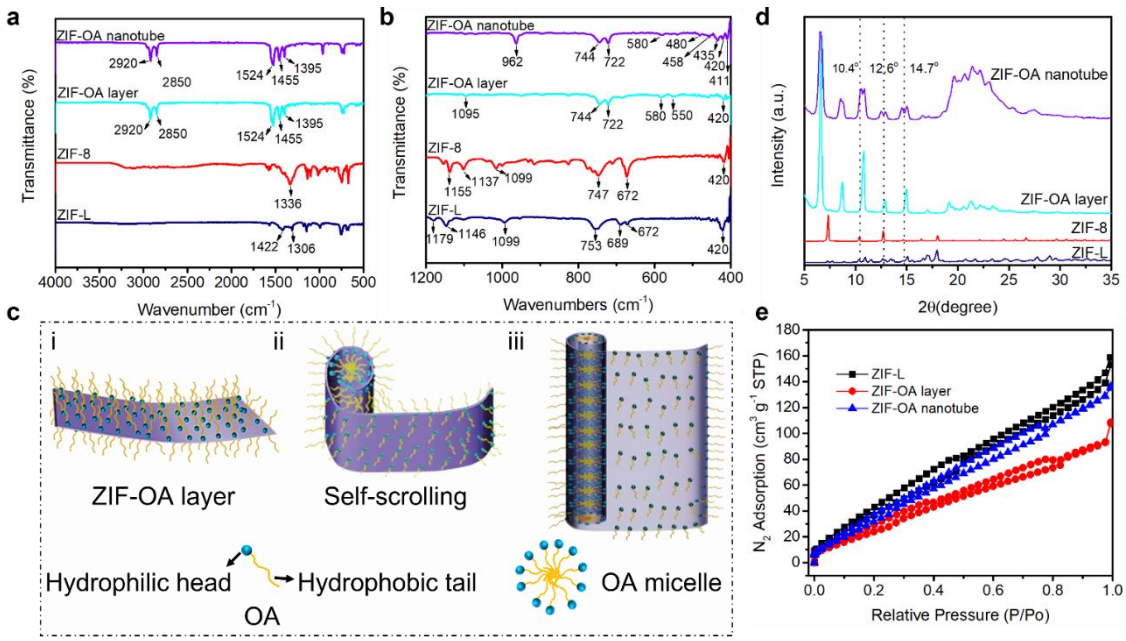

Figure 5.3. Properties and the formation mechanism of the ZIF−OAs. (a), (b) FTIR spectra of ZIF-L, ZIF-8, and the synthesized 2D ZIF−OA layer as well as the 1D ZIF−OA nanotube; (c) schematic diagram showing the proposed formation mechanism of ZIF−OA nanotubes from ZIF−OA layers; (d) XRD patterns of ZIF-L, ZIF-8, 2D ZIF−OA layer, and 1D ZIF−OA nanotube; (e) Nitrogen adsorption-desorption

isotherms of ZIF-L, 2D ZIF−OA layer, and 1D ZIF−OA nanotube

To scrutinize the chemical and structural properties of the interfacial synthesized ZIF−OAs, FTIR spectra of 2D ZIF−OA layers and 1D ZIF−OA nanotubes were analysed and compared with ZIF-L and ZIF-8 which are two of the most extensively studied ZIFs prepared from the same metal and ligand source. A summary of characteristic peaks of all the tested ZIFs can be found in Table 5.1 to Table 5.4. As shown in Figure 2a and Table 5.1, the FTIR spectrum of ZIF-L showed characteristic peaks at 1422 cm^{-1} and 1306 cm^{-1}, corresponding to the imidazole ring stretching and C-N bonds in the imidazole group, respectively. FTIR spectrum of ZIF-8 (Figure 2a and Table 5.2) showed an intense peak at 1336 cm^{-1}, which was ascribed to the in-plane bending vibration of the imidazole ring.

Table 5.1. FTIR characteristic peak assignments for the ZIF-L sample.

Wavenumber (cm^{-1})	**Assignment**
1422	Imidazole ring stretching
1306	Imidazole ring stretching
1179	Imidazole ring out-of-plane bending
1146	Imidazole ring out-of-plane bending
1099	Imidazole ring out-of-plane bending
753	Wagging vibration of N-H bonds
689	Zn-N bonds
672	Zn-N bonds
420	Zn-N bonds

Table 5.2. FTIR characteristic peak assignments for the ZIF-8 sample.

Wavenumber (cm^{-1})	**Assignment**
1336	Imidazole ring in-plane bending vibration
1155	Imidazole ring out-of-plane bending
1137	Imidazole ring out-of-plane bending
1099	Imidazole ring out-of-plane bending
747	Wagging vibration of N-H bonds
672	Zn-N bonds
420	Zn-N bonds

FTIR spectra of both ZIF−OA layer and ZIF−OA nanotube showed new intense peaks at 2920 cm^{-1} and 2850 cm^{-1}, which were attributed to the bending vibration of $–CH_2$ from the long aliphatic chain of oleic acid. This confirms the existence of oleic acid molecules in the interfacial synthesized ZIF−OA structures.

Table 5.3. FTIR characteristic peak assignments for the 2D ZIF−OA sample.

Wavenumber (cm^{-1})	**Assignment**
2920	$−CH_2−$ bending vibration
2850	$−CH_2−$ bending vibration
1524	Imidazole ring stretching
1455	Imidazole ring stretching
1395	Imidazole ring stretching
1095	Imidazole ring out-of-plane bending
744	Imidazole ring in-plane bending
722	Imidazole ring in-plane bending
580	Zn-O bonds

550	Zn-O bonds
420	Zn-N bonds

The characteristic peaks at 1524 cm^{-1}, 1455 cm^{-1}, and 1395 cm^{-1} were ascribed to the stretching vibration of the imidazole ring. Figure 5.3b presents FTIR spectra of different ZIF structures in the lower wavenumber region. For ZIF-L, peaks at 1179 cm^{-1}, 1146 cm^{-1}, and 1099 cm^{-1} correspond to the out-of-plane bending of the imidazole ring. The peak at 753 cm^{-1} was assigned to the wagging vibration of N-H bonds, and peaks at 689 cm^{-1}, 672 cm^{-1}, and 420 cm^{-1} were attributed to Zn-N bonds. For ZIF-8, peaks at 1155 cm^{-1}, 1137 cm^{-1}, and 1099 cm^{-1} correspond to the out-of-plane bending of the imidazole ring. The peak at 747 cm^{-1} was assigned to the wagging vibration of N-H bonds, and peaks at 672 cm^{-1} and 420 cm^{-1} were attributed to Zn-N bonds.

Table 5.4. FTIR characteristic peak assignments for the 1D ZIF-L sample.

Wavenumber (cm^{-1})	**Assignment**
2920	-CH_2- bending vibration
2850	-CH_2- bending vibration
1524	Imidazole ring stretching
1455	Imidazole ring stretching
1395	Imidazole ring stretching
962	Imidazole ring out-of-plane bending
744	Imidazole ring in-plane bending
722	Imidazole ring in-plane bending
580	Zn−O bonds
480	Zn−O bonds
458	Zn−O bonds

435	Zn−O bonds
420	Zn−N bonds
411	Zn−O bonds

For the ZIF−OA layer, the peak at 1095 cm^{-1}correspond to the out-of-plane bending of the imidazole rings, and peaks at 744 cm^{-1} and 722 cm^{-1} were attributed to the in-plane bending of the imidazole ring. Weak peaks at 580 cm^{-1} and 550 cm^{-1} were assigned to Zn−O bonds, and the peak at 420 cm^{-1} correspond to Zn−N bonds. For the ZIF−OA nanotube, the peak at 962 cm^{-1} corresponds to the out-of-plane bending of the imidazole ring, and peaks at 744 cm^{-1} and 722 cm^{-1} were attributed to the in-plane bending of the imidazole ring. Weak peaks in the range of 435 cm^{-1} to 580 cm^{-1}, and the peak at 411 cm^{-1} can be assigned to Zn−O bonds, and the peak at 420 cm^{-1} correspond to Zn−N bonds. The FTIR analysis results suggest that oleic acid molecules linked with zinc centres of ZIF structures via Zn−O bonds. Based on the above structural analysis of ZIF−OAs, a formation mechanism of 1D ZIF−OA structures from 2D ZIF−OA layers was proposed and depicted in Figure 5.3c. In the interfacial synthesis approach, zinc ions from the bottom aqueous phase and imidazole ligands from the top oil phase coordinated at the oil/water interface to form two dimensional ZIF layers. Meanwhile, the amphiphilic oleic acid molecule which is made up of a hydrophilic carboxylic acid head and a hydrophobic carbon tail regularly adsorbed at the interface with the hydrophilic head facing the water phase while the hydrophobic tail facing the oil phase. Therefore, during the formation of the ZIF structure, oleic acid not only acted as the

solvent for imidazole ligands in the oil phase, but also partially bonded with zinc ions from the aqueous phase by Zn−O bonds between Zn^{2+} and carboxylic acid group. Because of the participation of oleic acid molecules, as-synthesized ZIF−OA layers displayed a certain degree of flexibility and were easy to deform. When the temperature was increased, these flexible ZIF−OA layers tended to bend or curl. Meanwhile, oleic acid molecules tended to assemble via hydrophobic interactions among their hydrophobic tails to form micelles. The micellization of oleic acid molecules provided a driving force for the self-scrolling of ZIF−OA layers, producing 1D ZIF−OA scrolls and nanotubes.

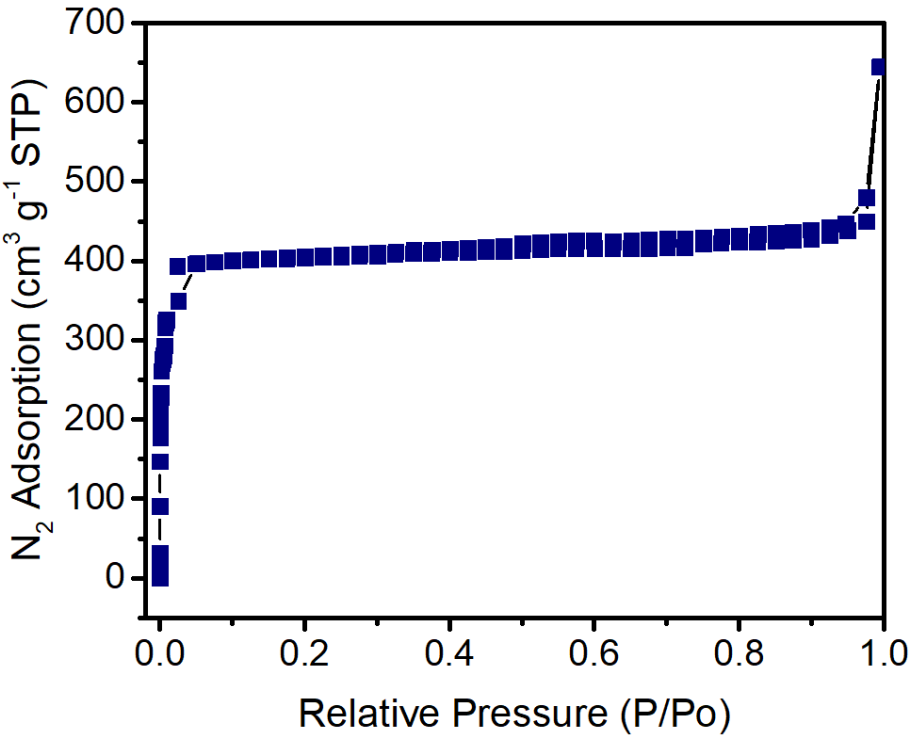

Figure 5.4. Nitrogen adsorption-desorption isotherm of the ZIF-8 sample

Crystal structures of ZIF−OA layers and nanotubes were determined by XRD and

compared with ZIF-L and ZIF-8, as shown in Figure 5.3d. The XRD pattern of ZIF-L exhibited characteristic peaks that were consistent with previously reported peaks. XRD pattern of ZIF-8 showed characteristic peaks at 2θ = 7.3º, 10.4º, 12.7º, 14.7º 16.4º, and 18.1º, which were identical to those reported in previous studies. XRD patterns of ZIF−OA layers and ZIF−OA nanotubes both showed weak peaks at 2θ = 10.4º, 12.6º, 14.7º, which were consistent with peaks in the XRD pattern of ZIF-8 and correspond to the crystallographic planes of (200), (211), and (220). In addition, ZIF−OA layers and nanotubes presented two new peaks at 2θ = 6.3º and 8.4º, suggesting their crystal structures were different from either ZIF-L or ZIF-8. The surface area of ZIF−OA layers and ZIF−OA nanotubes was analysed by measuring N_2 adsorption-desorption isotherms at 77 K. As shown in Figure 5.3e and Figure 5.4, ZIF-L, ZIF-8 and ZIF−OAs all displayed type-I isotherm. The ZIF-8 sample had a BET surface area of ~1108.6 $m^2 g^{-1}$, and the ZIF-L sample had a lower BET surface area of ~199.5 $m^2 g^{-1}$, which were consistent with previously reported values. The 2D ZIF−OA layers had a BET surface area of ~145.3 $m^2 g^{-1}$, and the 1D ZIF−OA nanotube had a BET surface area of ~198.2 $m^2 g^{-1}$ which was comparable to the surface area of ZIF-L nanosheets.

5.3 Surface property of ZIF−OAs

As discussed above, oleic acid molecules are linked to the interfacial synthesized ZIF−OA structures by forming Zn-O bonds between zinc centers and hydrophilic carboxylic acid heads of OA molecules. In this case, hydrophobic carbon tails of OA molecules were expected to cover the ZIF−OA surfaces, forming a hydrophobic shell

layer. To confirm this, surface properties of as-synthesized ZIF−OA products were investigated by performing water contact angle measurements and were compared with those of ZIF-L and ZIF-8 (Figure 5.5).

As shown in Figure 5.5a-c, ZIF-L powder with a 2D leaf-like morphology was easily wetted by water drops and had a WCA of ~15º ± 2º in air, suggesting a highly hydrophilic surface property. The ZIF-8 sample with a 3D truncated dodecahedra morphology was also easily wetted by water drops and showed a WCA of ~59º ± 2º in the air (Figure 5.5d-f), suggesting a hydrophilic surface property. The hydrophilic surface property of ZIF-L and ZIF-8 makes them sensitive to water/moisture content in varieties of applications. Interestingly, the interfacial synthesized 2D ZIF−OA layer sample showed excellent hydrophobic character with water drops staying spherical on the powder and a WCA of ~145º ± 2º in the air (Figure 5.5g-i).

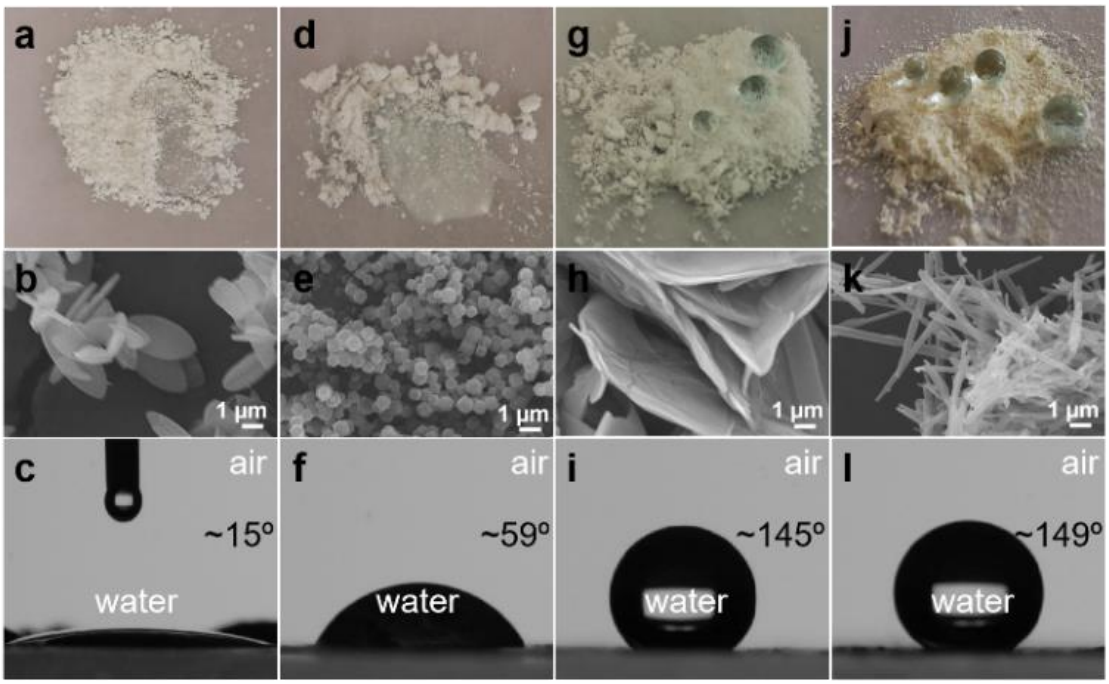

Figure 5.5. Surface properties of different types of ZIF structures. (a) A picture showing ZIF-L powder wetted by water drops; (b) SEM image of the ZIF-L showing 2D leaf-like morphology; (c) water contact angle (WCA) of the ZIF-L powder; (d) a picture showing ZIF-8 powder wetted by water drops; (e) SEM image of the ZIF-8 showing 3D truncated dodecahedra morphology; (f) WCA of the ZIF-8 powder; (g) a picture showing spherical water drops stay on ZIF−OA powder prepared by interfacial synthesis under room temperature; (h) SEM image showing 2D layered morphology of the ZIF−OA; (i) WCA of the 2D ZIF−OA powder; (j) a picture showing water drops stay on ZIF−OA powder prepared by interfacial synthesis under 50 ℃ for 48 h; (k) SEM image showing 1D nanotube morphology of the ZIF−OA; (l) WCA of the 1D ZIF−OA powder.

Likewise, the 1D ZIF−OA nanotubes also exhibited fascinating hydrophobic surface properties with a WCA of ~145º ± 2º in the air (Figure 5.5j-l). The hydrophobic property of both the 2D ZIF−OA layers and 1D ZIF−OA nanotubes remained unchanged for a long time. For example, 2D ZIF−OA layers and 1D ZIF−OA nanotubes were observed to stay floating on the water surface for up to 30 days (Figure 5.6a), with their WCAs of ~ 135º ± 2º and ~138º ± 2º, respectively (Figure 5.6b)

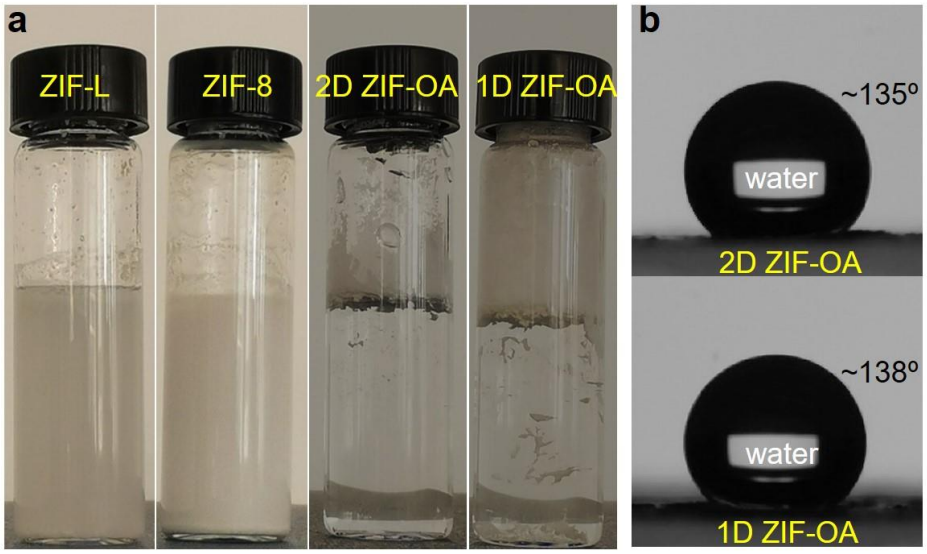

Figure 5.6. (a) Pictures of ZIF-L, ZIF-8, 2D ZIF−OA layers, and 1D ZIF−OA nanotubes in deionized water after 30 days. (b) Water contact angles of the 2D ZIF−OA powder and 1D ZIF-OA powder after being dipped in water for 30 days.

The highly hydrophobic surface properties of ZIF−OA layers and nanotubes suggest their excellent water/moisture stability which is significant for a wide range of real-world industrial applications such as gas separation, catalysis and liquid separation.

5.4 Chemical stability of ZIF−OAs

The water stability experiment was performed by soaking different ZIF samples (ZIF-L, ZIF-8, 2D ZIF−OA, 1D ZIF−OA) in deionized water for up to 30 days. The morphology variation as well as the structure change of the tested ZIFs after soaking, were monitored by SEM and XRD characterizations. The SEM observations indicated that the ZIF-L sample started to lose intact crystalline morphology after been soaked in

DI water for 7 days, and completely transformed to an amorphous phase after 30 days (Figure 5.7).

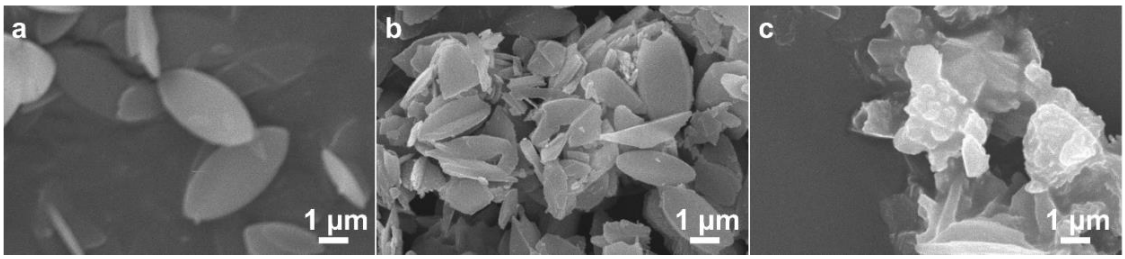

Figure 5.7. SEM images of ZIF-L after soaking in DI water for (a) 0 days, (b) 7 days, and (c) 30 days.

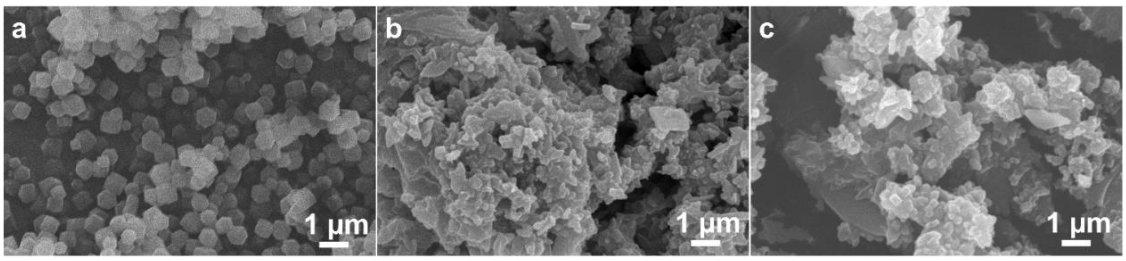

Figure 5.8. SEM images of ZIF-8 after soaking in DI water for (a) 0 days, (b) 7 days, and (c) 30 days.

Similarly, the ZIF-8 sample started to transform to an amorphous phase after 7 days in water (Figure 5.8).

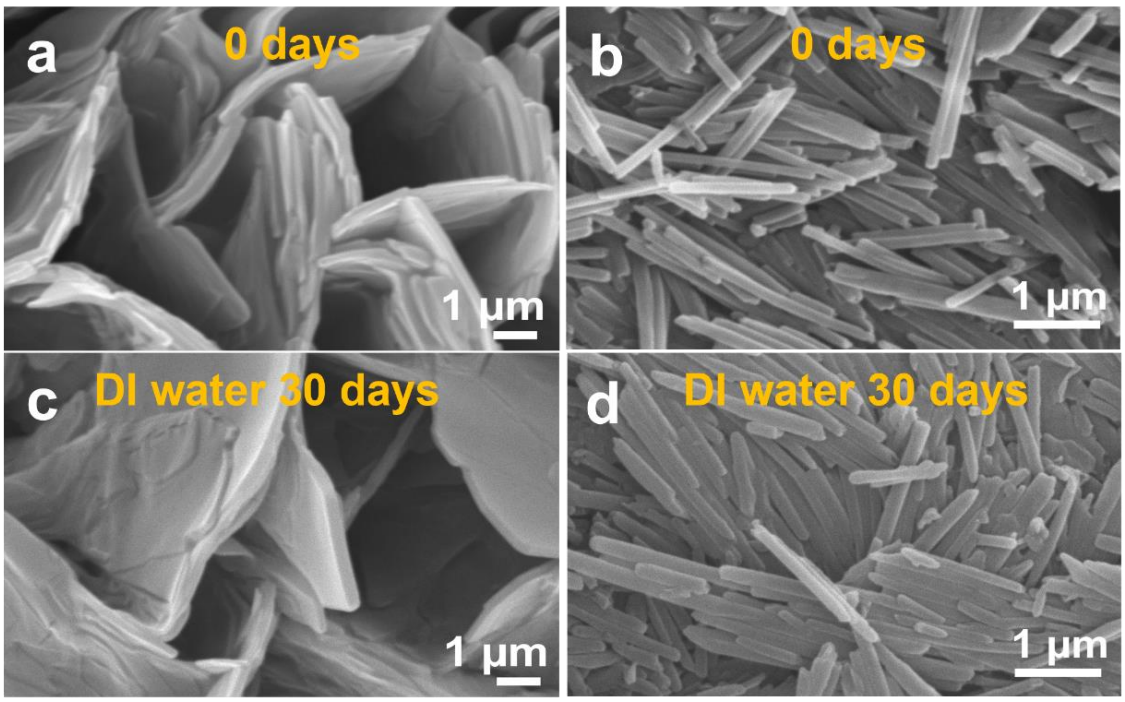

Figure 5.9. SEM images of 2D ZIF−OA layers after soaked in DI water for (a) 0 days, (c) 30 days; and 1D ZIF−OA nanotube after soaking in DI water for (b) 0 days, (d) 30 days.

These results indicated that hydrophilic ZIF-L and ZIF-8 samples both have insufficient long-term stability under a water environment. In comparison, the interfacial synthesized ZIF−OAs exhibited greatly enhanced water stability. As shown in Figure 5.9, the morphology of both 2D ZIF−OA nanolayers and 1D ZIF−OA nanotubes remained nearly unaffected after being soaked in DI water for up to 30 days (Figure 5.9a-d).

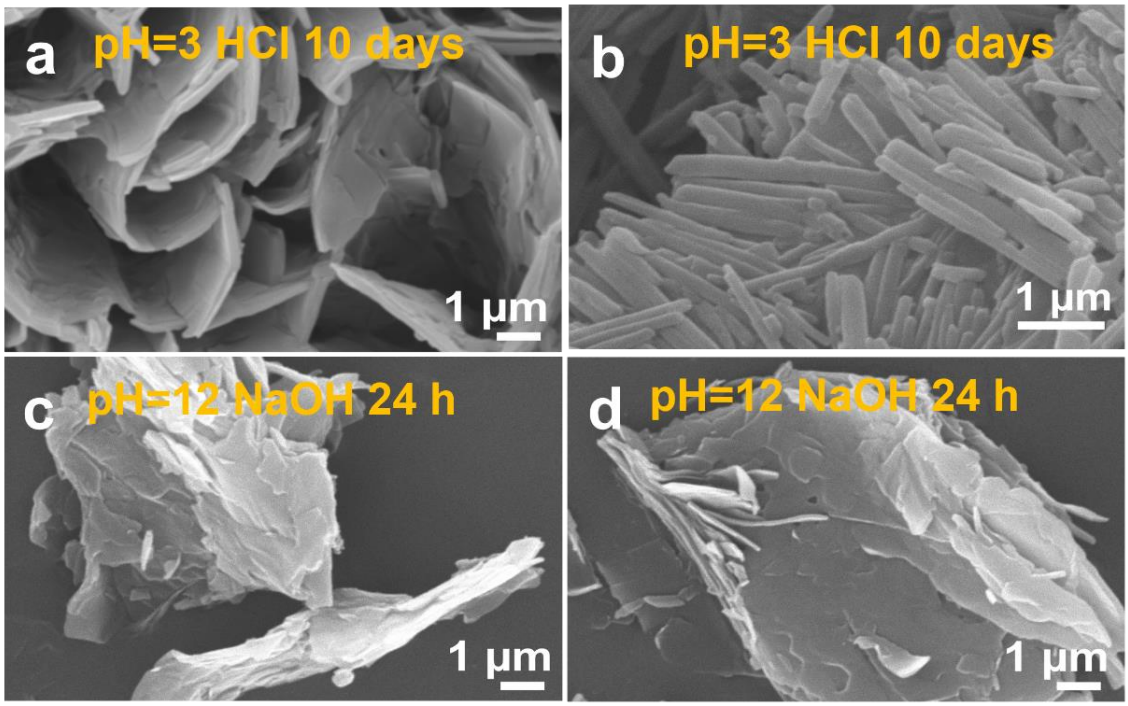

Figure 5.10. SEM images of 2D ZIF−OA layers after soaked in (a) pH = 3 HCl solution for 10 days, (c) pH = 12 NaOH solution for 24 h; and 1D ZIF−OA nanotube after soaking in (b) pH = 3 HCl solution for 10 days, (c) pH = 12 NaOH solution for 24 h

The exceptional water stability of ZIF−OAs was attributed to their highly hydrophobic nature which provided the metal-ligand bond with a shield against the attack from water molecules. With such a shield against the attack from water molecules, the ZIF-OAs adsorb only very small amounts of water at ambient conditions. In this way, the ZIF framework degradation by water can be effectively prevented. Therefore, the synthesized highly hydrophobic ZIF-OAs are expected to demonstrate outstanding water/water vapor resistance in both liquid separations and gas separations.

Furthermore, the chemical stability of different ZIFs was determined by soaking them

in solutions with different pH values. As shown in Figure 5.10a, b, ZIF−OAs were able to maintain their original morphology after being soaked in the pH = 3 HCl solution for up to 10 days. This indicated that the interfacial synthesized ZIF−OAs possess superior chemical stability under harsh acidic conditions. However, the ZIF−OAs showed insufficient stability under harsh alkaline solutions with their morphologies changed after being soaked in the pH = 12 NaOH solution for 24 h (Figure 5.10c, d).

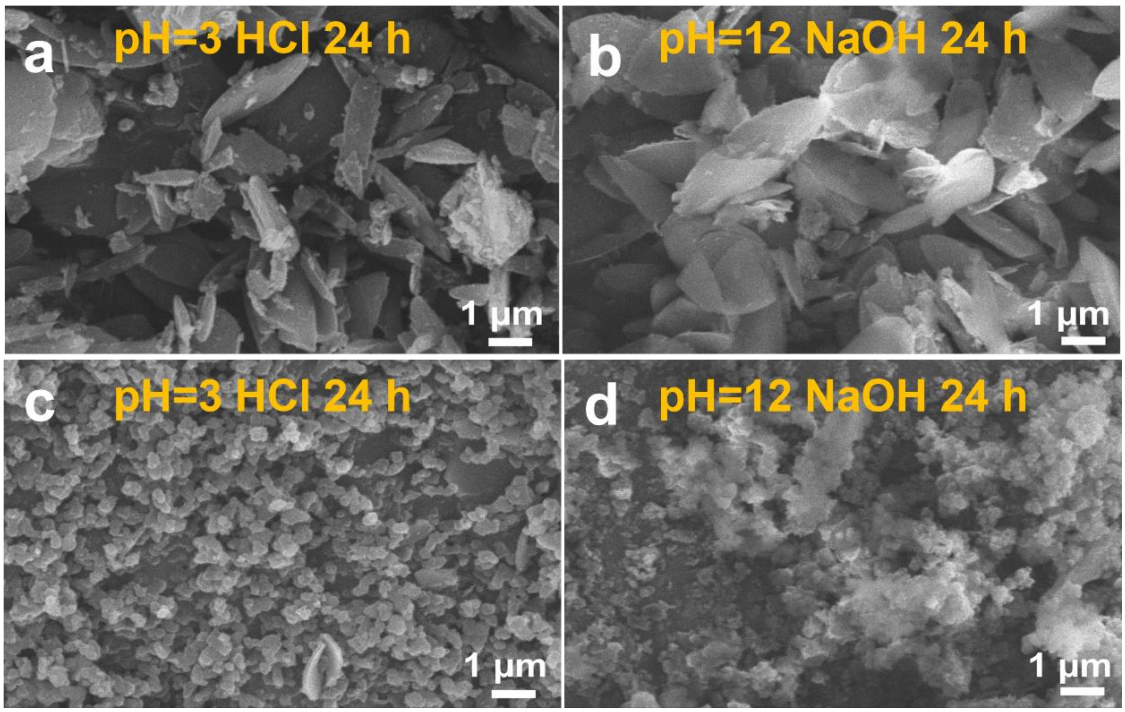

Figure 5.11. SEM images of (a) ZIF-L after soaking in pH = 3 HCl solution for 24 h, (b) ZIF-L after soaking in pH = 12 NaOH solution for 48 h, (c) ZIF-8 after soaking in pH = 3 HCl solution for 24 h, and (d) ZIF-8 after soaking in pH = 12 NaOH solution for 48 h.

For comparison, chemical stabilities of ZIF-L and ZIF-8 were also investigated. SEM

observations indicated that structures of ZIF-L and ZIF-8 were destroyed after soaking in pH = 3 HCl solution for 24 h, and in the pH = 12 NaOH solution 24 h (Figure 5.11). The stability tests confirmed that the ZIF−OAs synthesized in this work showed superior water stability and chemical stability under harsh acidic conditions compared to ZIF-L, ZIF-8.

5.5 Summary

In this chapter, a novel oil/water interfacial assembly method was designed to prepare oleic acid (OA) decorated ZIF nanostructures, named as ZIF−OAs. The prepared ZIF nanostructures showed superhydrophobic surface properties, and they demonstrated exceptional stability under the water environment. The main results can be summarized as:

(1) Two-dimensional ZIF−OA layers with their width in the range of ~2 μm to ~10 μm were prepared through the oi/water interfacial assembly method under room temperature. When increasing the synthesis temperature to 50 ℃, two-dimensional ZIF−OAs were observed to self-scroll to form one-dimensional nanotubes with their diameter in the range of ~100 nm to ~160 nm, and length in the range of ~2 μm to ~3μm.

(2) In the oil/water interfacial assembly process, oleic acid molecules not only acted as the solvent for imidazole ligands in the oil phase, but also partially bonded with zinc ions from the aqueous phase by Zn−O bonds between Zn^{2+} and a carboxylic acid group.

Therefore, the formed ZIF structures were decorated by large amounts of oleic acid molecules. When the temperature was increased, oleic acid molecules tended to assemble via hydrophobic interactions among their hydrophobic tails to form micelles. The micellization of oleic acid molecules provided a driving force for the self-scrolling of ZIF−OA layers, producing 1D ZIF−OA scrolls and nanotubes.

(3) The synthesized ZIF−OA nanostructures demonstrated interesting superhydrophobic surface properties with a water contact angle up to ~149º ± 2º. The superhydrophobic property was attributed to the decoration of oleic acid molecules in the ZIF nanostructures. Due to their superhydrophobicity, the synthesized ZIF−OAs showed exceptional stability under the water environment. Both two-dimensional ZIF−OA layers and one-dimensional ZIF−OA nanotubes showed unaffected morphologies after being soaked in deionized water for up to 30 days, and in pH = 3 HCl solution for up to 10 days.

5.6 References

[1] Jian M., Qiu R., Xia Y., Lu J., Chen Y., Gu Q., Liu R., Hu C., Qu J., Wang H., Zhang X., Ultrathin water-stable metal-organic framework membranes for ion separation, Sci. Adv., 2020; 6: eaay3998.

[2] Yanai N. Granick S., Directional self‐assembly of a colloidal metal–organic framework. Angew. Chem., 2012; 124: 5736-5739.

[3] Leelasree T., Selamneni V., Akshaya T., Sahatiya P. Aggarwal H., MOF based flexible, low-cost chemiresistive device as a respiration sensor for sleep apnea diagnosis, J. Mater. Chem. B., 2020; 8: 10182-10189.

[4] Cho H.Y., Yang D.A., Kim J., Jeong S.Y., Ahn W.S., CO_2 adsorption and catalytic application of Co-MOF-74 synthesized by microwave heating, Catal. Today, 2012; 185: 35-40.

[5] Li Y., Xu Y., Yang W., Shen W., Xue H. Pang H., MOF‐derived metal oxide composites for advanced electrochemical energy storage, Small, 2018; 14: 1704435.

[6] Venna S.R., Lartey M., Li T., Spore A., Kumar S., Nulwala H.B., Luebke D.R., Rosi N.L. Albenze E., Fabrication of MMMs with improved gas separation properties using externally-functionalized MOF particles, J. Mater. Chem. A., 2015; 3: 5014-5022.

[7] El-Mehalmey W.A., Safwat Y., Bassyouni M., Alkordi M.H., Strong interplay between polymer surface charge and MOF cage chemistry in mixed-matrix membrane for water treatment applications, ACS Appl. Mater. Interfaces, 2020; 12: 27625-27631.

[8] Ang H., Hong L., Polycationic polymer-regulated assembling of 2D MOF

nanosheets for high-performance nanofiltration, ACS Appl. Mater. Interfaces, 2017; 9: 28079-28088.

[9] Zou L., Hou C.C., Liu Z., Pang H., Xu Q., Superlong single-crystal metal–organic framework nanotubes. J. Am. Chem. Soc., 2018; 140: 15393-15401.

[10] Arbulu R.C., Jiang Y.B., Peterson E.J., Qin Y., Metal–organic framework (MOF) nanorods, nanotubes, and nanowires, Angew. Chem. Int. Ed., 2018; 57: 5813-5817.

[11] Muschi M., Lalitha A., Sene S., Aureau D., Frégnaux M., Esteve I., Rivier L., Ramsahye N., Devautour‐Vinot S., Sicard C., Menguy N., Formation of a single‐crystal aluminum‐based MOF nanowire with graphene oxide nanoscrolls as structure‐directing agents, Angew. Chem. Int. Ed., 2020; 59: 10353-10358.

[12] Zhu X.W., Zhou X.P., Li D., Exceptionally water stable heterometallic gyroidal MOFs: tuning the porosity and hydrophobicity by doping metal ions, Chem. Comm., 2016; 52: 6513-6516.

[13] Liu X., Demir N.K., Wu Z., Li K., Highly water-stable zirconium metal–organic framework UiO-66 membranes supported on alumina hollow fibers for desalination. J. Am. Chem. Soc., 2015; 137: 6999-7002.

[14] Qadir, N., Said, S.A., Bahaidarah H.M., Structural stability of metal organic frameworks in aqueous media–controlling factors and methods to improve hydrostability and hydrothermal cyclic stability, Microporous Mesoporous Mater., 2015; 201: 61-90.

[15] Makal T.A., Wang X., Zhou H.C., Tuning the moisture and thermal stability of metal–organic frameworks through incorporation of pendant hydrophobic groups.

Cryst. Growth Des., 2013; 13: 4760-4768.

[16] Huang G., Yang Q., Xu Q., Yu S.H., Jiang H.L., Polydimethylsiloxane coating for a palladium/MOF composite: highly improved catalytic performance by surface hydrophobization. Angew. Chem., 2016; 128: 7505-7509.

[17] Yang C., Kaipa U., Mather Q.Z., Wang X., Nesterov V., Venero A.F., Omary M.A., Fluorous metal–organic frameworks with superior adsorption and hydrophobic properties toward oil spill cleanup and hydrocarbon storage. J. Am. Chem. Soc., 2011; 133: 18094-18097.

Chapter 6: Superwetting ZIF−OA coated Janus membrane

6.1 Introduction

Janus is the god of transitions and dualities in ancient Roman myth and is depicted as having two faces-one facing the past, and one facing the future. [1, 2] In materials science, the term “Janus materials” refer to materials with asymmetric structures or properties on two sides, such as Janus particles [3], Janus nanosheets [4], and Janus membranes [5, 6]. Janus materials have attracted great research interest for various applications, such as sensors [7], fog collection [8], and advanced separations [9-11]. Among Janus materials, Janus membranes with asymmetric chemico-physical properties, such as wettability [12, 13] and charge property [14, 15], have gained enormous attention in the latest decade.

Janus membranes with asymmetric wettability on two faces have shown great promise in realizing advanced separations due to their unique unidirectional solute transport performance [5, 6, 16]. In fact, the unidirectional solute transport phenomenon can be widely found in nature [17]. An intriguing example is the desert beetle, which has a patterned hydrophobic and hydrophilic microstructure on its back, showing a unique ability to capture water from humid air [18]. Another example is provided by spider silk, which collects water drops from the air through a periodic joint/spindle-knot structure [1, 18]. Inspired by the characteristics of these natural creatures, a variety of

Janus membranes with asymmetric wettability have been developed to realize the unidirectional transport of solutes.

Based on preparation materials, Janus membranes that have been developed so far can be divided into three major categories: polymeric Janus membrane [2, 14, 17], inorganic Janus membrane [13], and polymeric-inorganic hybrid Janus membrane [10]. Reported preparation methods toward these Janus membranes can be classified into two categories: asymmetric fabrication and asymmetric modification. Asymmetric fabrication refers to those methods in which each side of the Janus membrane is fabricated respectively and then combined together, such as direct integration [19], sequential electrospinning [20], and sequential vacuum filtration [21]. Asymmetric modification refers to methods in which one side or each side of the Janus membrane is post-modified separately, such as single-side spray coating [22], electro-deposition [23], UV-degradation [24], and plasma activation [25]. Despite being efficient in fabricating various Janus membranes, most reported methods either rely on expensive devices, or involve high preparation temperature or multiple steps. Therefore, a facile and rapid method with low energy consumption is still highly required to obtain a high-performance Janus membrane.

6.2 Morphology and structure of ZIF−OAs coated Janus membrane

6.2.1 Contra-diffusion method for ZIF−OAs coated membrane

In this chapter, a contra-diffusion assisted oil/water interfacial fabrication method is

firstly developed to obtain Janus membrane with asymmetric wettability. In the fabrication process, the water phase containing metal ions and the oil phase containing organic ligands were added in a contra-diffusion [26] device, facing each side of a support membrane. As shown in Figure 6.1, a piece of microporous nylon membrane substrate was fixed between two contra-diffusion cells. One of the diffusion cells was filled with an aqueous solution of Zn $(NO_3)_2 \cdot 6H_2O$, while the other cell was filled with an oleic acid solution of 2-methylimidazole. The coordination interaction between zinc ions and 2-methylimidazole linkers occurred when the water phase and the oil phase contacted at the oil/water interface, forming ZIF nanostructures on the membrane surface.

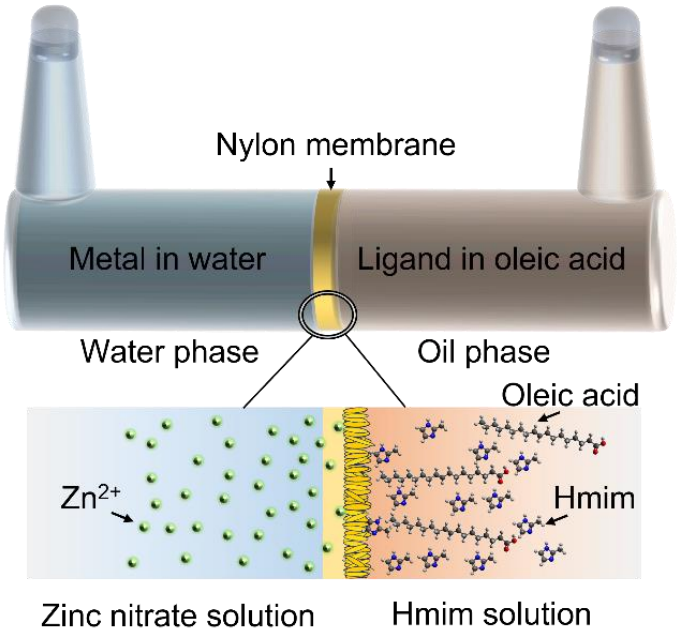

Figure 6.1. Schematic illustration of the preparation of ZIF−OAs coated membrane by

a contra-diffusion assisted oil/water interfacial preparation method

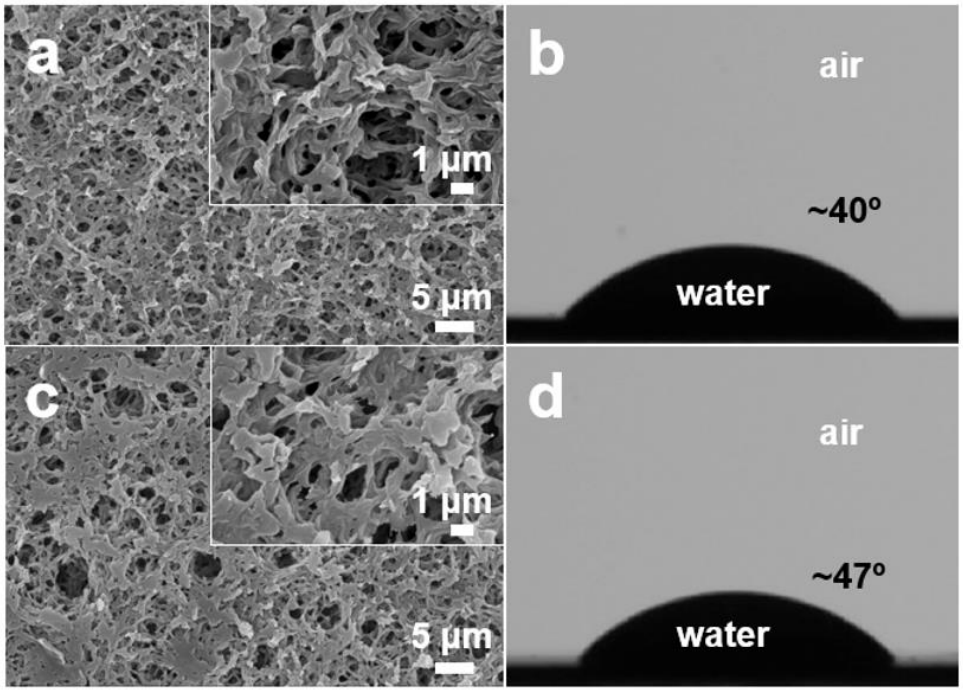

Figure 6.2. SEM images and water contact angles of (a), (b) top surface, and (c), (d) bottom surface of the bare Nylon support

Interestingly, selective growth of MOF crystals on the membrane surface was achieved by simply changing the adding sequence of the water phase and organic phase. During the membrane fabrication process, the prewetting procedure is crucial as it determines the selective growth of ZIFs crystals on the membrane surface. As shown in Figure 6.2, the bare nylon membrane substrate has a porous surface morphology on both sides. In addition, both surfaces are hydrophilic with water contact angles ~40 ± 2º. When the porous membrane is prewetted by the oil phase first, ZIFs crystals selectively grow on the membrane surface facing the water phase (Figure 6.3a, c). This is because the membrane pores/channels were pre-filled with the oleic acid solution, leading to the

formation of the oil/water interface near the membrane surface facing the water phase. The oil/water interface is where Zn $(NO_3)_2 \cdot 6H_2O$ and 2-methylimidazole contact and the crystallization occurs. Water contact angle (WCA) measurements showed that the as-prepared membrane has hydrophilic surfaces on both sides with WCAs of ~ 40 ± 2º (Figure 6.3b, d).

In contrast, when the porous membrane is prewetted by the water phase first, ZIFs crystals selectively grow on the membrane surface facing the oil phase (Figure 6.4a, c). This is because the membrane pores/channels were pre-filled with a water solution, leading to the formation of the oil/water interface near the membrane surface facing the oil phase. SEM images of the as-prepared membrane showed that the membrane surface facing the oil phase was fully covered by crystals (Figure 6.4a), while no crystals were found on the membrane surface facing the water phase (Figure 6.4c).

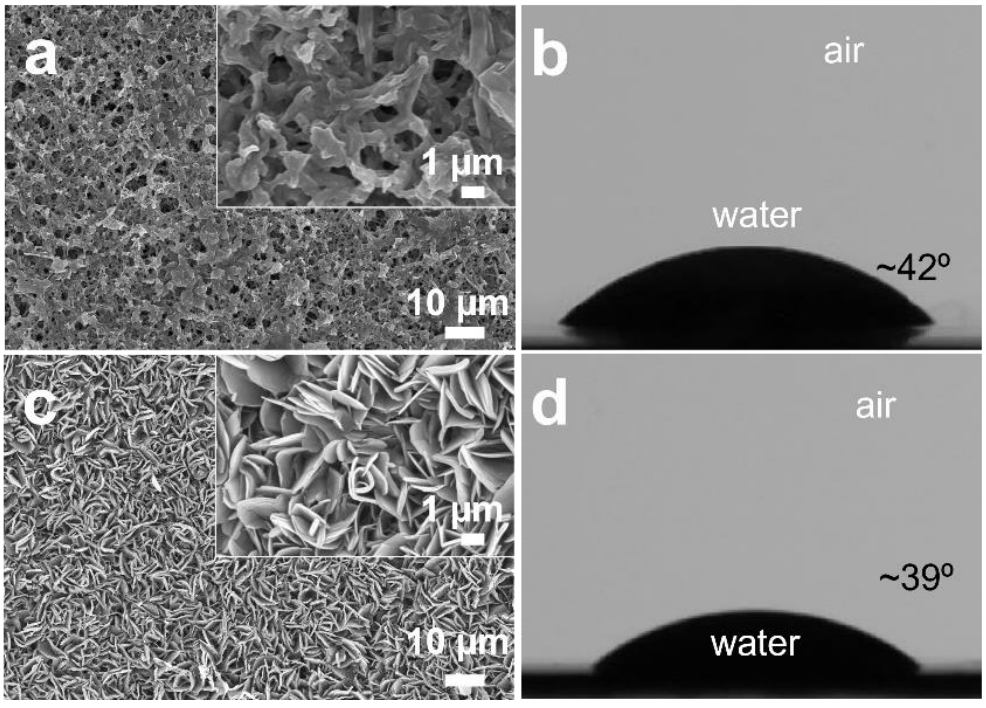

Figure 6.3. SEM images and water contact angles of (a), (b) the membrane surface facing the ligand solution (oil phase), and (c), (d) the membrane surface facing the metal solution (water phase).

Interestingly, water contact angle measurements showed that the as-prepared membrane had asymmetric surface wetting property on both sides. One of the membrane surfaces was highly hydrophobic with a WCA ~141º, while the other membrane surface was hydrophilic with a WCA ~38º.

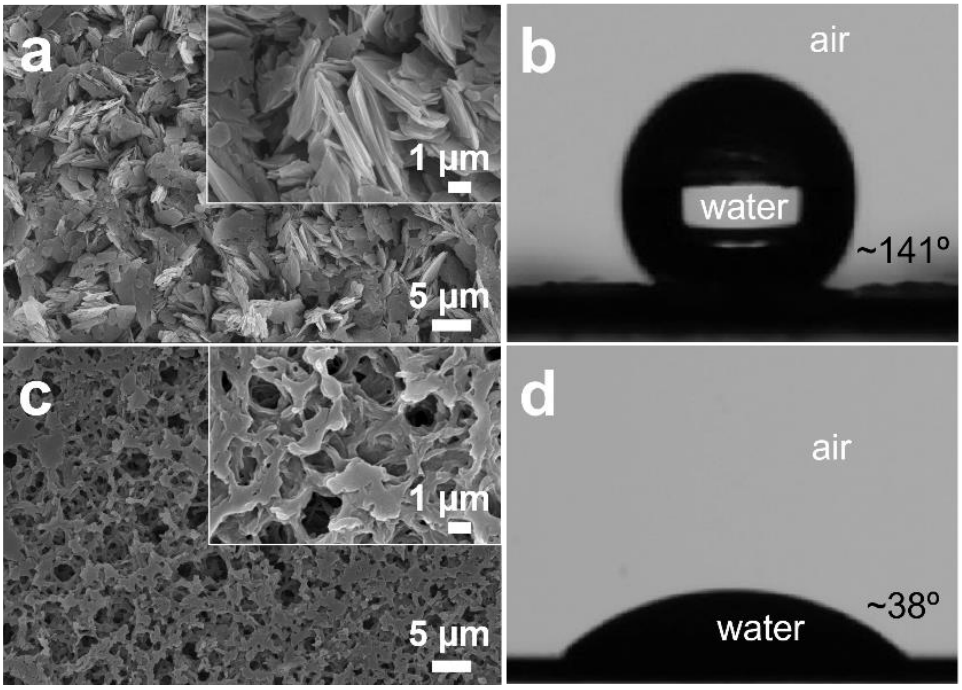

Figure 6.4. SEM images and water contact angles of (a), (b) the membrane surface facing the ligand solution (oil phase), and (c), (d) the membrane surface facing the metal solution (water phase).

The Janus surface wetting property of the prepared membrane suggested that they have

the potential to be employed for efficient liquid separation [5, 6, 16]. To evaluate the applicability of the prepared membrane for liquid separations, the stability of the membrane under a liquid environment was firstly tested.

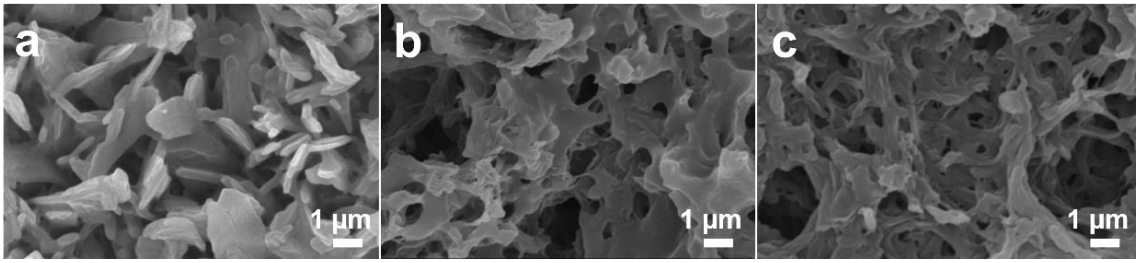

Figure 6.5. SEM images of (a) the ZIF−OAs coated membrane surface, and after soaked in (b) deionized water for 24 h, (c) methanol for 24 h.

The stability of the membrane under a liquid environment was tested by immersing the membrane in different solvents for 24 h and then monitoring the surface morphology changes. As shown in Figure 6.5, the ZIFs structures on the membrane surface (Figure 6.5a) were absent after being soaked in deionized water (Figure 6.5a) and methanol (Figure 6.5c) for 24 h. This indicated that the Janus membrane prepared using the contra-diffusion method had insufficient stability under both water environment and organic solvent environment. Therefore, despite their interesting Janus surface property, as-prepared membranes were not applicable for liquid separations due to insufficient long-term stability.

6.2.2 Drop-casting method for ZIF−OAs coated membrane

Alternatively, a simple drop-casting method was designed to prepare ZIF−OAs coated

membranes. As shown in Figure 6.6, a porous nylon membrane with a pore size of ~200 nm and a diameter of ~47 mm was employed as the support. Prior to the casting process, the nylon membrane was immersed in Zn $(NO_3)_2.6H_2O$ aqueous solution (1M) for 1 h. Then aqueous solution of Zn $(NO_3)_2.6H_2O$ (1.5 mL) was preferentially cast onto the nylon membrane surface, followed by the casting of oleic acid solution (0.2 mL) containing 2-methylimidazole ligands. Then the membranes were cured for 12 h under room temperature and 50 °C, respectively, to obtain different ZIF−OA nanostructures on the membrane surfaces. Then surface morphologies of membrane surfaces were observed using SEM (Figure 6.7a-c).

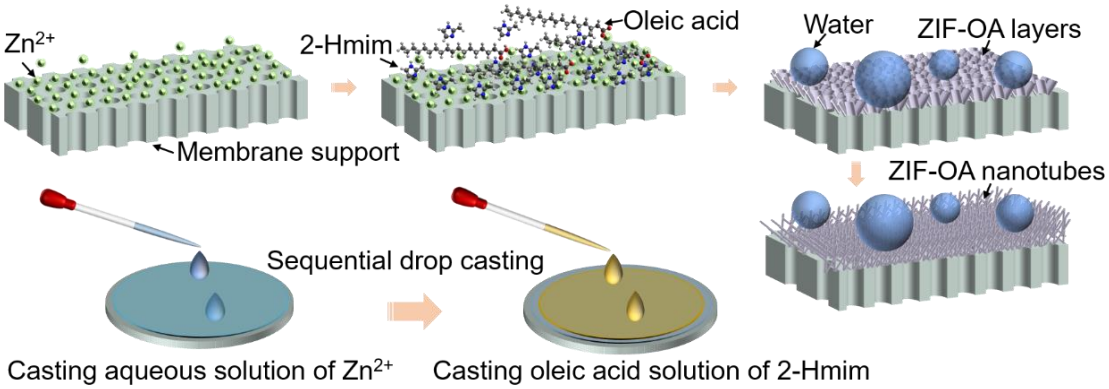

Figure 6.6. Schematic illustration showing the fabrication of Janus membrane with asymmetric wettability by a simple sequential drop-casting process.

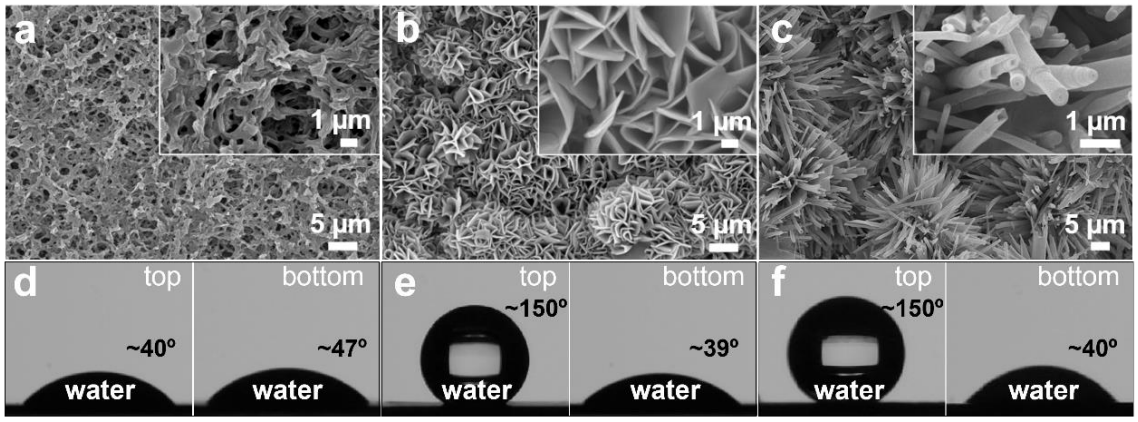

Figure 6.7. (a) SEM images of the bare nylon membrane surface; (b) SEM images of the membrane surface prepared by sequential drop-casting under room temperature; (c) SEM images of the membrane surface prepared by sequential drop-casting under 50 ℃; (d) WCA of top and bottom surfaces of the bare nylon membrane; (e) WCA of top and bottom surfaces of the ZIF−OA layers coated membrane; (f) WCA of top and bottom surfaces of the ZIF−OA nanotubes coated membrane.

As shown in Figure 6.7a, the pristine nylon membrane substrate showed a porous, rough surface. After the sequential drop-casting process under room temperature, the membrane surface was uniformly covered by a layer of 2D ZIF−OA structures (Figure 6.7b). After the sequential drop-casting process under 50 ℃, the membrane surface was covered by 1D ZIF−OA structures with a tubular morphology (Figure 6.7c). These SEM observation results confirmed that this simple sequential drop-casting method was effective for preparing ZIF−OA coated membranes. Surface properties of membrane surfaces were determined by performing water contact angle measurements. As shown in Figure 6.7d, the pristine porous nylon membrane showed hydrophilic surfaces on

both sides, with a WCA of ~40º and ~47º, respectively. After the sequential drop-casting process, the ZIF−OAs coated membranes exhibited asymmetric wettability with one surface showing superhydrophobic property (WCA up to ~150º) while the other surface showing hydrophilic property (WCA of ~40º), as presented in Figure 6.7e and f. Such asymmetric wettability indicated that the ZIF−OAs coated membranes exhibited Janus wetting property, which is beneficial for selective liquid separations.

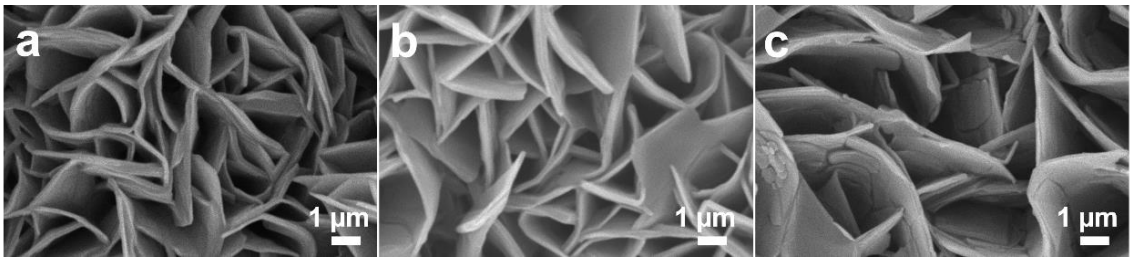

Figure 6.8. SEM images of (a) the ZIF−OAs coated membrane surface, and after soaked in (b) deionized water for 3 days, (c) methanol for 3 days.

To apply the prepared membranes for liquid separations, the stability of the membrane under a liquid environment is essential and has to be taken into consideration. Therefore, the stability of the membrane under a liquid environment was firstly tested by immersing the membrane in different solvents and monitoring the surface morphology changes. As shown in Figure 6.8, the ZIFs structures on the membrane surface (Figure 6.8a) were nearly unaffected after being soaked in deionized water (Figure 6.8a) and methanol (Figure 6.8c) for up to 3 days. This indicated that the Janus membrane prepared using the sequential drop-casting method had satisfactory stability under both water environment and organic solvent environment.

6.3 Molecular separation performance

The ZIF−OAs coated membrane prepared by the sequential drop-casting method was applied for molecular separation tests in organic solvent (methanol). The permeance of the membrane was determined by calculating the volume of methanol permeate per unit time. Meanwhile, the separation performance of the membrane was estimated using different organic dye molecules, including rose bengal (RB, MW = 1017.6 g mol^{-1}) and reactive black 5 (RB5, MW = 992 g mol^{-1}), The concentration of dye molecules in the solutions before and after the filtration tests was estimated by UV-Vis spectroscopy. As shown in Figure 6.9, the ZIF−OAs coated membrane prepared in this chapter was effective for separating organic dye molecules such as RB and RB5 from organic solvents like methanol.

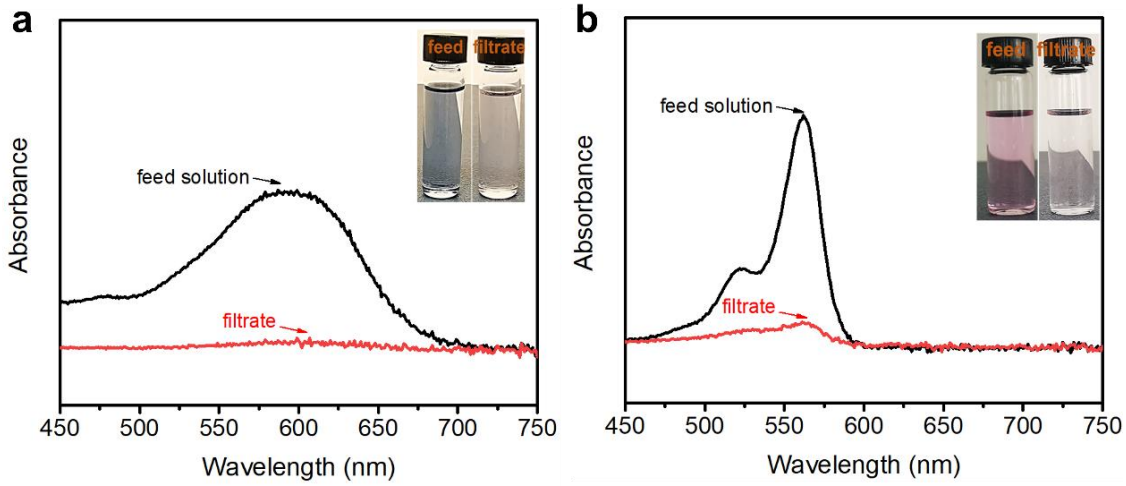

Figure 6.9. UV-Vis spectra of 5 mg L^{-1} of (a) Reactive black 5 solution, and (b) Rose bengal solution before and after filtration through the ZIF−OAs coated membrane. The insets show corresponding pictures of the solutions.

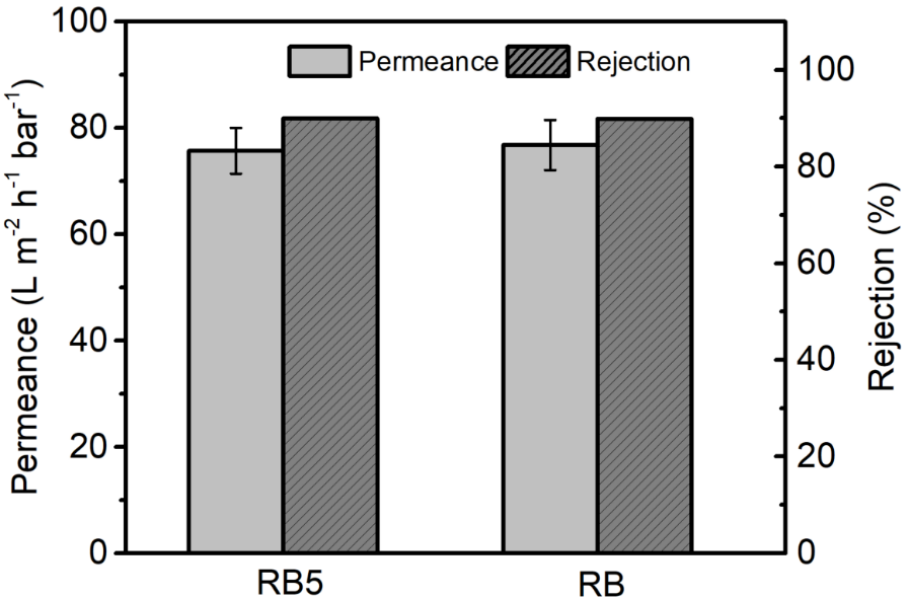

Figure 6.10. Permeance and rejection of the ZIF−OAs coated membrane for reactive black 5 (RB5) and rose bengal (RB) molecules.

The membrane permeances, as well as calculated dye rejections, are presented in Figure 6.10. As can be seen in Figure 6.10, the ZIF−OAs coated membrane exhibited ~90% rejections for reactive black 5 and rose bengal molecules in methanol, with permeances of ~75 ± 5 L m^{-2} h^{-1} bar^{-1}.

6.4 Summary

In this chapter, a contra-diffusion assisted oil/water interfacial preparation method and a sequential drop-casting method were designed to prepare ZIF−OAs coated

membranes. The prepared ZIF−OAs coated membranes showed interesting Janus surface wetting properties. The main results can be summarized as:

(1) In the contra-diffusion assisted oil/water interfacial preparation method, selective crystal growth on the membrane surface was achieved by simply changing the adding sequence of the water phase and organic phase into the diffusion cells. Especially, when the membrane was prewetted by the water phase first, ZIF nanostructures selectively grow on the membrane surface facing the oil phase. As-prepared membrane showed interesting Janus surface wetting property with one side hydrophilic (WCA of ~38º ± 2º), while the other side is highly hydrophobic (WCA of ~141º ± 2º). However, the membrane showed insufficient stability under both water environment and organic solvent environment.

(2) In the sequential drop-casting method, the prepared membrane surface was uniformly covered by two-dimensional ZIF layers when the membrane was cured under room temperature. When the membrane was cured under 50 °C, the membrane surface was covered by one-dimensional ZIF nanotubes. The prepared membranes showed Janus surface wetting property with one surface hydrophilic (WCA of ~40º ± 2º) while the other surface superhydrophobic (WCA of ~150º ± 2º). More importantly, the prepared membranes showed satisfactory stability under a liquid environment, with their surface morphology unaffected after being soaked in water and methanol for up to 3 days.

(3) The ZIF−OAs coated membrane prepared using the sequential drop-casting method was applied for dye molecules rejection from an organic solvent. The membrane was effective for organic dye molecules separation from methanol, with rejections above 90% and a permeance of ~75 ± 5 L m^{-2} h^{-1} bar^{-1}.

6.5 References

[1] Hui Z., Guo Z., Superwetting Janus membranes: focusing on unidirectional transport behaviors and multiple applications, J. Mater. Chem. A., 2019; 7: 12921-12950.

[2] Li T., Liu F., Zhang S., Lin H., Wang J., Tang C. Y., Janus polyvinylidene fluoride membrane with extremely opposite wetting surfaces via one single-step unidirectional segregation strategy, ACS Appl. Mater. Interfaces., 2018; 10: 24947-24954.

[3] Xie Q., Davies G. B., Harting J., Direct assembly of magnetic Janus particles at a droplet interface, ACS Nano., 2017; 11: 11232-11239.

[4] Luo D., Wang F., Vu B. V., Chen J., Bao J., Cai D., Willson R. C., Ren Z., Synthesis of graphene-based amphiphilic Janus nanosheets via manipulation of hydrogen bonding, Carbon., 2018: 126; 105-110.

[5] Yang J., Liu P., He X., Hou J., Feng Y., Huang Z., Yu L., Li L., Tang Z, Photodriven active ion transport through a Janus microporous membrane. Angew Chem Int Ed., 2020; 59: 6244-6248.

[6] Yang H. C., Hou J., Chen V., Xu Z. K., Janus membranes: exploring duality for advanced separation, Angew Chem Int Ed., 2016: 55: 13398-13407.

[7] Han H., Baik S., Xu B., Seo J., Lee S., Shin S., Lee J., Koo J. H, Mei Y., Pang C., Lee. C., Bioinspired geometry-switchable Janus nanofibers for eye-readable H_2 sensors, Adv. Funct. Mater., 2017; 27: 1701618.

[8] Xu Chen., Feng R., Song F., Wang X. L., Wang Y. Z., Desert beetle-inspired

superhydrophilic/superhydrophobic patterned cellulose film with efficient water collection and antibacterial performance, ACS Sustain. Chem. Eng., 2018; 6: 14679-14684.

[9] Lee Y.S., Kang B. K., Han N., Lee H. J., Choi W. S., An anti-overturn Janus sponge with excellent floating stability for simultaneous pollutant remediation and oil/water separation. J. Mater. Chem. A., 2018; 6: 16371-16381.

[10] Pan T. D., Li Z. J., Shou D. H., Shou W., Fan J. T., Liu X., Liu Y., Buoyancy assisted Janus membrane preparation by ZnO interfacial deposition for water pollution treatment and self-cleaning, Adv. Mater. Interfaces, 2019; 6: 1901130.

[11] Yang H. C., Hou H., Chen V., Xu Z. K., Janus membranes: exploring duality for advanced separation, Angew Chem Int Ed., 2016; 55: 13398-13407.

[12] Yang X., Yan L., Ran F., Pal A., Long J., Shao L., Interface-confined surface engineering constructing water-unidirectional Janus membrane, J. Membr. Sci., 2019; 576: 9-16.

[13] Hou L., Wang N., Man X., Cui Z., Wu J., Liu J., Li S., Gao Y., Li D., Jiang L., Zhao Y., Interpenetrating janus membrane for high rectification ratio liquid unidirectional penetration, ACS Nano, 2019; 13: 4124-4132.

[14] Liu S., Wu C., Hung W.S., Lu X., Lee K. R., One-step constructed ultrathin Janus polyamide nanofilms with opposite charges for highly efficient nanofiltration, J. Mater. Chem. A., 2017; 5: 22988-22996.

[15] Yu L., Zhang Y., Xu L., Liu Q., Borjigin B., Hou D., Xiang J., Wang J., One step prepared Janus acid-resistant nanofiltration membranes with opposite surface charges

for acidic wastewater treatment, Sep. Purif. Technol., 2020; 250: 117245.

[16] Li H. N., Yang J., Kang Z., Asymmetric surface engineering for Janus membranes, Adv. Mater. Interfaces, 2020; 7: 1902064.

[17] Fu C., Gu L., Zeng Z., Xue Q., Simply adjusting the unidirectional liquid transport of scalable Janus membranes toward moisture-wicking fabric, rapid demulsification, and fast oil/water separation, ACS Appl. Mater. Interfaces, 2020; 12: 51102-51113.

[18] Zheng Y., Bai H., Huang Z., Tian X., Nie F. Q., Zhao Y., Zhai J., Jiang L., Directional water collection on wetted spider silk. Nature, 2010; 463: 640-643.

[19] Wang H., Zhou H., Niu H., Zhang J., Du Y., Lin T. Dual-layer superamphiphobic/superhydrophobic-oleophilic nanofibrous membranes with unidirectional oil-transport ability and strengthened oil–water separation performance, Adv, Mater, Interfaces, 2015; 2: 1400506.

[20] Yang J., Wen G., Gou X., Song H., Guo Z., A study on the manufacture of Kevlar membrane modified by inorganic nanoparticles with universal applicability in separating diffident types of emulsions, J. Membr. Sci., 2018; 563: 326-335.

[21] Song H. M., Chen C., Shui X. X., Yang H., Zhu L. J., Zeng Z.X., Xue Q.J., Asymmetric Janus membranes based on in situ mussel-inspired chemistry for efficient oil/water separation, J. Membr. Sci., 2019; 573: 126-134.

[22] Luo Z.Y., Lyu S. S., Fu Y. X., Heng Y., Mo D.C., The Janus effect on superhydrophilic Cu mesh decorated with Ni-NiO/Ni $(OH)_2$ core-shell nanoparticles for oil/water separation, Appl. Surf. Sci., 2017; 409: 431-437.

[23] Waldman R. Z., Yang H. C., Mandia D. J, Nealey P. F., Elam J. W., Darling S. B.,

Janus membranes via diffusion-controlled atomic layer deposition, Adv. Mater. Interfaces, 2018; 5: 1800658.

[24] Wang Z., Wang Y., Liu G., Rapid and efficient separation of oil from oil-in-water emulsions using a Janus cotton fabric, Angew. Chem., 2016; 128: 1313-1316.

[25] Ma W., Zhang M., Li Y., Kang M., Huang C., Fu G., Flexible, durable and magnetic nanofibrous membrane with pH-switchable wettability for efficient on-demand oil/water separation, Environ. Sci. Nano, 2019; 6: 3699-3711.

[26] Yao J., Dong D., Li D., He L., Xu G., Wang H., Contra-diffusion synthesis of ZIF-8 films on a polymer substrate, Chem. Comm., 2011; 47: 2559-2561.

Chapter 7: Lamellar membranes for molecular separation[2]

7.1 Introduction

2D nanomaterial-based membranes, also known as lamellar membranes [1], are usually fabricated via the layer-by-layer stacking of ultrathin 2D nanosheets [2], such as graphene oxide (GO) [3-5], metal-organic frameworks (MOFs) [6], covalent organic frameworks (COFs) [7], MXenes [8, 9], and graphitic carbon nitride (g-C_3N_4) nanosheets [10]. These multilayered stacking membranes hold great promise for ultrafast molecular filtration applications due to their minimized molecular transport resistance and controllable channel size formed between adjacent nanosheets [11, 12]. In the recent decade, GO nanosheet-based membranes have attracted extra attention [13-15] as their permeability and selectivity could be controlled by the rational manipulation of the nanochannels (or interlayer spacing) between adjacent GO nanosheets [16]. Intercalation of nanoscale materials into the lamellar GO membrane structures has been widely adopted to control the interlay spacing [17-22]. The resulting GO membranes with expanded interlayer distance exhibit significantly enhanced permeability [20-22]. However, it has still been very challenging to enhance their overall separation efficiency due to the compromised molecular selectivity in the

[2] This chapter has been published in Chemical Engineering Journal 2020;12: 34413-34422.

presence of expanded nanochannels.

Metal-organic frameworks (MOFs), as a new class of crystalline materials with flexible nanostructures, have attracted widespread interest because of the almost infinite tunability of their pore structures and chemical functionalities [23-25]. In the past decades, MOFs have found extensive applications such as catalysis [26], energy storage [27], and gas separations [6]. More importantly, MOFs exhibit superior separation performance for various small molecules [28]. Compared to other traditional nanomaterials, MOFs have a great potential to be an effective intercalating spacer in lamellar GO membranes to alleviate the permeance-rejection trade-off because of their highly uniform and tunable pore structure [29, 30].

In this chapter, a novel facile, direct strategy was designed for the preparation of MOF-intercalated GO membranes with rationally regulated interlayer spacing for unprecedented ultrafast molecular separation. ZIF-8 crystals with a controlled size were formed via *in situ* crystallization between the GO interlayers. More specifically, zinc ions (Zn^{2+}) were captured by GO nanosheets and bonded to the oxygen functional groups on the basal planes increasing the interlayer spacing. Upon introducing organic ligands (2-methylimidazole in this case) into the lamellar GO structures, strong coordination bonds were formed between 2-methylimidazole and the intercalated Zinc ions, leading to the *in situ* crystallization of ZIF-8 nanocrystals and a further expansion of the interlayer spacing. Compared with the direct filtration of GO and MOF mixtures method [18, 19], this *in situ* assembly method promotes a more homogeneous

intercalation of MOFs in GO interlayers. Moreover, it is noteworthy that an asymmetric nanostructure can be formed in these membranes due to a "nutrition gradient" during the assembly process. These ZIF-8 intercalated GO membranes showed greatly enhanced permeability with an ultrahigh acetone permeance of ~10,030 L m^{-2} h^{-1} bar^{-1} and methanol permeance of ~6,816 L m^{-2} h^{-1} bar^{-1} and a dye rejection rate higher than 95% for charged organic dyes (reactive black 5 (RB5) and rose Bengal (RB)), promoting permeability-selectivity anti-trade-off behavior. More interestingly, the membrane showed smart, selective separation performance for various binary dye mixtures.

7.2 Morphology and structure of GO/ZIF-8 membrane

In this work, the pure GO-coated membrane was first fabricated by depositing the single-layered graphene oxide (SLGO) dispersion onto the surface of nylon membrane support. The fabrication process is schematically shown in Figure 7.1a.

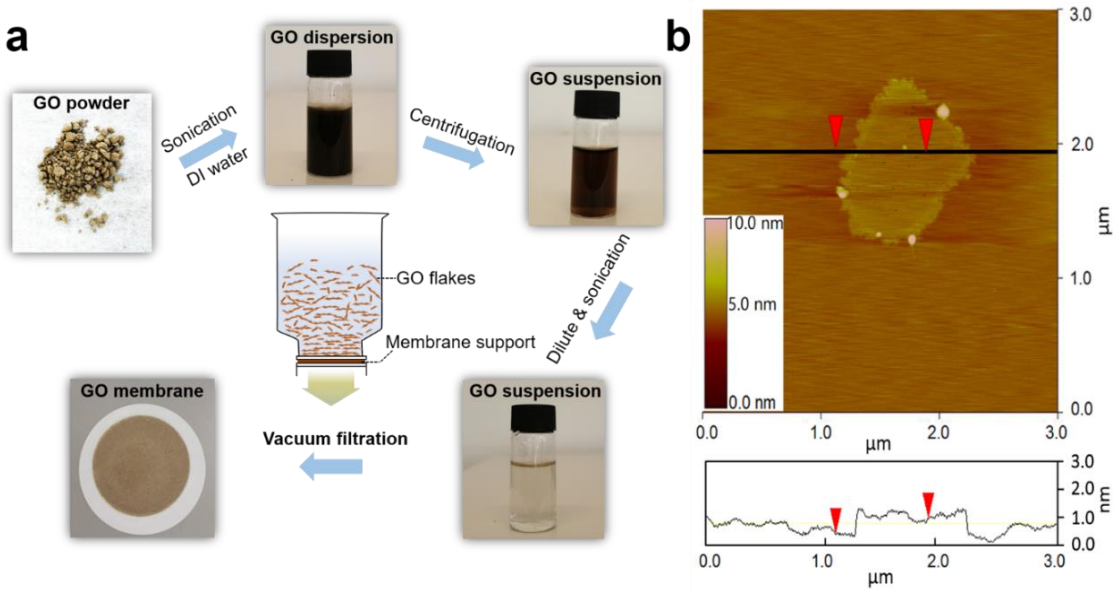

Figure 7.1. (a) Schematic diagram of the fabrication process of GO-coated membrane and (b) AFM image of a GO flake (top) and corresponding height profile across the black line (bottom).

AFM results confirmed that the GO flakes were single layered with a lateral size of ~1 μm and a thickness of ~0.8 nm (Figure 7.1b). The thickness of the GO layer was predicted by UV-Vis Spectroscopy using a pre-calibrated curve of GO concentration vs. absorbance at 600 nm wavelength (Figure 7.2a).

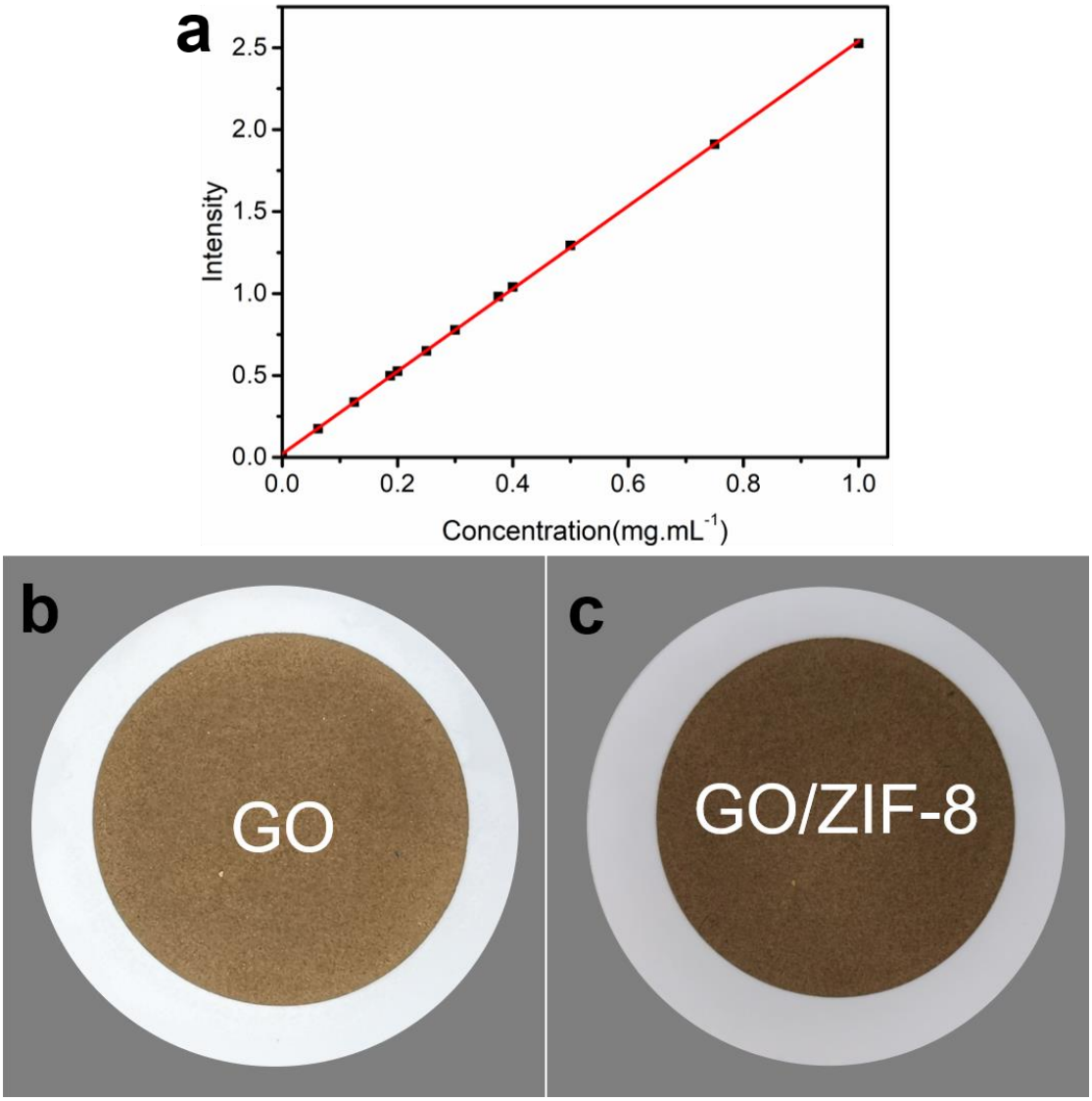

Figure 7.2. (a) The linear correlation between the concentration of GO dispersion and the UV absorbance; (b) a photograph of the GO coated membrane; and (c) a photograph of the as-synthesized GO/ZIF-8 membrane.

GO/ZIF-8 membranes with regulated nanostructures were fabricated using the facile process schematically illustrated in Figure 7.3.

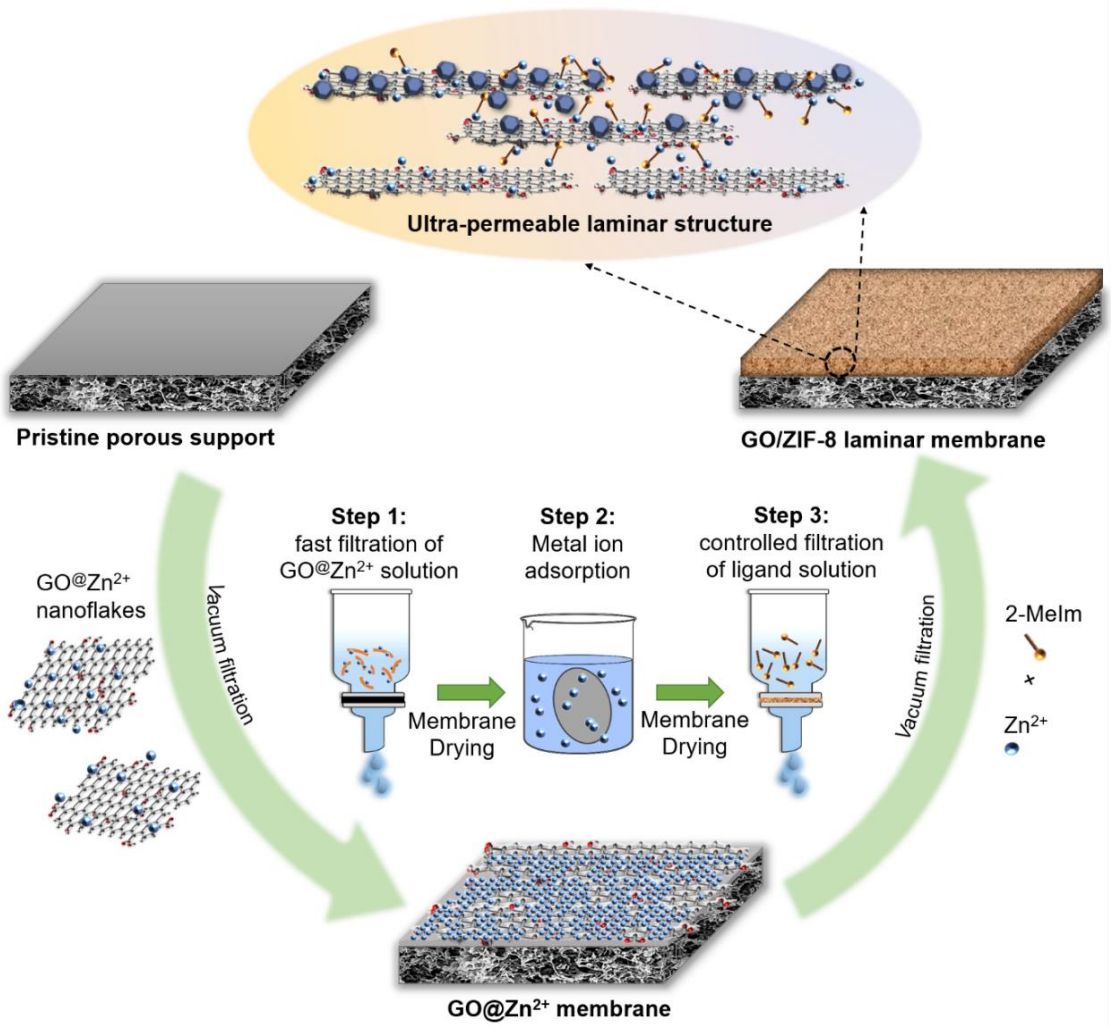

Figure 7.3. Schematic diagram of the fabrication process of the GO/ZIF-8 membrane

A microporous nylon membrane with a pore size of ~ 200 nm was firstly assembled in a Millipore vacuum filtration system. Then a mixture of Zn $(NO_3)_2$•$6H_2O$ and SLGO nanosheets was prepared by vigorous stirring for 1 h under room temperature and then filtrated through the membrane support. A Zn^{2+} intercalated GO membrane was finally prepared because zinc ions can be easily adsorbed on the GO nanosheets and bond to oxygen species (i.e., hydroxyl groups and epoxy groups) on the basal planes and also carboxylic acid groups at the edges, [31-33] leading to the bridging of neighboring GO sheets and enhancement in its mechanical stability. As the number of zinc ions was in

excess in the mixture, the remaining unbound zinc ions were either permeated through the membrane or intercalated in the channel between two adjacent GO sheets, resulting in a further increase of the interlayer spacing. When 2-methylimidazole molecules were slowly filtered through the saturated GO membrane, zinc ions anchored or weakly bonded on the external surface of the GO membrane preferentially reacted with the ligands, forming a thin layer of ZIF-8 film. However, the zinc ions absorbed and intercalated in the underneath lamellar structures were in contact with less concentrated 2-methylimidazole as it permeated through the above-described membrane structures.

The SEM image of the membrane surface (Figure 7.4a, b) and the photograph of the SLGO-coated membrane (Figure 7.2b) reveal that the pristine nylon membrane support, which has a highly porous structure (Figure 7.4a) has been uniformly covered by GO nanosheets (Figure 7.4b). The high-magnification SEM image in the inset of Figure 7.4b shows that the prepared GO membrane has an intact and smooth surface without any pinholes and visible cracks. SEM images of the zinc ion saturated GO membrane (Figure 7.4c) display a similar morphology, indicating that the addition of Zn $(NO_3)_2$•$6H_2O$ in the GO suspension and subsequent soaking treatment has not caused any damage to the membrane integrity.

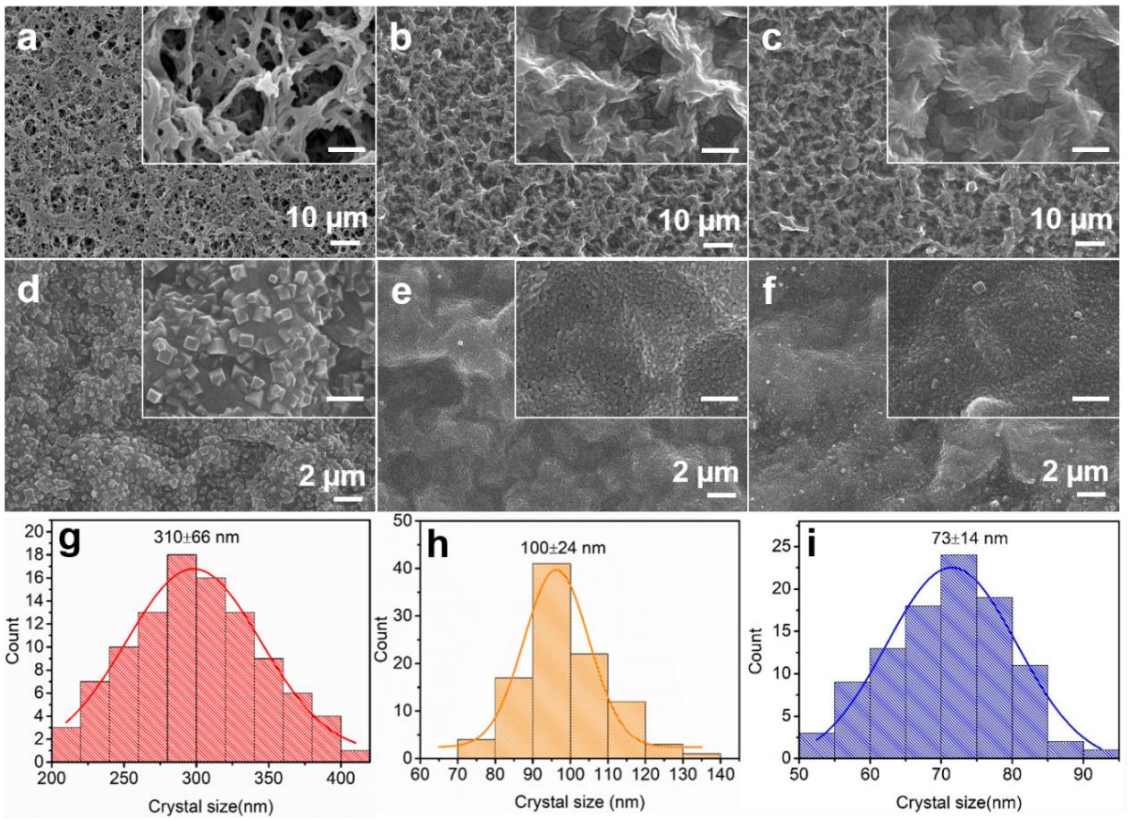

Figure 7.4. SEM images of (a) bare nylon support, (b) GO membrane, (c) GO membrane saturated with Zn^{2+} and GO/ZIF-8 membrane obtained with (d) 0.05 M Zn $(NO_3)_2 \cdot 6H_2O$, (e) 0.25 M $Zn(NO_3)_2 \cdot 6H_2O$ and (f) 0.5 M $Zn(NO_3)_2 \cdot 6H_2O$. Scale bars in insets of (a) to (c) and (d) to (f) are 2 μm and 1 μm, respectively. Crystal size distribution on the surface of GO/ZIF-8 membranes obtained with (g) 0.05 M $Zn(NO_3)_2 \cdot 6H_2O$, (h) 0.25 M $Zn(NO_3)_2 \cdot 6H_2O$ and (i) 0.5 M $Zn(NO_3)_2 \cdot 6H_2O$. The sizes of the crystals were estimated using the Digital Micrograph software

After filtration of the 2-methylimidazole solution, the membrane surface shows a slightly darker color (Figure 7.2c) comparing to the original GO membrane. The SEM image of the membrane surface (Figure 7.4d) shows that the original smooth GO surface was uniformly decorated by large amounts of nanocrystals. The high-

magnification SEM image shown in the inset further reveals that these nanocrystals have a uniform cubic morphology. The formation of ZIF-8 on the membrane surface was also confirmed by the FTIR analysis (Figure 7.5).

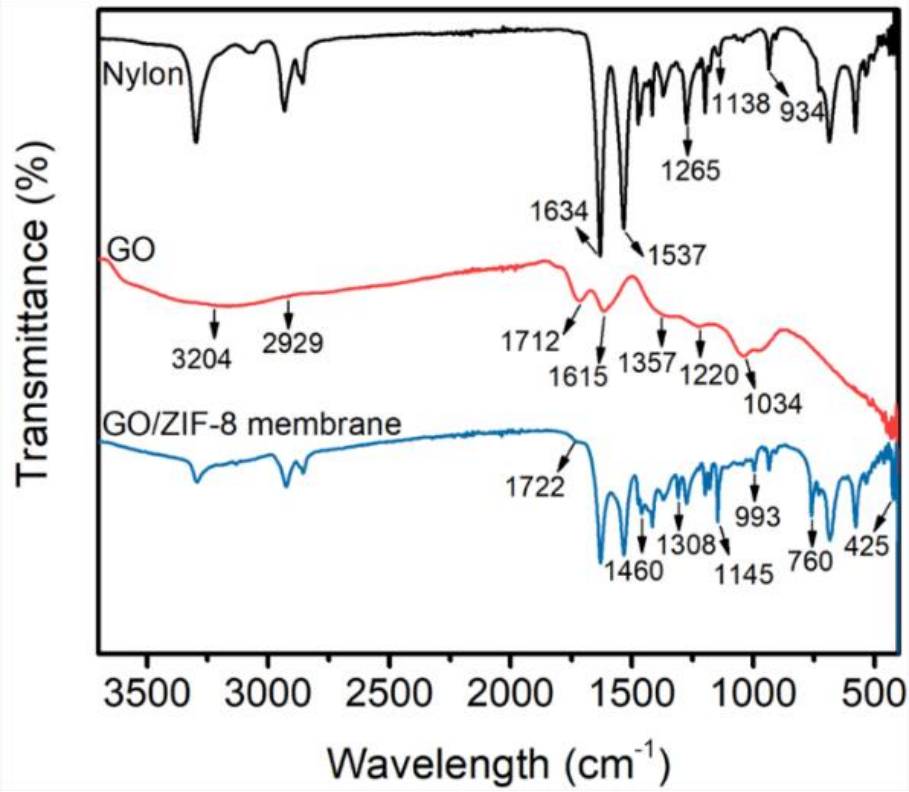

Figure 7.5. FT-IR spectra of the plain nylon membrane, pure GO, and the GO/ZIF-8 membrane

FT-IR spectra of the plain nylon membrane, pure GO, and the GO/ZIF-8 membrane was obtained from Nicolet iS10 FT-IR spectrometer. As shown in Figure S3, in the FT-IR spectrum of plain nylon membrane, the intense peak at 1634 cm^{-1} was ascribed to the vibration of the C−C bond, and the peak at 1537 cm^{-1} was ascribed to C=C vibration. Other peaks at 1265 cm^{-1} and 1138 cm^{-1} corresponded to the vibration of C−N and C−O−C bonds, respectively. The FT-IR spectrum of GO shows an intense peak at 3204

cm^{-1}, which was due to the O-H stretching vibration. Very weak peaks at 2929 cm^{-1} corresponded to the symmetric and asymmetric stretching vibration of $-CH_2-$. The peak at 1712 cm^{-1} was attributed to C=O stretching vibration, and the peak at 1615 cm^{-1} was due to C=C stretching. The peaks at 1357 cm^{-1}, 1220 cm^{-1} and 1034 cm^{-1} could be assigned to the O−H bending, C−O stretching of an epoxy group and C-O stretching of an alkoxy group, respectively. In the FITR spectrum of the GO/ZIF-8 membrane, the peak at 1460 cm^{-1} was due to the C=C vibration, and the weak peak at 1722 cm^{-1} was ascribed to the C=O stretching vibration in the GO skeleton. Compared to pure GO, the C=O stretching vibration in the GO/ZIF-8 membrane was reduced due to the coordination of Zn^{2+} with carboxyl groups on the edges of the GO sheets. The peaks located in the range from 1308 cm^{-1} to 993 cm^{-1} were due to the in-plane bending vibration of the imidazole ring from the ZIF-8. The peaks at 760 cm^{-1} and 425 cm^{-1} were assigned to the vibration of Zn-O and Zn-N bonds in ZIF-8 crystals, respectively.

Interestingly, it was found that the number and size of nanocrystals generated on the membrane surface can be varied by simply changing the concentration of Zn $(NO_3)_2 \cdot 6H_2O$ added in the GO dispersion. GO/ZIF-8 membranes prepared by increasing the Zn $(NO_3)_2 \cdot 6H_2O$ concentration to (0.25 M) and (0.5 M) are presented in Figure 7.4e and Figure 7.4f, respectively. It was observed that denser packing of nanocrystals was generated by increasing the Zn $(NO_3)_2 \cdot 6H_2O$ concentration, while the crystal size was decreased as confirmed by the crystal size distribution measurement. The size of the nanocrystals was determined by performing a statistic analysis using the

Digital Micrograph software. As shown in Figure 7.4g-i, when 0.05 M, 0.25 M, and 0.5 M of Zn $(NO_3)_2$•$6H_2O$ was used, the crystal size was ~310 nm, ~100 nm, and ~75 nm, respectively.

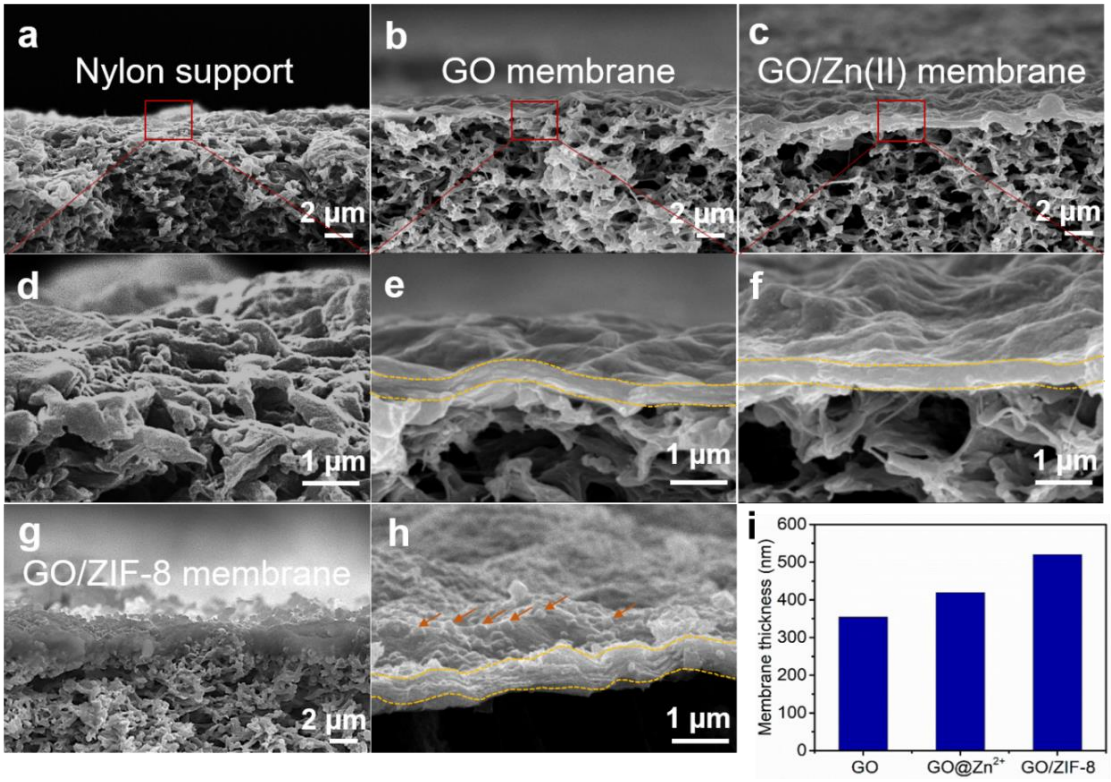

Figure 7.6. Cross-sectional SEM images of bare nylon support (a) and (d), GO coated membrane (b) and (e), GO@Zn^{2+} membrane (c) and (f) and GO/ZIF-8 membrane (g) and (h), and membrane thickness of different membranes (i). Arrows in (h) show some ZIF-8 crystals on the membrane surface.

To further analyze the nanostructures of as-synthesized GO/ZIF-8 membranes, cross-sectional morphologies were also studied in detail using SEM. As shown in Figure 7.6a, d, the pristine membrane substrate has a rough and porous microstructure, while the GO membrane shows an ultrathin GO layer deposited on the top surface (Figure 7.6b,

e). After saturation by zinc ions, the membrane shows no obvious change (Figure 7.6c, f) except for a slight increase in the top layer. After filtration of the 2-methylimidazole, scattered nanocrystals were formed on the membrane surface with further increased thickness (Figure 7.6g, h). As shown in Figure 7.6i, the pure GO membrane has a layer of SLGO nanosheets with a thickness of ~370 nm on the top surface. The thickness was slightly increased to ~400 nm for GO@Zn^{2+} membrane, further confirming the successful intercalation of Zn^{2+} in the GO structures. It has been reported that zinc ions can easily induce the ring-opening of epoxides on GO nanosheets, forming abundant extruding C-OH moieties. The newly generated C-OH moieties, together with the in-plane carbonyl groups, further facilitate the intercalation of zinc ions into the membrane nanostructures, thus leading to an increase in the interlayer spacing [31]. In the following course of 2-methylimidazole filtration, the zinc ions, which were adsorbed in the membrane surface or the several top layers of SLGOs, quickly coordinate with the organic linkers, triggering in-situ crystallization of ZIF-8 nanocrystals. The change of the interlayer spacing in the membrane before and after the formation of ZIF-8s was characterized by performing XRD measurements (Figure 7.7). The crystalline structure of nylon membrane support, GO coated nylon membrane and GO/ZIF-8 coated nylon membrane were determined by X-ray diffractometer (XRD, Bruker D8 Advance) with Cu Kα radiation (λ=1.54 Å) in a 2θ range of 5.0° ~ 40.0°. In the XRD pattern of nylon membrane support, intense peaks at 2θ = 14.0° and 2θ = 16.8° were recorded. These two peaks were maintained in the patterns for both GO coated membrane and GO/ZIF-8 coated membrane. Apart from peaks from the support, the GO coated membrane also

showed a weak diffraction peak at 2θ = 11.9°, corresponding to an interlayer distance of 7.4 Å. As shown in Figure 7.7, in the XRD pattern of GO/ZIF-8 coated membrane, the diffraction peak at 2θ = 10.9° was attributed to the GO coating, which corresponded to an interlayer distance of 8.1 Å. The diffraction peaks at 2θ = 7.3°, 10.4°, 12.7°, 14.8°, and 18.0° corresponded to the characteristic peaks of ZIF-8.

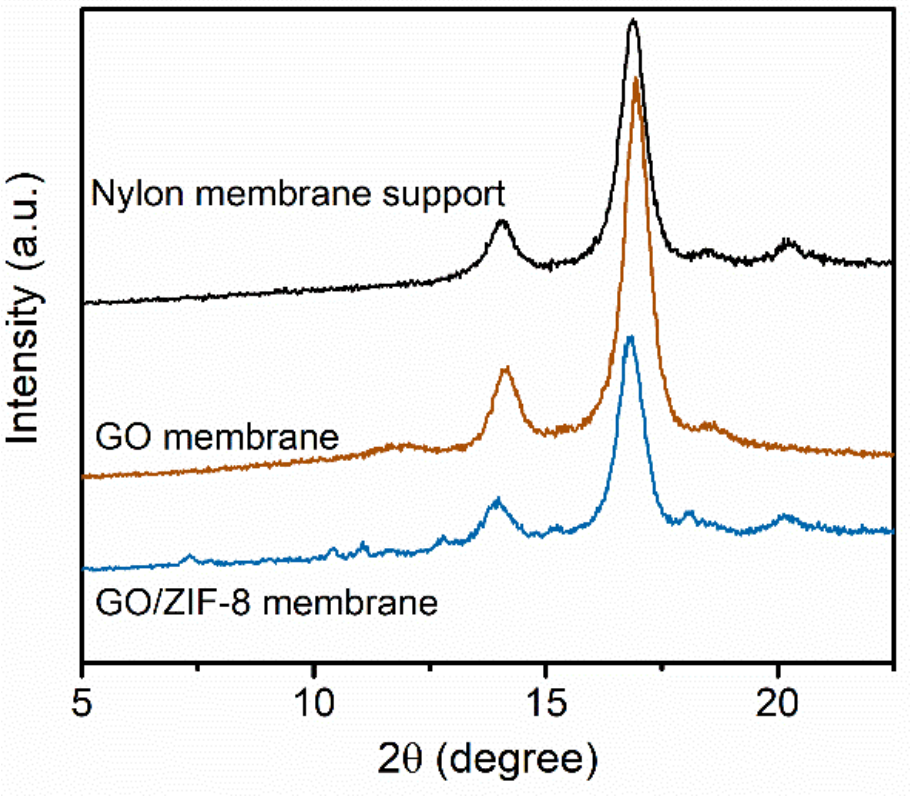

Figure 7.7. XRD spectra of the nylon membrane, GO coated membrane, and GO/ZIF-8 membrane

Different from the direct filtration of mixed GO nanosheets and MOF nanoparticles dispersion [29, 30], this *in situ* assembly process promoted the formation of a "three-region" asymmetric nanostructure in the membrane. On the membrane surface ("region

I"), it is clear to see that a thin film of ZIF-8 crystals was formed (Figure 7.4d−f and Figure 7.6h). As discussed earlier in this work, the zinc ions intercalated in the underneath layered structures were getting in contact with less concentrated 2-methylimidazole, which permeated through the above-layered structures. Therefore, smaller crystals followed by fewer crystalline domains were likely to form in the successive underneath GO interlayers ("region II") because a diffusion/sorption-controlled ligand concentration gradient was generated between the top membrane surface and bottom polyamide substrate. In principle, the region further from the top of the membrane surface was in contact with less concentrated 2-methylimidazole, as the later was gradually being consumed and coordinated in the above membrane layers to form ZIF nanograins or semi-crystalline gel domains. Therefore, it is reasonable to assume that in the bottom GO membranes ("region III") the intercalated Zn^{2+} were only simply coordinated with 2-methylimidazole ligands, forming non-crystalline species between the neighboring GO nanosheets, as opposed to crystals on the membrane surface. This hypothesis was confirmed by the cross-sectional SEM image of the membrane (Figure 7.6h) showing no visible nanocrystals formed near the bottom regions of the GO membranes, even when the concentration of Zn^{2+} was increased 10-fold, from 0.05 M to 0.5 M. However, the co-existence of these intercalating materials in the different regions of the membrane not only regulate well the entire membrane nanostructures but also expand the original GO structure significantly. The thickness of the resulting membrane increased from ~400 nm to ~520 nm, almost 1.5 times thicker than that of the starting pure GO membrane. With expanded nanochannels in the GO

layers and abundant effective intercalated spacer materials, the GO/ZIF-8 membranes exhibited highly efficient molecular filtration with superior permeation and rejection rates.

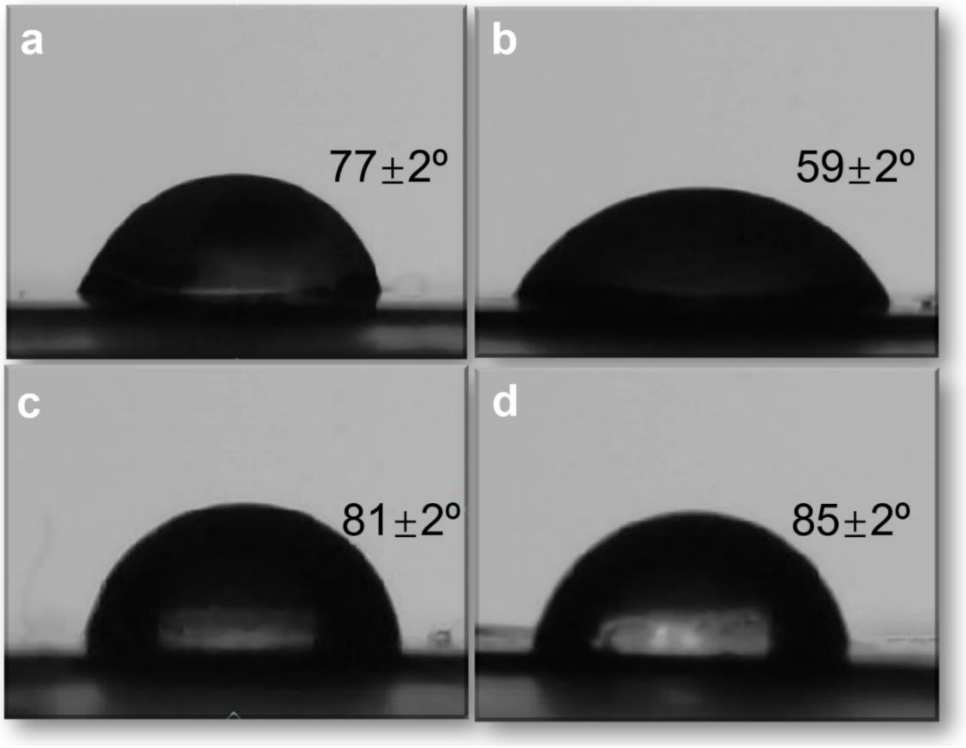

Figure 7.8. Static water contact angles of (a) pristine nylon membrane support, (b) GO membrane, (c) GO@Zn^{2+} membrane, and (d) GO/ZIF-8 membrane.

Apart from the nanochannel size, membrane permeation performance can also be largely affected by the wetting properties of the membrane surface. In the present work, both static and dynamic water contact angle (WCA) measurements were performed to characterize the membrane wetting property.

The static water contact angles for different membranes show that the WCA for the nylon membrane was ~77 ± 2º (Figure 7.8a), suggesting a hydrophilic nature of the support. After coated with a thin layer of graphene oxide, the WCA decreased to ~59 ± 2º (Figure 7.8b), indicating an enhancement in the membrane hydrophilicity. This can be attributed to the existence of abundant oxygen functionalities, such as hydroxyl groups and epoxy groups, on the GO nanosheets [1-3]. Surprisingly, the contact angle increased to ~81 ± 2º for the GO@Zn^{2+} membrane (Figure 7.8c). This could be explained by the ion exchange between zinc ions and protons (H^+) on oxygen functionalities of the GO nanosheets [31], leading to a decrease in the membrane hydrophilicity and thereby an increase in the contact angle. For the GO/ZIF-8 membranes, their WCA further increased to ~85 ± 2º (Figure 7.8d), which could be attributed to the hydrophobic nature of ZIF-8 crystals [30].

To further understand the surface wetting properties of these membranes, dynamic contact angles were also analyzed by recording contact angle variations for a period of 20 s. As shown in Figure 7.9a, a drop of water fully spread on the pristine nylon supports within ~15 s because of the fast diffusion of water into their porous microstructures. After coated with a thin layer of GO on the surface, the time for complete spreading of the water drop decreased to ~5 s (Figure 7.9b), indicating the significantly enhanced membrane hydrophilicity.

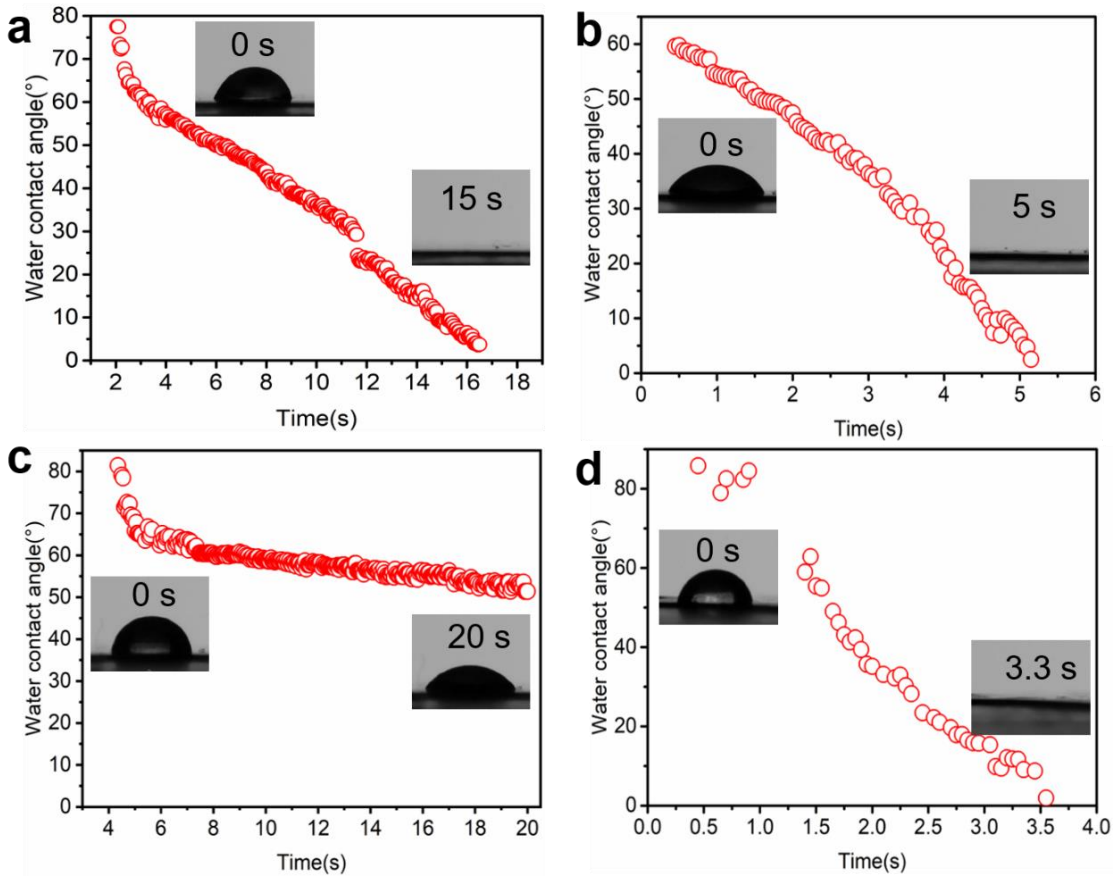

Figure 7.9. Dynamic water contact angles of (a) pristine nylon membrane support, (b) GO-coated membrane, (c) GO@Zn^{2+} membrane, and (d) GO/ZIF-8 membrane.

When the GO membrane was saturated with Zn^{2+}, the water droplet became more stable on the membrane surface with an equilibrium WCA of ~ 51 ± 2º at 20 s (Figure 7.9c), confirming a decreased membrane hydrophilicity. Interestingly, despite an increased static WCA of ~86º ± 2º for the GO/ZIF-8 membrane, the spreading time for the water drop dramatically decreased to ~3.3 s (Figure 7.9d). This is because of the intercalation of ZIF-8 nanocrystals and pre-crystalline domains, forming enlarged nanochannels between the adjacent GO nanosheets, which greatly promotes the spreading and diffusion of water, although the GO/ZIF-8 membrane surface was nearly hydrophobic.

The ultrafast water spreading and diffusion phenomenon on the GO/ZIF-8 membrane suggests that the solvent transport process through the membrane is significantly accelerated, further revealing the potential of these GO/ZIF-8 membranes for ultrafast molecular filtration.

7.3 Molecular separation performance

To verify these preliminary results, the molecular filtration performance of the GO/ZIF-8 membrane was first evaluated using organic dyes. The membrane prepared with 0.25 M Zn $(NO_3)_2$•$6H_2O$ was used for the following filtration tests as it showed more uniform crystal growth on the surface compared to the others. The permeances of membranes obtained at different fabrication steps were determined by calculating the volume of methanol permeate per unit time. Meanwhile, separation performances of these membranes were estimated using a rose bengal (RB, MW = 1017.6 g mol^{-1}) solution (5 μM). Methanol permeances, as well as calculated RB rejection, are summarized and compared in Figure 7.10a.

The concentration of RB in the solutions before and after the filtration tests was estimated by UV-Vis spectroscopy (Figure 7.10b and Figure 7.11). As can be seen in Figure 7.10a, the original GO membrane exhibited methanol permeance of ~125 L m^{-2} h^{-1} bar^{-1} with an RB rejection of ~98%, which is comparable to reported values. [20,23] After the intercalation of Zn^{2+}, the methanol permeance for the GO@Zn^{2+} membrane slightly increased to ~377 L m^{-2} h^{-1} bar^{-1} due to the small expansion of the nanostructures and wider interlay spacings.

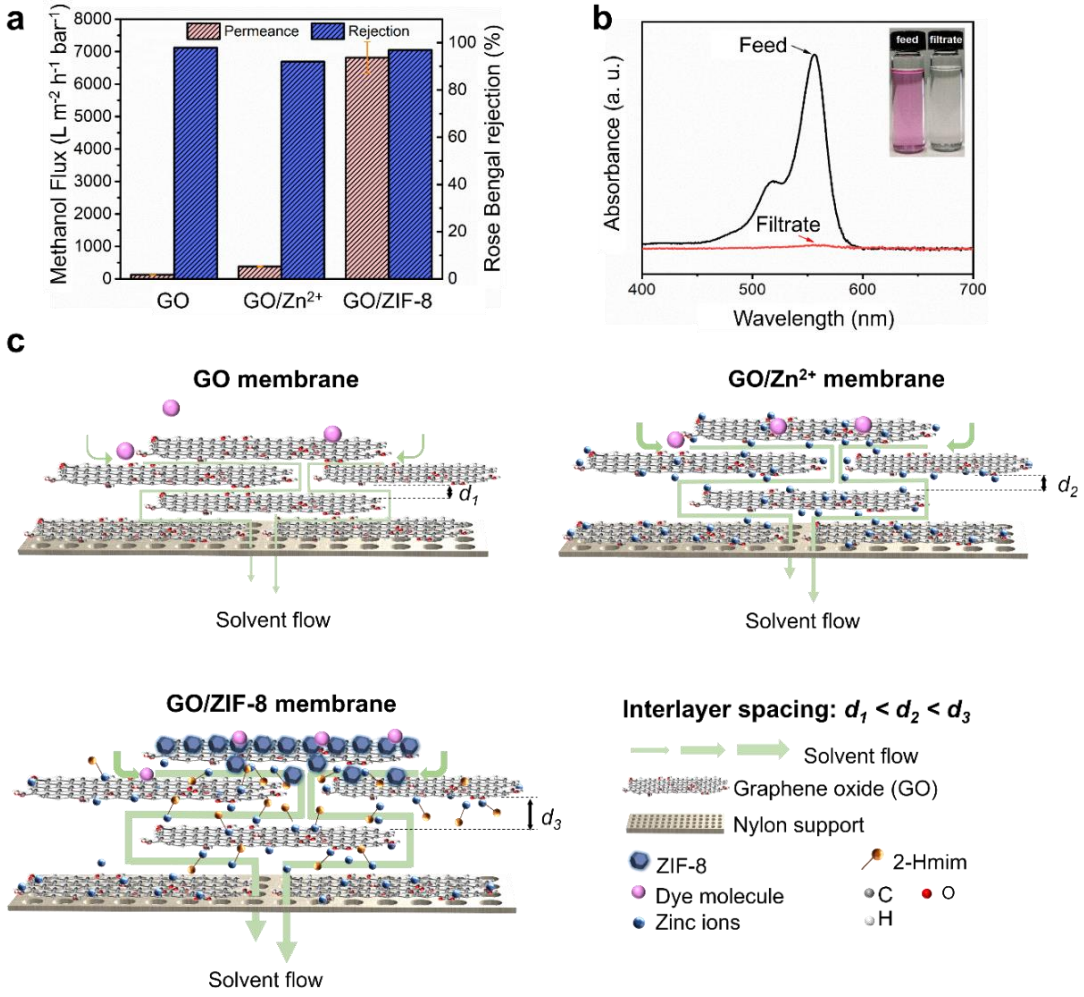

Figure 7.10. (a) Methanol permeance and rose bengal (RB) rejection of GO membrane, GO@Zn^{2+} membrane, and GO/ZIF-8 membrane; (b) UV-Vis absorption spectra of RB solution before and after filtrated through the GO/ZIF-8 membrane; the inset shows corresponding pictures of the RB feed, and filtrate solution; (c) schematic interpretation of the membrane structure and possible molecule transport mechanism of the GO membrane, GO@Zn^{2+} membrane and GO/ZIF-8 membrane.

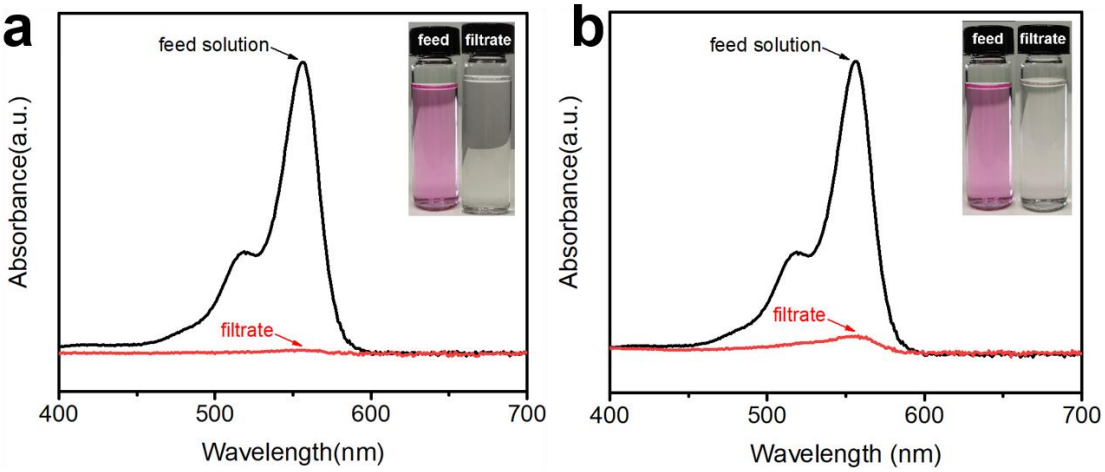

Figure 7.11. UV-Vis spectra of the Rose bengal solution before and after filtration through (a) the GO coated membrane and (b) the GO@Zn^{2+} membrane. The insets show corresponding pictures of the solutions.

This was accompanied by an RB rejection decrease to ~90%, indicating that the intercalated Zn^{2+} showed no apparent gating effect on the permeance of RB. However, for the GO/ZIF-8 membrane, the methanol permeance dramatically increased to ~6,816 L m^{-2} h^{-1} bar^{-1}, which is over 100 times higher than that of most commercial NF membranes [13,16,18]. More importantly, the membrane still exhibited a satisfactory RB rejection of ~97%, which is comparable to the original GO membranes, indicating that the GO/ZIF membranes possess an effective gating effect on the permeance of small organic dye molecules, whilst achieving ultrafast permeance of solvent.

In this work, the potential separation mechanisms of the GO membranes before and after in-situ MOF crystallization are schematically explained in Figure 7.10c. Typically, in a GO membrane, there are 2 forms of diffusional nanochannels, which are vertical

nanochannels, including in-plan nanosized defects/pores and the nanogaps formed between the edges of neighboring GO nanosheets, and horizontal nanochannels, which are also known as interlayer spacing (d_1). These nanochannels interconnect to form numerous tortuous molecular diffusion pathways [2]. Therefore, the transport of molecules in a lamellar GO membrane mainly depends on the size and length of these structural nanochannels, and size exclusion appears to be the dominant separation mechanism [2]. In principle, the interlayer spacing (d_1), defects on GO basal plane, and nanogaps between GO nanosheets must be small enough to reject undesired molecules to achieve good selectivity. An increase in any nanochannel size theoretically leads to a higher molecular diffusion rate but a sacrifice in the rejection rate. Similarly, in the GO@Zn^{2+} membranes, zinc ions adsorbed on the GO sheets via strong surface complexation with the oxygen functionalities [30]. Meanwhile, excessive zinc ions were intercalated between the interlayer capillaries, forming an increased interlayer spacing (d_2). Indeed, the solvent transport rate was more than two times higher than that of the GO membrane, while the RB retention rate was reduced to only 90%. In GO/MOF membranes, the coordination of 2-methylimidazole with the intercalated zinc ions in the lamellar structures leads to a further expansion of the nanochannels. Therefore, a further enlarged interlayer spacing (d_3) was formed, leading to a dramatic increase of the permeation flux. More importantly, the dye retention rate of the membrane can be maintained because of the strong interactions between dye molecules and the membrane. On the one hand, the ZIF-8 film formed on top of several nanolayers (“region I”) acts as a prescreening molecular sieve, which selectively adsorbs and

separates the organic dyes. This is because each aromatic imidazole ring in ZIF-8 structures consists of two double bonds and a pair of electrons from the pronated nitrogen, which could easily form π-π stacking interactions with aromatic rings of organic dyes [28]. Besides, charged molecules could be absorbed on the membrane via electrostatic interactions, as ZIF-8 crystals are positively charged [34]. On the other hand, the Zn^{2+}-2-methylimidazole coordinated pairs in the underneath lamellar structures ("region II") also contributed to the retention of dye molecules due to π-π stacking interactions formed between the 2-methylimidazole and aromatic rings in organic dyes [28]. In addition, nanochannels near the bottom regions of the GO membranes ("region III") were less expanded due to the "nutrition gradient" during the assembly process as discussed above.

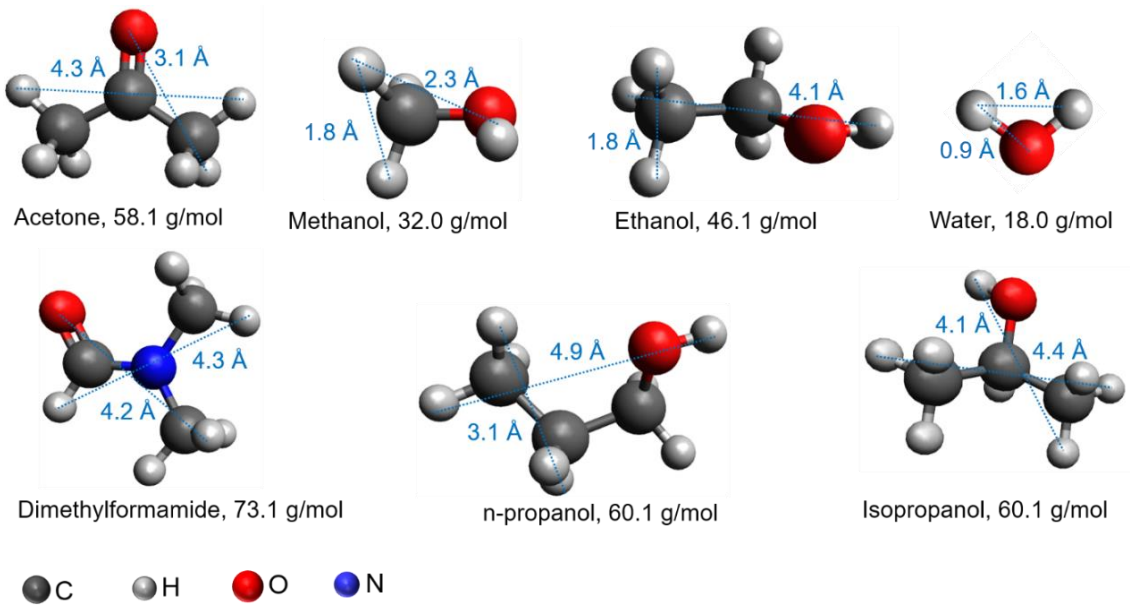

Figure 7.12. Molecular properties of the solvents used in the study. The molecular sizes were estimated using Avogadro software.

Therefore, nanochannels in this region could further contribute to the molecules retention by size exclusion. As a result, this membrane exhibited a dramatically enhanced solvent transport rate and also high retention of solutes, suggesting the permeance-rejection anti-trade-off behavior.

Table 7.1. Molecular properties of different solvents

Solvent	Formula	Molecular weight (g mol^{-1})	Molecular size (Å)	Viscosity (ŋ, mPa.s)
Acetone	C_3H_6O	58.1	4.3×3.1	0.32
Methanol	CH_3OH	32.0	2.3×1.8	0.61
Ethanol	C_2H_5OH	46.1	4.1×1.8	0.89
N,N-Dimethylmethanamide	C_3H_7NO	73.1	4.3×4.2	0.92
Water	H_2O	18.0	1.6×0.9	1.10
n-Propanol	C_3H_8O	60.1	4.9×3.1	1.96
Isopropanol	C_3H_8O	60.1	4.4×4.1	2.04

Many industrial separation processes involve the treatment of large quantities of organic liquid mixtures and thus require a stable membrane material for different organic solvents. The GO/ZIF-8 membranes synthesized in this work show great potential for ultrafast and sustainable molecular separations because of the high stability of GO and ZIF-8 in organic media [12, 14, 35, 36]. In this work, their permeation performance in various solvents was tested using the vacuum filtration apparatus under a low pressure of 0.5 bar (Figure 7.13a). The molecular structures and properties of these tested solvents are summarized in Figure 7.12 and Table 7.1. The permeance of different solvents as a function of their viscosity (ŋ) was plotted in Figure 7.13b.

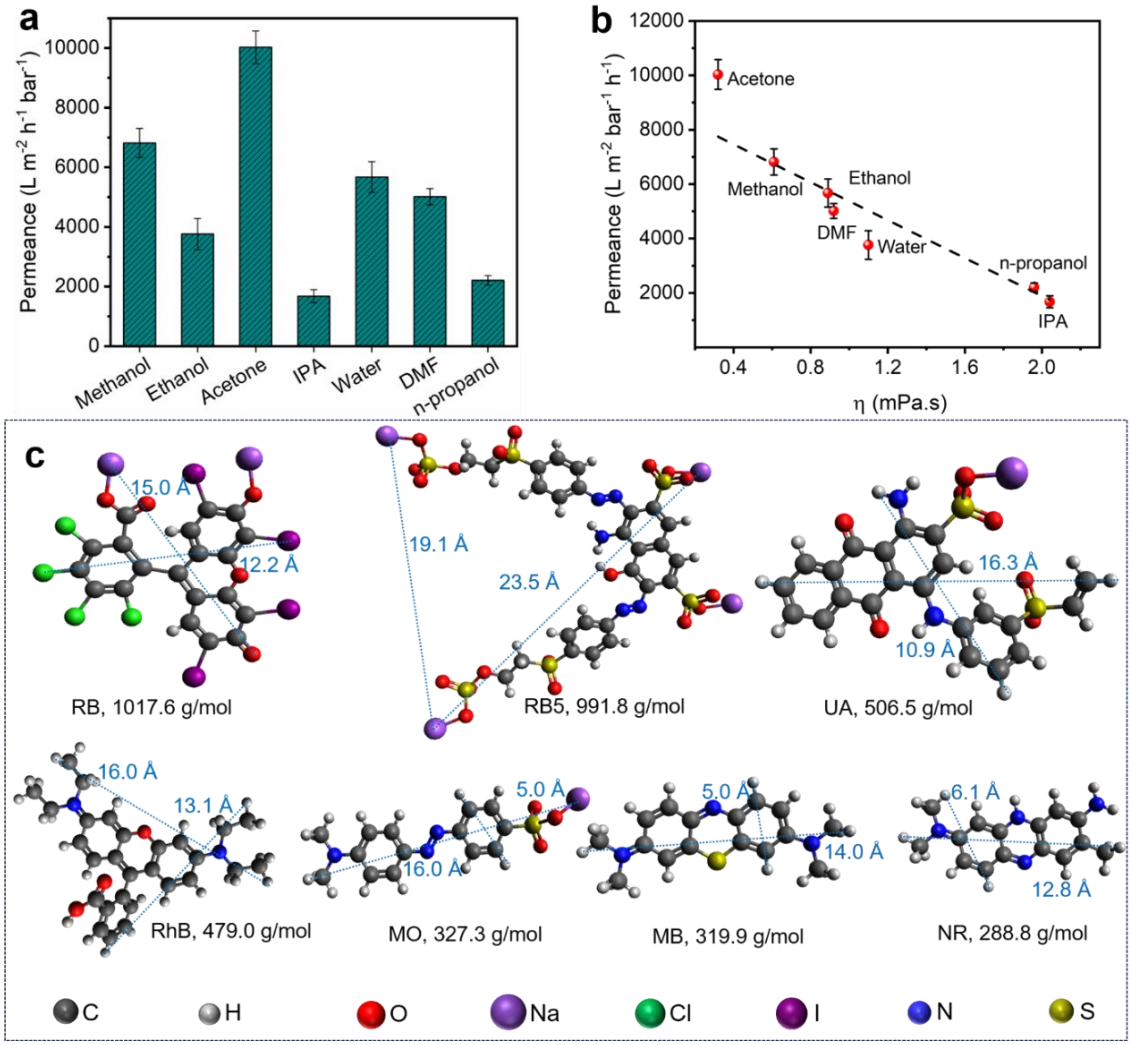

Figure 7.13. (a) Permeance of the GO/ZIF-8 membrane for different organic solvents; (b) solvent permeance plotted as a function of their viscosity; (c) molecular properties of different dyes tested in this work (molecular sizes were obtained using the Avogadro software).

As shown in Figure 7.13a, b, when the viscosity of the solvent increases, its permeance decreased almost linearly in GO/MOF membranes. However, these membranes have an acetone permeance up to ~10,030 L m^{-2} h^{-1} bar^{-1} and a methanol permeance up to

~6,816 L m^{-2} h^{-1} bar^{-1}, which are two orders of magnitude higher than conventional organic solvent nanofiltration materials reported in the literature.

Table 7.2. Molecular properties of different dyes

Dye	**Formula**	**Molecular weight (g mol^{-1})**	**Molecular size (nm)**	**Charge**	**Permeance (L m^{-2} h^{-1} bar^{-1})**	**Rejection (%)**
Methylene blue	$C_{16}H_{18}ClN_3S$	319.9	1.4×0.5	+	6576. 8	17
Neutral red	$C_{15}H_{17}ClN_4$	288.8	1.3×0.6	+	6653.7	35
Rhodamine B	$C_{28}H_{31}ClN_2O_3$	479.0	1.6×1.3	+	6257.2	57
Rose bengal	$C_{20}H_2Cl_4I_4Na_2O_5$	1017.6	1.5×1.2	-	6180.3	97
Reactive black 5	$C_{26}H_{21}N_5Na_4O_{19}S_6$	991.8	2.4×1.9	-	6025.8	97
Uniblue A	$C_{22}H_{15}N_2NaO_7S_2$	506.5	1.6×1.1	-	6279.1	89
Methyl orange	$C_{14}H_{14}N_3NaO_3S$	327.3	1.6×0.5	-	6505.5	24

To have a systematic understanding of the separation performance of GO/ZIF-8 membranes, their single and mixture molecular filtration tests (in methanol media) were further performed in the presence of organic dyes with various molecular sizes and different charge properties, i.e., methylene blue (MB), neutral red (NR), rhodamine B (RhB), rose bengal (RB), reactive black 5 (RB5), uniblue A (UA), and methyl orange (MO).

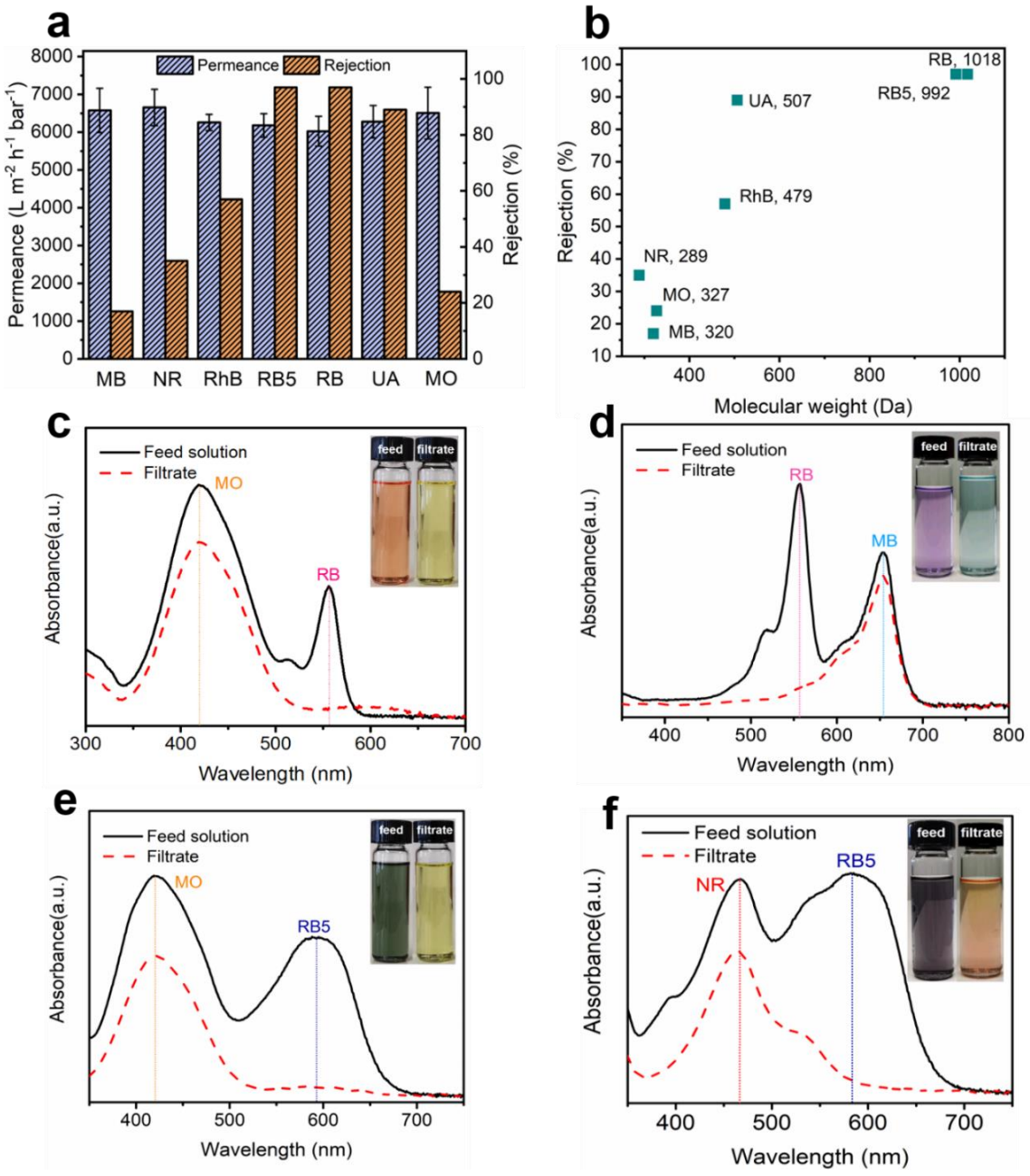

Figure 7.14. (a) Permeance and rejection of the GO/ZIF-8 membrane for different types of dyes; (b) rejection of different dyes as a function of molecular weight; UV-Vis spectra of mixed dye solutions and the filtrates of (c) rose Bengal (RB) and methyl orange (MO); (d)rose bengal (RB) and methylene blue (MB); (e)reactive black 5 (RB5)

and methyl orange (MO); (f) Reactive black 5 (RB5) and neutral red (NR). Insets in (c) to (f) show pictures of the corresponding feed mixture and filtrate solution.

Molecular structures and properties of the tested dyes are presented in Figure 7.13c and Table 7.2. The molecular structures and sizes were obtained using the Avogadro software. The results of organic solvent filtration tests in the presence of different organic dyes are plotted in Figure 7.14a, b, and their corresponding UV-Vis spectra of the feed and permeate samples are shown in Figure 7.15.

As suggested by Figure 7.14a, b, the dye rejection performance was influenced by the molecular properties of the solutes, including molecular weight and size, molecular shape, as well as charge properties. All tests show an ultrafast methanol flux (>6,000 L m^{-2} h^{-1} bar^{-1}) but with significantly different rejection rates. The membrane showed ~97% and ~98% rejection towards rose bengal (RB, 1018 Da) and reactive black 5 (RB5, 992 Da), respectively, and a lower rejection rate of ~90% for uniblue A (UA, 507 Da), which indicated that the cut-off size of the membrane lies in the range of 510~1020 Da. The rejection for RB5 is slightly higher than RB due to RB5 having a cross-shaped molecular structure which is more difficult to deform when passing through the membrane nanochannels, as well as a larger molecular size (2.4 nm x 1.9 nm) in comparison with RB (1.5 nm x 1.2 nm). Dye rejection performance of our GO/ZIF membranes was also influenced by the charge properties of the dyes. For instance, the membrane showed a much lower rejection of ~57% for the positively

charged rhodamine B (RhB, 479 Da), which has a similar molecular weight and size as UA, whose rejection rate was ~90%.

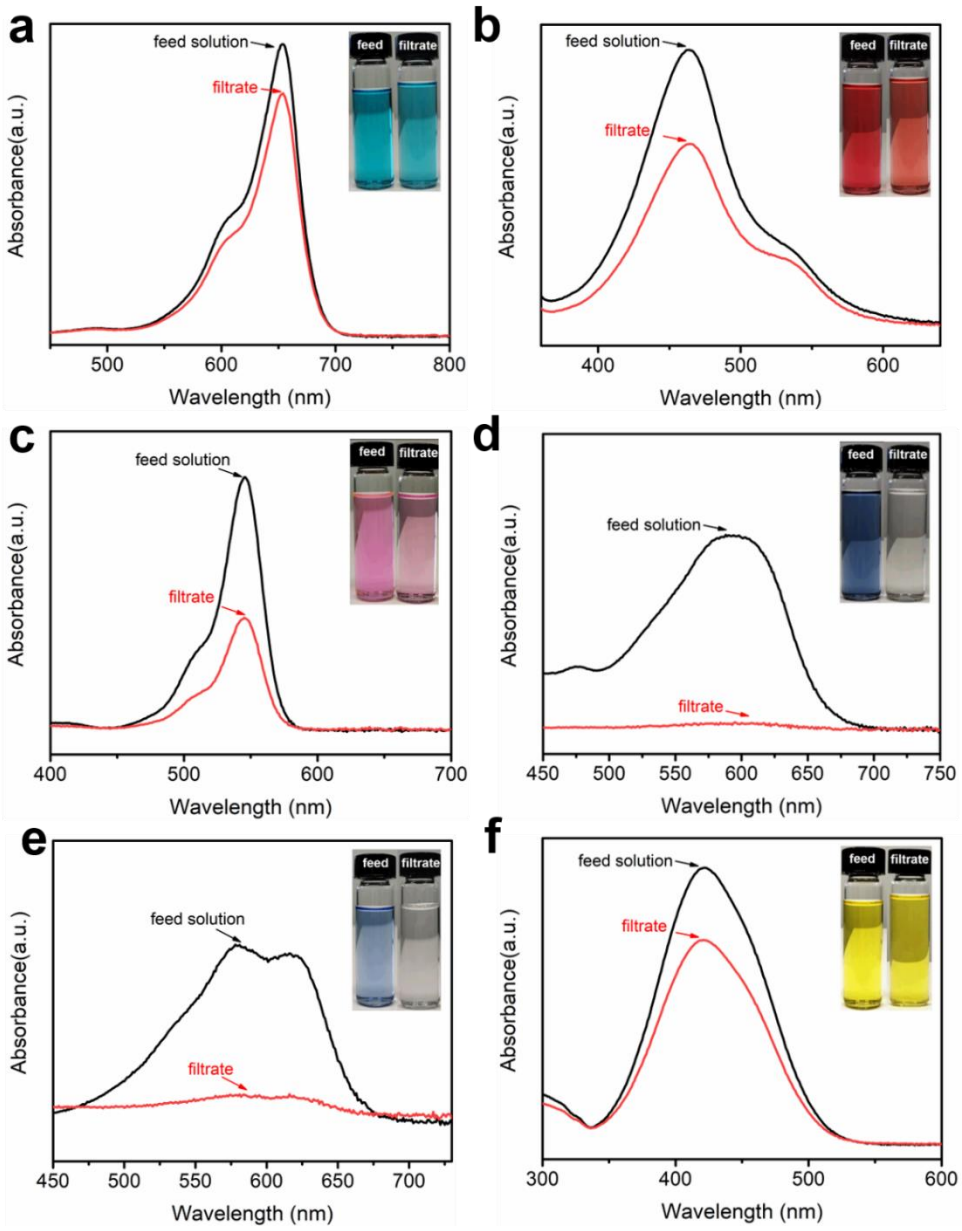

Figure 7.15. UV-Vis spectra of different dye solutions before and after filtrated through the GO/ZIF-8 membrane: (a) methylene blue; (b) neutral red; (c) rhodamine B; (d) reactive black 5; (e) uniblue A, and (f) methyl orange.

The much higher rejection of UA could be elucidated by the adsorption of anionic UA molecules in the positive membrane nanostructures via electrostatic interactions, as ZIF-8 crystals are positively charged [28].

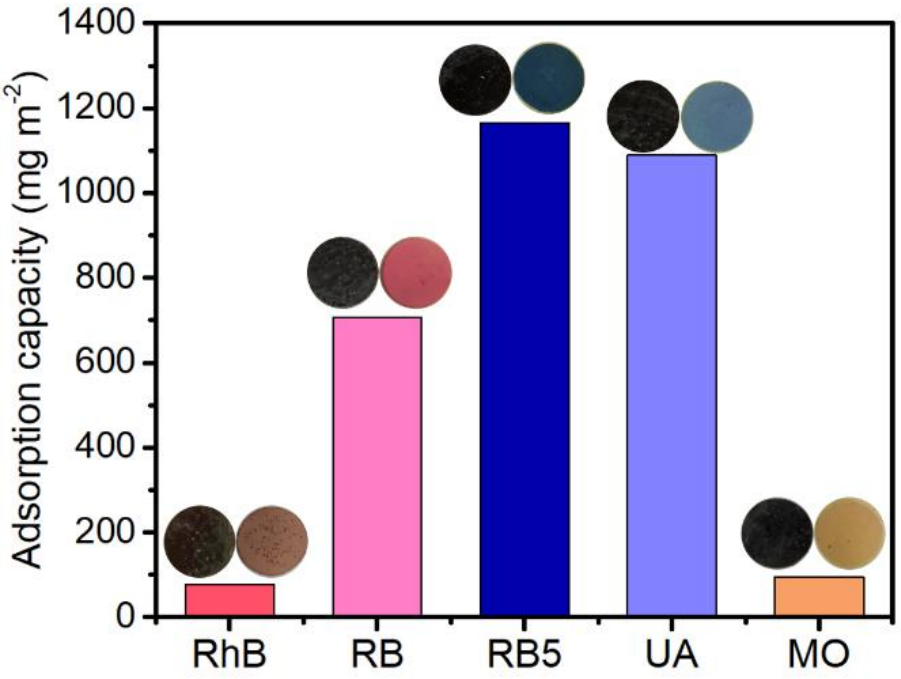

Figure 7.16. Adsorption capacity of the GO/ZIF-8 membrane surface for different types of organic dyes. The insets are the photos of the membrane surfaces before and after the adsorption test.

Five types of dyes, including rhodamine B (RhB), rose bengal (RB), reactive black 5 (RB5), uniblue A (UA), and methyl orange (MO), were employed for the adsorption test. The membrane samples were processed using a hollow punch with a diameter of 10 mm to ensure the same surface area for each sample. The adsorption experiment was performed by immersing the membrane samples with the same surface areas in 20 mL dye solutions with a concentration of 50 mg/L for 12 h. The concentration of dye in the

solution before and after the adsorption was monitored by UV-vis measurement. The amount of adsorbed dye was calculated by $Q = \frac{(C_0 - C_t) \times V}{A}$, where C_0 (mg/L) is the initial dye concentration in the feed solution, and C_t (mg/L) is the dye concentration in the solution after adsorption. V (L) is the solution volume, and A (m^2) is the effective surface area for adsorption. As shown in Figure 7.16, the adsorption test results indicated that the GO/ZIF-8 membrane have different adsorption performance towards different dyes. The adsorption capacity of the membrane for RB5, UA, RB, MO, and RhB were 1165.6 mg/ m^2, 1089.2 mg/ m^2, 707 mg/ m^2, 95.5 mg/ m^2 and 76.4 mg/ m^2, respectively. The relative higher adsorption capacity of the membrane for RB5 and UA could be attributed to the presence of both benzene rings and sulfonate groups in their molecules. On the one hand, the benzene rings could form π-π stacking interactions with imidazole rings in ZIF-8s on the membrane surface. On the other hand, sulfonate groups contributed to the strong electrostatic attraction between the dye molecules and the Zn (II) centers in ZIF-8.

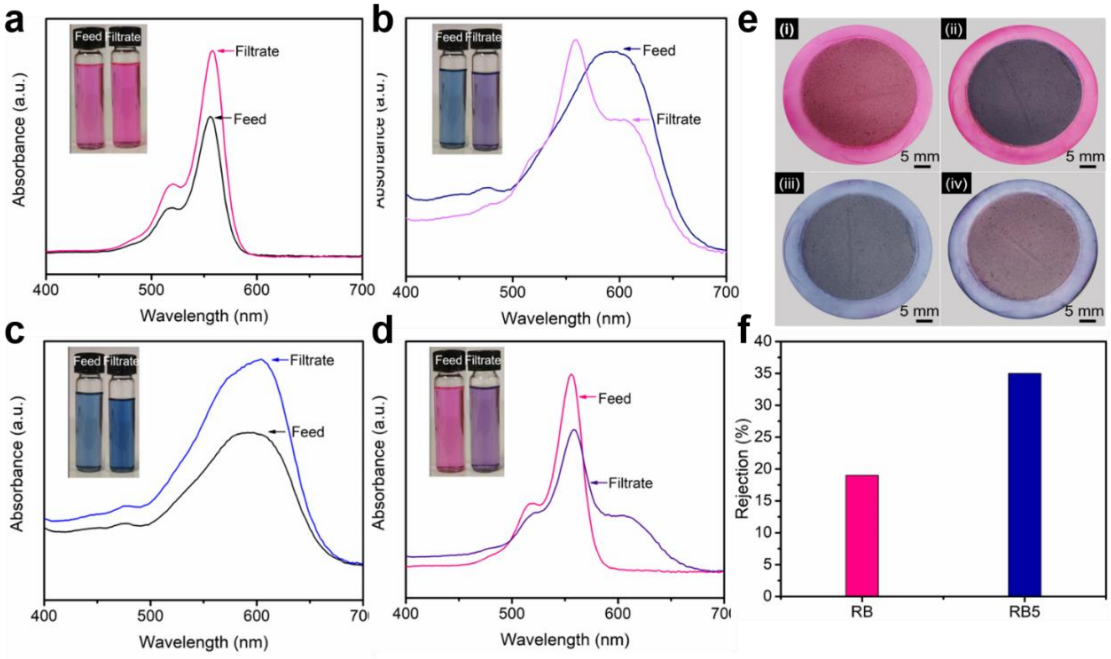

Figure 7.17. Separation performance of the GO/ZIF-8 membrane after saturated with dye adsorption. UV-Vis spectra of (a) rose bengal (RB) solution, and (b) reactive black 5 (RB5) solution before and after filtration through the rose bengal saturated GO/ZIF-8 membrane. UV-Vis spectra of (c) reactive black 5 solution, and (d) rose bengal solution before and after filtration through the reactive black 5 saturated GO/ZIF-8 membrane. The insets are pictures of the feed and filtrate solutions. (e) Photos of the dye saturated membranes: i) the rose bengal saturated GO/ZIF-8 membrane, ii) the rose bengal saturated GO/ZIF-8 membrane after separating reactive black 5, iii) the reactive black 5 saturated GO/ZIF-8 membrane, iv) the reactive black 5 saturated GO/ZIF-8 membrane after separating rose bengal. (f) Rejection of the dye saturated membrane for rose bengal and reactive black 5.

A rose bengal saturated membrane was first used for rejecting both rose bengal (RB)

and reactive black 5 (RB5) solutions. The results indicated that when RB solution (20 mL, 10 mg L^{-1}) was filtrated across the RB saturated membrane, an increased RB concentration was determined in the collected filtrate (Figure 7.17a). This was because some RB molecules that were initially adsorbed on the membrane were carried to the filtrate by the methanol flow. When RB5 solution (20 mL, 10 mg L^{-1}) was filtrated across the RB saturated membrane, a decreased RB5 concentration was determined in the collected filtrate (Figure 7.17b). Then an RB5 saturated membrane was also used for rejecting both RB and RB5 solutions. The results indicated that when RB5 solution was filtrated across the RB5 saturated membrane, an increased RB5 concentration was determined in the collected filtrate (Figure 7.17c). This was because some RB5 molecules that were initially adsorbed on the membrane were carried to the filtrate by the methanol flow. When RB solution (20 mL, 10 mg L^{-1}) was filtrated across the RB5 saturated membrane, a decreased RB concentration was determined in the collected filtrate (Figure 7.17d). Pictures of the dye saturated membranes were presented in Figure 7.17e. The results showed that after saturated with dyes adsorption, the GO/ZIF-8 membrane still remained ~20% and ~35% rejections for RB and RB5, respectively (Figure 7.17f), which was attributed to the size exclusion effect of the membrane.

Based on the above results, it is worth noting that the dye rejection of the GO/ZIF membrane is governed by electrostatic interactions and adsorption of organic dyes on the membrane surface and numerous nanochannels in the membrane, but also size/shape-selection of the well-regulated GO/ZIF nanostructures.

7.4 Mixture organic dye separation

In industry, it is very challenging to separate molecules with small sizes and shape differences from a heavily contaminated organic effluent. In this work, we confirmed these GO/ZIF-8 membranes have great potential for smart, selective separations of mixed dyes with completely different molecular properties. When an organic mixture of dyes was filtered through the membrane, larger dyes were removed from the organic solution, while smaller ones mostly remained in the filtrate. In this study, the selective separation performance of the GO/ZIF membranes was evaluated by filtering the methanol mixtures of rose bengal/methyl orange, rose bengal/ methylene blue, reactive black 5/methyl orange, or reactive black 5/neutral red. The concentrations of the dyes in the feed solution and the filtrate were determined by UV-Vis spectra (Figures 7.14 c-f). Their corresponding dye rejection ratios were shown in Figure 7.18. The insets show pictures of mixtures before and after filtration. It was observed that the feed mixture solutions exhibited the blend color of two dyes (e.g., purple for the mixture of RB and MB), while the filtrate only showed the color of dyes with a smaller size (blue for MB). These results indicate the successful separation of larger dye molecules from the binary mixtures of organic dyes. In the binary mixture of organic dyes, larger dye molecules like rose bengal (RB) and reactive black 5 (RB5) tended to form stronger interactions with both the membrane surface and numerous nanochannels inside the membrane than smaller dye molecules like methyl orange (MO), methylene blue (MB), and neutral red (NR). For example, in the case of RB/MO mixed dye solution, RB molecules tended to

form stronger π-π conjugation with aromatic imidazole rings in the membrane because they possess a larger number of aromatic rings than MO molecules. In the RB/MB mixed dye solution, apart from stronger π-π conjugation between RB molecules and aromatic imidazole rings, electrostatic interactions between the negatively charged RB molecules and the positively charged ZIF-8 on the membrane surface also contributed to the higher rejection rate of RB. Similarly, in the case of RB5/MO and RB5/NR mixed dye solutions, RB5 molecules tended to form stronger π-π conjugation with aromatic imidazole rings in the membrane because they possess a larger number of aromatic rings than MO and NR molecules. In addition, abundant sulfonate groups in RB5 molecules contributed to electrostatic interactions between RB5 molecules and the Zn (II) center in ZIF-8. As a result, the membrane demonstrated a higher rejection rate toward RB5 molecules in the binary mixture of RB5.

UV-Vis spectra of the filtrates further confirm that the concentration of larger dyes (RB and RB5) decreased to <5%, whereas the concentration of smaller dyes (MO, MB, and NR) remained almost unchanged (Figure 7.18).

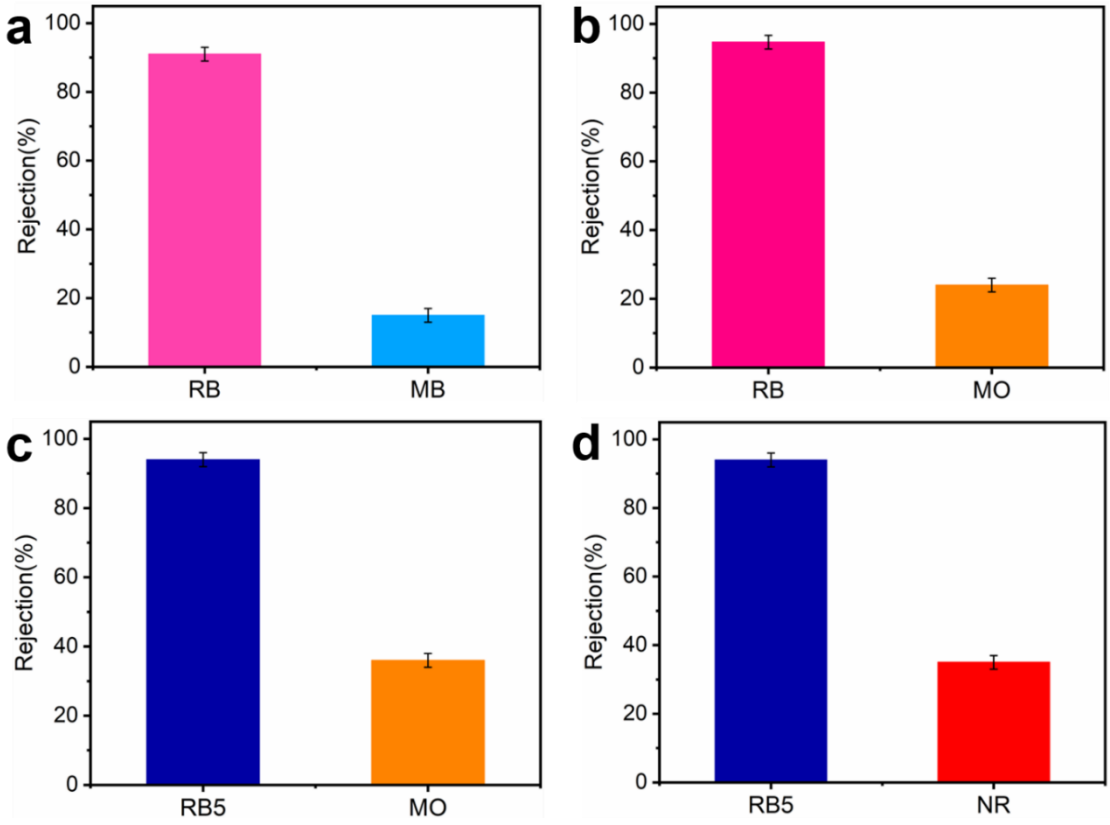

Figure 7.18. Rejection ratio of different dyes in the separation of binary dye solutions: (a) rose bengal and methylene blue; (b) rose bengal and methyl orange; (c) reactive black 5 and methyl orange; (d) reactive black 5 and neutral red.

Note that the permeance of organic solvent in each test was larger than 6,000 L m^{-2} h^{-1} bar^{-1}, which again confirms the excellent permeability of the GO/ZIF membranes.

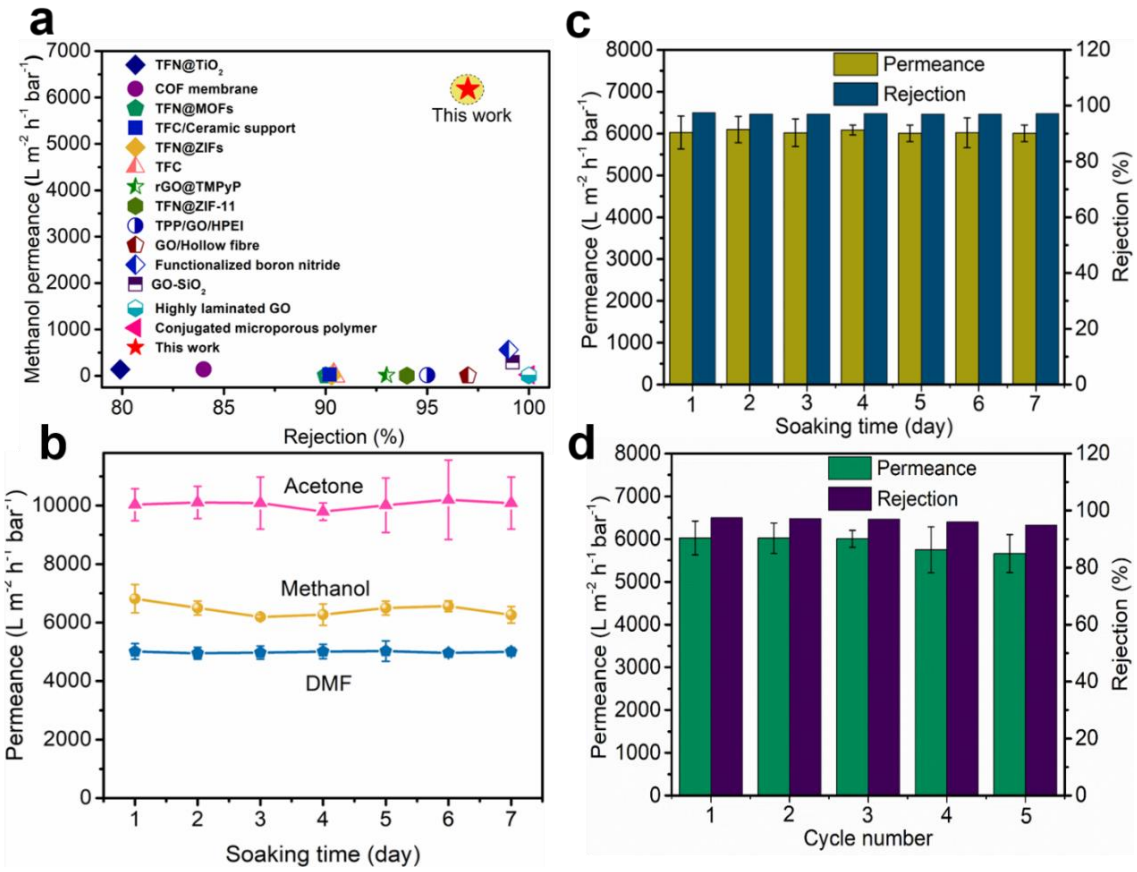

Figure 7.19. (a) Comparison of the nanofiltration performance of the GO/ZIF-8 membrane in methanol media versus previously reported membranes; (b) solvent permeance of the GO/ZIF-8 membrane after soaking in methanol for a different time; (c) permeance and dye rejection of the GO/ZIF-8 membrane after soaking in methanol for a different time; (d) permeance and dye rejection of the GO/ZIF-8 membrane in a cyclic test.

As illustrated in Figure 7.19a and Table 7.3, the membrane developed in this work showed superior performance compared to previously reported membranes.

Table 7.3. Comparison of previously reported membranes for dye rejection in methanol media

Membrane	Fabrication method	Probe molecule	Probe molecule MW (g mol^{-1})	Methanol permeance (L m^{-2} h^{-1} bar^{-1})	Rejection (%)	Ref.
TFC	Interfacial polymerization	Rose bengal	1017.6	3.04	90.4	[37]
TFN@MOFs	Interfacial polymerization	Styrene oligomers (PS)	232	3.9	90	[38]
TFN@ZIF-11	Interfacial polymerization	Sunset yellow	452.4	4.9	>90	[39]
TFN@ZIFs	Interfacial polymerization & dip-coating	Sunset yellow	452.4	8.7	90	[40]
Conjugated microporous polymer	Surface-initiated polymerization	Protoporphyrin-IX	562.7	22	100	[41]
TFC/ceramic support	Interfacial polymerization	Acid fuchsin	585.5	26.3	90.2	[42]
TFN@TiO_2	Interfacial polymerization	Bromothymol blue	624.4	139.4	79.9	[43]
GO/hollow fiber	Vacuum filtration	Methyl orange	327.3	3.97	97	[44]
Highly laminated GO	Vacuum filtration	Brilliant blue	792.9	7.5	100	[45]
rGO+TMPyP	Vacuum filtration	Evans blue	960.8	13	93	[46]
TPP/GO/HPEI	Pressure-assisted filtration	Alcian blue	1299	14.9	95	[47]
Solvent solvated rGO	Vacuum filtration	Acid fuchsin	585.5	78	70.1	[48]
COF membrane	Organic linkers baking	Rose bengal	1017.6	138	84	[49]
GO-SiO_2	Vacuum filtration	Brilliant blue	792.9	290.1	99.2	[50]
Functionalized boron nitride	Vacuum filtration	Evans blue	960.8	560	99	[51]
GO/ZIF-8	**Vacuum filtration**	**Rose bengal**	**1017.6**	**6816**	**97**	**This work**

The long-term separation stability of these GO/ZIF membranes, including the solvent resistance and cyclic performance, were studied in detail in this work. The solvent-resistant property of the membranes was evaluated by monitoring the variation of the permeance and RB rejection after soaking the membrane in methanol for different periods. The results show that after soaking the membrane in methanol for a long period of 7 days, the permeance for different solvents (acetone, methanol, DMF) (Figure 7.19b) and rejection for RB (Figure 7.19c) remained nearly unchanged throughout this period, indicating the good integrity and regeneration capability of these membranes. The additional cyclic separation tests using freshly synthesized GO/ZIF membranes revealed that the RB rejection remained greater than ~95% for 5 cycles of tests, with permeance higher than 5600 L m^{-2} h^{-1} bar^{-1}, suggesting the membrane has satisfactory stability and stable dye separation performance after a short period of intense tests as shown in Figure 7.19d. Overall, the ultrafast permeance, excellent rejection, and selective separation performance of the GO/ZIF-8 membranes make them highly promising for energy-efficient, ultrafast molecular separations.

7.5 Summary

In this chapter, a facile *in situ* assembly strategy was developed to fabricate graphene oxide and MOF nanocrystals composite membranes. The prepared membranes showed two-dimensional lamellar structures, and they were applied for molecular separations in organic solvents. The main results can be summarized as:

(1) Lamellar membranes composed of single-layer graphene oxide nanosheets and ZIF-8 nanocrystals were prepared using a vacuum filtration assisted *in situ* assembly strategy. The interlayer spacing of these lamellar membranes was determined by the intercalation of fully crystalline ZIF-8 nanocrystals, semi-crystalline ZIF domains, and simple coordinates of Zn^{2+}–2-methylimidazole in membrane nanostructures.

(2) The prepared GO/ZIF-8 membranes showed excellent permeability towards different types of organic solvents. The acetone permeance of the membrane was as high as ~10,030 L m^{-2} h^{-1} bar^{-1} and the methanol permeance was up to ~6,816 L m^{-2} h^{-1} bar^{-1}. The excellent solvent permeability was attributed to the expanded interlayer nanochannel size of the GO/ZIF-8 membranes.

(3) The GO/ZIF-8 membranes exhibited a high rejection rate of > 97% for organic dye molecules, such as rose bengal and reactive black 5. In addition, the GO/ZIF-8 membranes were capable of realizing the selective separation of binary dye mixtures, such as rose bengal/methylene blue, and reactive black 5/ methyl orange mixtures. The excellent rejection performance of the GO/ZIF-8 membranes was attributed to the combination of adsorption, electrostatic interaction, and size-sieving mechanisms.

7.6 References

[1] Kang Y., Xia Y., Wang H., Zhang X., 2D laminar membranes for selective water and ion transport, Adv. Funct. Mater., 2019; 29: 1-17.

[2] Liu G., Jin W., Xu N., Graphene-based membranes, Chem. Soc. Rev., 2015; 44: 5016-5030.

[3] Joshi R. K., Carbone P., Wang F. C., Kravets V. G., Su Y., Grigorieva I. V., Wu H. A., Geim A. K., Nair R. R., Precise and ultrafast molecular sieving through graphene oxide membranes, Science, 2014; 343: 752-754.

[4] Li H., Song Z., Zhang X., Huang Y., Li S., Mao Y., Ploehn H. J., Bao Y., Yu M., Ultrathin, molecular-sieving graphene oxide membranes for selective hydrogen separation, Science, 2013; 342: 95-98.

[5] Dikin D. A., Stankovich S., Zimney E. J., Piner R. D., Dommett G. H. B., Evmenenko G., Nguyen S. T., Ruoff R. S., Preparation and characterization of graphene oxide paper, Nature, 2007; 448: 457-460.

[6] Hu Y., Wei J., Liang Y., Zhang H., Zhang X., Shen W., Wang H., Zeolitic imidazolate framework/graphene oxide hybrid nanosheets as seeds for the growth of ultrathin molecular sieving membranes, Angew. Chemie. Int. Ed., 2016; 55: 2048-2052.[7] Yang H., Yang L., Wang H., Xu Z., Zhao Y., Luo Y., Nasir N., Song Y., Wu H., Pan F., Jiang Z., Covalent organic framework membranes through a mixed-dimensional assembly for molecular separations, Nat. Commun., 2018; 10: 1-10.

[8] Ding L., Wei Y., Wang Y., Chen H., Caro J., Wang H., A two-dimensional lamellar

membrane: MXene nanosheet stacks, Angew. Chemie Int. Ed., 2017; 56: 1825-1829.

[9] Wang J., Chen P., Shi B., Guo W., Jaroniec M., Qiao S. Z., A regularly channeled lamellar membrane for unparalleled water and organics permeation, Angew. Chem. Int. Ed., 2018; 57: 6814-6818.

[10] Wang Y., Li L., Wei Y., Xue J., Chen H., Ding L., Caro J., Wang H., Water transport with ultralow friction through partially exfoliated g-C3N4 nanosheet membranes with self-supporting spacers, Angew. Chem. Int. Ed., 2017; 56: 8974-8980.

[11] Mi B., Graphene oxide membranes for ionic and molecular sieving, Science, 2014; 343: 740-742.

[12] Wang S., Mahalingam D., Sutisna B., Nunes S. P., 2D-dual-spacing channel membranes for high performance organic solvent nanofiltration, J. Mater. Chem. A., 2019; 7: 11673-11682.

[13] Thebo K. H., Qian X., Zhang Q., Chen L., Cheng H. M., Ren W., Highly stable graphene-oxide-based membranes with superior permeability, Nat. Commun. 2018; 9: 1-8.

[14] Dreyer D. R., Park S., Bielawski C. W., Ruoff R. S., The chemistry of graphene oxide, Chem. Soc. Rev., 2010; 39: 228-240.

[15] Yeh C. N., Raidongia K., Shao J., Yang Q. H., Huang J., On the origin of the stability of graphene oxide membranes in water, Nat. Chem., 2015; 7: 166-170.

[16] Gao S. J., Qin H., Liu P., Jin J., SWCNT-intercalated GO ultrathin films for ultrafast separation of molecules, J. Mater. Chem. A., 2015; 3: 6649-6654.

[17] Liu J., Wang N., Yu L. J., Karton A., Li W., Zhang W., Guo F., Hou L., Cheng Q.,

Jiang L., Weitz D. A., Zhao Y., Bioinspired graphene membrane with temperature tunable channels for water gating and molecular separation, Nat. Commun., 2017; 8: 1-9.

[18] Goh K., Jiang W., Karahan H. E., Zhai S., Wei L., Yu D., Fane A. G., Wang R., Chen Y., All-carbon nanoarchitectures as high-performance separation membranes with superior stability, Adv. Funct. Mater., 2015; 25: 7348-7359.

[19] Gao T., Wu H., Tao L., Qu L., Li C., Enhanced stability and separation efficiency of graphene oxide membranes in organic solvent nanofiltration, J. Mater. Chem. A., 2018; 6: 19563-19569.

[20] Han Y., Jiang Y., Gao C., High-flux graphene oxide nanofiltration membrane intercalated by carbon nanotubes, ACS Appl. Mater. Interfaces, 2015; 7: 8147-8155.

[21] Tang X., Qu Y., Deng S. L., Tan Y. Z., Zhang Q., Liu Q., Fullerene-regulated graphene oxide nanosheet membranes with well-defined laminar nanochannels for precise molecule sieving, J. Mater. Chem. A., 2018; 6: 22590-22598.

[22] Huang H., Song Z., Wei N., Shi L., Mao Y., Ying Y., Sun L., Xu Z., Peng X., Ultrafast viscous water flow through nanostrand channelled graphene oxide membranes, Nat. Commun., 2013; 4: 1-9.

[23] Lu G., Li S., Guo Z., Farha O. K., Hauser B. G., Qi X., Wang Y., Wang X., Han S., Liu X.,. Duchene J. S, Zhang H., Zhang Q., Chen X., Ma J., Loo S. C. J., Wei W. D., Yang Y., Hupp J. T., Huo F., Imparting functionality to a metal–organic framework material by controlled nanoparticle encapsulation, Nat. Chem., 2012; 4: 310-316.

[24] Farha O. K., Yazaydin A. Ö., Eryazici I., Malliakas C. D., Hauser B. G., Kanatzidis

M. G., Nguyen S. T., Snurr R. Q., Hupp J. T., De novo synthesis of a metal–organic framework material featuring ultrahigh surface area and gas storage capacities, Nat. Chem., 2010; 2: 944-948.

[25] Furukawa H., Cordova K. E., O'Keeffe M., Yaghi O. M., The chemistry and applications of metal-organic frameworks, Science, 2013; 341: 1230444.

[26] Fortea-Pérez F. R., Mon M., Ferrando-Soria J., Boronat M., Leyva-Pérez A., Corma A., Herrera J. M., Osadchii D., Gascon J., Armentano D., Pardo E., The MOF-driven synthesis of supported palladium clusters with catalytic activity for carbene-mediated chemistry, Nat. Mater., 2017; 16: 760-766.

[27] Zhang H., Liu X., Wu Y., Guan C., Cheetham A. K., Wang J., MOF-derived nanohybrids for electrocatalysis and energy storage: current status and perspectives, Chem. Commun., 2018; 54: 5268-5288.

[28] Abdi J., Vossoughi M., Mahmoodi N. M., Alemzadeh I., Synthesis of metal-organic framework hybrid nanocomposites based on GO and CNT with high adsorption capacity for dye removal, Chem. Eng. J., 2017; 326: 1145-1158.

[29] Ying Y., Liu D., Zhang W., Ma J., Huang H., Yang Q., Zhong C., High-flux graphene oxide membranes intercalated by metal–organic framework with highly selective separation of aqueous organic solution, ACS Appl. Mater. Interfaces, 2017; 9: 1710-1718.

[30] Zhang P., Gong J. L., Zeng G. M., Song B., Liu H. Y., Huan S. Y., Li J., Ultrathin reduced graphene oxide/MOF nanofiltration membrane with improved purification performance at low pressure, Chemosphere, 2018; 204: 378-389.

[31] Park S., Lee K. S., Bozoklu G., Cai W., Nguyen S. B. T., Ruoff R. S., Graphene oxide papers modified by divalent ions—enhancing mechanical properties via chemical cross-linking, ACS Nano., 2008; 2: 572-578.

[32] Wang H., Yuan X., Wu Y., Huang H., Zeng G., Liu Y., Wang X., Lin N., Qi Y., Adsorption characteristics and behaviors of graphene oxide for Zn (II) removal from aqueous solution, Appl. Surf. Sci., 2013; 279: 432-440.

[33] Sitko R., Turek E., Zawisza B., Malicka E., Talik E., Heimann J., Gagor A., Feist B., Wrzalik R., Adsorption of divalent metal ions from aqueous solutions using graphene oxide, Dalton. Trans., 2013; 42: 5682-5689.

[34] Khan M. S., Khalid M., Shahid M., What triggers dye adsorption by metal organic frameworks? The current perspectives, Mater. Adv., 2020; 1: 1575-1601.

[35] Nie L., Goh K., Wang Y., Lee J., Huang Y., Karahan H. E., Zhou K., Guiver M. D., Bae T.H., Realizing small-flake graphene oxide membranes for ultrafast size-dependent organic solvent nanofiltration, Sci. Adv., 2020; 6: eaaz9184.

[36] Li Y., Li J., Soria R.B., Volodine A., Bruggen B. V., Aramid nanofiber and modified ZIF-8 constructed porous nanocomposite membrane for organic solvent nanofiltration, J. Memb. Sci., 2020; 603: 118002.

[37] Hai Y., Zhang J., Shi C., Zhou A., Bian C., Li W., Thin film composite nanofiltration membrane prepared by the interfacial polymerization of 1, 2, 4, 5-benzene tetracarbonyl chloride on the mixed amines cross-linked poly (ether imide) support, J. Memb. Sci., 2016; 520: 19-28.

[38] Sorribas S., Gorgojo P., Téllez C., Coronas J., Livingston A.G., High flux thin film

nanocomposite membranes based on metal–organic frameworks for organic solvent nanofiltration, J. Am. Chem. Soc. 2013; 135: 15201-15208.

[39] Echaide-Górriz C., Navarro M., Téllez C., Coronas J., Simultaneous use of MOFs MIL-101 (Cr) and ZIF-11 in thin film nanocomposite membranes for organic solvent nanofiltration, Dalt. Trans. 2017; 46: 6244-6252.

[40] Sarango L., Paseta L., Navarro M., Zornoza B., Coronas J., Controlled deposition of MOFs by dip-coating in thin film nanocomposite membranes for organic solvent nanofiltration, J. Ind. Eng. Chem. 2018; 59: 8-16.

[41] Liang B., Wang H., Shi X., Shen B., He X., Ghazi Z.A., Khan N.A., Sin H., Khattak A.M., Li L., Tang Z., Microporous membranes comprising conjugated polymers with rigid backbones enable ultrafast organic-solvent nanofiltration, Nat. Chem. 2018; 10: 961-967.

[42] Xia L., Ren J., Weyd M., McCutcheon J.R., Ceramic-supported thin film composite membrane for organic solvent nanofiltration, J. Memb. Sci. 2018; 563: 857-863.

[43] Peyravi M., Jahanshahi M., Rahimpour A., Javadi A., Hajavi S., Novel thin film nanocomposite membranes incorporated with functionalized TiO2 nanoparticles for organic solvent nanofiltration, Chem. Eng. J. 2014; 241: 155-166.

[44] Aba N.F.D., Chong J.Y., Wang B., Mattevi C., Li K., Graphene oxide membranes on ceramic hollow fibers–Microstructural stability and nanofiltration performance, J. Memb. Sci. 2015; 484: 87-94.

[45] Yang Q., Su Y., Chi C., Cherian C.T., Huang K., Kravets V.G., Wang F.C., Zhang

J.C., Pratt A., Grigorenko A.N., Guinea, F., Ultrathin graphene-based membrane with precise molecular sieving and ultrafast solvent permeation, Nat. Mater. 2017; 16: 1198-1202.

[46] Gao T., Huang L., Li C., Xu G., Shi G., Graphene membranes with tunable nanochannels by intercalating self-assembled porphyrin molecules for organic solvent nanofiltration, Carbon. 2017; 124: 263-270.

[47] Hua D., Chung T.S., Polyelectrolyte functionalized lamellar graphene oxide membranes on polypropylene support for organic solvent nanofiltration, Carbon. 2017; 122: 604-613.

[48] Huang L., Chen J., Gao T., Zhang M., Li Y., Dai L., Qu L., Shi G., Reduced graphene oxide membranes for ultrafast organic solvent nanofiltration, Adv. Mater. 2016; 28: 8669-8674.

[49] Kandambeth S., Biswal B.P., Chaudhari H.D., Rout K.C., Kunjattu H S., Mitra S., Karak S., Das A., Mukherjee R., Kharul U.K., Banerjee, R., Selective molecular sieving in self-standing porous covalent-organic-framework membranes, Adv. Mater. 2017; 29: 1603945.

[50] Wang S., Mahalingam D., Sutisna B., Nunes S.P., 2D-dual-spacing channel membranes for high performance organic solvent nanofiltration, J. Mater. Chem. A. 2019; 7: 11673-11682.

[51] Chen C., Wang J., Liu D., Yang C., Liu Y., Ruoff R.S., Lei W., Functionalized boron nitride membranes with ultrafast solvent transport performance for molecular separation, Nat. Commun. 2018; 9: 1-8.

Chapter 8: Conclusions and Future Work

To realize an energy-efficient liquid separation process demands the development of materials with special properties and nanostructures, outstanding stabilities, and superior separation characteristics. The major goals of this PhD work are to advance the development of functional materials for energy-efficient liquid separations by investigating a series of bioinspired materials and membranes. Overall, this project developed new fabrication routes for the preparation of bioinspired membranes, proposed new energy-efficient separation processes for liquid separation, and provided important insights into the logics for the design of bioinspired materials.

An energy-effective and time-saving methods were firstly explored to develop zeolitic imidazolate frameworks (ZIFs) coated mesh films. The mesh films exhibited bioinspired superwetting surface properties and were employed for highly efficient oil/water separations. To enhance the water stability of ZIFs, a novel oil/water interfacial assembly strategy was developed to prepare ZIFs with superhydrophobic surface properties. Furthermore, a simple sequential drop casting method was explored to prepare the superhydrophobic ZIFs-coated polymer membranes. As-prepared membranes were effective for dye molecules separation in organic solvent. Another important factor influencing the energy-efficient liquid separation is the permeation rate of the membrane materials. Membranes with ultrafast solvent transport rate can largely reduce the energy consumption in the separation processes. To further enhance the

membrane permeability, graphene oxide (GO)/ZIF composite membranes with a nacre-like lamellar structure were developed. The obtained lamellar membranes exhibited well-defined nanochannels with ultrafast solvent transport. Moreover, these membranes provided selective molecular separation performance for various binary dye mixtures with high separation efficiencies. The main conclusions in this PhD work are summarized in this chapter.

8.1 Superwetting mesh for oil/water mixture separation

Novel ZIF-L nanoplates coated stainless steel mesh films with hierarchical porous structures have been successfully fabricated via a rapid seeding and secondary growth process under ambient conditions, i.e., 1 h at 25 °C and 101 kPa. The as-synthesized meshes showed extraordinary in-air superamphiphilicity, underwater superoleophobicity, and underoil superhydrophobicity. The intelligent ZIF-L mesh films exhibited switchable superwetting properties and demonstrated superior separation performance for immiscible oil/water mixture separation with a permeation flux as high as ~1.35×10^5 L m^{-2} h^{-1} and an oil (or water) rejection rate of above 99.99%. The oil (or water) intrusion pressure was found up to ~2.0 kPa, which is higher than most reported values for mesh-based materials. The energy-efficient, and time-saving fabrication route reported in the present work is of vital importance in the rapid and economical mass production of ZIF-based materials.

8.2 Lamellar membrane for molecular separation

A facile and direct *in situ* assembly strategy for the synthesis of 2D lamellar membranes with superior permeability by combining the advantages of SLGO nanosheets and MOF nanocrystals. In these membranes, the fully crystalline ZIF-8 nanocrystals, semi-crystalline ZIF domains, and simple coordinates of Zn^{2+}−2-methylimidazole intercalated in membrane nanostructures contributed to the excellent membrane permeability and organic dye rejection. These membranes exhibited an inspiring ultrahigh acetone permeance up to ~10,030 L m^{-2} h^{-1} bar^{-1} and methanol permeance up to ~6,816 L m^{-2} h^{-1} bar^{-1} while maintaining a high rejection (>97%) of organic molecules which have an Mw > 900 g mol^{-1}, e.g., RB and RB5. The excellent rejection performance is ascribed to the combination of adsorption, electrostatic interaction, and size-sieving mechanisms. These membranes also demonstrated outstanding smart, selective separation performance for binary dye mixtures with excellent solvent permeation and cyclic performance, which make them highly promising for a wide range of industrial applications. Overall, this work provides a valuable understanding in the design of hybrid lamellar GO membranes that overcome the permeance-rejection trade-off for ultrafast molecular filtration.

8.3 Superhydrophobic MOF nanotubes with enhanced stability

An oil/water interfacial assembly method was designed to prepare oleic acid (OA) decorated ZIF nanostructures, denoted as ZIF−OAs. Two-dimensional ZIF−OA layers

were obtained through the oil/water interfacial assembly method at room temperature. The self-scrolling of the two-dimensional ZIF−OAs was driven by the micellization of the amphiphilic oleic acid molecules which are decorated on the surface of the crystals. The prepared ZIF nanostructures showed superhydrophobic surface properties with water contact angles up to ~149º ± 2º. More importantly, they demonstrated exceptional stability under water environment with morphologies unaffected after being soaked in deionized water for up to 30 days, and in pH = 3 HCl solution for up to 10 days.

8.4 Superwetting Janus membrane for molecular separation

A contra-diffusion assisted oil/water interfacial preparation method and a simple sequential drop-casting method were designed to prepare ZIF−OAs coated membranes. In the contra-diffusion assisted oil/water interfacial preparation method, selective crystal growth on the membrane surface was achieved by simply changing the adding sequence of the water phase and organic phase into the diffusion cells. However, the prepared membrane showed insufficient stability under a liquid environment. In the sequential drop-casting method, the prepared membrane surface was uniformly covered by two-dimensional ZIF layers and one-dimensional ZIF nanotubes when the membrane was cured under room temperature and 50 ℃, respectively. The prepared ZIF−OAs coated membranes showed interesting Janus surface wetting properties with one surface hydrophilic (WCA of ~40º ± 2º) while the other surface superhydrophobic (WCA of ~150º ± 2º). The ZIF−OAs coated membrane was effective for molecular separation from the organic solvent with rejections above 90% for organic dyes.

8.5 Contributions

The results presented in this thesis make a valuable contribution to promoting the large-scale preparation of bioinspired materials and membranes. The results obtained in this work contributed to promoting the practical application of bioinspired membranes for challenging liquid separations. For example, the seeding and secondary growth method developed in chapter 4 provides a facile preparation route for bioinspired superwetting mesh films. The oil/water interfacial assembly method designed in chapter 5 provides a direct synthesis route for bioinspired superhydrophobic MOF nanomaterials. The sequential drop-casting method developed in chapter 6 provides a simple preparation approach to bioinspired superwetting porous membranes. The lamellar membrane developed in chapter 7 provides a promising candidate for ultrafast selective molecular separations.

8.6 Future work

The research undertaken in this PhD study successfully developed a series of bioinspired film and membrane materials for energy-efficient liquid separations. Although the main results represented are inspiring, there are still some aspects of the research requiring further improvements. Suggestions for future work are summarized as follows:

8.6.1 ZIF-L coated materials for miscible oil/water separations

In this PhD work, a rapid seeding and secondary growth process was applied to prepare

ZIF-L coated mesh films under ambient conditions. It is expected that this time-saving and energy-efficient preparation procedure can be applied to prepare various ZIF-L coated porous materials. For example, a similar preparation strategy can be used to fabricate ZIF-L coated porous sponge materials with bioinspired superwetting properties. The ZIF-L coated sponge materials are promising for oil/water separation by the selective oil adsorption from the oil/water mixture. In addition, the ZIF-L coated mesh films were employed for the separation of immiscible oil/water mixtures in this study. However, industrial oily wastewater usually exists in the form of miscible oil/water emulsions. It is expected that ZIF-L coated porous flat/hollow fiber polymer membranes can be prepared using a similar strategy. These ZIF-L coated membranes are expected to be effective for more challenging oil/water separation, i.e., surfactant stabilized oil/water emulsion separations.

8.6.2 Chemical stability enhancement of ZIF-L coated materials

Another aspect of this study that requires further optimization is the enhancement of the stability of ZIF-L coated materials under the water environment. Like the majority of MOFs materials reported so far, ZIF-L coated meshes prepared in this study still have limited stability when exposed to water content, especially in a strongly acidic or alkaline environment. This instability issue is due to the weak metal-ligand coordination bonding of ZIF-L. Enhanced chemical stability of ZIF-L coated materials would contribute greatly to promoting their practical applications in industrial processes. Therefore, it is worth investigating feasible methods for improving the chemical

stability of ZIF-L coated membrane materials in the future. Moreover, it is meaningful to systematically investigate the mechanism of the ZIF-L dissolution or transformation under the water environment with various pH conditions. These fundamental studies would provide significant insights into the design of stable ZIF-L based materials for liquid separations in the future.

8.6.3 ZIF−OA coated materials for switchable oil/water separations

In this PhD work, a simple sequential drop-casting method was developed to coat water-stable ZIF−OA nanostructures onto the porous membrane surface. The ZIF−OA membrane was applied for molecular separation in organic solvents. For future work, it is expected that this sequential drop-casting method can be applied to prepare ZIF−OA coated membranes with larger pore sizes than in this work, or porous sponges for oil/water separations. Due to the excellent superhydrophobicity of ZIF−OA nanostructures, the prepared porous materials are likely to exhibit interesting Janus surface property with asymmetric wettability. Therefore, these ZIF−OA coated materials are promising for switchable oil/water separations with one side effective for oil-removing and the other side effective for water-removing. In addition, it would be meaningful to investigate methods to improve the mechanical stability of these ZIF−OA coated materials in the future.

8.6.4 GO/MOF lamellar membranes for water treatment

Another aspect that requires further improvement in this PhD study is the investigation

of GO/MOF composite lamellar membranes for continuous water treatment. In this work, a facile vacuum-assisted *in situ* assembly strategy was developed to prepare GO/ZIF-8 composite lamellar membranes for molecular separations in organic solvents. It is expected that this facile method can be applied to intercalate other types of MOF crystals inside the GO interlayers, producing new GO/MOF lamellar membranes with controllable interlayer spacing. Water stable MOFs can be preferentially chosen as the intercalated objects. In this case, the prepared GO/MOF lamellar membranes are promising for challenging water treatment, such as ions separation.